SEISMIC VULNERABILITY OF RC FRAME AND SHEAR WALL STRUCTURES IN SINGAPORE

LI ZHIJUN

NATIONAL UNIVERSITY OF SINGAPORE

2006

SEISMIC VULNERABILITY OF RC FRAME AND SHEAR WALL STRUCTURES IN SINGAPORE

LI ZHIJUN

(*M.ENG., B.ENG., SOUTH CHINA UNIVERSITY OF TECHNOLOGY*)

A THESIS SUBMITTED

FOR THE DEGREE OF DOCTOR OF PHILOSOPHY

DEPARTMENT OF CIVIL ENGINEERING

NATIONAL UNIVERSITY OF SINGAPORE

2006

ACKNOWLEDGEMENT

I would like to take this opportunity to express my profound gratitude and sincere appreciation to my supervisor Professor T. Balendra and my co-supervisor Associate Professor Tan Kiang Hwee, for their kind guidance, systematic guidance and supervision throughout the course of this study.

I also like to thank the staffs of the Structural Laboratory for their help and advice. Many thanks to Mr. Sit Beng Chiat, Mr. Edgar Lim, Mr. Ang Beng Onn, Ms Annie Tan, Mr. Ow Weng Moon, Mr. Kamsan Bin Rasman, Mr. Yip Kwok Keong, Mr. Ong Teng Chew, Mr. Yong Tat Fah, Mr Wong Kah Wai, Stanley, and Mr. Martin who help in many ways in the experiment. Special acknowledgement is given to Mr. Choo Peng Kin, Mr. Koh Yian Kheng and Mr. Ishak Bin A Rahman who had assisted and guided me tremendously in the experiment.

Gratitude is extended to my seniors Dr. Kong Kian Hau, Dr. Kong Sia Keong and Ms Suyanthi Sakthivel; friends and colleagues Mr. Michael Perry, Ms Wu Hong, Mr. Duan Wen Hui, Mr. Zhou En Hua, Ms. Yu Hongxia, Mr. Kan Jian Han, Mr. Wiryi Aripin, Mr. Chen Jun, Mr. Zhao Dian Feng, Mr. Gao Xiao Yu, Dr. Li Jin Jun and Ms Zhou Yu Qian for their help and encouragement.

I am greatly indebted to my mother and brother who have encouraged me a lot and made many sacrifices during the study.

I am grateful to my lecturers, relatives and friends who have supported the study in many ways.

TABLE OF CONTENT

SUMMARY

Because Singapore is located on a stable part of the Eurasian Plate, with the nearest earthquake fault 400 km away in Sumatra, buildings in Singapore were designed according to the British Standard without any seismic provision. However, due to the far-field effects of earthquakes in Sumatra (Balendra et al. 1990), they are occasionally subjected to tremors due to earthquakes occuring at the Sumatra. In the last two years (2004 and 2005), tremors were felt five times in Singapore due to the strong earthquakes at Sumatra, which highlight the earthquake threat to Singapore.

This study focuses on seismic vulnerability of frame and shear wall structures in Singapore, designed primarily for gravity loads, when they are subjected to far field effects of earthquakes in Sumatra. The evaluation of the seismic vulnerability is achieved by comparing the demand curve and capacity curve in the acceleration-displacement (A-D) format.

The demand curve is obtained based on the accelerograms of bedrock motions due to the worst earthquake scenario in Sumatra, and soil profiles of the selected sites (located at Marine Parade, Katong Park and Katong area). The worst earthquake scenario is identified as an earthquake with M_w=9.5, at 600 km away from Singapore, by incorporating the data from two recent earthquakes that occurred in Sumatra (M_w=9.3 Aceh earthquake in December 26 2004; and M_w=8.7 Nias earthquake in March 28 2005).

To establish the accuracy by FEA analytical model to determine the capacity of a full scale building, experimental studies of a 1/5-scale shear wall model and a

1/2-scale frame model under pushover and cyclic loading were carried out. The modeling parameters, such as initial effective stiffness reduction factors and hysteresis rules, were obtained from the tests. The established FEA models were verified using the test results. It is shown that the pushover test can be a simplified representation of the cyclic test, by comparing the results from the pushover tests with those from the cyclic tests. In the frame tests, a strong column–weak beam mechanism was observed, although the frame was designed according to BS8110(1985) without any seismic provision. And the results from the shear wall tests revealed that the shear walls fail at the base due to shear. Retrofitting using glass fiber reinforced polymer (GFRP) system was proposed, and the cyclic behavior of shear wall structures retrofitted with GFRP system was investigated experimentally. The FEA model for the GFRP retrofitted structure was established and validated using the test results.

Two case studies have been carried out for the vulnerability study: (1) a 4-story frame building, representing typical low-rise buildings; and (2) a 25-story shear wall-frame building, representing typical high-rise buildings. In the case studies, the pushover and dynamic collapse analysis for the full scale structures are carried out. From these two case studies, it is concluded that low-rise buildings in Singapore would meet the demand, but in certain cases, high-rise buildings in Singapore may suffer some damage due to the worst possible earthquake. For such insufficient cases, a seismic retrofitting scheme using FRP system is proposed.

LIST OF FIGUES

LIST OF TABLES

LIST OF SYMBOLS

A	Cross sectional area
A_e	Effective confined area
A_g	Gross sectional area
A_s	Effective shear area Sectional area of tensile reinforcing bars
A_s'	Sectional area of compressive reinforcing bars
A_v	Area of transverse reinforcement
A_{ws}	Area of one layer of horizontal reinforcement
b	Width of a section
b_w	Width of the web
BRC bars	Smooth welded steel mesh bars produced by BRC Ltd, UK Reinforcing steel bars stock holders & distributors
c	Height of neutral axis
CAM	Component attenuation model
d	Effective height of a section
d_1	Effective depth of the compressive reinforcing bars
d_2	Effective depth of the tensile reinforcing bars
D*	Displacement of equivalent SDOF system
E	Elastic (Young's) modulus
E_c	Elastic (Young's) modulus of concrete
E_f	Elastic (Young's) modulus of FRP
Es	Elastic (Young's) modulus of steel
f_{cu}	Concrete compressive cube strength

f_c'	Concrete compressive cylinder strength
f_{cc}'	Compressive cylinder strength of confined concrete
f_{co}'	Compressive cylinder strength of unconfined concrete
f_s	Stress in tensile reinforcing bars
f_s'	Stress in compressive reinforcing bars
f_y	Yield stress of longitudinal reinforcing bars
F	Internal force vector
F_c	Force in concrete
F_s	Force in tensile reinforcing bars
F_s'	Force in compressive reinforcing bars
F*	Force of equivalent SDOF system
FEA	Finite element analysis
FRP	Fibre reinforced polymer
g	Acceleration of gravity
G	Shear modulus Cylindrical attenuation factor for CAM
GFRP	Glass fibre reinforced polymer
G_{gx}	Gravity load of structure at level x
GLD	Gravity load designed
G_{max}	Initial shear modulus
h	Member dimension in the direction of bending
h_f	Thickness of the slab
h_x	Height of level x above the base

H	Height of a building
HDB	Housing & Development Board of Singapore
I	Moment of inertia
I_g	Moment of inertia of gross concrete section
I_{yy}	Moment of inertia of a section in y-y direction
I_{zz}	Moment of inertia of a section in z-z direction
J_{xx}	Torsional moment of inertia of a section in x-x direction
k	Neutral axis depth factor
k_0	Initial elastic stiffness
K	Stiffness of a section
L	Length of the wall Length of the beam span
m_j	Story mass at level j
m*	Equivalent mass of SDOF system
M	Moment Diagonal mass matrix
MB	Yield moment at the onset of cracking
MBy	Yield moment about y-y axis at balance failure
MBz	Yield moment about z-z axis at balance failure
M_c	Moment resistance provided by concrete
MDOF	Multi-degree-of-freedom
M_L	Ritcher magnitude of earthquakes
M_s	Moment resistance provided by tensile reinforcing bars
M_s'	Moment resistance provided by compressive reinforcing bars

M_w	Moment magnitude of earthquakes
M_y	Yield moment
MYy	Yield moment about y-y axis
MYz	Yield moment about z-z axis
M_u	Ultimate moment
M0	Yield moment corresponding to axial load equal to zero
M1B	Yield moment corresponding to P=2/3PB
M2B	Yield moment corresponding to P=1/3PB
N	Axial force
N_{spt}	N value of the standard penetration test for soil (blow/30cm)
N_u	Axial compression force
P	Internal axial force
PB	Axial compression force at onset of cracking (2D RUAUMOKO) Axial compression force at balance failure (3D RUAUMOKO)
PC	Height of the plastic centriod of a section Axial compression yield force (3D RUAUMOKO)
PI	Plasticity index for the soil
PRA	Peak rock acceleration
PT	Axial tension yield force (3D RUAUMOKO)
PYC	Axial compression yield force (2D RUAUMOKO)
PYT	Axial tension yield force (2D RUAUMOKO)
r	Bilinear factor for hysteresis rules
r_y	Bilinear factor of a section about y-y direction

r_z	Bilinear factor of a section about z-z direction
R	Distance to epicenter for CAM
RC	Reinforced concrete
R_c	Corner radius in a rectangular column with rounded corners
s	Spacing of reinforcing bars
S	Undrained shear strength
S_a	Spectra acceleration
S_d	Spectra displacement
S_h	Spacing of horizontal wall reinforcement
S_v	Spacing of longitudinal wall reinforcement Spectra velocity
SDOF	Single-degree-of-freedom
t	Thickness of a section Time
t_f	Thickness of FRP sheet
T	Fundamental period of vibration
u	Displacement
$\dot{u}$	Velocity
$\ddot{u}$	Acceleration
$\ddot{u}_g(t)$	Ground acceleration as a function of time
U	Lateral displacement vector
v	Shear capacity of a section (MPa)
v_c	Shear capacity provided by concrete (MPa)
v_s	Shear capacity provided by transverse reinforcement (MPa)

v_f	Shear capacity of FRP wrap (MPa)
v_{ult}	Ultimate shear resisting capacity (MPa)
V	Shear force
V_b	Base shear
V_f	Shear capacity of FRP wrap (kN)
W_g	Unfactored dead load of structure
α	Unloading stiffness degradation parameter for hysteresis models Source factor for CAM Factor for equivalent rectangular block of concrete in compression
β	Reloading stiffness degradation parameter for hysteresis models Inelastic attenuation factor for CAM Factor for equivalent rectangular block of concrete in compression
ε_c	Strain of concrete
ε_{cc}	Crushing strain of confined concrete
ε_{cy}	Strain of concrete corresponding to first yielding of reinforcement
ε_{co}	Crushing strain of unconfined concrete
ε_{cu}	Ultimate strain of concrete
ε_f	Effective FRP strain at failure
ε_s	Strain of tensile reinforcing bars
ε_s'	Strain of compressive reinforcing bars
ε_y	Yield strain of reinforcing bars
ζ	Damping ratio of soil
ξ	Damping ratio
γ	Shear strain Factor used in CAM Factor for equivalent rectangular block of concrete in compression

κ	Curvature of a section
ρ	Reinforcement ratio of the tensile reinforcing bars
ρ'	Reinforcement ratio of the compressive reinforcing bars
ρ_f	FRP shear reinforcement ratio
ρ_{sc}	Reinforcement ratio
ρ_t	Effective reinforcement ratio of longitudinal tensile bars
ρ_{wh}	Effective reinforcement ratio of horizontal tensile bars in walls
σ_c	Concrete stress
σ_0	Average axial stress over a section
υ	Poisson ratio
ω	Circular frequency
Γ	Modal participation factor
Δ	Roof displacement Incremental values, eg Δt
Δ_y	Yield displacement/ deformation
Δ_u	Ultimate displacement/ deformation
ϕ_j	Displacement shape at story level j
ϕ_y	Curvature corresponding to first yielding of reinforcement
ϕ_u	Ultimate curvature

CHAPTER 1 INTRODUCTION

1.1. Background

Because Singapore is located on a stable part of the Eurasian Plate, with the nearest earthquake fault 400 km away in Sumatra, the buildings in Singapore were designed according to British Standard (BS8110 1985) without any seismic provision. Since BS8110 code does not consider the earthquake loads, buildings in Singapore can be referred to as gravity-load-designed (GLD) structures. That is they are designed to resist gravity load, wind load and a notional lateral load (1.5% of the weight of the building), without any earthquake loads. However, due to the far-field effects of earthquakes in Sumatra (Balendra et al. 1990), buildings in Singapore, of which most are reinforced concrete (RC) shear wall and frame structures, are occasionally subjected to tremors that occur at the Sumatra fault and the subduction of the Indian-Australian plate into the Eurasian Plate (as shown in Figure 1.1).

In the last two years (2004 and 2005), tremors were felt several times in Singapore due to the strong earthquakes at Sumatra, according to the reports on newspaper (Strait Times, Today and Lian He Zao Bao). These earthquakes are: the earthquake on April 10, 2005 (moment magnitude M_w=7.3, 700 km away from Singapore), the earthquake on March 28, 2005 (M_w=8.7, 600 km away), the earthquake on Dec 26, 2004 (M_w=9.3, 950 km away), the earthquake on July 25, 2004 (M_w=7.3, 400 km away) and that on February 22, 2004 (M_w=5.8, 400 km away) (Here, moment magnitude M_w is used instead of the more widely-known Richter scale M_L, because it

gives a more scientific measure of the energy released in an earthquake and M_L is less sensitive for an earthquake with magnitude larger than 7). These reported tremors highlight the earthquake threat to Singapore, which is briefly introduced in the next paragraph.

Seismic waves generated at the epicenter can be categorized into two groups: (1) high frequency waves, which have high intensity but damp out rapidly during propagation; (2) low frequency waves, which possess large displacement properties and damp out relatively slowly. Because the high frequency waves generated at Sumatra faults damp out quickly during propagation to Singapore, the seismic waves reach Singapore bedrock are often rich in low frequency waves. Although the peak ground acceleration (PGA) of the low frequency waves may be very low, the induced motions may have disproportional high displacement and possibly high velocity characteristics. In addition, such low frequency waves may be amplified more than 10 times to reach the ground level through the soft soil layers in Singapore, if the natural period of the soil site is close to the predominant period of the bedrock motion (This kind of amplification due to resonance is called site amplification effect). Furthermore, such amplification may be further enlarged, if the natural period of the building supported on such soil sites is close to the predominant period of the ground motion. Therefore, due to the large displacement properties that low frequency waves possess and the amplification by the soil, buildings in Singapore may suffer from large displacement that may cause damage. Balendra et al. (1990) revealed that an earthquake of magnitude 7.6 at Richter scale 400 km away from Singapore could cause

a shear force demand of 2-4% of weight of the building, which is larger than the notional lateral load(1.5% of weight) in the design.

Thus, there is a need to evaluate the seismic vulnerability of RC shear wall and frame structures in Singapore in case a larger or nearer earthquake may occur in the future. Experimental and numerical studies of seismic vulnerability of such structures should be carried out, and seismic retrofitting scheme should be proposed if needed.

1.2. Literature review

1.2.1. Overview of seismic studies of RC GLD structures

Besides buildings in Singapore, old RC structures built in other non-seismic or low-seismic regions, like the eastern and central United States and Korea, are also GLD structures. Such RC GLD structures are the result of the old codes which did not consider seismic load. Although different codes are used, RC GLD structures in different regions share some common features such as: (Aycardi et al. 1994; Lee and Woo 2002b)

1. Minimal transverse reinforcement in columns or shear walls for confinement and shear resistance; the spacing of hoops of column/shear wall transverse reinforcement is relatively large.
2. Little or no transverse shear reinforcement in beam-column joints.
3. Lap splices of columns or shear walls are located in the potential plastic hinge zones at the bottom.

These common deficiencies may result in similar performance when the GLD buildings are subjected to seismic load. Thus, it is advisable to review the previous research of RC GLD structures, even if they were designed according to codes other than BS8110(1985)

The concern for the vulnerability of RC GLD structures is relatively recent, and research work has been carried out in USA, Korea and Singapore. According to different design codes, the research work can be divided into three groups:

1. Research work at SUNY Buffalo University, Cornell University, UC Berkeley and Hanyang University on the seismic performance and retrofitting technology of RC GLD frames designed according to American code (ACI nonseimic code) (Aycardi et al. 1994; Bracci et al. 1995b, 1995a; Kunnath et al. 1995b, 1995a; ElAttar et al. 1997; Mosalam and Naito 2002; Han et al. 2004)
2. Research work at Korea University on the performance of RC GLD frames designed according to Korean practice of nonseismic detailing under seismic loading (Lee and Sung-W 1998; Lee and Woo 2002b, 2002a)
3. Research work in Singapore on the performance and retrofitting scheme of GLD RC frames and shear walls designed according to British Standard (BS8110 1985). (Balendra et al. 1999; Balendra et al. 2001; Koh 2003; Kong et al. 2003a; Perry 2003; Suyanthi 2003; Li et al. 2004; Dhakal et al. 2005)

1.2.2. Research of GLD buildings designed according to ACI code

The research work at SUNY Buffalo University started from the component tests and analysis, followed by the test of scaled frames. This led to the development of a seismic evaluation methodology, and finally an effective and economical retrofitting scheme.

Aycardi et al.(1994) tested four column specimens, loaded with low and high levels of axial forces, with and without lap splices, representing interior and exterior columns at floor slab and beam soffit levels. They also tested one 1/3 scale external beam-column joint subassemblage and one 1/3 scale internal joint subassemblage. They reported that structural components with detrimental details of GLD structures could reach their flexural strength and still sustain their gravity loads during large cyclic deformations. For example, column specimens were found to be able to sustain at least 70% of the maximum load capacity for two cycles of 4% drift. It was reported that the failure mode was dependent on the level of axial load, although the failure in the columns was flexurally dominated. For instance, the failure mode for exterior subassemblage was weak beam-strong column mechanism while the interior subassemblage was weak column-strong beam mechanism. In this study, it was also reported that the plastic hinge lengths in columns were 0.74h to 1.35h under large axial load and 0.47h to 0.6h under low axial load, where h is the column dimension in the direction of bending.

Based on the work of Aycardi et al.(1994), Bracci et al. (1995a) performed a 3-story 1/3 reduced scale model test on the shake table. They concluded that the

inherent lateral strength and flexibility of GLD structures are adequate to resist minor earthquakes and avoid major damage, but they may suffer from substantial side-sway deformations exceeding recommended limits for moderate to severe earthquakes. It was reported that GLD structures were dominated by weak column-strong beam behavior and may suffer from side-sway/soft-story collapse mechanism at the ultimate load. It was found that a critical mechanism formed at a base shear of 15% of the building weight.

The evaluation methodology including damage modeling proposed by Kunnath et al (1995b) was used to identify the seismic performance of 3-, 6-, and 9-story GLD RC buildings. The analysis of tests was performed by a computer program IDARC (First version was introduced in 1987, and the latest version was distributed in 2004), which is a nonlinear analysis program for frame-wall structures subjected to seismic excitations. Results of the analysis matched well with those of the experiments.

The research of Cornell University was to see the performance of the GLD building under realistic seismic force. ElAttar et al.(1997) tested a 1/6 scale 2-story office building and a 1/8 scale 3-story one-bay by three-bays office buildings on the Cornell University shake table. They concluded that the reinforcement details in the GLD building may not be sufficient to develop a complete failure mechanism, because before these details fail, a premature soft-story mechanism may occur due to the lack of sufficient strength in columns as compared to beams. In addition, they drew the conclusion that the GLD frame without infilled walls would experience large lateral deformations during the test and the slab contribution to beam negative moment

flexural strength may alter the relatively ductile strong column-weak beam mechanism to soft-story mechanism. It was noted in their study that significant stiffness deterioration occurred in the test due to wide cracking and pullout of some reinforcing bars. This stiffness deterioration resulted in large displacements and a pronounced P-Δ effect.

The research work in UC Berkeley concentrated on the seismic performance of the GLD perforated waffle-slab systems. In this study, Mosalam and Naito (2002) conducted two reduced scale identical specimen, modeling half the height of an interior column with a portion of the waffle slab bounded by the centerlines of adjacent bays. In the test, bidirectional quasi-static lateral loading is applied at the test column end. It was found that the system possessed high deformation ductility with only minor damage to the waffle slab. The failure mode reported was the formation of stable plastic hinging at the junction between the column and the waffle-slab joints.

The study of Han et al.(2004) focused on the seismic performance of Ordinary Moment-Resisting Concrete Frames (OMRCF) designed primarily for gravity loads. A 3-story OMRCF was designed according to the minimum design requirements in ACI code (ACI318 1989). A 1/3-scale 3-story model was constructed and tested under quasi-static reversed cyclic lateral loading. It was found that the overall behavior was quite stable without abrupt strength degradation. It was reported that the base shear of 15% of the weight was achieved in the test. Capacity spectra method was carried out to evaluate the seismic performance of the frame, and the results showed that this 3-story

OMRCF could resist design seismic loads of zones1, 2A, 2B and 3 with soil type S_A and S_B.

1.2.3. Research of GLD buildings designed according to Korean nonseismic detailing

The research work of Korea University focused on the seismic performance of low-rise RC frames designed to the Korean practice of non-seismic detailing, and the influence of masonry infills and scale effects of such RC frames.

Lee and Sung (1998) investigated the influence of the scale factor to the seismic performance of RC frames. They manufactured one 1/2.5 and one 1/10 model subassemblages, and applied quasi-static reversed load to these subassemblages. The strength, stiffness, energy dissipation, failure modes and local deformations were compared. It was concluded that the strength and crack pattern of the two models were similar, while the initial stiffness, energy dissipation capacity and failure mode of the two models were different. The initial stiffness and energy dissipation capacity of the 1/10 model were smaller than those of 1/2.5 model.

Lee and Woo (2002a) performed 2-bay 3-story 1/5 scale masonry-infilled RC frame tests, under a series of earthquake simulation loading and a pushover loading, to investigate the influence of masonry-infills. They concluded that masonry infills could be beneficial to the seismic performance of the structure, because they contribute to the large increase in the stiffness and strength of the global structure, and the amount of the increase in strength is greater than additional inertia forces due to the infills.

Lee and Woo (2002b) conducted a 1/5 scale 3-story RC frame designed according to the Korean practice of non-seismic detailing, and tested the model using shake table. A pushover test was finally performed, due to the limitation of the capacity of the shake table. It was reported that the model revealed fairly good resistance to the higher levels of earthquakes, though it was not designed against earthquakes. The drifts observed were approximately within the allowable limit. The analysis by IDARC-2D program (First version was introduced in 1987, and the latest version was distributed in 2004) revealed that the overall displacement ductility ratio was 2.4 and the overstrength coefficient was 8.7.

The above research is for GLD buildings designed according to ACI code (ACI318 1989) and Korean practice of nonseismic detailing (Lee and Woo 2002b), which are different from British Standard (BS8110 1985) used in Singapore. Since different design codes or practices may result in different detailing, which will influence the seismic behavior of the structures, the studies in USA and Korea could only be used for reference if the structures in Singapore are under consideration. In the next section, the research work in Singapore is reviewed.

1.2.4. Research of GLD buildings in Singapore designed according to BS8110 code

Both experimental and numerical studies have been carried out in Singapore, for the GLD buildings designed according to BS8110(1985).

1.2.4.1. Experimental study

At the National University of Singapore, Kong (2003) conducted a pushover test on a large scale one-story one-bay bare frame, and found that this building possessed considerable overstrength to sustain tremors due to far field effects in Sumatra. Kong (2004) conducted a test of a scaled model, which is the lower critical region of a 25-story RC shear wall structure. The results of the tests showed that RC shear wall has significant overstrength but nominal ductility.

At the Nanyang Technological University, Dhakal et al. (2005) performed six full-scale tests of beam-column joint specimens under reversed cyclic loading. The cyclic displacements were applied at different speeds varying from slow quasi-static loading to high-speed dynamic loading (20HZ), to evaluate the response of the specimens subjected to excitations of different frequencies. It was found that the joints experienced severe damage, and joint shear failure occurred before the formation of a plastic hinge in the adjoining members.

In the above research, monotonic static pushover loading or cyclic loading were used in the pseudo-static loading tests. However, no comparison between pushover behavior and cyclic behavior has been carried out, so whether the results from pushover test can be a simplified representation of the cyclic behaviors is yet to be found out.

For the seismically designed structures, it was found that pushover behavior can be a backbone representation of the cyclic behavior. Lefas et. al. (1990) and Penelis and Kappos (1997) tested some rectangular walls, under both pushover and cyclic

loads. They found that the tested pushover curves formed the backbone of the tested cyclic curves. Dolsek and Fajfar(2002) performed the pushover analysis of a 3D 3-story frame specimen, which had been tested under cyclic loading. The resulting analytical pushover curves enveloped the tested cyclic curves. Ei-Tawil and Kuenzli (2002) analyzed the shear walls, which were tested by Oesterle et. al. (1976,1979) and Pilakoutas and Elnashai (1995), under both pushover and cyclic loading. They found that the analytical pushover curves could be the backbone of the analytical cyclic curves.

However, for the GLD structures, because the details such as lap splices and reinforced confinement at joints, are quite different from the structures with seismic provision, whether the pushover loading test behavior will form the backbone representation of the cyclic behavior is yet to be established. For this purpose, tests of GLD frame and shear wall structures under pushover and cyclic loading, and the comparison between the pushover and cyclic results should be carried out.

In conclusion, the above research in Singapore mainly focuses on experimental studies under pushover loading or cyclic loading. The comparison of the experimental results between pushover loading and cyclic loading is yet to be carried out. Furthermore, since the scaled model tests might not represent the behavior of a full scale building, FEA numerical models for full scale buildings should be established.

1.2.4.2. FEA numerical study

Balendra et al.(1999) analyzed the overstrength and ductility of three GLD frames, namely 3-, 6- and 10-story three bay frames, by non-linear pushover analysis using ABAQUS (Hibbit et al. 2003). They showed that the frames possess significant overstrength and considerable ductility due to the redistribution of internal forces in the inelastic range. The influence of infill walls on the response modification factor was also investigated in their research. Balendra et al.(2001) performed nonlinear pushover analysis using ABAQUS to investigate a 16-story RC GLD frame building. Kong (2004) established a microscopic FEA model using ABAQUS to calculate the capacity of a 25-story GLD frame-shear wall building.

In the above numerical studies, pushover analysis using ABAQUS was performed. However, there are some limitations of ABAUQS, such as it cannot be used to perform dynamic collapse analysis, and it cannot consider the initial effective stiffness reduction due to the micro cracks in the members. Therefore another software RUAUMOKO (Carr 2002a, 2002b) was introduced recently, and FEA models using RUAUMOKO were developed by Koh (2003), Perry (2003) and Suyanthi (2003). In their studies, full scale FEA models for a 16-story frame building and a 25-story GLD shear wall-frame building were established. Seismic capacities of these buildings were calculated by performing the pushover and dynamic collapse analysis. Their research provided a good analytical tool to evaluate the seismic performance of the full scale buildings. However, some important parameters in their models, like initial effective stiffness reduction factors and parameters for hysteresis rules, were obtained from the

research work of buildings designed according to other codes instead of BS8110(1985) code. The accuracy of their FEA models needs to be evaluated, and those important parameters should be obtained from the experimental test of GLD buildings designed according to BS8110(1985). In the following sections, the literature review of such parameters is addressed.

Initial stiffness

Definition of initial stiffness is based on the effective stiffness definition given by Paulay and Priestley (1992). A typical nonlinear relationship between loads and displacement under pushover loading is shown in Figure 1.2. For simplification, an idealized bilinear response is often used in analysis to represent the actual observed response. In Figure 1.2, S_y defines the yield or ideal strength S_i of the member, and Δ_y defines the corresponding yield displacement. The slope of the idealized linear elastic response, $K = S_y / \Delta_y$, is defined as initial stiffness, which is equal to the effective secant stiffness of the real load-displacement curve at a load of about $0.75 S_y$.

It was reported that the initial stiffness obtained from the test was less than that of the uncracked gross section (Bracci et al. 1995b; Filiatrault et al. 1998). According to Bracci, the reason for such differences stems from the initial cracking of the member sections due to gravity loads (particularly in beams), micro-cracking generated from concrete curing, and minor construction loadings. Macgregor (2005) pointed out that micro-cracks, which consist of bond cracks and mortar cracks, have an enormous effect on stiffness of structures. Aktan et al.(1985) also observed that the

experimentally measured initial stiffness differed by more than 100 percent from the analytically generated one. They concluded that micro-cracking, due to shrinkage induced by volumetric changes, was identified as the main factor leading to reduced stiffness of walls upon first loading. The phenomenon that the measured experimental initial stiffness is less than the theoretical stiffness of the uncracked gross section are also reported by many other researchers (Hirosawa 1975; Kenneally and Burns 1986; Elnashai et al. 1988, 1990; Pilakoutas and Elnashai 1995; Lopes 2001).

In order to incorporate the reduction effect of initial stiffness into the analysis, the reduced initial stiffness instead of the gross section stiffness should be used in the FEA model. As an example, Bracci (1995a) used the initial stiffness reduction factors obtained from the test, to establish FEA model using IDARC-2D (First version was introduced in 1987, and the latest version was distributed in 2004). It was shown that the FEA model could predict the experimental results well. Filiatrault et al.(1998) conducted FEA modeling using RUAUMOKO, and validated the model using the experimental results obtained from shake table tests of two half-scale RC moment resisting frames. In the FEA model, they used the equivalent moment of inertia I_{eq} (less than half of I_g, the moment of inertia of gross section) obtained from the test, as the input of initial moment of inertia. As a result, good correlation between numerical and experimental results was achieved. Harries et al. (1998) carried out nonlinear dynamic analyses of four couple wall prototype structures using RUAUMOKO. In their FEA models, reduced initial stiffness, based on the Explanatory Notes on Canadian Standards Association (CAS) Standard A23.3 Clause 21.2 (CPCA 1995), was used as

input parameters. Han et al. (2004) performed modal analysis of 3-story OMRCF structure using SAP2000(1997). In the FEA models, they used the reduced stiffness as specified in the ATC-40 document (1996), as a result, the 1st modal natural period predicted by FEA is only 4.3% larger than the test result. Therefore, in order to establish an accurate FEA model, it is wise to select the appropriate initial stiffness reduction factor, which is the ratio of the initial stiffness (or equivalent moment of inertia I_{eq}) obtained from the test over the uncracked section stiffness (or gross moment of inertia I_g) .

Such a reduction factor has been suggested in some literature. Bracci (1995a) suggested 0.55 to 0.6 for columns and 0.25 to 0.35 for beams. Filiatrault et al.(1998) suggested 0.40 for columns and 0.38 for beams of the nominally ductile frame, and 0.43 for columns and 0.34 for beams of the ductile frame. Harries et al. (1998) used 0.7 for columns and 0.17-0.2 for coupling beams. The reduction factors recommended by Paulay and Priestley (1992),CPCA (1995) and ATC-40 (1996) are listed in Tables 1.1-1.3

Hysteresis rules

Otani (1981) compared several most commonly used hysteresis rules and discussed the effect of the stiffness parameters to the structural response. He pointed out that stiffness would reduce due to flexural cracking of concrete and tensile yielding of steel, in the process of loading. Thus, in order to capture the seismic behavior of

structures, stiffness degradation should be considered in the FEA analysis. One way to incorporate the stiffness degradation is to define the hysteresis rule.

Filiatrault et al.(1998) used the Q-HYST degrading stiffness hysteresis, which was proposed by Saiidi and Sozen (1979), in their FEA model. The parameters for the Q-HYST hysteresis rule were obtained from the shake table tests. Harries et al. (1998) selected the Modified Takeda degrading stiffness hysteresis rule (Otani 1981) to model the RC coupling beams, and chose a Ramberg-Osgood hysteresis rule to model the steel coupling beams. The parameters for hysteresis rules were obtained by comparing the predicted responses with test results.

According to Otani (1981), for RC structures, the most often used hysteresis rule is the Modified Takeda model. The diagram of this hysteresis rule and the corresponding parameters are shown in Figure 1.3. Three parameters are used to define this hysteresis rule. They are:

1. Unloading stiffness parameter, $\alpha = \dfrac{(\dfrac{k_0}{k_u} - 1)(d_m - d_j)}{d_j}$. This parameter controls the fatness of the hysteresis loop and the plastic residual deformation.
2. Post yield stiffness factor or bilinear factor, $r = \dfrac{k_1}{k_0}$. This parameter influences the strength enhancement after yielding.
3. Reloading stiffness parameter, $\beta = \dfrac{d_{p1}}{d_p}$. This parameter reflects the stiffness degradation between two nearby cycles

1.2.5. Seismic demand and seismic adequacy evaluation for buildings in Singapore

The studies mentioned in the above sections focus on experimental evaluation of seismic performance of GLD structures, and FEA models of full scale GLD buildings to obtain their strength capacities. In order to evaluate the seismic adequacy of such buildings, seismic demands due to base motions generated from the worst earthquake scenario need to be found out. The procedure to determine the seismic demands for buildings in Singapore includes: (1) seismic hazard analysis to identify the worst earthquake scenario in Indonesia as the design earthquake; (2) establishment of attenuation relationships to obtain the bedrock motions at Singapore due to the design earthquake; (3) consideration of soil profile amplification to get the surface motions at the building base.

Several studies have contributed to obtain seismic demands in Singapore. Pan (1997) pointed out that the response of a building to long-distance earthquakes is dependent on the type of structural systems and the local geological conditions. It is found that tall buildings founded on Quaternary deposit, i.e. the Kallang Formation, are particularly apt to respond to the long-distance Sumatra earthquakes. Pan et al. (2002) conducted the numerical simulation that successfully reproduced the acceleration waveforms recorded at KAP seismic station for the Sumatra earthquake on 1 April 1998, based on the linear site response analysis for vertically propagating shear wave.

Megawati et al.(2002) identified the 1833 Sumatran subduction earthquake (M_w=9.0) as the worst-case scenario earthquake, based on a series of ground motion simulations of potential earthquakes that may affect Singapore. An extended reflectivity method was used to simulate bedrock motions in Singapore, which have a long duration of 250 seconds and a predominant period between 1.8s and 2.5s, due to the hypothesized earthquake. It is estimated that the 90-percentile horizontal peak ground acceleration is 33gal (3.3%g) and the maximum 90-percentile horizontal spectral acceleration is 100 gal, without considering the soil amplification effect.

Balendra et al. (2002) analyzed the seismic faults that cause long distance earthquakes for Singapore and identified the worst earthquake scenarios in each of these faults: a M_w=7.8 Sumatran-fault earthquake 400 km away from Singapore, and a M_w=8.9 Sumatran-subduction earthquake 600 km away. The bedrock motions in Singapore were estimated by using a validated seismic hazard predictive model, the component attenuation model (CAM). It is found that the elastic base shear demand corresponding to the bedrock motions when accounted for amplification by soft soil is 6%-10% of the weight of the building.

Megawati et al. (2003) focused on assessment of the seismic hazards of Singapore and established representative ground motion prediction models. A set of attenuation relationships for Sumatran-fault segments is derived based on synthetic seismograms, and ground motions are simulated for earthquakes with M_w ranging from 4.0 to 8.0, within a distance range from 174 to 1379 km. Megawati et al. (2005) developed a new set of attenuation relationships for the Sumatran-subduction

earthquakes using synthetic seismograms that account for source and path effects. The derived attenuation relationships cover a long distance range from 150 to 1500 km and consider uncertainties in rupture parameters, such as stress drop, strike, dip and rake angles. It is estimated that a large event with M_w greater than 7.8 and at a distance of 700 km in this particular subduction zone may generate destructive ground motions in Singapore.

Based on the soil surface motions determined by Balendra et al. (2002), several studies have been carried out, to evaluate the seismic adequacy of middle to high-rise buildings in Singapore. Suyanthi (2003) carried out the dynamic collapse analysis of a 10-story frame and a 16-story frame buildings, using the surface motions due to the worst earthquake scenario as the base excited motions. Koh (2003) performed the dynamic collapse analysis of a 25-story buildings, and Perry (2003) conducted the dynamic collapse analysis of a 16-story non-symmetric frame buildings. Kong (2004) investigated a 16-story frame building and a 25-story shear wall-frame building by comparing their capacity curves and the seismic demand curves due to the design earthquake.

However, these studies were based on the earthquake records without incorporating the records of the two recent strong earthquakes: the M_w=9.3 Aceh earthquake in 2004 and the M_w=8.7 Nias earthquake in 2005. Because of the occurrence of these two strong earthquakes, the predicted seismic demands due to the worst earthquake scenario may increase, and thus the results of previous assessment of

seismic adequacy may change. Furthermore, seismic adequacy of low-rise buildings in Singapore is yet to be carried out.

1.2.6. Overview of seismic retrofitting of GLD buildings

If the seismic adequacy of GLD buildings is insufficient, seismic retrofitting may be required. Seismic retrofitting refers to wise modification of the structural properties of an existing building, in order to enhance its strength and ductility for future earthquake (Aoyama and Yamamoto 1984). The traditional seismic retrofitting methods are: adding new shear walls or infilled walls, adding braced system and jacketing of structural members with steel or concrete. These methods can increase the lateral force carrying capacity and stiffness of structures, and thus reach the target of retrofitting.

Kunnath et al (1995a) carried out an extensive parametric study of the original GLD buildings with refined detailing characteristics, to improve their seismic resistance. They reported that the improved performance could be achieved by altering the details in critical regions. A cost evaluation of various detailing schemes was also conducted by them to evaluate the effectiveness of retrofit strategies. Bracci et al. (1995b) used prestressed concrete jacketing to retrofit a 1/3 scale model RC frame that had been previously tested, and performed shake table test. They concluded that the seismic performance of vulnerable (soft-story prone) GLD frames may be effectively enhanced by this concrete jacketing method, and thus the failure mode can be changed to a beam side-sway mechanism with acceptable story deformation levels.

However, the traditional methods have some disadvantages. In these methods, adding new shear walls will introduce additional mass to the existing footings (Wyllie 1996). Adding braced system may alter the magnitude and distribution of the seismic loads and may lead to unexpected local failure(Lombard et al. 1999). In addition, jacketing is labor intensive and is poor in resisting weather attack (Teng et al. 2001). As a promising alternative, fibre reinforced polymer (FRP), an advanced composite reinforcing material, has been introduced in the field of seismic retrofitting in recent years. A successful example of the application of seismic retrofit using FRP in actual projects is the retrofit of a 7-story hotel in Los Angeles (Elhassan and Hart 1995). The columns of this hotel suffered significant diagonal cracks during the magnitude 7.5 Landers earthquake of 28 June 1992 and was retrofitted by glass FRP (GFRP) jackets. As a result, this building did not suffer any damage during the 1994 Northridge earthquake. Due to its excellent characteristics, such as high strength to weight ratio, immunity to corrosion, easy and fast installation, FRP is widely used for seismic retrofitting nowadays and attracts considerable research study.

Recently, some research on FRP retrofitting for GLD structures has been carried out (Harajli and Rteil 2004; Kong 2004; Harajli 2005). Kong (2004) focused on FRP retrofitting for shear failure of shear wall structures, and Harajli and Rteil (2004) and Harajli (2005) focused on FRP retrofitting for flexural and bond failure of GLD columns.

Kong (2004) proposed a retrofitting scheme using FRP for the shear wall structure under test. It was found that this retrofitting scheme is effective in the pushover test of the retrofitted specimen.

Harajli and Rteil (2004) conducted the experimental investigation to evaluate the seismic performance of RC columns designed for gravity load and confined externally with carbon FRP (CFRP) sheets. The specimens were 150x300x1000 mm columns projecting outside a stiff column stub. All specimens experienced significant slip of the column reinforcement and widening of one single crack, located at the column-stub interface. Such failure was due to the deficiency of GLD columns that the columns were spliced at the column base. It was reported that confining the columns with CFPR reduced the bond deterioration, considerably increased the energy absorption and dissipation capabilities, and resulted in significant improvement in the seismic performance.

Harajli (2005) concentrated on analytical evaluation of the effect of externally wrapped FRP sheets on the response of GLD rectangular columns with spliced longitudinal reinforcement at the column base. Bond strength degradation of the spliced reinforcement and effect of FRP confinement on the concrete stress-strain response were taken into account in the analytical scheme, to evaluate the strength capacity and ductility of the columns. And a design equation was proposed to calculate the area of FRP sheets needed in the retrofitting. It was shown that the analytical results agreed well with limited experimental data.

The studies above focused mainly on experimental investigations and some empirical analytical equations or theories, and did not discuss the numerical FEA models, which can help to evaluate the performance enhancement of structures due to FRP retrofitting, and thus can help to propose the effective scheme for upgrading.

Recently, for monotonic loading, some FEA models of FRP retrofitting structures have been proposed. Buyle-Bodin et al. (2002) proposed a 2D FEA model used to analyze the flexural behavior of externally bonded CFRP RC structures under pushover loading. In this model, the CFRP plates were modeled using two-node linear bar elements. Eusebio et al (2002) used software DIANA (2000) to perform 2D FEA modeling of FRP retrofitting masonry panels. They used SPRING element to simulate the constraint on deformation provided by FRP strips, but they did not consider the improvement of concrete strength due to FRP confinement. Kong et al. (2003a) proposed a 3D microscopic FEA model using program ABAQUS to simulate shear walls wrapped with GFRP. However, for cyclic loading, 3D FEA modeling has not been reported. This may be due to the difficulty of FEA modeling to capture the cyclic behavior of concrete.

1.3. Objective and scope

The objectives of this thesis are: to evaluate the seismic vulnerability of frame and shear wall structures in Singapore, designed primarily for gravity loads, when they are subjected to far field effects of earthquakes in Sumatra, and to propose a retrofitting scheme for structures which are vulnerable.

For this purpose, the seismic demand and the capacity of the structure will be obtained and compared in the acceleration- displacement (A-D) format. The demand will be obtained based on the accelerograms of bedrock motions due to the worst earthquake scenario in Sumatra (design earthquake), and soil profiles of the selected sites (located at Marine Parade, Katong Park and Katong area). The two recent strong earthquakes in Sumatra will be considered when the design earthquake is identified. On the other hand, in order to establish a reliable and elegant FEA analytical model to determine the capacity of full scale frame and shear wall structures, experimental investigations will be carried out for a 1/5-scale shear wall model and a 1/2-scale frame model under pushover and cyclic loading. A retrofitting scheme using FRP system for shear wall structures will also be investigated experimentally and analytically. Two case studies will be carried out, for evaluation of the seismic vulnerability and demonstration of the above mentioned procedure: (1) a 25-story shear wall-frame building, representing the typical high-rise building; and (2) a 4-story frame structure, representing the typical low-rise building. For the cases of insufficient seismic adequacy, FRP retrofitting scheme will be proposed.

1.4. Organization of the thesis

This thesis has seven chapters with Chapter 1 devoted to background information and literature review. Chapter 2 describes the experimental research of two frame specimens under pushover and cyclic loading. The seismic behaviors of the frame specimens are investigated. Chapter 3 addresses the finite element modeling

using RUAUMOKO and the validation of the FEA models using test results. Modeling parameters for frame structures are obtained from the test. Chapter 4 describes the experimental research of two shear wall specimens under cyclic loading. The seismic behaviors of the shear wall specimens are investigated and shear retrofitting using FRP is evaluated. Chapter 5 describes the macroscopic FEA models using RUAUMOKO to predict the behavior of the specimens with and without FRP retrofitting, and a 3D microscopic FEA model using ABAQUS to predict the cyclic behavior of test specimens. Modeling parameters for shear wall structures are obtained from the test. Chapter 6 introduces the process to obtain the new seismic demand curves for design earthquake, and evaluate the seismic vulnerability of the GLD buildings in Singapore. The methods to estimate the amount of FRP needed for retrofitting are also presented in this chapter. Chapter 7 presents the conclusion of the study and recommendations for the future work.

Table 1.1 Effective member moment of inertia (Paulay and Priestley 1992)

Component	Range	Recommended value
Rectangular beams	0.30-0.50 I_g	0.40 I_g
T and L beams	0.25-0.45 I_g	0.35 I_g
Columns, P>0.5 $f_c^{'}A_g$	0.70-0.90 I_g	0.80 I_g
Columns, P=0.2 $f_c^{'}A_g$	0.50-0.70 I_g	0.60 I_g
Columns, P=-0.05 $f_c^{'}A_g$	0.30-0.50 I_g	0.40 I_g

P=axial load on the columns, positive value denotes compressive force while negative value denotes tensile force;

$f_c^{'}$=the compressive strength of concrete;

A_g=gross area of section;

I_g =moment of inertia of gross concrete section, neglecting the reinforcement

Table 1.2 Effective member moment of inertia (CPCA 1995)

Component	Recommended value
Beams	0.35I_g
Columns	0.70I_g
Walls-uncracked	0.70 I_g
Walls-cracked	0.35 I_g
Flat plates and flat slabs	0.25 I_g

Table 1.3 Component initial stiffness (ATC-40 1996)

Component	Recommended value
Beam, non-prestressed	0.50E_cI_g
Beam, prestressed	E_cI_g
Columns in compression	0.70E_c I_g
Columns in tension	0.50E_c I_g
Walls, uncracked	0.80 E_cI_g
Walls, cracked	0.50E_c I_g

E_c = Young's module of concrete

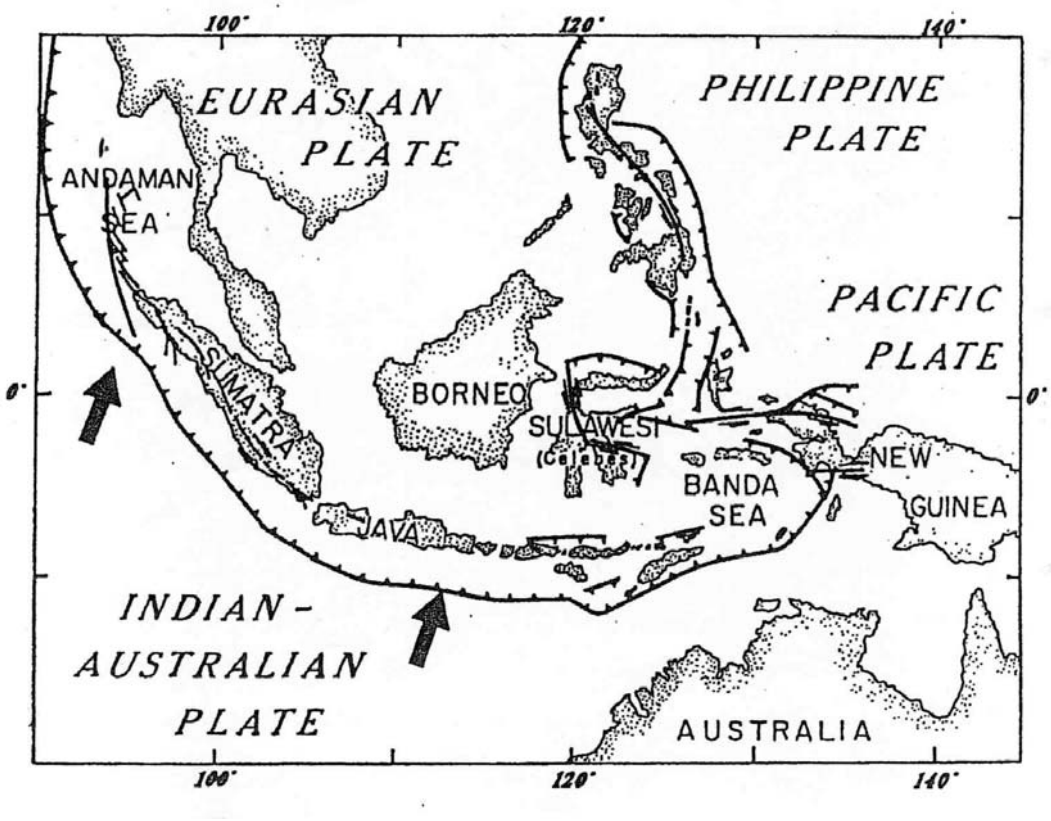

Figure 1.1 Sumatra fault and subduction of the Indian-Australian Plate into Eurasian Plate (Balendra et al. 2001)

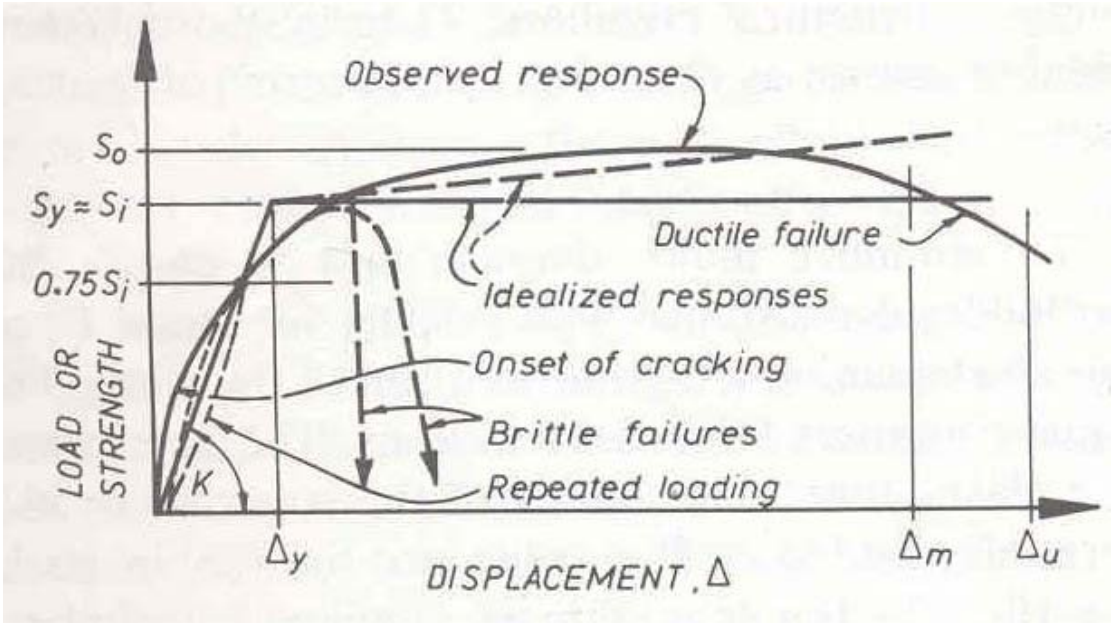

Figure 1.2 Typical load-displacement relationship for a reinforced concrete member (Paulay and Priestley 1992)

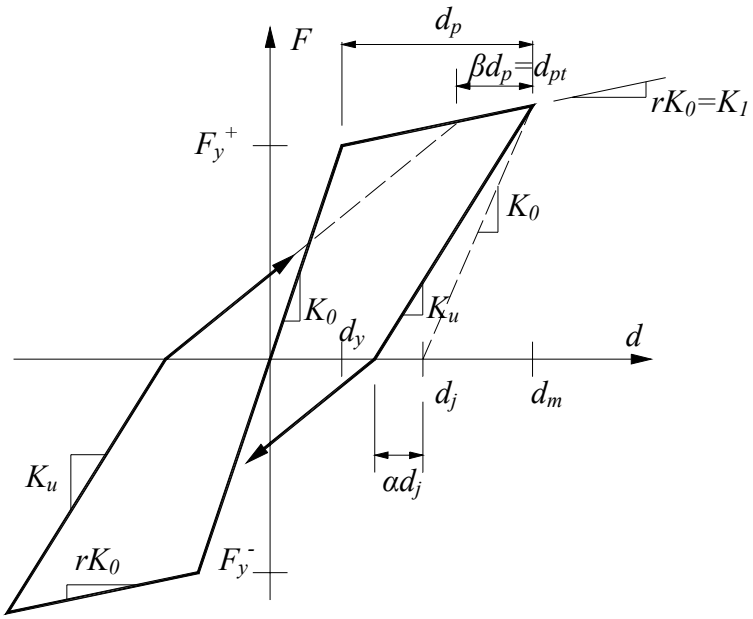

Figure 1.3 Modified Takeda Hysteresis model

CHAPTER 2 EXPERIMENTAL STUDY OF A 4-story FRAME STRUCTURE

2.1. Introduction

Experimental study of a 4-story Housing & Development Board (HDB) frame building is described in this chapter. The experimental model is a 1/2 scale, one and a half bay model, representing the lower two stories of the critical frame of this 4-story building. This 4-story building was built in 1970s in Singapore and designed according to BS8110(1985) without any seismic provision. Two specimens, one under pushover loading (control) and another under cyclic loading, were tested to investigate the seismic performance of the old HDB frame structure in Singapore.

The objectives of the tests are as follows:

1. Whether the results of a pushover test would envelop those of a cyclic test for frame specimens detailed according to BS8110(1985).
2. To investigate the crack pattern and failure mechanism of the frame specimens under pushover and cyclic loading.
3. To check whether there is any initial stiffness reduction for the frame model.
4. To obtain the parameters describing the hysteresis behaviors of members.

2.2. Experimental model

Bracci (1995a) performed a shake table test on a 3-story 1:3 scale GLD frame model designed according to the non-seismic ACI code (ACI318 1989). It was observed that considerable inelastic deformations and hysteretic energy dissipation occurred on the first and second stories. ElAttar (1997) tested two small-scale GLD RC frame building models on shake table at Cornell University. The models were a 1/6 scale 2-story office building and a 1/8 scale 3-story one-bay by three-bays office building. It was found that most of the deformation, damage and energy dissipation of the two test models occurred in the first-story columns. Lee and Woo (2002b) tested a 1:5 scale 3-story GLD RC frame model constructed according to Korean practice of nonseismic detailing using a shake table. They reported that the collapse mechanism was the soft-story mechanism of the first story, and that plastic hinges and cracks occurred mainly at the lower second stories. Since the lower two stories are the critical parts in GLD frames, it is reasonable to choose only the lower two stories of the prototype for experimental study.

The prototype of the test frame model is a typical 4-story GLD HDB building built in 1970s in Singapore. The first story height is 3.2 m and the height of the remaining three stories is 2.7 m. Designed compressive strength of concrete is 20 MPa. Figure 2.1(a) shows the plan view of the prototype building. The critical frame with the weakest lateral resistant capacity, the frame having the least number of columns, was chosen for study. (see Figure 2.1 a and b) . Because the thickness of columns in the prototype is only 200 mm, in order to avoid a too small column width in the scaled

model, scale 1:2 was selected. Due to the space limitation in the lab, the left one and a half bay (with the larger span) and the lower two stories of this critical frame was selected as the experimental model. By assuming the points of contraflexure at the middle of the beams under lateral loading, the critical frame was separated at the middle of the 2nd bay with a pin support (as shown in Figure 2.1 c). For simplicity and to be conservative, slabs and infill walls were not incorporated in test specimens, since masonry infills could be beneficial to the seismic performance of the structure (Lee and Woo 2002a) and the slab diapharam effect helps increase the in-plane stiffness. Because the test specimen is only the lower two stories of the 4-story frame, a constant axial load representing the weight of the above stories was applied on the top of the columns using prestressing strands.

Two specimens (as shown in Figure 2.2), one under pushover loading (control specimen S1) and another under cyclic loading (specimen S2), were fabricated and tested. Figure 2.3 (a) shows the dimensions of the test model. Thickness of the frame was 100 mm throughout.

2.2.1. Model scaling similitude

To maintain the dimension similitude, dimensions of columns and beams, and the thickness of the concrete cover in the experimental model were chosen as half of the prototype. For the similitude of reinforcement, because the yield strength of reinforcing bars used in the experiment was different, yield forces instead of yield stress were selected as the target to fulfill the material similitude. In the experimental

model, 10 mm deformed bars, 8mm smooth BRC bars (smooth welded steel mesh bars produced by BRC Ltd, UK Reinforcing steel bars stock holders & distributors) and 7 mm BRC smooth bars were chosen. These reinforcing bars corresponded to D20, D16 and D13 reinforcing bars respectively in the prototype, where D denotes diameter. As shown in Table 2.1, errors between the yield forces of the selected reinforcing bars and the target forces are within 12%, a reasonable range.

In order to model gravity load properly, mass similitude was considered. According to the similitude law, the volume of the model is $1/2^3$ of the prototype, while the stress similitude requires that mass should reduce to $1/2^2$ of the prototype. To get rid of this error, an additional mass ($1/2^2$-$1/2^3$=1/8 mass of prototype) was added on the experimental model. This additional weight and the load from the upper 3rd and 4th story were applied on the top of columns through prestressing

2.2.2. Material properties

Figure 2.3 shows the dimensions and reinforcement details of the specimen. Longitudinal reinforcing bars in columns were BRC round high strength bars (smooth welded steel mesh bars with design yield strength of 525 MPa) with diameter of 8 mm (first story) and 7 mm (second story). Longitudinal reinforcing bars in beams were 10 mm diameter high yield deformed bars (design yield strength of 460 MPa). Transverse bars in beams and columns were all 6 mm diameter mild round bars (design yield strength of 250 MPa), with a spacing of 280 mm. All reinforcing bars in base blocks were 10 mm diameter high strength deformed bars (design yield strength of 460 MPa).

Stress-strain curves of these reinforcing bars are shown in Figure 2.4 and properties of them are listed in Table 2.2. 3D view of the whole steel cages is shown in Figures 2.5. 3D views of the lap splices and joints are shown in Figures 2.6-2.8. It is noted that lap splices were located just above the base block and the 1st floor level. For convenience and stability when erecting the whole frame cage, tacked welding was done at each touch point of the crossing reinforcing bars.

Concrete was mixed and cast in the structural laboratory of National University of Singapore, and cured for 28 days. The mix property was 1:3.15:3.78:0.85, by weight of cement; fine aggregates (natural sand); aggregates (10 mm max size) and water. The high water-cement ratio was chosen so as to achieve a low concrete cube strength in between 20 to 30 MPa that represents the concrete design strength in 1970s in Singapore. Casting of a frame was arranged into three batches: casting of base blocks first, then the first story and finally the second story. For each casting batch, twelve test cubes (100 mm x 100 mm x 100 mm), six test cylinders (100 mm x 200 mm) and three test prisms (100 mm x 100 mm x 400 mm) were cast. Cubes were used to evaluate the cube compressive strength in 3 days, 7 days,14 days, 28 days; cylinders were used to obtain Young's Modulus and the cylinder compressive strength; and the prisms were used for the modulus of the rupture test. Table 2.3 lists the details of concrete strength. Average cube strength of concrete was 25.3 MPa for specimen S1 and 25.8 MPa for specimen S2. And average Young Modulus of the concrete was 19.07 GPa for S1 and 20.38 GPa for S2.

2.3. Test setup and test procedure

2.3.1. Details of the setup

Two specimens were tested in an upright position. Figure 2.9 shows the 3D view of the set-up of the test specimens and Figure 2.10 shows the side view of the set-up. The set-up includes an actuator, a lateral loading whiffle tree system, a prestressing system and a lateral support system. Locations of these components are specified in Figure 2.10. Specimen S1 was tested under pushover loading. Lateral load was applied from the hydraulic actuator (650 kN), which was fixed on the reaction wall, at a slow rate (0.01 mm/s) to push the specimen S1 until its failure. Specimen S2 was tested under displacement-controlled cyclic loading.

A whiffle tree system was designed and fabricated to transfer the later load from the actuator to the two story beam ends by pin joints. The details and dimension of it are shown in Figure 2.11 and a 3D view is shown in Figure 2.12. The location of the steel plate on the whiffle tree, which was used to connect to the actuator by bolting, was chosen to have an inverted triangular distributed load to the beam levels. Pin joint connections were used to connect the whiffle tree system to the beam ends. At each beam end, two L angles were used to sandwich the beam end by bolting at the longer face, and were bolted to the pin joint at the shorter face. In this way, the lateral load could be transferred from the actuator, through the whiffle tree system and pin joint connection, and finally to beams.

Concrete blocks at column bases were rigidly mounted to a strong beam, which was anchored to the strong floor slab and to the strong wall. A total of fourteen 24 mm

diameter bolts (G8.8) were used to connect each base block to the strong beam. Thus a fixed end condition at the base was simulated. In order to prevent out-of-plane movement and instability, four lateral supports, bolted to two steel frames, were used to sandwich the test specimen. Figure 2.13 shows the 3D view of the lateral support system.

To simplify the test process, distributed loads on beams were ignored. However, vertical loads from the upper two stories and the additional weight for the compensation of mass were applied on columns through prestressing technique. Prestressing was conducted only one day before the testing to minimize the prestress loss. Prestressing forces, 59.7 kN for the internal column and 38.6 kN for the external column, were applied on the top of columns through four seven-wire strands, two for the internal column and another two for the external column. The seven-wire strand has a diameter of 9.6 mm, and a nominal cross area of 55 mm^2. The Young's modulus of the strand is 195 kN/mm^2. Each strand for the internal column would have to be jacked up to 2784 micro strain, and the strand for the external column would have to be jacked up to 1799 micro strain. In order to avoid out of plane displacement or twisting, two jacks were jacked together for one column (as shown in Figure 2.14). Several runs (in each run only 400 micro strain was applied to one strand to avoid concrete crushing during prestressing) were conducted and repeated before the target strain was achieved. In every run, the internal column was jacked before the external column.

2.3.2. Instrumentation

Strain gauges were attached to reinforcing bars in the frame and to the outside surface of the concrete, to record the change of strain in specimens during the test. Locations of the strain gauges were chosen at the important places of interest, such as sections with maximum moment, joint regions and possible failure locations. Figure 2.15 shows the locations of strain gauges on reinforcing bars (TML's FLA-5-11 with gauge length of 5 mm) and Figure 2.16 shows the locations of strain gauges on concrete surfaces (TML's PFL-30-11 with gauge length of 30 mm).

Displacement transducers were used to measure lateral displacements, and measure vertical displacements at some important locations for rotation calculation. Four types of displacement transducers were used in the test: range of 25 mm, 50 mm, 100 mm and 200 mm. Aluminum plates and angles were used to provide smooth surfaces for tips of displacement transducers to rest on. They were attached to the concrete using "Araldite" rapid epoxy adhesive. The locations of the displacement transducers are shown in Figure 2.17. At each level, transducers were used to measure the horizontal displacements (labels D1 to D6, 200 mm range). At each concrete block, a transducer was used to measure the horizontal displacement of the block (labels D7 and D8, 100 mm range), and two transducers (labels D9 to D12, 25 mm range) were used to measure the relative vertical displacements between two points on the block to calculate the rotation of the block. At each joint area, four transducers were used to measure vertical (Labels D13 to D20, 25 mm range) or horizontal (Labels D21 to D28, 100 mm range) deformation of the joint panel, which could be used to calculate the

rotation of the joint. A 3D view of the transducers at a joint is shown in Figure 2.18. Furthermore, two omega gauges (as shown in Figure 2.19) were used at each joint to measure the extension/shorten deformation at the two crossing diagonal directions.

2.3.3. Loading history and test procedure

Specimen S2 was subjected to cyclic loading in the horizontal direction. The movement of the actuator (650 kN) was by displacement control. The loading history curve is shown in Figure 2.20, which was based on a quasi-static procedure for cyclic loading history proposed by Park (1988). The procedure including two important concepts: 1. find out the displacement due to the first yielding of reinforcement; 2. two cycles are needed for the same displacement amplitude after yielding. And because the structure under study is gravity-load-designed structure of which the post-yielding performance may be weak (the increase of displacement may not be much after yielding), the focus of observation was on the behaviors of the pre-yielding stage. In the cyclic displacement history, the yield displacement of 20mm was found by the test under pushover loading, so that after 20mm, two cycles for each displacement amplitude were adopted. And more displacement steps (3mm, 6mm, 9mm, and 15mm) were suggested to observe the pre-yielding behaviors. The rate of loading was selected to be small enough that inertia forces are insignificant. It changed twice: 0.01 mm/s in the first 3 cycles (peak displacement of 3 mm, 6 mm and 9 mm); 0.05 mm/s in the fourth cycle (peak displacement of 15 mm), and 0.1 mm/s in the final cycles (peak displacement of 20 mm twice and 40 mm twice). In the testing, at each peak

displacement, the displacement would be held constant for 5 minutes for crack checking. The actuator would be stopped immediately after the failure of specimen.

2.4. Experiment results and interpretation

2.4.1. Global response

2.4.1.1. General behavior in the pushover test

In the testing, for every 3 mm displacement (2nd floor displacement) increment, the lateral load was held several minutes for crack checking. Figure 2.21 depicts the crack pattern and the failure mode in the pushover test, and the primary locations for crack development.

The first flexural crack was observed to occur at the bottom of the internal column (location 1), when the 2nd floor displacement was 2.0 mm (with the applied force at around 20.0 kN). When the 2nd floor displacement reached 4.0 mm (with the applied force at around 29.5 kN), inclined flexural-shear cracks first appeared on beams at locations 2 and 3, which were around 100 mm (0.5*d*, where *d* is the effective height of the beam) away from columns, and the flexural cracks at location 1 began to develop into shear cracks. Just a few fine cracks occurred at the external column bottom (location 4). When the 2nd floor displacement increased to around 6.7 mm (with the applied force at around 37.6 kN), some new shear cracks developed on beams (locations 5, 6 and 7), and more and more new shear cracks developed at the bottom of columns (above locations 1 and 4).

The first flexural cracks at the beam-column interface occurred at the 2nd story (locations 8 and 9), when the 2nd floor displacement increased to 11.5 mm (with the applied force at around 49.5 kN). When the 2nd floor displacement increased to 14.5 mm (with the applied force at around 55 kN), shear cracks on beams formed further away from the joints (locations 10 and 11, about 1 *d* away from the external column). The first diagonal shear crack at the beam-column joint was formed at the 2nd story external joint (location 12), when the 2nd floor displacement increased to 20.0 mm (with the applied force at around 63.8 kN).

The first yielding of the reinforcing bars ($\varepsilon_y = 0.0028$ as listed in Table 2.2) occurred at the bottom of the internal column, when the 2nd floor displacement was about 21.3 mm (with the applied force at around 65.4 kN). And the first yielding of beam reinforcement ($\varepsilon_y = 0.0025$ as listed in Table 2.2) occurred at the first story beam, when the 2nd floor displacement was about 22.7 mm (with the applied force at around 67.0 kN).

When the 2nd floor displacement increased to 26.0 mm (with the applied force at around 70.0 kN), the flexural cracks at the 1st story beam-column interface formed (locations 13 and 14). With the displacement continued to increase, yielding of beam reinforcing bars at the location of the beam-column interface developed very fast, as a result, cracks at the beam-column interface (locations 8,9,13 and 14) became wider and extended longer until the beam reinforcing bars broke.

When cracks at the beam-column interface ceased to develop, yielding of the column reinforcing bars at the tension side started to develop dramatically, and the

corners at column bases under compression started to bulge. The applied force reached the maximum value of 81.3 kN, when the 2nd floor displacement reached 50.2 mm. When the 2nd floor displacement increased to 56 mm, tension side of columns lifted from the concrete blocks and the corners of columns under compression crushed, which resulted in the dramatic drop of the applied force. The failure of the frame (see photos in Figure 2.21) started with the beam failure with large cracks at beam-column interfaces, and ended at the column failure with crushing of concrete at the corners under compression. Most of the cracks were concentrated on beams and bottoms of columns. Except for some small cracks, no obvious failure occurred at joint areas and the other parts of columns. It can be concluded from the pushover test that the test frame is a strong column - weak beam structure.

After the test, the concrete was knocked off at the failure locations (bottom of columns and beam ends near joints) to expose reinforcing bars. It was found that the outermost reinforcing bars at these locations were broken due to the tensile load caused by the bending moment (as shown in Figure 2.22). Thus, the ultimate failure mode of the frame is a flexural tensile or compressive failure at the plastic hinge.

2.4.1.2. General behavior in the cyclic test

The lateral load was applied based on displacement control, according to the cyclic loading history shown in Figure 2.20. Since the displacement shown in Figure 2.20 is at the height of the actuator, the displacement stated in this section will refer to this displacement instead of the 2nd floor displacement. At every cycle, the lateral load

was held 5 minutes at the peak displacement value for crack checking. Figure 2.23 shows the crack pattern, the failure mode, and the primary locations for crack development in the cyclic test.

In the 1st cycle (3 mm cycle), the first crack, which was a shear crack, occurred on the 1st story beam (location 1, about 0.5*d* away from the external column, where *d* is the effective height of the beam) and other shear cracks occurred at locations 2 and 3 (about 0.5*d* away from the internal column). The first flexural crack at the beam-column joint interface occurred at location 4 when the specimen was pulled to -3 mm.

In the 2nd cycle (6 mm cycle), new cracks are concentrated on bottoms of beams (locations 5 and 6), and the first flexural crack on the internal column occurred at location 7. In the 3rd cycle (9 mm cycle), more shear cracks on beams occurred further away from the joints, and flexural cracks at beam-column interfaces became wider. The first shear cracks on the external column formed at location 8.

In the 4th cycle (15 mm cycle), the first yielding on the reinforcing bars occurred at the 1st story beam, and a large shear crack developed quickly starting from the top of the 1st story beam about 600 mm away from the external column, to the bottom about 200 mm away (location 9). The first diagonal joint crack appeared at the 1st story beam external column joint (location 10).

In the 5th cycle (the 1st 20 mm cycle), the large shear crack at location 9 became wider, and cracks at the beam-column interfaces also opened wider. More shear cracks on columns occurred at higher locations above locations 7 and 8, and more shear

cracks on beams appeared further away from the joints. Several diagonal cracks occurred at the 2nd story beam column joints (locations 11 and 12).

In the 6th cycle (the 2nd 20 mm cycle), the large shear crack at location 9 became very wide. The first flexural crack on the upper part of the external column also occurred at location 13. It is noted that at column bases, the tension sides lifted up from the block because of the continuous deformation of the column reinforcing bars after yielding.

In the 7th cycle (40 mm cycle), the specimen was firstly pushed until 40 mm. At 40 mm displacement, the width of the large shear crack at location 9 became more than 50 mm and the longitudinal reinforcing bars, passing the crack, could be seen deformed largely under the shear force (as shown in Figure 2.23 photo A). The 1st story beam could be considered failed because of this large shear crack, and the overall lateral load was near the capacity of the specimen obtained in the pushover test. Even if the beam failed first, the lateral load was still maintained without dropping dramatically, until columns failed and a collapse mechanism formed. Several new shear cracks occurred at the 2nd story external beam-column joints and the top part of the external column. More new shear cracks developed at the bottom part of columns.

When the specimen was unloaded and was pulled to -30 mm displacement, an unexpected local failure occured at the 2nd story beam at location 14. The reason of this kind of failure is due to the insufficient anchorage and insufficient shear links at the beam end loading part. As a result, reinforcing bars slipped under pulling force, and a large brittle shear crack formed with the spalling of concrete bottom cover.

After this local failure, the load dropped dramatically and the test was stopped. Finally, the specimen was pushed until column flexural failure: concrete crushing at the compression corner and the tension side column lifting up from the concrete block (as shown in Figure 2.23 photos B and C). Because the damage caused by the local failure at location 14, the push load thereafter could reach about 60kN only, which is roughly three fourths of the capacity of the specimen (81 kN) obtained from the pushover test.

The difference of the beam failure mode between S1 and S2 may be attributable to the adjustment of the locations of beam shear links when S2 was fabricated. The failure of the 1st story beam end of S2 may be considered as an abnormal local failure, because this kind of large cracks was only concentrated at one location of the beam and didn't occur at other parts of beam ends. Although the beam failure of the cyclic test specimen (S2) is different from that of the pushover test specimen (S1), the failure mechanism is similar: strong column–weak beam mechanism with failure starting from the beam failure and ending in the column flexural failure.

2.4.1.3. Global performance

Figure 2.24 shows the Load-displacement relationship of the specimens under pushover and cyclic loading. From Figure 2.24, it can be seen that the curves of the pushover test can roughly represent the trend of the backbone of the cyclic test curves, and the ultimate loads obtained from these two tests are nearly the same (around 81 kN). Although the backbone curve of the cyclic test exceeds slightly the pushover

curves, considering the higher concrete strength of the cyclic test specimen (S2) and higher loading rates in the cyclic test after the 3rd cycle (a higher loading rate may induce a higher resistance according to Paulay and Priestley (1992)), it is reasonable to draw the conclusion that the pushover test can be a simple and backbone representation of the cyclic test. Thus, the load- 2nd floor displacement curve of the pushover test is used to evaluate the global performance of the specimens as shown in Figure 2.24 (a).

It is observed in Figure 2.24 that the negative displacement of the hysterisis curves is not as large as that in the positive direction and not symmetrical to each other. The reason may be as follows. The actuator was bolted to the loading system mounted on the wall. During the negative displacement, that is, during pulling, the bolts are under tension forces, and the load from the actuator may not be transferred to the specimen as effectively as during the pushing stage (positive displacement).

From Figure 2.24 (a), it can be seen that when first yielding in the reinforcing bars occurred, the 2nd floor displacement Δ_y was 21.3 mm. This corresponded to an overall drift ratio of 0.76%. When the maximum load of 81.3 kN was reached, the 2nd floor displacement Δ_u was 50.2 mm and the corresponding overall drift ratio was 1.8%. At the maximum displacement Δ_{max}=76.0 mm, which corresponded to 80% of the maximum load, the overall drift was 2.8%. The corresponding ductility factor is Δ_{max}/Δ_y=3.57.

2.4.2. Local responses

2.4.2.1. Local responses in pushover test

Figure 2.25 shows the joint rotation histories in the pushover test. At the mid point of each side of a rectangular joint panel, a transducer was used to measure the deformation at that point, along the direction of the panel side. Using the relative displacement of the two vertical transducers, as well as two horizontal transducers at each joint, joint rotations at the beam/column direction were computed.

From Figure 2.25 (a), it can be seen that the rotations measured at two directions of the 1st story joints are nearly the same, which shows that the 1st story joints were remained rigid without severe damage. This corresponds to the observation that few shear cracks formed at the first story joints. Thus, the first story joints were strong in the test.

From Figure 2.25(b), it can be seen that, for the 2nd story joints, the rotation at the beam direction (curves 7 and 8) is different from that at the column direction (curves 3 and 4), which shows that the 2nd story joint panels had some deformation and were no longer in rigid. This may be due to the joint shear cracks concentrated on the 2nd story joints. Since such difference is not too much, the damage of the 2nd story joints is minor. From the observation that the beam direction rotation is larger than the column direction rotation at the 2nd story joints, the strong column-weak beam mechanism is confirmed again.

2.4.2.2. Local responses in cyclic test

Figure 2.26 shows the hysteretic curves in the cyclic test (the abscissa is curvature and the ordinate is the base shear) at column ends, beam ends and joints. At the sections under consideration (beam ends, column ends and joints), strain gauges were used to measure the strain reading of all reinforcing bars and concrete surfaces. Note that the tensile strain is positive and compressive strain is negative. The curvature at a section is calculated according to equation (2.1)

$$\frac{\varepsilon_1 - \varepsilon_2}{D} \tag{2.1}$$

Where,

ε_1 =the strain gauge reading of the left outermost reinforcing bars for the column section, or the strain gauge reading of the upper outermost reinforcing bars for the beam section;

ε_2 =the strain gauge reading of the right outermost reinforcing bars for the column section, or the strain gauge reading of the bottom outermost reinforcing bars for the beam section;

D =the distance between the locations where ε_1 and ε_2 were measured.

In order to facilitate comparison of hysteretic shapes at different locations, same scales are used: curvature range is from -0.000025 rad/mm to 0.000025 rad/mm and base shear range is from -85 kN to 85 kN. Beam ends of both story and bottoms of both columns (failure locations) experience the most severe inelastic excursion. Other parts of columns and joint areas exhibit relatively small excursion and even in elastic range. The maximum excursion in beam ends is larger than that in column ends. All

these observations from Figure 2.26 imply the strong column-weak beam mechanism of the test frame.

By comparing the load vs. curvature curves of columns and beams, it can be seen from Figure 2.26 that the external column experiences larger excursion than the internal column, and that the 2nd story beam experiences larger excursion than the 1st story beam. By comparing the curves at the four joints, it can be noticed that the 2nd story external joint exhibits the most severe excursion whereas the 1st story internal joint exhibits the least severe excursion. These comparisons show that the external column is slightly weaker than the internal column, and the 2nd story beam is slightly weaker than the 1st story beam.

Since the observation of hysteretic behaviors in the cyclic test from Figure 2.26 shows similar results as that of pushover behaviors through Figure 2.25, it could be concluded that the pushover test can be a simplified representation of the cyclic test.

2.4.3. Moment-curvature curves of the sections

Based on the strain gauge reading of all reinforcing bars and concrete surfaces at a section, the forces in all reinforcing bars and the height of neutral axis of a section can be calculated, and then the moment resistance generated by the forces from reinforcing bars and compression concrete can be determined. Here, ideal bilinear stress-strain curve of steel bars with the hardening factor of 0.01, and Hognestad stress-strain curve of concrete (Macgregor 2005) are assumed in the calculation. Figure 2.27 shows the moment-curvature curves of the beam and column sections in the

pushover test. The theoretical relationship between moment (M) and curvature (κ) of a section is:

$$\kappa = \frac{M}{EI} \tag{2.2}$$

Where,

E=the Young's Modulus of a section;

I =the second moment of inertia, for an ideal uncracked rectangular section with width b and height h, $I = \frac{bh^3}{12}$ assuming gross section;

EI=the flexure stiffness of a bending section, which is the tangent stiffness of the moment-curvature curve.

The moment-curvature relationship based on the ideal uncracked section was calculated according to equation (2.2), and was compared with the moment-curvature curves obtained from the pushover test as shown in Figure 2.27. It is worthwhile noting that by comparing the tangent stiffness of the moment-curvature curves, the flexural stiffness (EI) obtained from the test is less than that of the ideal uncracked section. This confirms that there exists the initial stiffness reduction in the actual structures, due to initial cracking of member sections, and micro-cracking generated from concrete curing and minor construction loadings, as reported by other researchers (Hirosawa 1975; Kenneally and Burns 1986; Elnashai et al. 1988, 1990; Bracci et al. 1995b; Pilakoutas and Elnashai 1995; Filiatrault et al. 1998; Lopes 2001).

The reduction factors, ratios of initial stiffness in the test over uncracked section stiffness, are calculated as: 0.492 for internal column, 0.708 for external column and 0.354 for beams. These reduction factors are consistent with those suggested by Bracci

(1995b) (0.55 to 0.6 for columns and 0.25 to 0.35 for beams) and ATC (1996) (0.7 for columns and 0.5 for beams).

Figure 2.28 shows the comparison of moment-curvature curves between the pushover and cyclic test. The cyclic test curves for columns can match the pushover test well including the initial stiffness (as shown in Figure 2.28 a and b). The cyclic test curve for the beam is shifted towards the push direction (positive moment), because of the formation of the large shear crack at the 1st story beam, but the stiffness of the cyclic curve still matches with the pushover test curve (as shown in Figure 2.28 c). The observation from Figure 2.28 again confirms that the pushover test can be a simplified representation of cyclic test and the initial stiffness of the member section is less than the uncracked section stiffness. It is noted that the stiffness of the member sections is reduced with the increasing cycles. The stiffness reduction factors of fully cracked section (stiffness in the last cycle) relative to the uncracked property are: 0.286 for internal column and 0.172 for external column.

From the moment-curvature relationship, the parameters of Modified Takeda Hysteresis model (as shown in Figure 1.3) were obtained: $\alpha = 0.4, \beta = 0.1$ for beams and $\alpha = 0.5, \beta = 0.1$ for columns, where α is the unloading stiffness degradation parameter and β is the reloading stiffness degradation parameter. These values are the average of those from different cycles and will be used in the chapter 3 for FEA modeling. Since the bilinear factor *r* varied from section to section, an analytical method for calculation is given in Appendix A and the accuracy of this method is validated in Chapter 3.

2.5. Summary

This Chapter focused on the experimental investigation of the seismic behavior of GLD RC frame structures in Singapore. For this purpose, a half scale, 2-story frame, which has one and a half bay, was tested under pushover and cyclic loading. Test results revealed that, although the fame was designed without any seismic provision, the experimental model showed relatively good seismic performance: strong column-weak beam mechanism; good ductility capability with ultimate ductility factor of 3.4 and ultimate total story drift of 2.8%; failure mode which was dominated by flexural behavior instead of shear failure. And test results showed that the pushover test could be a simplified representation of the cyclic test.

Important information, such as reduction factors of initial effective stiffness (0.492 for internal column, 0.708 for external column and 0.354 for beams) and parameters of The Modified Takeda hysteresis rule ($\alpha = 0.4, \beta = 0.1$ for beams and $\alpha = 0.5, \beta = 0.1$ for columns), were obtained from the test and will be used for developing a FEA model for frame structure in Chapter 3.

Table 2.1 Similitude for reinforcement

Member	Prototype in 1970s		Half scale model in the test			
	Diameter (mm)	Yield force (kN) (*)	Diameter (mm)	Yield force (kN)	Target force (kN) (*)x0.25	Error
Beam	D20	169.04	D10	37.11	42.26	12%
Column 1	D16	104.93	BRC 8	26.38	26.23	0.60%
Column 2	D13	75.99	BRC 7	20.19	19.00	6%

* The yield force was obtained from material tests

Table 2.2 Steel reinforcement properties used in the test

Diameter	Surface	f_y(MPa)	f_u(MPa)	E(Gpa)	ε_y	ε_u
6 mm	Smooth	250	456.2	103.5	0.0024	0.33
BRC 8 mm	Smooth	530	641	188	0.0028	0.032
BRC 7 mm	Smooth	520	566	190	0.0028	0.031
10 mm	Deformed	473.1	565.9	189	0.0025	0.145

Where,

f_y=yield stress

f_u=ultimate or rupture stress

E=initial Young's modulus

ε_y =yield strain

ε_u =ultimate strain

Table 2.3 Parameters of frame specimens tested

Specimen	Cube strength f_{cu} (MPa)	Young's modulus E(GPa)	Modulus of rupture f_r (MPa)	Cylindrical strength f_c'(MPa)
S1(pushover)	25.3	19.07	3.96	20.28
S2(cyclic)	25.8	20.38	4.01	21.16

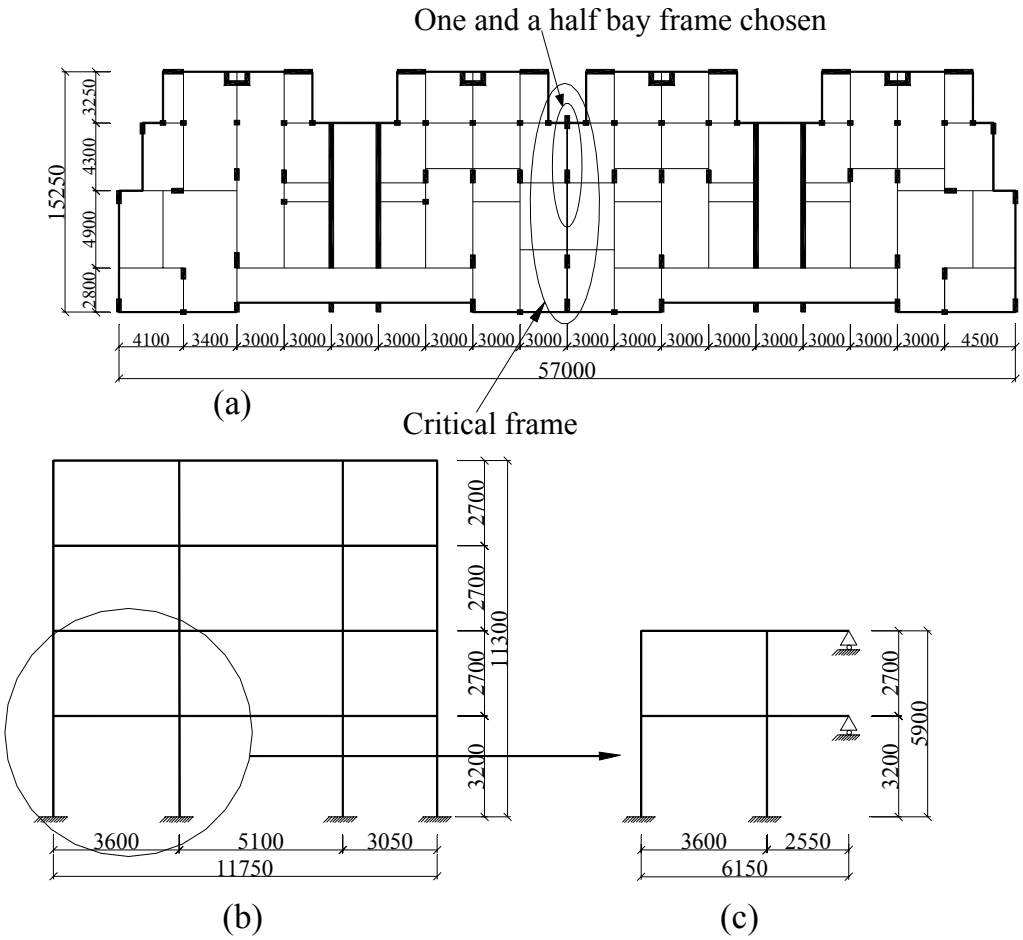

Figure 2.1 Prototype structure: (a) plan view of the whole building (b) selected critical frame (c) two story- one and a half bay frame chosen for the test model

Figure 2.2 3D view of the test frame specimen

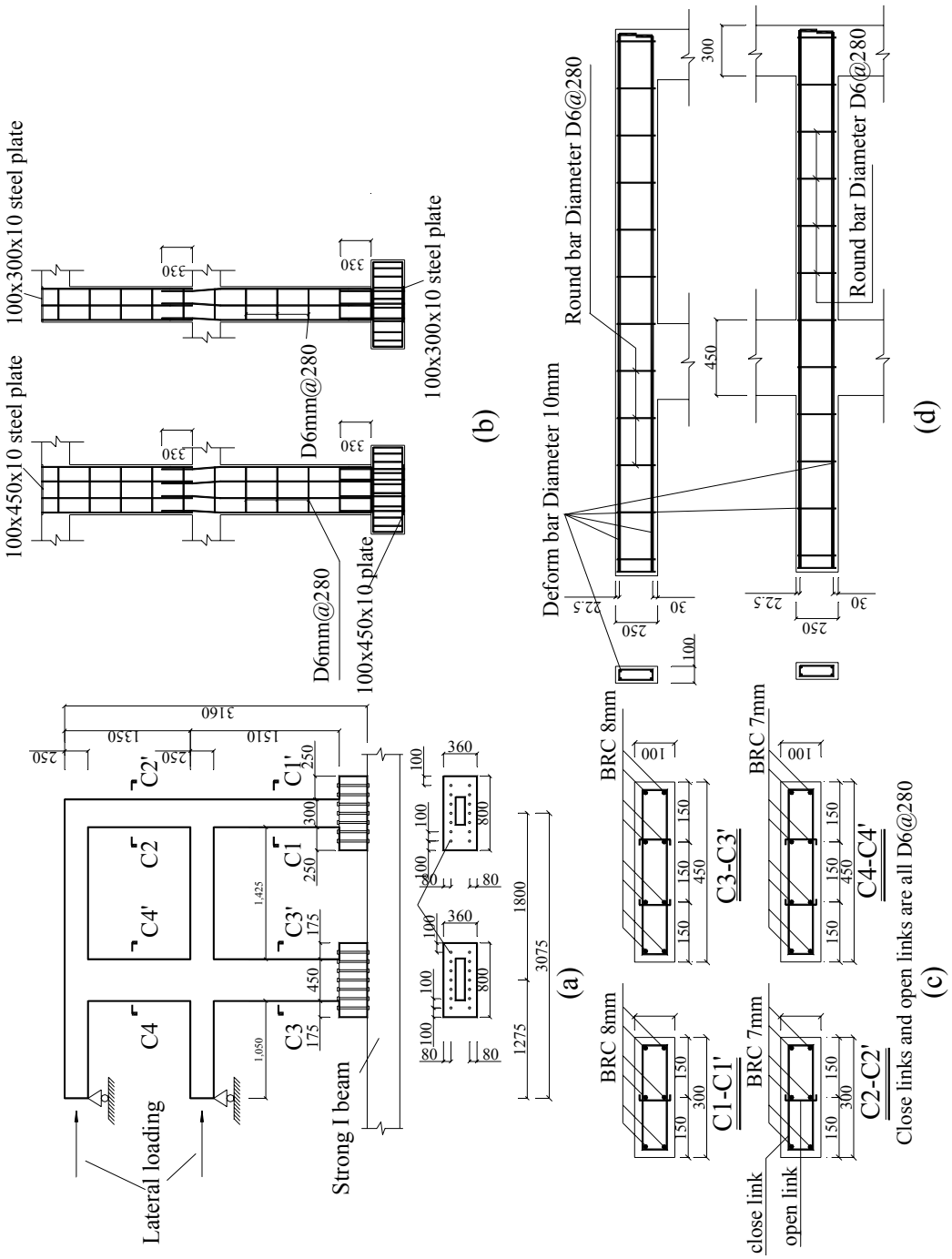

Figure 2.3 The experimental model: (a) test specimen dimension (b) reinforcement details in columns (c) cross section of columns (d) reinforcement details in beams

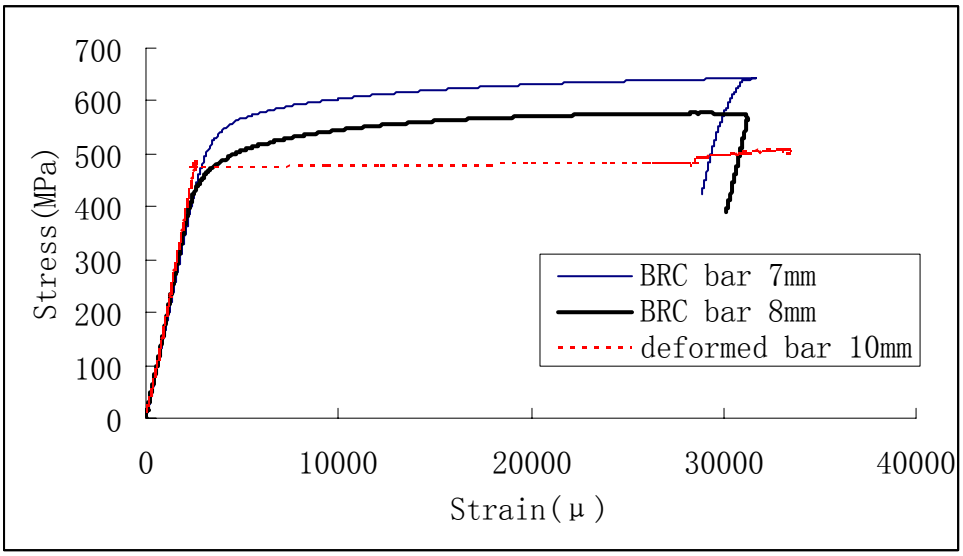

Figure 2.4 The stress- strain curve of steel reinforcement used in model

Figure 2.5 3D view of the whole frame steel cage

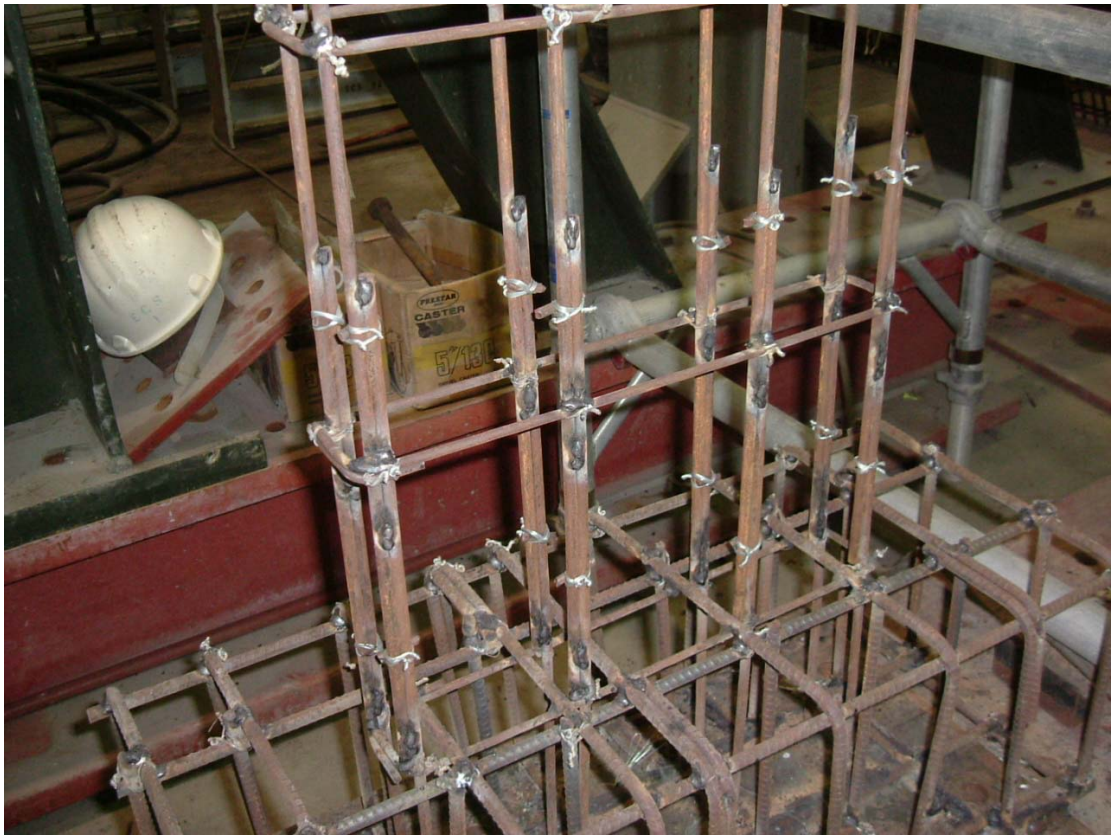

Figure 2.6 3D view of the lap splice of columns above the base block

Figure 2.7 3D view of the lap splice of columns above the 1st story joints

Figure 2.8 3D view of the 2nd story joints

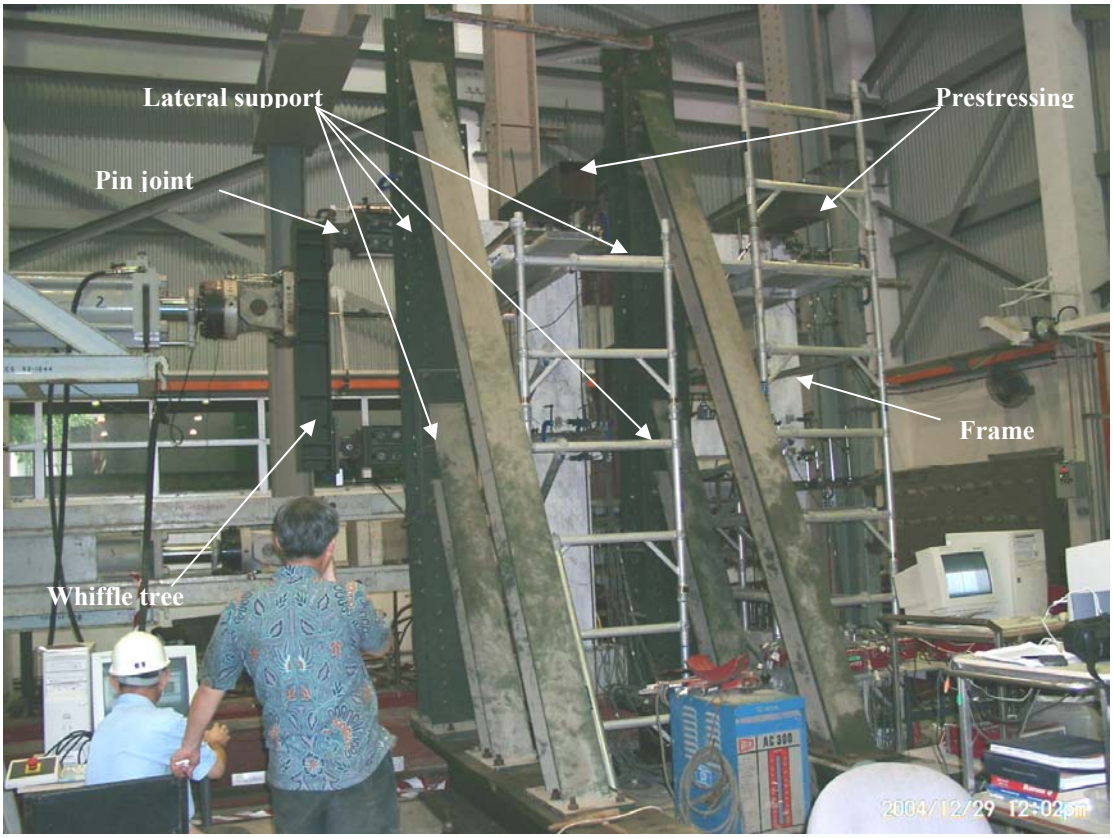

Figure 2.9 3D view of the test set-up

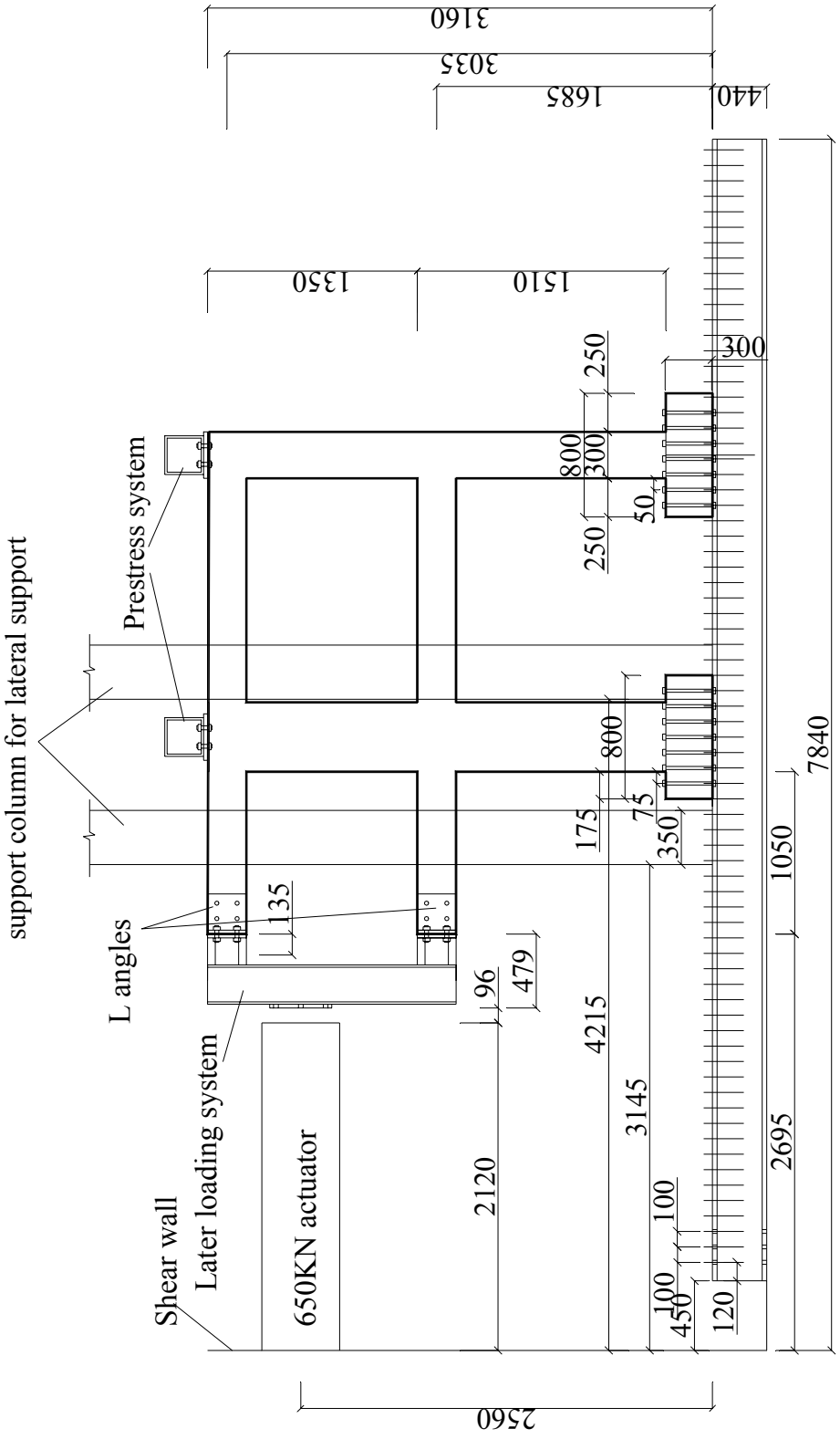

Figure 2.10 Side view of the set-up

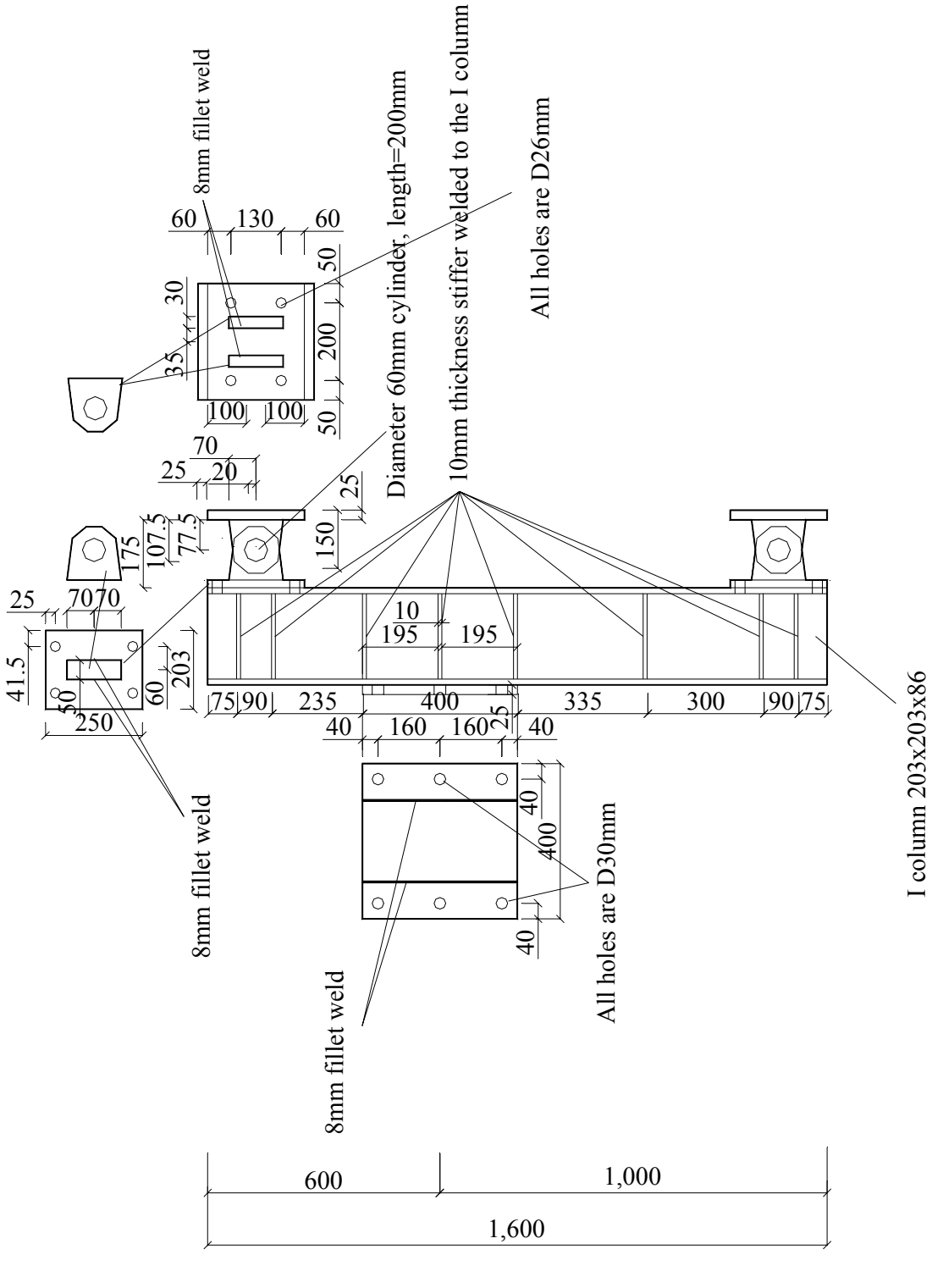

Figure 2.11 Details of the lateral whiffle tree loading system

Figure 2.12 3D view of the lateral loading whiffle tree system

Figure 2.13 3D view of the lateral support

Figure 2.14 Two jacks were used together for one column

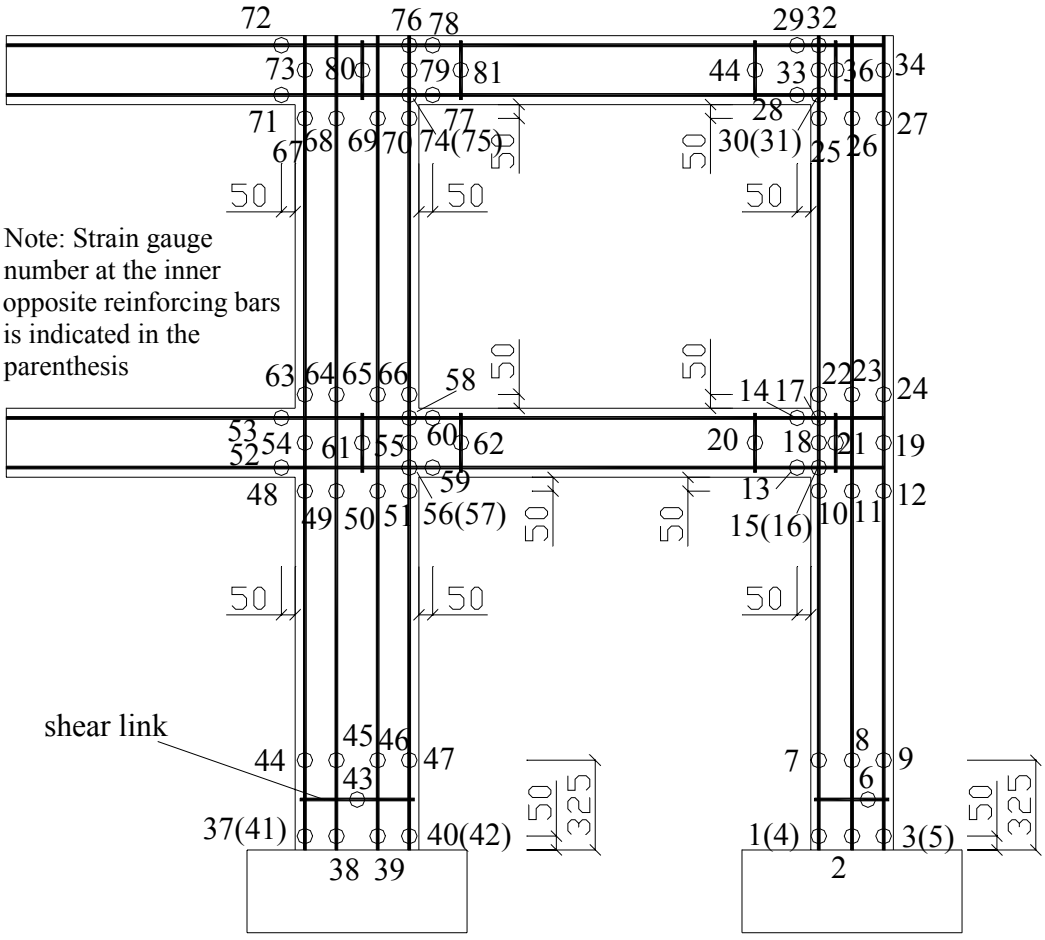

Figure 2.15 Locations of the strain gauges on the reinforcing bars

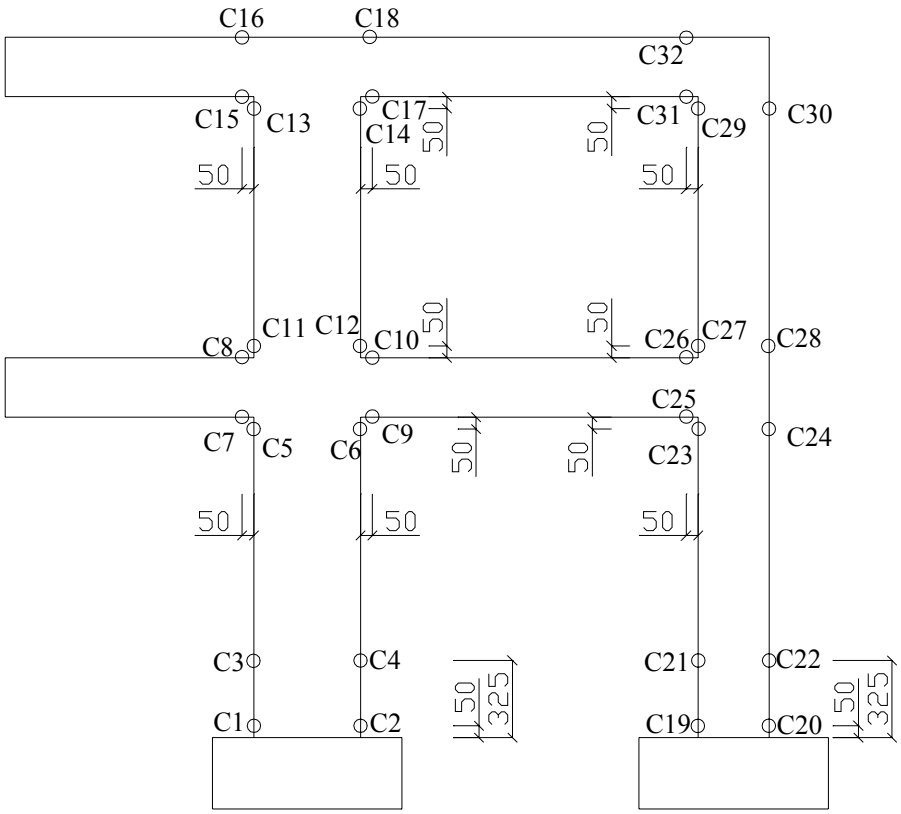

Figure 2.16 Locations of the strain gauges on the concrete surface

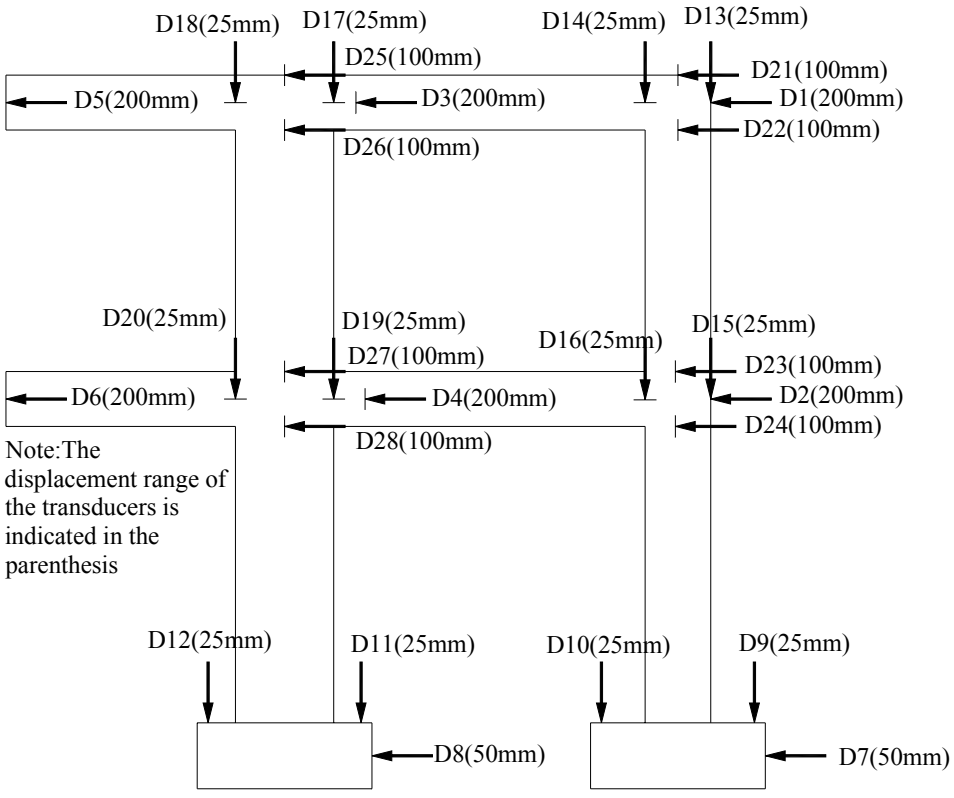

Figure 2.17 Locations of transducers

Figure 2.18 3D view of the transducers at the 1st story external joint

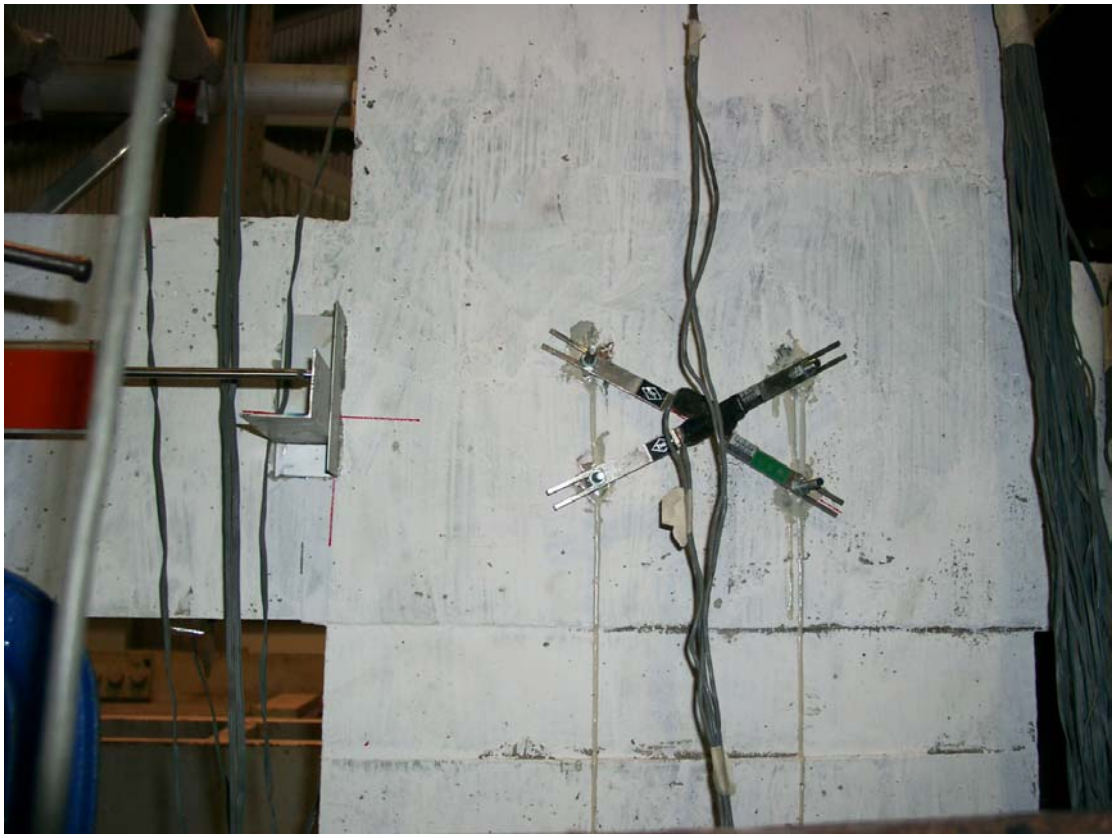

Figure 2.19 3D view of the omega gauges used at a joint

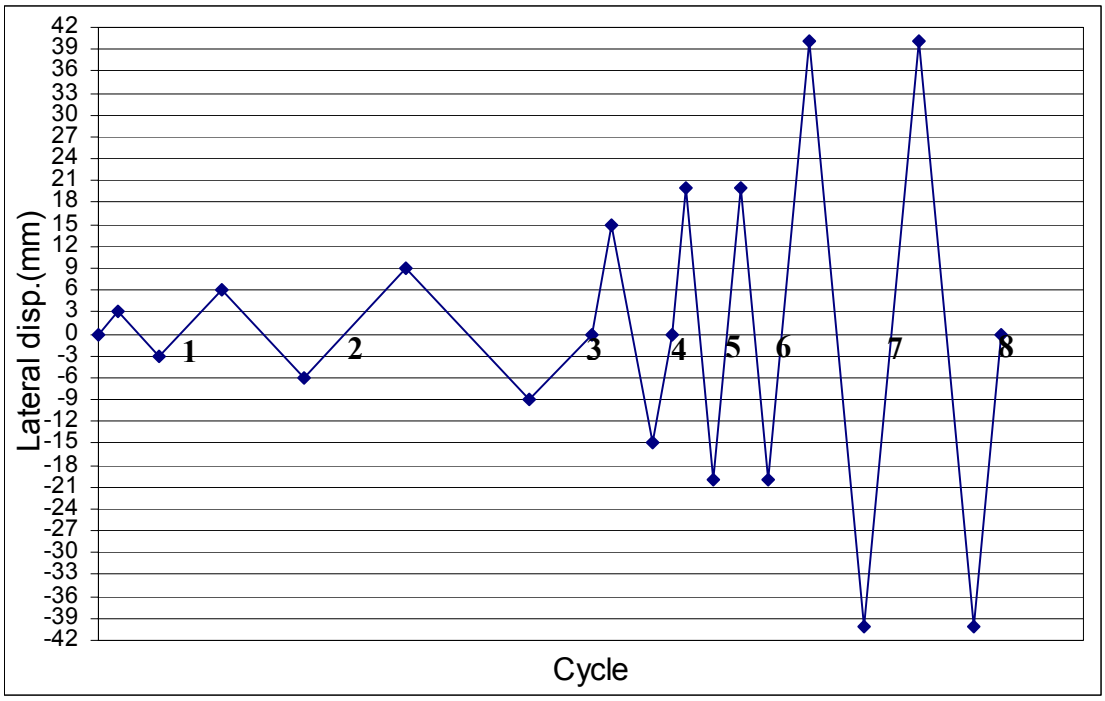

Figure 2.20 Cyclic loading history

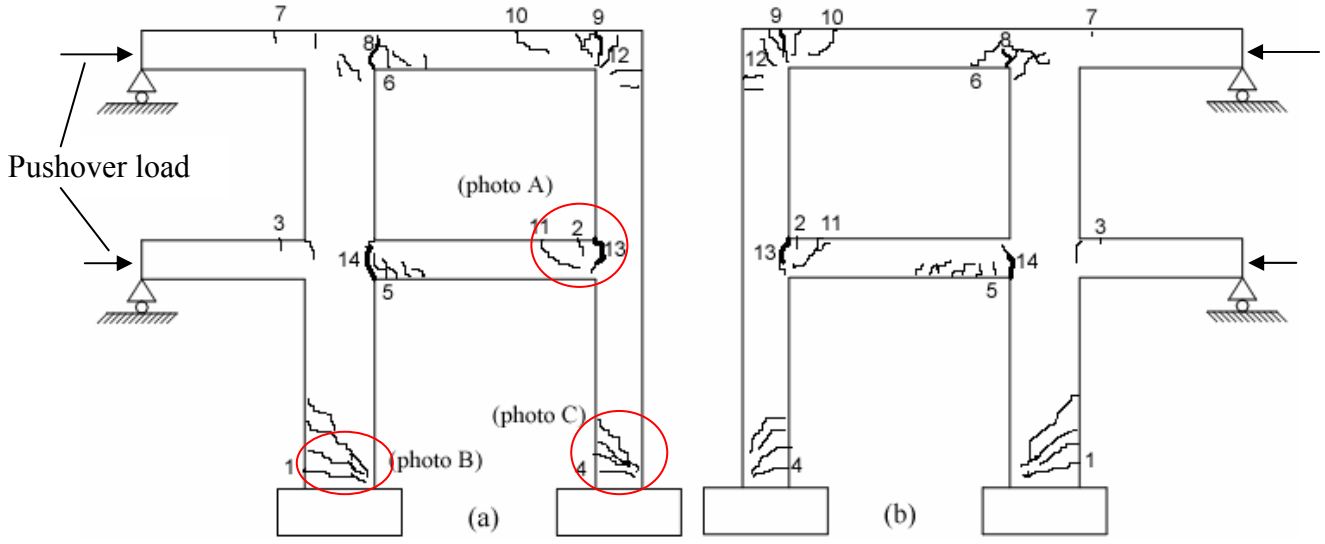

Photo A Photo B Photo C

Figure 2.21 Crack pattern and failure mode of specimen S1 (a) front view (b) back view

(a) (b)

Figure 2.22 Breaking of the outermost tension reinforcing bars: (a) location of the base column (b) location of the beam-column interface

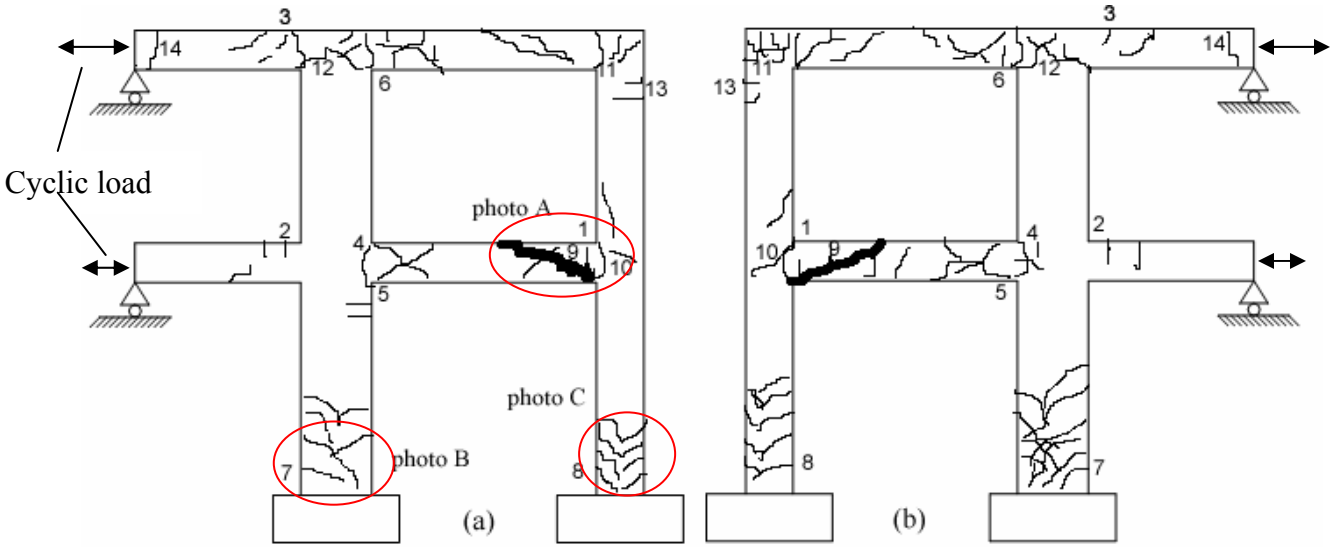

Photo A Photo B Photo C

Figure 2.23 Crack pattern and failure mode of specimen S2 (a) front view (b) back view

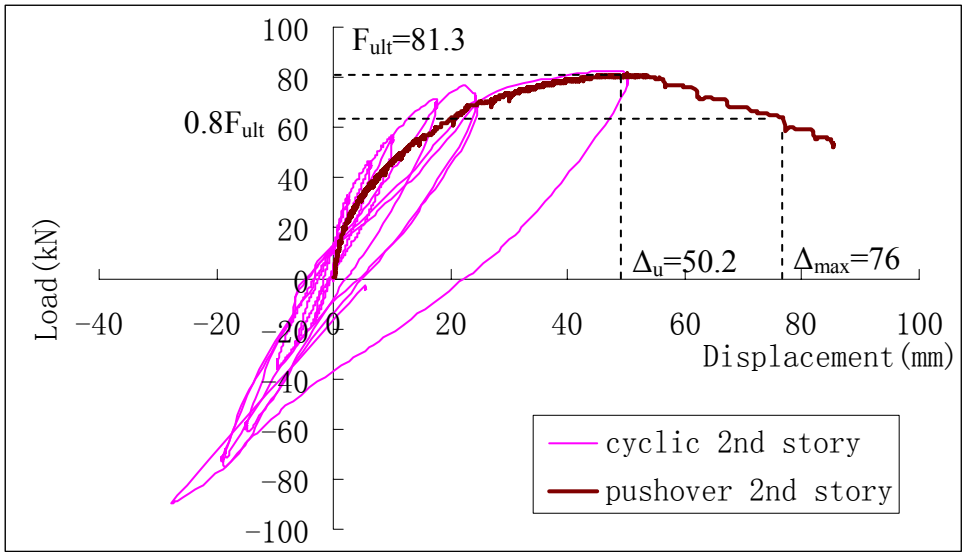

(a)

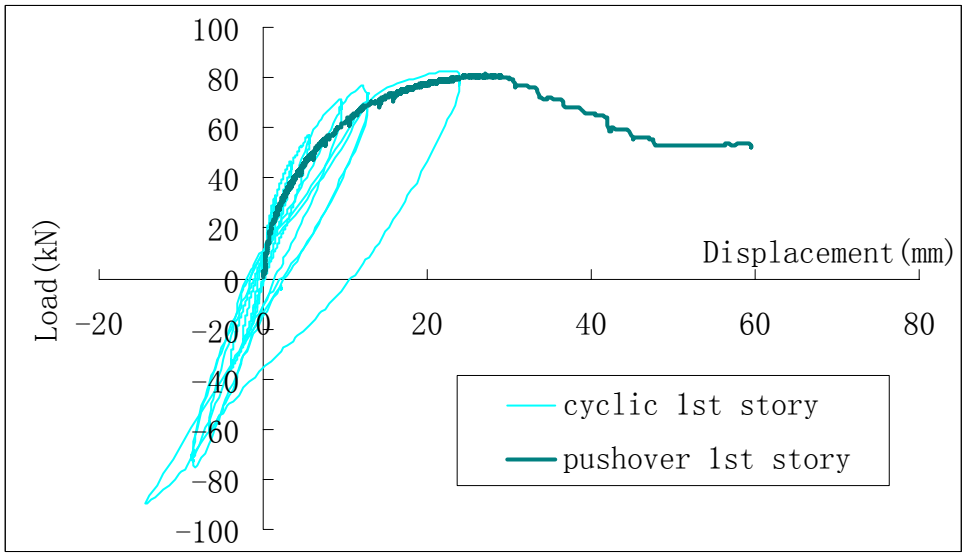

(b)

Figure 2.24 Load-displacement relationship: (a) 2nd floor displacement (b) 1st floor displacement

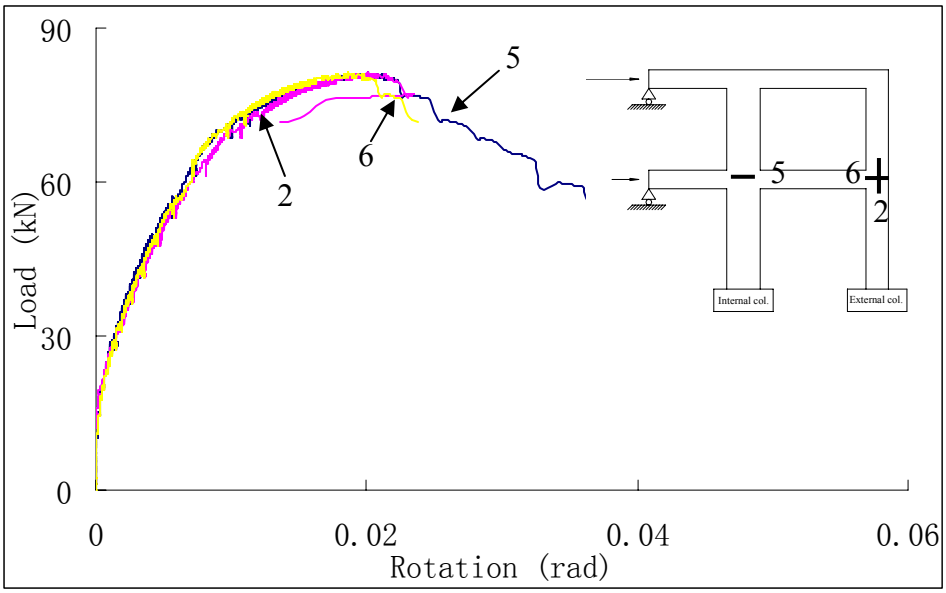

(a)

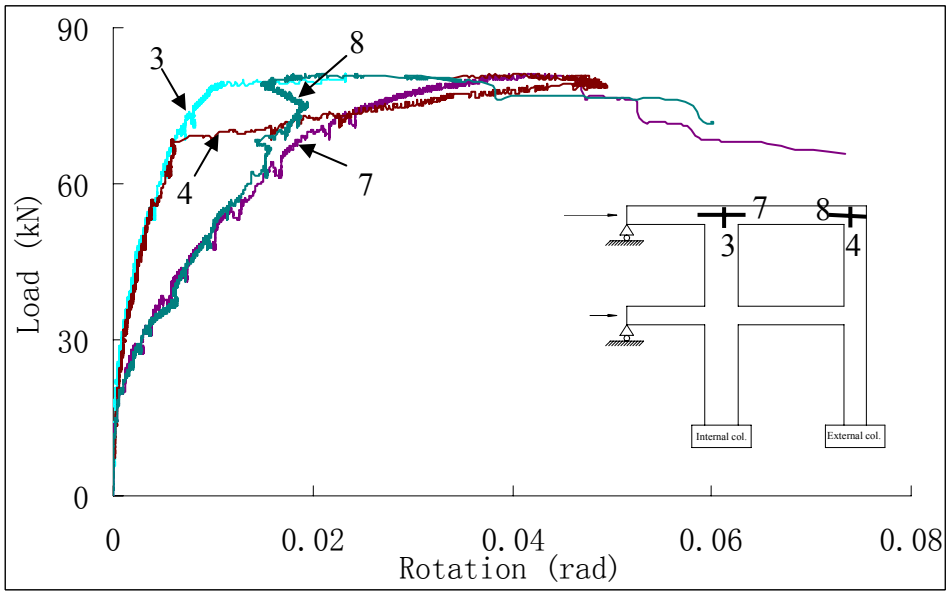

(b)

Figure 2.25 Joint rotation histories in pushover test (a) 1st story joints (b) 2nd story joints

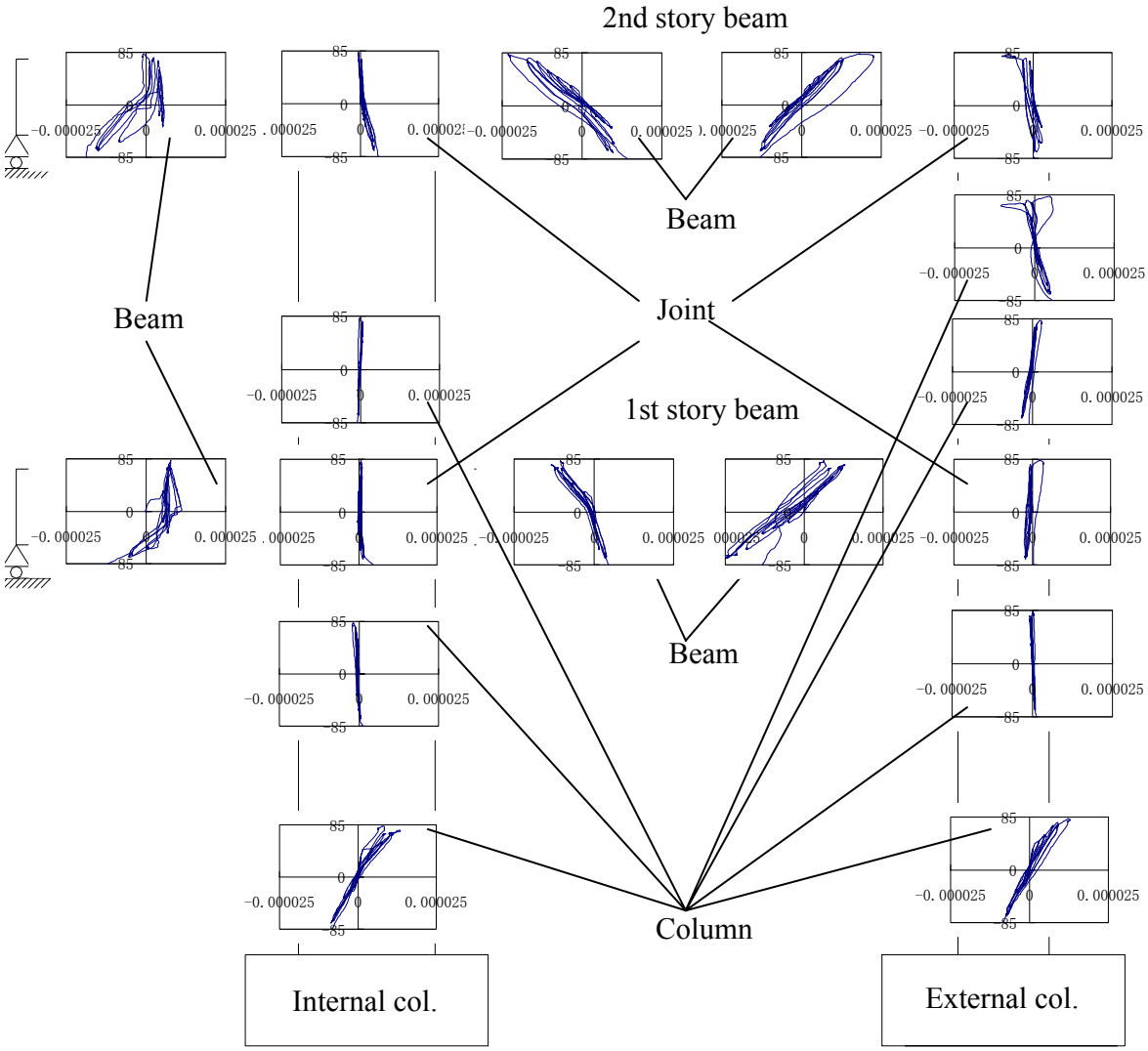

Figure 2.26 Base shear force (kN) vs. curvature (rad/mm) curves at different locations

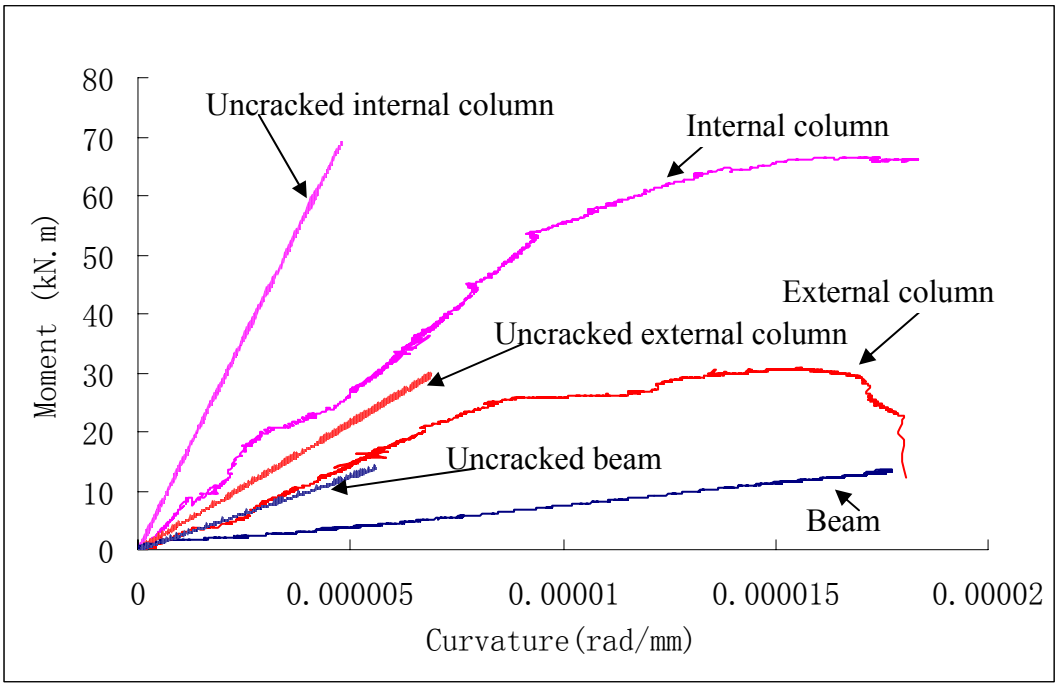

Figure 2.27 Moment-curvature curves of sections in the pushover test

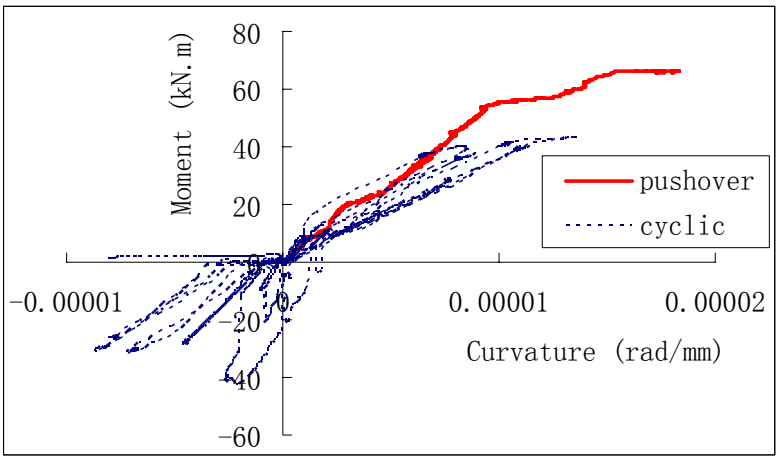

(a)

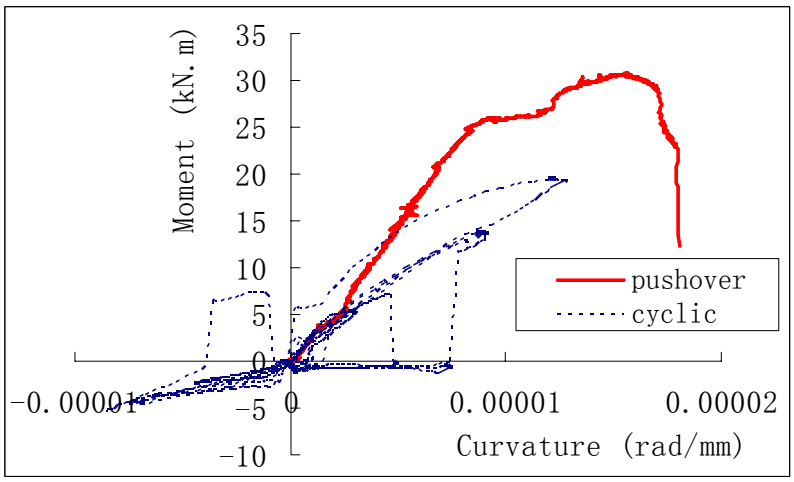

(b)

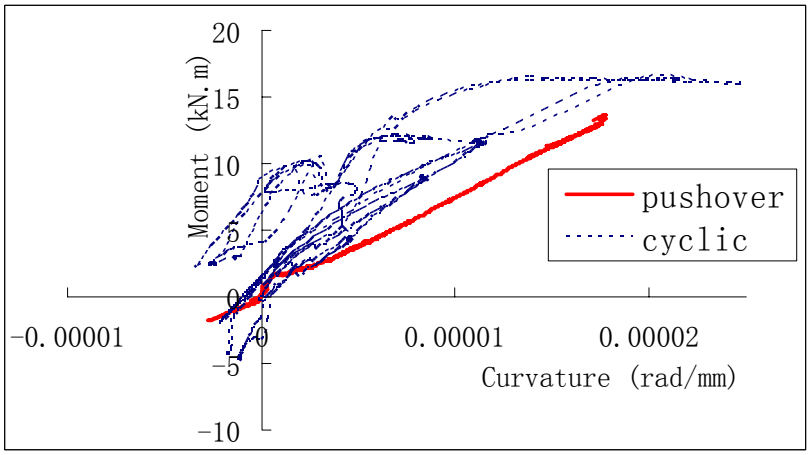

(c)

Figure 2.28 Comparison of moment-curvature curves between pushover and cyclic test: (a) internal column (b) external column (c) beam

CHAPTER 3 DEVELOPMENT OF THE FEA MODEL FOR FRAMES

3.1. Introduction

With the initial stiffness reduction factors, unloading stiffness degradation parameter α and reloading stiffness degradation parameter β for the Modified Takeda Hysteresis model determined in Chapter 2, and the bilinear factor *r* calculated according to Appendix A.5, a 2D nonlinear macroscopic finite element analysis (FEA) model using RUAUMOKO is developed, for the adaptive pushover and cyclic analysis. The established FEA model is validated using the test results. In this chapter, the software RUAUMOKO will be introduced first. Then the details of FEA modeling and comparison of results between FEA and test will be described.

3.2. FEA model using RUAUMOKO

3.2.1. Overview of RUAUMOKO

The program RUAUMOKO, which was developed by Carr (2002a,2002b) at the University of Canterbury in New Zealand, is designed to produce a piece-wise time-history response of nonlinear 2D and 3D frame structures to ground excitations. It can also be used for pushover analysis. The majority of this program is written in Fortran 77 with some features from Fortran 90 and Fortran 95. The program provides

several different options to model mass, damping and stiffness matrices and a wide variety of members such as frame-type member, quadrilateral finite element member and special members like spring, contact, impact and foundation members. There are large numbers of different hysteresis rules available to represent the force-displacement relationship in members.

The input of the program can be conducted in the form of onscreen prompts or using a text input file. Often the text input file is recommended, because it is easier to be revised and reused. The input parameters include control parameters (title, earthquake transformation, structural parameters, output and plotting parameters, iteration parameters), nodes, elements, member properties, weights, loads, shape and earthquake excitation. In the definition of sectional member properties for the RC frame member, initial effective moment of inertia (I) and Young's modulus of concrete (E) are the input parameters. Thus, the initial stiffness reduction effect can be account for by reducing the input moment of inertia (I) by a factor, while keeping the Young's modulus of concrete (E) unchanged. The parameters for hysteresis rules are also the options for defining member property.

The program output can be generated in the form of onscreen graphics or exported to the text output file. The output file contains the data of mode shapes and natural frequencies, time-history results, and envelope of the forces at nodes and in members. Another post processor program DYNAPLOT in the same RUMUAUMO package can be used to extract values from the output database file and Excel program can be used to analyze these values.

3.2.2. FEA modeling

3.2.2.1. FEA meshing

The nonlinear macroscopic 2D FEA model using RUAUMOKO 2D (Carr 2002a) was developed to model the test specimens under pushover and cyclic loading. Figure 3.1 shows the elements and nodes of the FEA model. Two 2D frame-type elements (as shown in Figure 3.2) were used for modeling: the concrete beam-column member and the one component beam member. The inelastic flexural behavior of these two frame-type elements follows the concept of the Giberson one component model (Carr 2002a) as shown in Figure 3.3. In the Giberson one component model, plastic hinges are possible to form at one or both ends of the member, and all nonlinear deformations of the member are lumped in the two rotational springs at the ends.

The concrete beam-column member differs from the one component beam member in that the axial force affects the current yield moments. In the modeling, interaction of axial loads and moment in columns should be accounted for, while such interaction can be neglected in beams. Therefore, columns were simulated using concrete beam-column frame member (Elements 1-4), and beams were simulated using one component beam member (Elements 5-8).

According to the details of frame members, five different sectional properties were defined. The number of sectional properties is also shown with the corresponding elements in Figure 3.1. In the next section, parameters of sectional properties will be described in detail.

3.2.2.2. Sectional properties

The definition of a cross section includes elastic section properties (elastic Young modulus, shear modulus, cross-sectional area, effective moment of inertia, and weight of the member), initial force (prestressed force or self-weight), section strength properties, yield surfaces and hysteresis rules. The details of the input values are as follows.

Elastic sectional properties

Elastic (Young's) modulus of the concrete is obtained from the concrete cylinder test (E=19.07 GPa for specimen S1 and E=20.38 GPa for specimen S2). Shear modulus, the cross-sectional area and the effective shear area were calculated using the formula as given in Appendix A.1. The effective moment of inertia I was calculated by multiplying the moment of inertia of the gross section with the reduction factor obtained from the test (0.492 for internal column, 0.708 for external column and 0.354 for beams). The input values of the elastic sectional properties of S1 and S2 are listed in Tables 3.1 and 3.2.

Hinge properties

Aycardi et. al (1994) tested four column specimens and two 1/3 scale beam-column subassemblages. It was found in their study that plastic hinge lengths were 0.74h to 1.35h for columns with large axial loads, and 0.47h to 0.6h for columns with low axial load, where h is the member dimension in the direction of bending.

Therefore, for the lengths of plastic hinges, 1.0h for columns and 0.5h for beams were used, because the axial load in beams is quite small.

Material strength and yield surface of members

The concrete compressive strength (25.3 MPa for specimen S1 and 25.8 MPa for specimen S2) and reinforcing bar strength (473 MPa for beam longitudinal bars, 525 MPa for column longitudinal bars and 250 MPa for transverse bars) were obtained from the test. The contribution of reinforcing bars was through the calculation of yield moment of the RC sections based on ACI code (ACI318 2002). When yield moment of columns was calculated, the interaction between axial load and moment was considered. Appendix A.2 shows how the seven parameters: *PYC*, *PB*, *MB*, *M1B*, *M2B*, *M0* and *PYT* are calculated, to define the interaction yield surface. The values of these parameters for input are listed in Table 3.3. For beams, interaction between axial load and moment is neglected, so that only the yield moment of the beam section is needed for input. Based on the method shown in Appendix A.3, the input yield moment of section 5 was calculated as 14.13kN.m.

Hysteresis rule

The stiffness degradation was considered by defining hysteresis rules. The Modified Takeda Hysteresis as shown in Figure 1.3 was used herein, and the parameters to define this hysteresis rule are unloading stiffness degradation parameter

$\alpha = \frac{(\frac{k_0}{k_u} - 1)(d_m - d_j)}{d_j}$, reloading stiffness degradation parameter $\beta = \frac{d_{p1}}{d_p}$ and bilinear factor $r = \frac{k_1}{k_0}$. The discussion of these parameters is specified in Chapter 1. The values of α and β ($\alpha = 0.4, \beta = 0.1$ for beams and $\alpha = 0.5, \beta = 0.1$ for columns) were obtained from the moment-curvature curves in the cyclic test as specified in Chapter 2.

The value of bi-linear factor r varies from section to section and is calculated according to equation (3.1), by assuming the bilinear moment-curvature relationship.

$$r = \frac{\phi_y (M_u - M_y)}{M_y (\phi_u - \phi_y)} \tag{3.1}$$

Where,

ϕ_y =curvature corresponding to the first yielding

ϕ_u =curvature corresponding to concrete crush

M_y =yield moment

M_u =ultimate moment

The detail for *r* calculation is given in Appendix A.5, and corresponding results for all sections are listed in Tables 3.1 and 3.2.

3.2.2.3. Boundary condition and loads

Boundary conditions of the base of columns (Nodes 1 and 2) were simulated as fixed ends, and the left ends of beams (Nodes 3 and 6) were treated as pin supports. Nodes on each floor were slaved for x translation (The 1st floor nodes were slaved to

master Node 4 and the 2nd floor nodes to master Node 7) to simulate the rigid diaphragm effect of slabs.

3.2.2.4. Vertical and lateral loads

Vertical prestressing loads on the top of the columns were considered as the initial prestress concentrated load in column members when sectional properties were defined. The initial forces are -59.71 kN in sections 1 and 3, and -38.59 kN in sections 2 and 4. There are two ways to deal with the distributed gravity load in beams: one way is to calculate the moment and shear force at the beam ends due to the distributed load, and then input them as the initial force, when beam sectional property is defined, another way is to input the node loads due to this distributed load in LOAD option. Here the second method was adopted and the vertical gravity loads were input as the nodal loads in LOAD option.

Mass is considered by the input of weight in the WEIGHT option. It is noted that mass and load have to be applied separately on the structure, because mass is used to calculate inertia load while gravity load is used for the static analysis. This means that the input of mass is independent of the input of load, even if such gravity load is due to the mass. The 1st story mass was applied as a concentrated mass at the master Node 4, and the 2nd story mass was applied at Node 7.

Lateral loads were applied at Nodes 4 and 7. And the ratio of the load at Node 4 and 7 was calculated based on inverted triangular load distribution from the column base to the height of the 2nd floor. The input of this ratio was incorporated in the

SHAPE option. For pushover test, adaptive pushover analysis was performed and the lateral loads were increased step by step, until the displacement at node 7 reached the measured 2nd floor displacement corresponding to the maximum load in the test. The scale of the lateral load is one of the control parameters and the default value is 1, which can be adjusted to a value larger than 1 if the lateral load is too small. For cyclic test, adaptive cyclic analysis was performed, and the lateral loads were applied by displacement-control. The displacement history is input in EQUAKE option.

In order to consider the P-Δ effect induced by the gravity load and the lateral load, large displacement option or P-Δ option can be used. With the large displacement option, the nodal coordinates and stiffness of the members due to the changes of member forces and geometry are updated at every time step. However, with the P-Δ option, the stiffness of the members is adjusted only after the static analysis rather than each time step. Therefore, large displacement option instead of P-Δ option was selected in the analysis.

3.3. Comparison of FEA and experimental results

3.3.1. Natural periods

Free vibration test was conducted for specimen S1, and the natural periods were obtained through the Fourier transform and logarithmic decrement method. The measured 1st, 2nd and 3rd modal natural periods obtained from the test for specimen S1 are 0.204s, 0.057s and 0.028s. The modal analysis was carried out before the main

analysis was conducted, to obtain the natural frequencies and the mode shape. The predicted 1st, 2nd and 3rd modal natural periods for specimen S1 obtained from the modal analysis are 0.212s, 0.05s and 0.026s, which are quite close to test values (errors within 5%). Thus, the proposed FEA model can represent the dynamic property of the test specimen quite well.

3.3.2. Load-displacement curves

Figure 3.4 (a) compares of load-2nd floor displacement curves between test and FEA analysis for the specimen (S1) under pushover loading. It can be seen from Figure 3.4 (a), the curve predicted by the FEA model matches the test result reasonably well.

Figure 3.4 (b) shows the comparison for the specimen (S2) under cyclic loading, and Figure 3.5 shows the cycle by cycle comparison between test and FEA results. In the FEA model, the input for the displacement of the master Node 7 (2nd floor) is taken as the 2nd floor displacement measured in the test. The displacement of the master Node 4(1st floor) is taken 0.506 of the value at Node 7, based on the inverted triangular distribution of displacement. As can be seen from Figures 3.4(b) and 3.5, except for some difference of the first 3 cycles, the FEA results agree with the cyclic test results well, which confirms that the proposed FEA cyclic model is reliable for predicting the hysteresis performance under cyclic loading. The reason for the discrepancy in the first three cycles is that a bilinear moment-curvature relationship was assumed in the FEA

and the hysteresis rule did not account for the stiffness degradation before yielding. The FEA therefore predicted an almost linear relation in the first three cycles.

3.3.3. Failure mode

Because the failure of the cyclic test was influenced by the unexpected local failure, data from cyclic test are not enough for comparison. Since the conclusion that pushover test could be a simplified representation of cyclic test were drawn from the test results, here only pushover test results are used to validate the FEA model for failure mode and ultimate capacity prediction.

Figure 3.6 shows the FEA envelope results of maximum moment and maximum shear in members. Based on the strain gauge reading on reinforcing bars and concrete surface, moment of sections in the test was calculated as shown in Figure 2.27. Table 3.5 shows the comparison of maximum moment between pushover analysis and test. It is seen from Table 3.5 that the FEA model can predict the maximum moment in members in a reasonable range (errors within 15%).

The moment capacity M was calculated according to sectional analysis, and the shear capacity was calculated based on ACI code (ACI318 2002), of which the procedures are given in Appendix A.4 and Appendix C. The results of moment and shear capacities are listed in Table 3.6. The maximum moment and shear in members predicted by FEA (as shown in Figure 3.6) are also listed in Table 3.6 for comparison.

As can be seen from Table 3.6, the maximum shear values in members are less than the shear capacity, which means no local shear failure should occur. The

maximum moment values at the bottom of the 1st story internal column, bottom of the 1st story external column and all beam ends are larger than the corresponding moment capacity, so that local flexural failure should occur at these locations. Thus, the failure of the specimen S1 should be due to local flexural failure occurred at the bottom of columns and beam ends, rather than shear failure. That is, the specimen under pushover loading is weak in flexure-but strong against shear failure mechanism. This conclusion agrees with the observed failure mode in the pushover test. Thus, it can be safely concluded that the proposed FEA model can predict the failure mode and failure mechanism of experimental model.

3.3.4. FEA model for the full scale structure

The above mentioned FEA model was proposed for the test specimen. Through the comparison between the FEA results and test results, it is shown that the proposed FEA model can predict the dynamic properties, load-displacement relationship, hysteresis performance and failure mode of the test specimens well. With the proper initial stiffness reduction factors and hysteresis rule parameters, the proposed FEA model can be used to analyze the full scale structures.

As for the initial stiffness reduction factor, only one factor for columns and one for beams should be suggested for easier implementation. Therefore, trial and error FEA analysis for the specimen S1 was performed, and a factor 0.58 for columns and 0.35 for beams is suggested (as shown in Figure 3.7).

For parameters of the hysteresis rule, relationship of the parameters between scaled down model and full scale model should be built up. According to similitude law, for full scale structure (assume a scale factor *S*, for example, *S*=1/2 means half scale), curvature $d^* = \frac{d}{S}$ and moment $F^* = S^3 F$, then the stiffness $k^* = \frac{F^*}{d^*} = S^4 \times \frac{F}{d} = S^4 k$.

Thus, parameters for full scale structure are :

$$\alpha^* = \frac{(\frac{k_0}{k_u}^* - 1)(d_m^* - d_j^*)}{d_j^*} = \frac{(\frac{S^4 k_0}{S^4 k_u} - 1)(\frac{d_m}{S} - \frac{d_j}{S})}{\frac{d_j}{S}} = \frac{(\frac{k_0}{k_u} - 1)(d_m - d_j)}{d_j} = \alpha \tag{3.2}$$

$$\beta^* = \frac{d_{p1}^*}{d_p^*} = \frac{\frac{d_{p1}}{S}}{\frac{d_p}{S}} = \frac{d_{p1}}{d_p} = \beta \tag{3.3}$$

Therefore, parameters α and β obtained from the scaled experimental model can also be used to analyze the full scale structures. Based on the procedure as given in Appendix A.5, the bilinear factor *r* depends on the reinforcement details and axial load of a section, and has no relation with the scale effects. Since the predicted FEA results using the *r* values calculated by this procedure can match with the test results, it can be say that this procedure is validated and can be used for the full scale model.

3.4. Summary

A 2D nonlinear macroscopic FEA model using RUAUMOKO was developed for frames under pushover and cyclic loading. This FEA model was validated using the test results, to obtain a reliable FEA model for analysis of the full scale frame

structures. It is shown that this model can predict dynamic properties, load-displacement relationship, hysteresis performance and failure mode of the test specimens, with reasonable accuracy.

The initial stiffness reduction factors, 0.58 for columns and 0.35 for beams, are suggested for GLD frame structures. The unloading stiffness degradation parameter α and reloading stiffness degradation parameter β for the Modified Takeda Hysteresis model are suggested as: $\alpha = 0.4, \beta = 0.1$ for beams and $\alpha = 0.5, \beta = 0.1$ for columns. The procedure for bilinear factor *r* calculation was validated using the frame test results. All these factors and parameters will be used in Chapter 6 to develop FEA models for full scale structures.

Table 3.1 Values of elastic section properties and bilinear factors (Specimen S1)

Section	E(kN/m^2)	G(kN/m^2)	A(m^2)	As(m^2)	I(m^4)	r
Section 1	1.91E+07	7.95E+06	0.045	0.038	3.74E-04	0.041
Section 2	1.91E+07	7.95E+06	0.030	0.025	1.59E-04	0.068
Section 3	1.91E+07	7.95E+06	0.045	0.038	3.74E-04	0.053
Section 4	1.91E+07	7.95E+06	0.030	0.025	1.59E-04	0.109
Section 5	1.91E+07	7.95E+06	0.025	0.021	4.61E-05	0.016

Table 3.2 Values of elastic section properties and bilinear factors (Specimen S2)

Section	E(kN/m^2)	G(kN/m^2)	A(m^2)	As(m^2)	I(m^4)	r
Section 1	2.04E+07	8.49E+06	0.045	0.038	3.74E-04	0.037
Section 2	2.04E+07	8.49E+06	0.030	0.025	1.59E-04	0.089
Section 3	2.04E+07	8.49E+06	0.045	0.038	3.74E-04	0.041
Section 4	2.04E+07	8.49E+06	0.030	0.025	1.59E-04	0.073
Section 5	2.04E+07	8.49E+06	0.025	0.021	4.61E-05	0.015

Table 3.3 Values to define the yield surface (Specimen S1)

Section	*PYC*	*PB*	*MB*	*M1B*	*M2B*	*M0*	*PYT*
1	-978.27	-703.24	41.55	59.89	53.12	19.86	211.01
2	-669.19	-470.39	19.96	27.95	27.92	14.31	158.26
3	-930.44	-682.36	38.51	56.48	48.01	15.28	161.55
4	-633.31	-452.68	18.55	25.99	24.82	11.04	121.16

Note: the unit for PYC, PB and PYT is kN, and for MB, M1B, M2B and M0 is kN.m. Compressive force is negative while tensile force is positive

Table 3.4 Values to define the yield surface (Specimen S2)

Section	*PYC*	*PB*	*MB*	*M1B*	*M2B*	*M0*	*PYT*
1	-993.44	-727.82	43.09	63.80	56.14	21.97	211.01
2	-679.29	-489.11	20.54	29.58	26.78	15.58	158.26
3	-945.63	-704.03	39.81	59.30	51.97	17.06	161.55
4	-643.44	-468.85	19.05	27.36	25.54	12.18	121.16

Table 3.5 Comparison of maximum moment between the pushover analysis and test

Member	Pushover analysis(kN.m)	Test(kN.m)	Error
Internal column	56.55	66.55	15.0%
External column	37.8	33.04	13.3%
Beams	15.46	13.65	13.2%

Table 3.6 Moment and shear capacities compared with the predicted maximum moment and shear of specimen S1

Member	Moment capacity (kN.m)	Max moment (kN.m)	Shear capacity (kN)	Max shear (kN)
Internal column (1st story)	48.12	56.55*	60.82	47.99
Internal column (2nd story)	32.90	30.25	58.86	37.72
External column (1st story)	28.54	37.80*	39.03	32.59
External column(2nd story)	21.14	15.27	37.78	16.80
Beam (1st story)	14.56	15.27*	28.70	17.15
Beam (2nd story)	14.56	15.27*	27.80	16.96

Note: * means the max value exceeds the capacity value

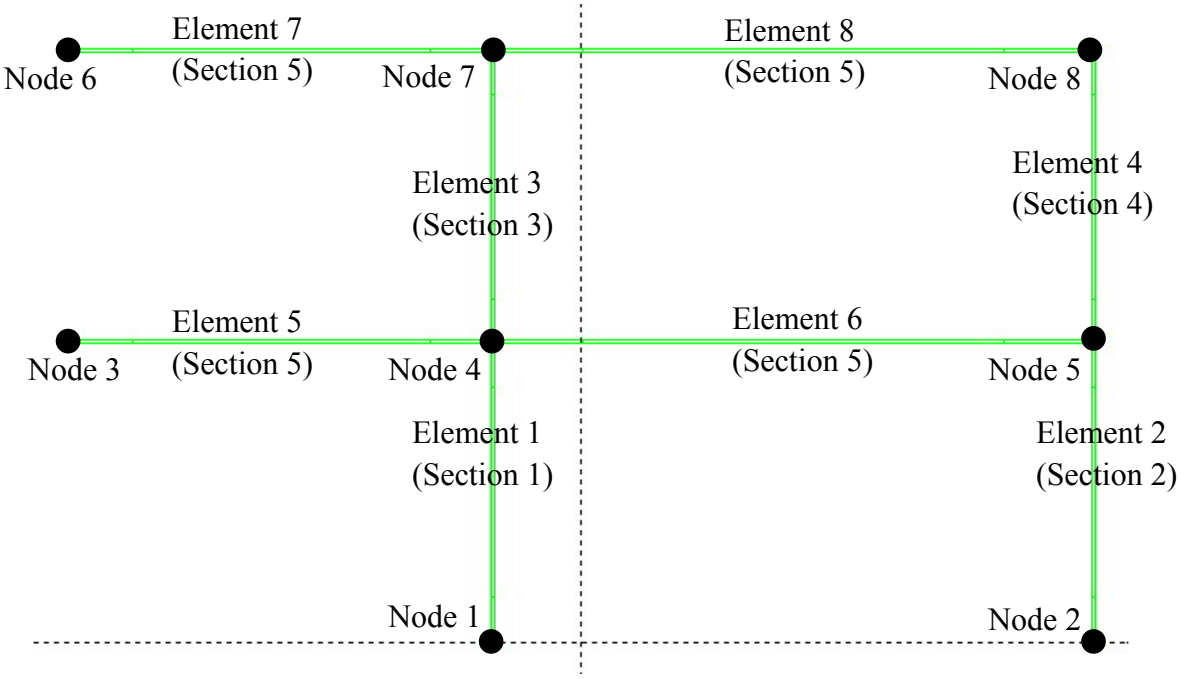

Figure 3.1 Nodes, elements and sectional properties of the FEA model

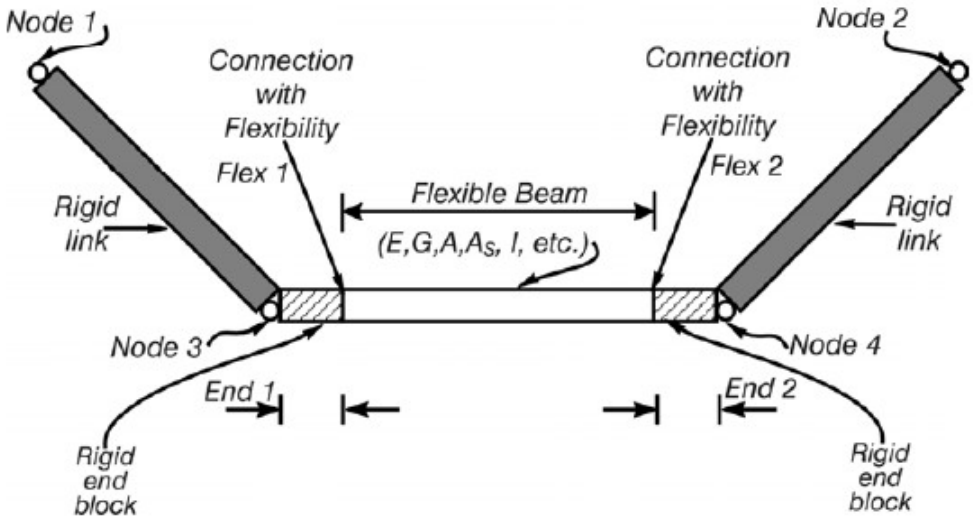

Figure 3.2 2D Frame-type element (Carr 2002a)

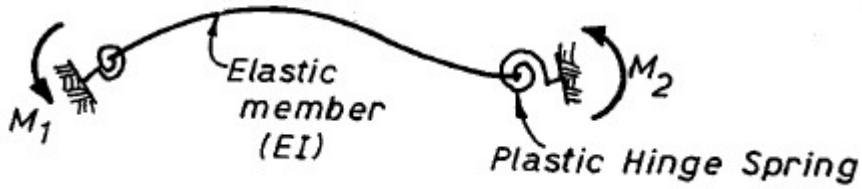

Figure 3.3 Giberson one-component beam model (Carr 2002a)

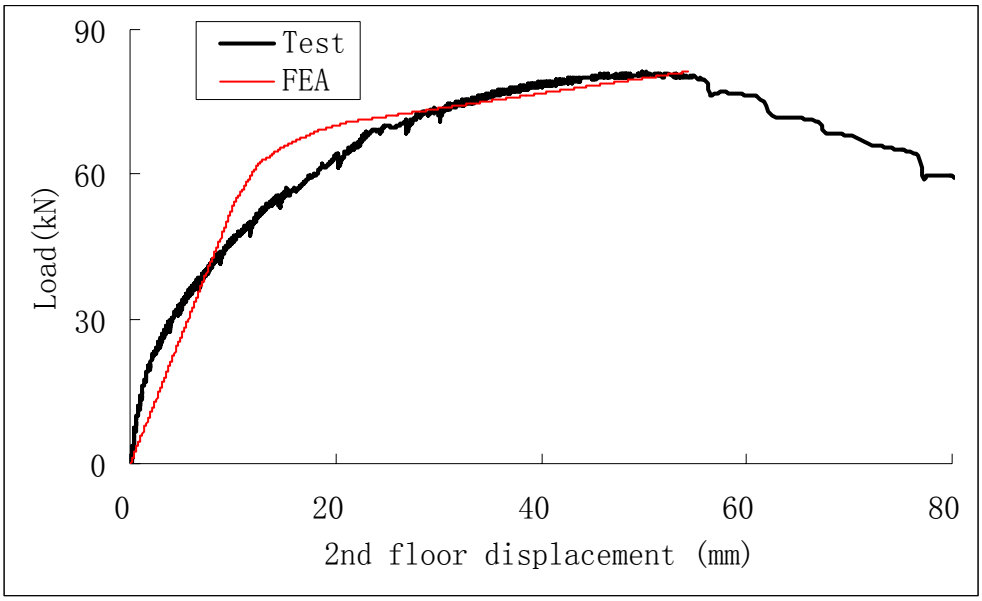

(a)

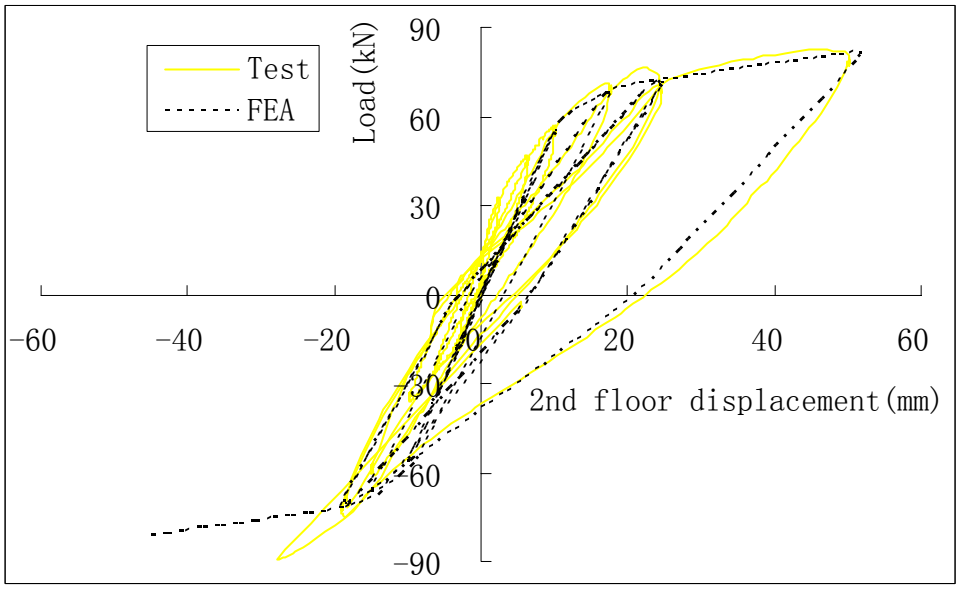

(b)

Figure 3.4 Comparison between test results and FEA results: (a) specimen S1 under pushover loading; (b) specimen S2 under cyclic loading.

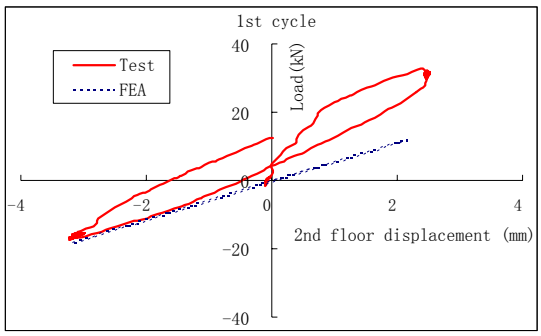

(a) 1st cycle

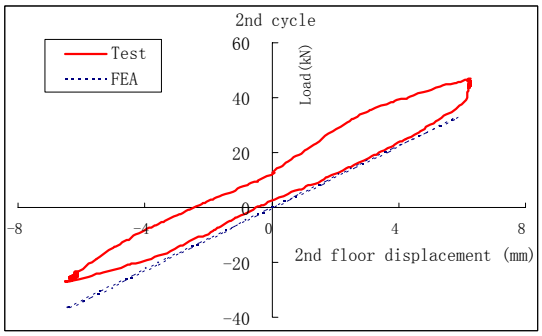

(b) 2nd cycle

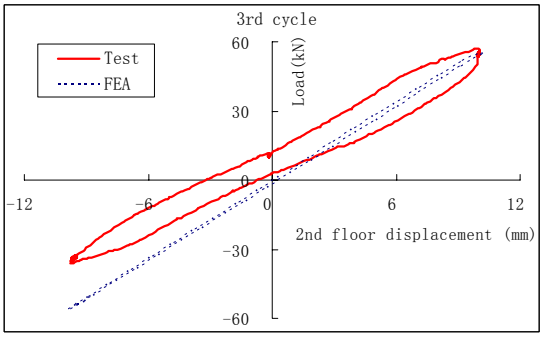

(c) 3rd cycle

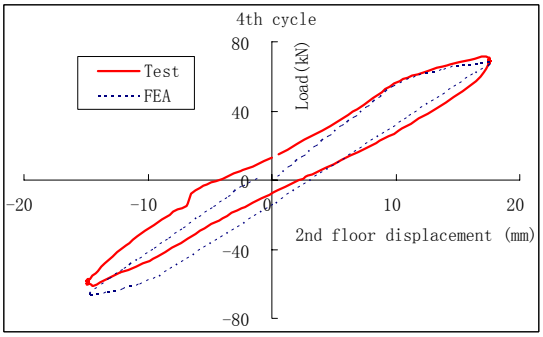

(d) 4th cycle

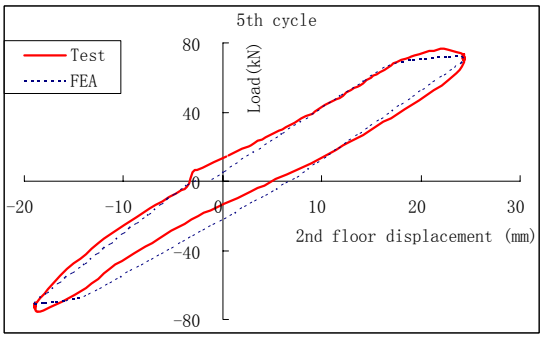

(e) 5th cycle

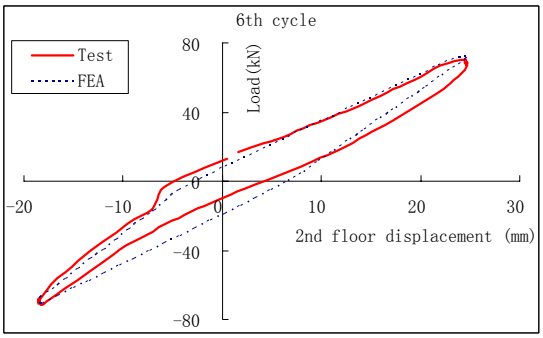

(f) 6th cycle

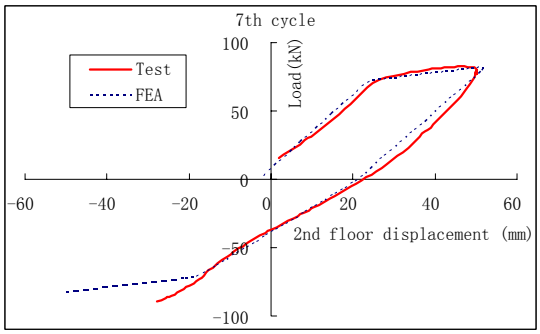

(g) 7th cycle

Figure 3.5 Cycle by cycle comparison between test and FEA.

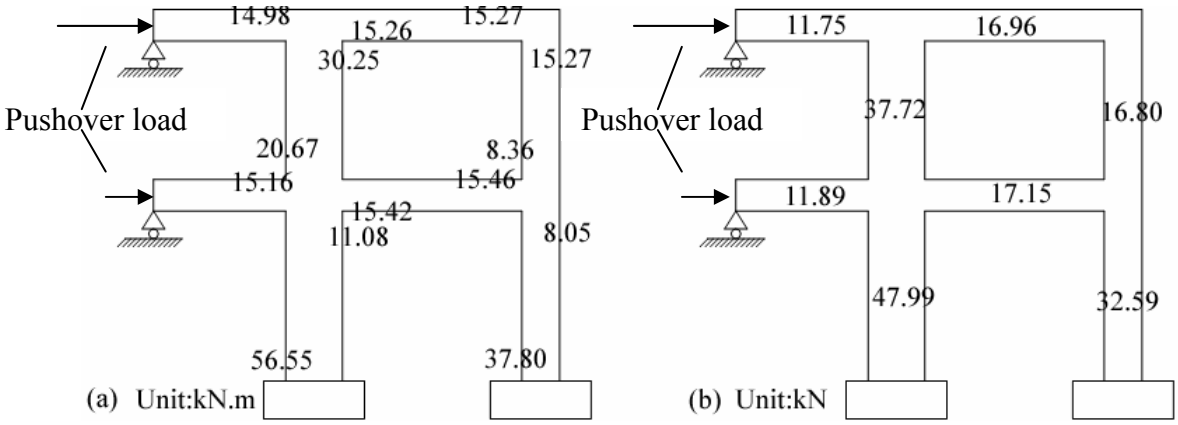

Figure 3.6 Maximum moment and shear in members in the pushover analysis using RUAUMOKO: (a) moment envelope; (b) shear envelope.

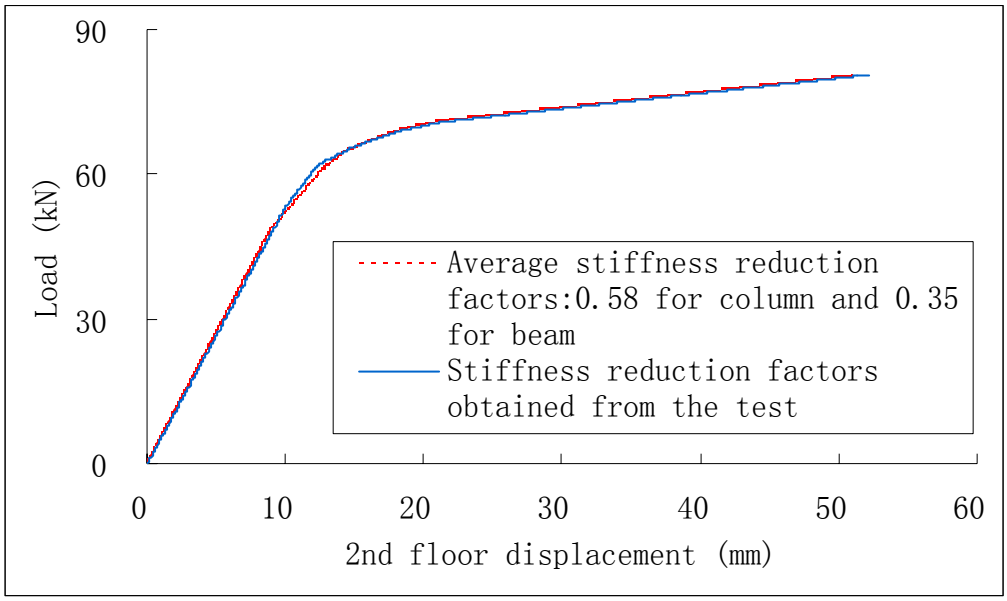

Figure 3.7 Comparison of FEA results with individual stiffness reduction factors and with average stiffness reduction factors.

CHAPTER 4 EXPERIMENTAL STUDY OF A 25-story SHEAR WALL STRUCTURE

4.1. Introduction

The experimental study of a shear wall structure under pushover loading has been carried out by Kong (2003). In this chapter, the experimental study of the same model under cyclic loading is described. The experimental model is a 1/5 scaled model, representing the lower critical regions of the shear wall of a 25-story RC shear wall-frame building. This 25-story building was designed according to BS8110(1985) without seismic provision and built in late 1970s in Singapore. The test under pushover loading (Kong et al. 2003b) revealed that the shear wall failed at the base due to shear. Since a brittle shear failure mode is undesirable for structures under seismic loading, experimental investigation of glass fiber reinforced polymer (GFRP) retrofitted shear wall model was carried out. Totally two specimens, one control and one FRP-wrapped, were tested in the laboratory.

The objectives of the tests are as follows:

1. To investigate the seismic behaviors of the shear wall structure under cyclic loading. And see whether the experimental results of pushover tests would envelop the cyclic tests, for shear wall specimens detailed according to BS8110(1985).
2. To what extent the FRP-wrapping would enhance the performance.

3. To obtain initial stiffness reduction factors and parameters describing the hysteresis behaviors for shear walls, for developing FEA models

4.2. Experimental model

A 25-story point block designed and constructed according to BS 8110 was considered as the prototype for cyclic loading test. The plan view of the prototype is shown in Figure 4.1. The lower 2.6 stories of the prototype were chosen for the test. The plan view of the prototype wall is shown in Figure 4.2. As can be seen from Figure 4.2, with respect to loading direction Z, the I-shaped wall was made of symmetrical left and right flanges. Because the testing specimen is only the lower 2.6 stories of a 25-story I-shaped shear wall, a constant axial load, representing the weight of the above stories, was applied on the top of the specimen through prestressing.

Two scaled models (as shown in Figure 4.3), one control (specimen S1) and another retrofitted using FRP system (specimen S2), were fabricated and tested under lateral cyclic loading. The model wall was 1036 mm high (2-story height, each story level 508 mm). The height of the test specimen including the upper loading beams was 1314 mm (2.6 stories). Figure 4.4 shows the plan view and geometry of the test model. The length of the flange wall was 657 mm, and that of the web wall was 955 mm. Thickness of the wall was 45 mm throughout.

4.2.1. Scale factor

A scale factor of 5.0 was used to build the test model. The following ratios between prototype and test model were maintained when the prototype shear wall was scaled down:

1. Wall dimension: the wall length to thickness ratio and height to depth ratio should be maintained;
2. Shear span to depth ratio ($H / L = H \times V / LV = M / VL$) was maintained at 2.

Where,

M =prototype moment at the flange base

V =prototype base shear force at the flange

L =length of the flange wall in prototype

H =height of the flange wall in prototype

The objective to maintain shear span to depth ratio is to make sure the ultimate shear capacity is the same between the scaled model and the prototype wall, based on an empirical formula (4.1) proposed by Hirosawa (1975) .

$$v_{ult} = 0.0679\rho_t^{0.23}(f_c'+1.76)/(M/VL+0.12)^{0.5} + 0.845(f_{wh}\rho_{wh})^{0.5} + 0.1\sigma_0 \quad (4.1)$$

Where,

v_{ult} =ultimate shear resisting capacity (MPa)

ρ_t =effective tensile reinforcement ratio, $\rho_t = 100A_{st}/t(L-a_1/2)$

A_{st} =area of longitudinal reinforcement in tension-side boundary column

t =average thickness of wall section

L =length of the wall

a_1 =length of the boundary column or wall edge region which is normally taken as 10% of wall length

M = moment at the base

V = base shear force

M/VL =shear span to depth ratio

ρ_{wh} =effective horizontal wall reinforcement ratio, $\rho_{wh} = A_{ws}/tS_h$

f_{wh} =yield stress of the horizontal wall reinforcement (MPa)

f_c' = Concrete compressive cylinder strength

A_{ws} =area of one layer of horizontal reinforcement

S_h =spacing of horizontal wall reinforcement

σ_0 =average axial stress over entire wall cross section

Reinforcement ratios in the scale model are the same as those in the prototype (as shown in Table 4.1). According to equation (4.1), if there is no change in the reinforcement ratios, the factor that influences the ultimate shear capacity is M/VL (equal to shear span to depth ratio). Thus, shear span to depth ratio is maintained here to make sure the ultimate shear capacity between the scaled model and the prototype the same.

From the FEA analysis of the full scale 25-story shear wall (Kong 2004), a ratio of 2 is sound to be reasonable to reflect the behavior of the full scale wall. Therefore, a height of 1314 mm (2.6 stories) was calculated for the scaled model by maintaining height to depth ratio at 2.

3. Axial load ratio $N/(f_{cu}A_g)$ is maintained.

Where,

N =axial load from the above stories

A_g =gross cross section area of the wall base

f_{cu} =concrete compressive strength.

According to Lefas et. al (1990), a representative axial load ratio for high-rise buildings is 0.2. The ratio calculated according to BS8110(1985) of the prototype 25-story shear wall is 0.24 for $f_{cu} = 30$ MPa, which is quite near to the suggested value by Lefas et al. Therefore, an axial load ratio of 0.24 is chosen to represent the axial load ratio of high-rise buildings ($f_{cu} = 30$ MPa) in low seismic regions. By maintaining axial load ratio, axial stress in the scaled model is kept the same with the prototype wall.

4.2.2. Material scaling simulation

For the individual steel reinforcement, the diameter and its spacing similitude conditions were not maintained due to the limitation of available steel reinforcement in the laboratory. However, in the scaled model, the spacing and diameter of the steel reinforcement were properly chosen, to maintain the same reinforcement ratios and fulfill the material similitude of yield forces.

Walls in Singapore do not have boundary columns. However, according to Meyer (1984), if the walls have no boundary columns, 10% of wall length on each end can be defined as the boundary or edge regions. In order to simulate the boundary regions in the scaled model, the diameter of 10 mm, for the two vertical reinforcement

bars of both ends of flanges, was chosen. This diameter was larger than the rest reinforcement bars of 8 mm in the flange walls.

The material characteristics of concrete are the same as that of the prototype, as shown in Table 4.1. Because the thickness of the wall is quite small, the same concrete cover as that in prototype was selected in the experimental model, in order to avoid serious concrete spalling and cracking during the construction. Although two layers of steel reinforcement and the transverse steel reinforcement were used in the prototype, only one layer of steel reinforcement was used in the model, to satisfy the requirement for thickness of the concrete cover. Transverse reinforcement was not used and the confinement effect was ignored in the scaled model, because there is very little confinement effects in the prototype wall due to its large aspect ratio (Subedi et al. 1999). Therefore, the minimum cover chosen was 13 mm, which was larger than the aggregate size of 10 mm to prevent softening of regions near the concrete surface.

For shear strengthening by GFRP, the minimum thickness of FRP composite laminate needs to be determined in order to sustain the required shear force. According to the finite element analysis on the 25-story point block (Kong 2004), the base shear/building gravity load has to be 7% to prevent initiation of shear failure at the wall base. Because the gravity load of the building was 36266kN (unfactored dead load), the total base shear=7%×36266=2539kN. If the shear core wall is assumed to sustain all the shear force, the other part of the structure will not fail first. The seismic force in Z direction is sustained by both of the flanges of the I-shape shear wall, so each flange needs to take up to 2539/2=1269kN and the shear stress in the prototype

flange wall would be 1.66 MPa. Thus, shear force for each flange wall of the model would be 1.66 MPa × 45 mm × 657 mm=48.96 kN.

According to Seible et. al (1994), the shear capacity of FRP is:

$$V_f = 0.004 E_f t_f d \tag{4.2}$$

Where,

V_f =shear capacity due to FRP composite laminates

$0.004E_f$ =the allowable stress level in FRP based on allowable strain of 0.004 above which aggregate interlock is lost

t_f =thickness of FRP composite laminates

d=0.8 times the actual wall length.

Table 4.2 lists the properties of the GFRP fiber used to retrofit the shear wall. Assuming that the FRP composite laminates take up the entire force 48.96kN, the thickness of FRP can be calculated using equation (4.2). From this equation and noting that the FRP composite laminates are on both sides of the flange, the minimum required thickness for shear strengthening of wall would be 0.164 mm. Since the minimum thickness of GFRP available was 0.353 mm, one layer of GFRP laminate was used to meet the requirement.

4.2.3. Material properties

Overall 3D view of reinforcing bars in the wall specimen is shown in Figure 4.5. Details of the reinforcing bars in the wall and block are shown in Figure 4.6 and 4.7. Three types of steel reinforcement were used in the tests: (1) 10 mm high yield

deformed bars, used in the base blocks, and as the vertical edge reinforcing bars in the flange wall; (2) 8 mm high yield smooth BRC (smooth welded steel mesh bars produced by BRC Ltd, UK Reinforcing steel bars stock holders & distributors) bars, used as the vertical reinforcing bars in the center portion of the flange wall ;(3) 6 mm smooth mild steel bars, used as the vertical reinforcing bars in the web wall, and as the horizontal transverse bars. The stress-strain relationship of these reinforcing bars is shown in Figure 4.8 and the properties of them are listed in Table 4.3.

Concrete was mixed and cast (as shown in Figure 4.9) in the structural laboratory of National University of Singapore and cured for 28 days. The mix property was 1:3.15:3.78:0.85, by weight of cement; fine aggregates (natural sand); aggregates (10 mm max size) and water. For each specimen, a total of twelve test cubes (100 mm x 100 mm x100 mm), six test cylinders (100 mm x 200 mm) and three test prisms (100 mm x 100 mm x 400 mm) were cast. Table 4.4 lists the details of concrete strength. The average concrete cube compressive strength and Young's Modulus were 31.71 MPa and 22.92 GPa for S1, and 27.58 MPa and 20.89 GPa for S2.

A layer of unidirectional GFRP laminate (properties are shown at Table 4.2) was used to wrap specimen S2. Before the concrete wall was wrapped, the corners and edges of the wall had to be rounded first to avoid damage to the FRP sheets. And then, primer was applied as the first coat on the wall before wrapping (as shown in Figure 4.10) and saturant was used as the final coat after wrapping. The properties of the primer and saturant are shown in Table 4.5.

Because stress in the upper half wall is different from that in the lower half wall, two pieces of GFRP sheets were used for each side of the wall (flange or web wall). A total of eight pieces of GFRP sheets were used to cover the whole wall. All the fibers were aligned in the horizontal direction of the wall. For one flange wall, two pieces of GFRP sheets (538 mm in height and 1380 mm in length) were used, one around the top half wall and the other around the bottom half wall. For the web wall, four pieces of GFRP sheets were used (538 mm in height and 955 mm in length), two covering the front and back part of the web wall for the first story, and the other two covering the second story. There was no overlap at the interface between the first and second story.

At the flange wall-web wall joints FRP bolts (made by smaller FRP sheets) were used to anchor FRP sheets and then the FRP bolts were covered by GFRP strips. Locations of FRP bolts are shown in Figure 4.11 and 4.12.

4.3. Test setup and test procedure

4.3.1. Details of the setup

The wall specimens were tested in an upright position. Figures 4.13 and 4.14 show the 3D views of the setup for specimens S1 and S2, respectively. The front, side and plan view of the test set up are shown respectively in Figures 4.15, 4.16 and 4.17. The flange wall base block was rigidly mounted to the two strong beams, which were anchored to the deep floor slab and to the strong wall, through 30 mm diameter high strength (G8.8) bolts. A total of fourteen 24 mm diameter bolts (G8.8) were used to

connect each flange base block to the strong beam, in order to create a fixed base condition. The web wall base block was just resting on the top of another shorter strong beam.

As for lateral load transfer, the load was transferred from the actuator to a Beam P, then to three U beams, and finally to the walls through eight L angles. One end of the actuator was mounted to the strong wall, and the other end was connected by nine bolts (G8.8) to a steel plate, which was fully welded to a Beam P. Twelve bolts (G3.6) were used to connect Beam P to the top of three loading U beams, which were used to apply a vertical prestressing load on the wall (as shown in Figure 4.18). Finally these U beams were connected to L angles (as shown in Figure 4.19), which were connected to flange walls by G3.6 bolts.

For axial load transfer, prestressing was used to simulate the axial force from the upper stories. One seven-wire strand was anchored and treaded through each end of the Beams U (as shown in Figure 4.20). Altogether twelve strands were used to pass through the three U Beams to create a vertical preload. The seven-wire strand has a diameter of 12.9 mm, and nominal cross area of 100 mm^2. The design yield strength of each strand was 130.2 kN and the Young's modulus was 195 GPa. Another end of the strand was anchored to the bottom Beam T, which was bolted to the laboratory floor. At intervals of strand anchorage location, stiffeners were used to prevent local failure of Beam T.

Prestressing was conducted only one day before the final test to minimize the prestress loss of strands. In order to maintain an axial compression ratio of 0.24 on the

specimens, each of the twelve strands on the control specimen (S1) would have to be jacked up to 2631 micro strain corresponding to the strand force of 51.31kN. Similarly, for the FRP wrapped specimen (S2), the strand strain is 2577 micro strain with the corresponding strand force of 50.25kN.

Because there was only one jacket for 12.99 mm strand in the laboratory, each time only one strand could be prestressed to certain strain (the strain could be read from the strain gauges attached on the strands). In order to minimize the influence among strands, a sequence of prestressing of one run was adopted: Ca->Cb->Cd->Cc->Ad->Ac->Bb->Ba->Ab->Aa->Bd->Bc. (the denotation is shown in Figure 4.17). Each run only 400 micro strain was added on one strand to avoid concrete crushing during the prestressing. The sequence of the prestressing was repeated until the target strain was achieved.

In order to prevent out of plane failure, lateral support was installed at 2/3 height of the wall, namely 691 mm above the base block. The lateral support was a pair of C channel with rollers to contact with the wall. The rollers allowed in plane movement of the wall but prevented out of plane movement. 3D view of the lateral support is shown in Figure 4.21.

4.3.2. Instrumentation

Strain gauges were attached to reinforcing bars in the wall and to the outside surface of the wall, to record the change of strain in the specimen during the test. Figures 4.22, 4.23 and 4.24 show respectively the locations of reinforcing bar strain

gauges (TML's FLA-5-11 with gauge length of 5 mm), concrete strain gauges on the surface of the wall (TML's PFL-30-11 with gauge length of 30 mm), and FRP strain gauges on the surface of the wrapping FRP (TML's FLA-30-11 with gauge length of 30 mm). For the strain gauges on the surface of concrete wall or wrapping FRP, two strain gauges were used at one location point: one was attached in vertical direction and another in horizontal direction. Strain gauges were placed at the same locations on both specimens, so that the readings could be compared.

Displacement transducers were used to measure the lateral displacement, and the vertical displacement of some locations to calculate the plane rotation. Three types of displacement transducers were used in the test: range of 25 mm, 50 mm and 100 mm. Aluminum plates and angles were used to provide a smooth surface for the tip of the displacement transducer to rest on. They were attached to the concrete or FRP surface using "Araldite" rapid epoxy adhesive. Locations of the displacement transducers are shown in Figure 4.25. Transducers with labels of DCT, DC, D5R, D5L, D6R, D6L, D7R and D7L were used to measure the lateral displacement of the wall, transducers D1R, D1L, D2R, D2L, D3R, D3L, D4R and D4L were used to measure the vertical displacement of the wall, and transducers D8R, D8L, DBR and DBL were used to measure the movement of the base blocks.

4.3.3. Loading history and test procedure

The wall specimens were subjected to cyclic loading in Z direction. The movement of the actuator (650kN) was by displacement-control. The displacement

loading history was based on a quasi-static procedure for cyclic loading history proposed by Park (1988). And the proposed loading rate was selected based on trial runs. The loading history curve is shown in Figure 4.26. The displacement at yield Δ_y =15 mm was found by pushover trial test. Thus, two cycles of the same displacement amplitude after 15 mm displacement are needed (Park 1988). The rate of loading changed twice: 0.006 mm/s in the first 3 cycles (peak displacement of 3 mm, 6 mm and 9 mm); 0.01 mm/s in the fourth cycle(peak displacement 12 mm), and 0.05 mm/s in the final cycles (peak displacement of 15 mm twice and 30 mm twice). In the testing, at each peak displacement, the displacement would be held constant for two minutes, for checking the cracks in specimen S1 or the FRP debonding in specimen S2. The actuator would be stopped immediately after the failure of specimens.

4.4. Experimental results and interpretation

4.4.1. Global response

4.4.1.1. General behavior of control wall (specimen S1)

The specimen was whitewashed before the test for cracks checking (as shown in Figure 4.27). In the test, the specimen developed the first flexural crack at the tension side of the flange wall, when the actuator displacement (2.6-floor level, with 1.314m above the block) was 3 mm and the corresponding applied load was 76.5kN (1st cycle). At a displacement of 6 mm and load of 102.0kN (2nd cycle), flexural cracks at the tension side of flange wall extended to form inclined shear cracks of less than 1 mm in

width. At first, the fine shear cracks were concentrated at the two corners of the flange wall. Later, with increasing displacement, these shear cracks developed wider and extended to the center region of the flange wall, and new shear cracks began to appear at locations higher and closer to the middle of the wall.

From 3rd to 4th cycle, with the actuator displacement being 9 mm to 12 mm and the corresponding load ranging from 160.5kN to 174.0kN, inclined shear cracks developed dramatically across the flange wall, diagonally from the center of bottom flange wall up to the edges of the 2nd floor level. The first and only yielding occurred at 10 mm diameter deform bar ($\varepsilon_y = 0.0029$ as listed in Table 4.3), when the actuator displacement was 11.2 mm and the corresponding applied force was 163.0kN (4th cycle).

From the 4th to 5th cycle, more cracks appeared, and the existing shear cracks were extended and widened (the crack pattern is shown in Figure 4.28). As a result, the corresponding load started to decrease, from 174.0kN in the 4th cycle to 156.0kN in the 5th cycle. When the displacement reached 15 mm, the concrete of the right flange wall corner spalled (as shown in Figure 4.29).

In the 7th cycle (displacement of 30 mm), the cracks on the bottom center region of the flange wall and those on the top region were connected. This resulted in a dramatic shear failure at a displacement of 20.9 mm, diagonally across the right flange wall from the base to the second floor level (as shown in Figures 4.30, 4.31 and 4.32). At the same time, another large diagonal crack region occurred on the left flange wall

(as shown in Figure 4.33), and the concrete spalled off corner of the left flange wall (as shown in Figure 4.34).

4.4.1.2. General behavior of the FRP wrapped wall (specimen S2)

In the test, by tapping with a coin, the debonding of FRP was checked.

The first yielding of the steel reinforcement occurred at the bottom of the outermost 10 mm deformed bar ($\varepsilon_y = 0.0029$ as listed in Table 4.3), when the actuator displacement was 9.3 mm and the corresponding force was 139.5 kN (4^{th} cycle or 12 mm displacement cycle).

In the first 4 cycles, no debonding of FRP was observed. First FRP debonding appeared at the left flange wall corner (as shown in Figure 4.35) and at the right flange wall corner (as shown in Figure 4.36), when the displacement was 15 mm (5^{th} cycle). The first FRP debonding at the web wall occurred when it was subjected to tensile force at 15 mm displacement (as shown in Figure 4.37).

In the 6^{th} cycle (the second run of 15 mm displacement cycle), the debonding region of the flange wall enlarged (see Figure 4.38). In the 7^{th} cycle (30 mm displacement cycle), when displacement reached 16 mm, the right flange wall corner started to crush when it was under compression (as shown in Figure 4.39). Immediately after this, the corresponding applied force dropped from 204kN to 143.8kN. When displacement continued to increase, crushing of the right flange wall corner became worse and the debonding of FRP of this region enlarged dramatically

(as shown in Figure 4.40). After that, the corner of the left flange wall crushed and FRP debonding region enlarged (as shown in Figure 4.41).

After the first 30 mm peak displacement was passed and the opposite direction displacement of 23.5 mm was reached (7^{th} cycle), the right flange wall concrete corner crushed and the nearby FRP debonded dramatically and followed by FRP rupture (as shown in Figure 4.42). As a result, the applied force dropped quickly, which indicated the failure of the specimen.

4.4.1.3. Load-displacement relationship

The load-displacement relationships of control specimen (S1) at different locations are shown in Figures 4.43 and 4.44. Because there are noises in the reading data due to limitation in the function of the actuator (650kN) for slow loading rate and small displacement increment during the test, trend lines of these data were used for comparison. The hysteresis curves for comparison are therefore not continues at the ends. Figure 4.43 shows the comparison of load-displacement relationships at flange wall, between the actuator level and the 1^{st} floor level. It is observed that the displacement at the actuator level is larger than the 1^{st} floor, but the shape of hysteresis curves is similar. Figure 4.44 shows the comparison of load-displacement relationships at the 1^{st} floor level, between the flange wall and the web wall. The difference between these two curves is insignificant, which indicates that no joint failure occurred at the web wall-flange wall interface.

The load-displacement relationships of FRP wrapped specimen (S2) at different locations are shown in Figures 4.45 to 4.47. Figure 4.45 shows the comparison of load-displacement relationships at flange wall, between the actuator level and the 2nd floor level. And Figure 4.46 shows comparison of load-displacement relationships at flange wall, between the 2nd floor level and the 1st floor level. From these two figures, it can also be observed that the displacement increase with the height of the locations with the similar shape of hysteresis curves. Figure 4.47 shows the comparison of load-displacement relationships at the 1st floor level, between the flange wall and the web wall. The two curves are nearly the same in Figure 4.47, which shows that no joint failure occurred at the web wall-flange wall interface.

The load-actuator displacement relationship of the non-FRP-wrapped specimen under cyclic test and pushover test are compared in Figure 4.48. It is observed that the load-displacement curve under the pushover test forms the backbone of that under the cyclic test. The slight exceedance of cyclic test curve over the pushover curve at the ultimate stage is due to the higher concrete strength of the specimen under cyclic test (f_{cu}=31.71 MPa for the cyclic test specimen, while f_{cu}=31.13 MPa for the pushover test specimen(Kong 2004)).

Similar comparison of the FRP wrapped specimen is shown in Figure 4.49. Again it is observed that the load-displacement curve of the push over test envelopes that of the cyclic test. The slight exceedance of cyclic test curve over the pushover curve at the ultimate stage is due to the higher concrete strength of the specimen under

cyclic test (f_{cu}=27.58 MPa for the cyclic test specimen, while f_{cu}=22.96 MPa for the pushover test specimen (Kong 2004)).

The observed crack pattern and failure behavior in the cyclic test is also similar to that in the pushover test performed by Kong(2004). The above observation confirms that the pushover test is a simple and backbone representation of the cyclic behavior, even for the GLD shear walls designed according to BS8110(1985).

The comparison of the load- actuator displacement relationship between the FRP wrapped specimen and the control specimen under cyclic loading is shown in Figure 4.50. And the cycle by cycle comparison is shown in Figure 4.51. It is obvious that the ultimate strength, the ultimate displacement and the energy dissipated of the FRP wrapped specimen are larger than those of the control specimen. The improvement of ultimate load capacity and corresponding displacement is up to 20% to 30%, which shows that the proposed FRP retrofit scheme is effective in improving the seismic performance of the GLD shear walls designed according to BS8110(1985).

4.4.1.4. Ductility, failure mode, and stiffness

As the actuator level corresponds to the 2.6 story level, the displacement at the actuator level was chosen for study. When first yielding in the reinforcing bars occurred, the actuator level displacement Δ_y was 11.23 mm for specimen S1 and 10.11 mm for specimen S2. This corresponded to an overall drift ratio of 0.85% for specimen S1 and 0.77% for specimen S2, respectively. For specimen S1, when the maximum load of 184.0 kN was reached, the actuator displacement Δ_u was 11.64

mm and the corresponding overall drift ratio was 0.89%. For specimen S2, when the maximum load of 238.4 kN was reached, the actuator displacement Δ_u was 21.35 mm and the corresponding overall drift ratio was 1.62%. Thus, the ductility factor Δ_u / Δ_y was calculated as 1.03 for specimen S1 and 2.11 for specimen S2. That is, the ductility of FRP-wrapped specimen S2 is much larger than that of the control specimen S1.

The control specimen (S1) shows a brittle shear failure mode: Diagonal shear cracks appeared and propagated with increasing displacement. Finally, a very large diagonal crack region formed dramatically and the concrete at the two ends of this region spalled, indicating failure of the specimen. The first yielding of the steel reinforcement occurred just before the shear failure. The failure mode of the FRP-wrapped specimen (S2) was less brittle with debonding followed by concrete crushing and FRP rupture, at the compression base of the flange wall.

From the comparison of failure mode and ductility between the control specimen and FRP-wrapped specimen, it can be seen that the proposed FRP retrofitting scheme can change the failure mode of the shear wall from a brittle shear failure to a less brittle FRP debonding and rupture failure, and results in a much higher ductility factor.

The influence of FRP system to the stiffness of the specimens can be seen from Figures 4.50 and 4.51. It is observed the stiffness of the FRP wrapped specimen is slightly higher than the control specimen, but the difference is not much.

4.4.2. Local response

4.4.2.1. Local response in control specimen (S1)

Figure 4.52 shows the load vs. strain relationship in reinforcing bars at different locations of the flange wall (S1). To facilitate comparison of these curves at different locations, the scales of the axes are chosen to be the same: strain range is from -4000 micro strain to -4000 micro strain, and base shear range is from -200 kN to 200 kN. Tension strain reading is denoted as positive and compression strain is denoted as negative. As can be observed from Figure 4.52, only the strain gauge reading of bottom of the outermost 10 mm deformed bar (strain gauge 14) exceeded the yield strain ($\varepsilon_y = 0.0029$ as listed in Table 4.3). Other locations had no yielding until the failure of the specimen, and the longitudinal reinforcing bars showed little inelastic excursion in the test. This means that the flexure deformation of the specimen was relatively small, which is reasonable because the specimen failed due to shear instead of flexure. It can be observed that the strain at the middle and higher locations is smaller than that at the edge and lower locations. This shows that the weakest part of the shear wall is at the bottom edges.

The moment-curvature curves of the I section obtained from the control specimen test is shown in Figure 4.53. The moment was calculated by multiplying the lateral load by the distance from the loading point to the section where curvature was measured. For specimen S1, $E = 22.9 \times 10^9$ Pa, $I = 2.43 \times 10^{-3}$ m^4, and $EI = 5.56 \times 10^7$ N.m^2. Based on $\kappa = \frac{M}{EI}$, the moment-curvature relationship of uncracked I section is calculated and shown in Figure 4.53 for comparison. From

Figure 4.53, it is shown that the initial stiffness of the test shear wall specimen was less than that of the theoretical uncracked section.

The specimen can be treated as a fixed end column with I section, and thus the stiffness can be calculated according to $K = \frac{3EI}{h^2}$, where h is the height of the shear wall. Since EI obtained from the moment-curvature relationship of the specimen S1 is $EI_{test} = 4.47 \times 10^7$ N.m^2, the initial stiffness reduction factor of specimen S1 is $\frac{K_{test}}{K} = \frac{3EI_{test}/h^2}{3EI/h^2} = \frac{EI_{test}}{EI} = \frac{4.47 \times 10^7}{5.56 \times 10^7} = 0.8$.

From the moment-curvature relationship, the parameters of hysteresis rules were obtained: $\alpha = 0.5, \beta = 0.7$. These parameters are used in the FEA model using RUAUMOKO in Chapter 5. Since the bilinear factor *r* varied from section to section, an analytical method for calculation is given in Appendix A and the accuracy of this method is validated in Chapter 5.

4.4.2.2. Local response in FRP wrapped specimen (S2)

Figure 4.54 shows the load vs. strain in reinforcing bars curves at different locations of the flange wall (S2). To facilitate comparison of these curves at different locations, the scales of the axes are chosen to be the same: strain range is from -9000 micro strain to -9000 micro strain, and base shear range is from -250kN to 250kN. As can be observed from Figure 4.54, the bottom of the outermost 10 mm deformed bar (strain gauge 12) experienced obvious inelastic excursion strain, and some other locations in the outmost reinforcing bars (strain gauges 8 and 13) experienced inelastic

excursion in the last loading cycle. Comparing Figure 4.54 with Figure 4.52, it can be seen that the FRP-wrapped specimen S2 developed more flexural deformation than the control specimen S1. It is also worthwhile noting that the ratio of the strain developed in the horizontal shear resistant bars (strain gauges 1, 4 and 5) to that in the longitudinal reinforcing bars is smaller in specimen S2 than in specimen S1. This implies that the incorporation of FRP wrapping change the shear dominant response to flexural dominant response, or at least reduces the shear dominant response.

The distribution of the horizontal FRP strain in the flange wall FRP strain gauges is shown in Figure 4.55, and the shear crack pattern of the control specimen S1 is also shown in the same figure for comparison. As can be seen from Figure 4.55, the distribution of the FRP strain value matches the crack pattern quite well: FRP strain was larger at the locations across the cracks, and the maximum FRP strain was at the bottom edges of the wall corners where cracks were concentrated. As for the maximum horizontal FRP strain in the web wall, the value was very small (0.0003), which also matches the fact that little cracks formed on the web wall. Because the larger strain developed in FRP, the higher confinement force was provided by FRP reinforcement, and as the larger FRP strain occurred at the place across the cracks, it is reasonable to conclude that the FRP system provided higher confinement force at locations where crack concentrated. That is, FRP wrapping could help restrain the development of shear cracks and thus improve the seismic performance for shear resistance.

4.5. Summary

This Chapter focused on the experimental investigation of the seismic behavior of GLD RC shear wall structures in Singapore. For this purpose, a 1/5 scale model, representing the lower critical regions of a 25-story shear wall, was tested under cyclic loading. And a retrofitting scheme using GFRP system for shear walls under cyclic loading was also investigated experimentally.

Test results revealed that the shear wall failed at the base due to shear, and the proposed retrofitting scheme could change the brittle shear failure mode to a less brittle failure mode and effectively improve the global and local performance of the specimen. The comparison of the results of the cyclic loading tests and pushover loading tests (Kong et al. 2003b) shows that the pushover test can be a simple and backbone representation of the cyclic behavior of GLD shear wall structures designed according to BS8110 (1985).

Important information, such as reduction factors of initial effective stiffness (0.8 for shear walls) and parameters of the Modified Takeda Hysteresis model ($\alpha = 0.5, \beta = 0.7$ for shear walls), were obtained from the test, and will be used for developing FEA models for shear wall structures in the Chapter 5.

Table 4.1 Comparison of model and prototype I-shape wall

(a)Geometric Properties	**Model**	**Prototype**
Height of model	1314mm	6675.12mm
Length of web wall	955mm	4876.8mm
Length of flange wall	657mm	3352.8mm
Thickness of all walls	45mm	228.6mm
Length of edge portion of flange wall	101mm	516.5mm
Length of mid portion of flange wall	455mm	2319.7mm
(b)Rebar in central wall	**Model**	**Prototype**
Ratio of vertical rebar(f_y =250MPa)	0.79%	0.75%
Spacing d_v@S_v	1x6mm@80mm	2x12.7mm@152.4mm
Ratio of horizontal rebar(f_y =250MPa)	0.18%	0.21%
Spacing d_h@S_h	1x6mm@256mm	2x9.5mm@304.8mm
(c)Rebar in side wall	**Model**	**Prototype**
Ratio of vertical rebar(edge portion)(fy=460MPa)	3.46%	3.43%
Spacing d_v@S_v	1x10mm@51mm	2x25.4mm@129mm
Ratio of vertical rebar(middle portion)(fy=460MPa)	1.72%	1.76%
Spacing d_v@S_v	1x8mm@65mm	2x22.2mm@193.3mm
Ratio of horizontal rebar(f_y=250MPa)	0.18%	0.12%
Spacing d_h@S_h	1x6mm@256mm	2x6.35mm@228.6mm
(d)At the web-flange wall joint	**Model**	**Prototype**
Ratio of vertical rebar(f_y=460MPa)	2.50%	2.97%
Diameter	1x8mm	4x22.2mm
(e)Material Properties	**Model**	**Prototype**
f_{cu} (MPa)	31.71,27.58	30
f_y (MPa)	350,482,525	250-460
E_c (GPa)	22.92,20.89	23.2
E_s (GPa)	103.5,166,142	200
Thickness of GFRP laminate (mm)	0.353	0.164

1x= one layer of rebar

2x= two layers of rebar

d_v =diameter of vertical steel reinforcement

d_h =diameter of horizontal steel reinforcement

S_v =spacing of vertical steel reinforcement

S_h =spacing of horizontal steel reinforcement

f_{cu} =concrete cube compressive strength

f_y =steel yield stress

E_c =concrete elastic modulus

E_s =reinforcement elastic modulus

Table 4.2 Mbrace EG900 glass fiber reinforced ploymer

Density	Thickness	Fiber orientation	Young's modulus	Ultimate tensile strength	Ultimate tensile strain
915g/m^2	0.353mm	Unidirectional	69.65Gpa	1667.7MPa	0.02

Table 4.3 Steel reinforcement properties

Diameter	Surface	f_y(MPa)	f_u(MPa)	E(Gpa)	ε_y	ε_u
6 mm	Smooth	250	456.2	103.5	0.0024	0.33
8 mm	Smooth	525	548.2	142	0.0037	0.02
10 mm	Deformed	481.8	565.9	166	0.0029	0.145

f_y=yield stress

f_u=ultimate or rupture stress

E=initial Young's modulus

ε_y =yield strain

ε_u =ultimate strain

Table 4.4 Parameters of wall specimens tested

Specimen	Cube strength f_{cu} (MPa)	Young's modulus (GPa)	Modulus of rupture f_r (MPa)	Cylindrical strength f_c'(MPa)
S1(control)	31.71	22.92	4.06	25.08
S2(FRP)	27.58	20.89	3.47	23.71

Table 4.5 Properties of Mbrace primer and saturant

Properties	Mbrace primer (epoxy)	Mbrace saturant (impregnation resin)
Flexural strength	24 MPa	124 MPa
Flexural modulus	593 MPa	3731 MPa
Compressive strength	24 MPa	86 MPa
Compressive modulus	669 MPa	2621 MPa
Tensile elastic modulus	717 MPa	3034 MPa
Tensile stress at yield	12 MPa	54 MPa

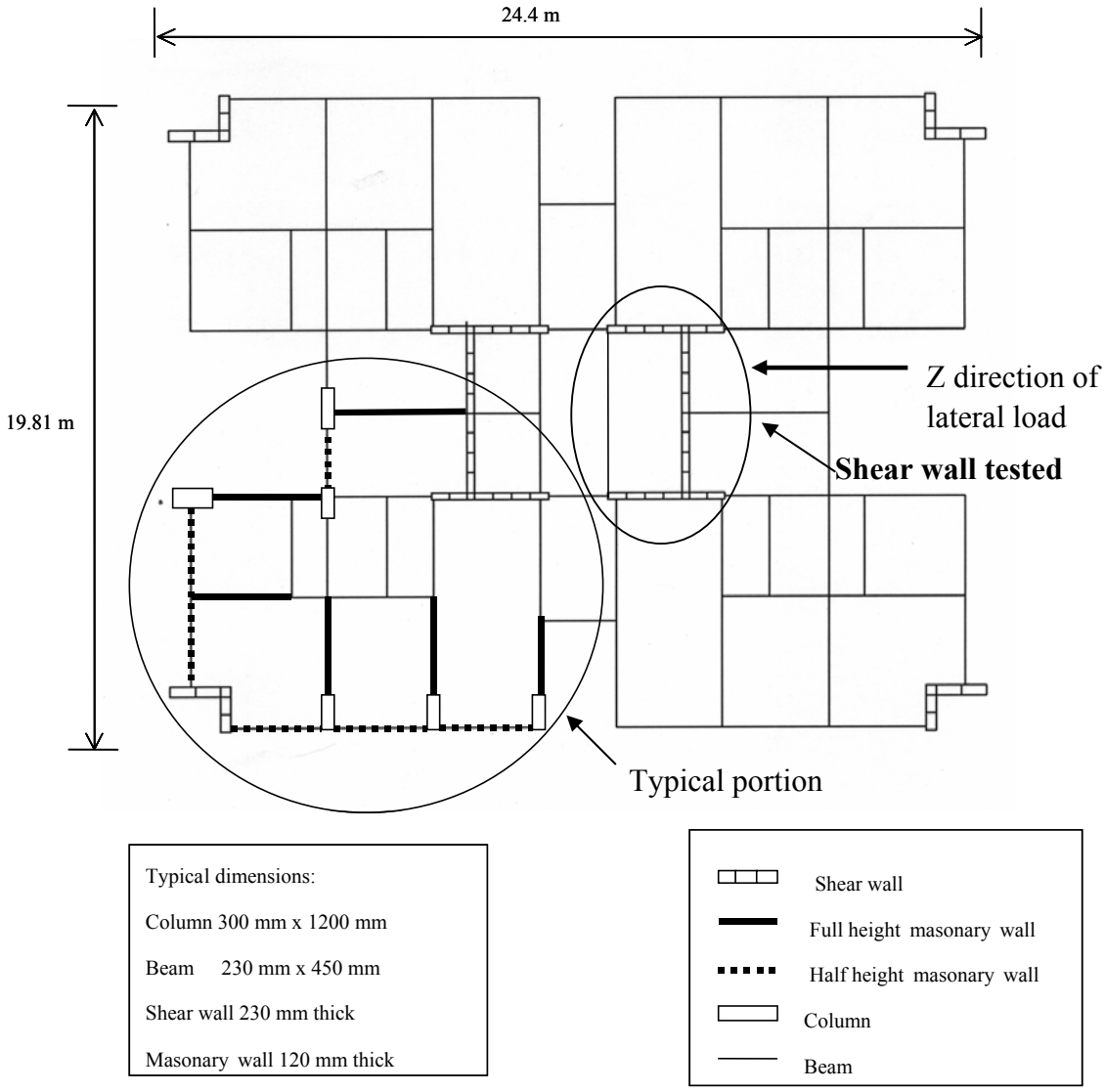

Figure 4.1 Plan view of 25-story point block

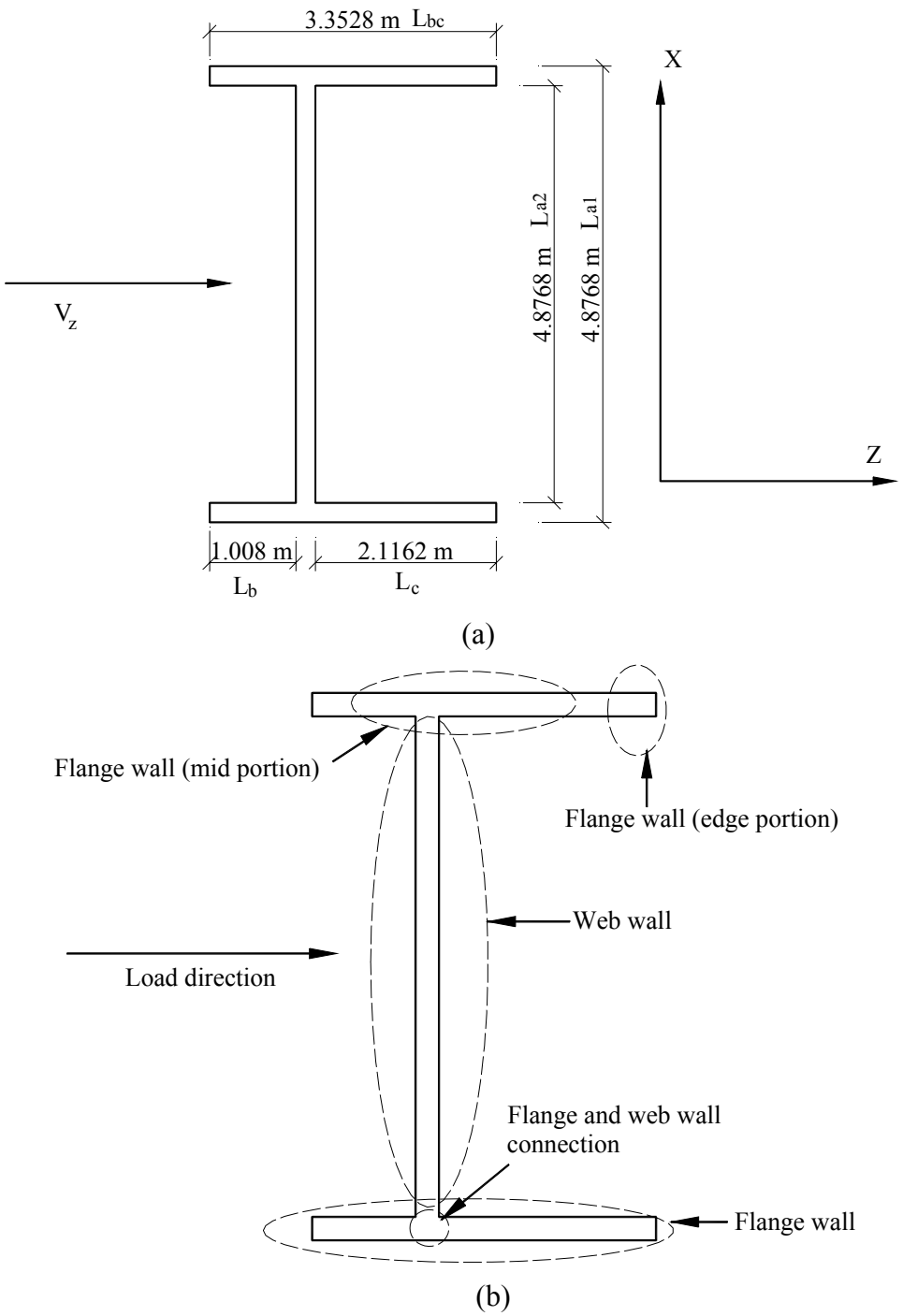

Figure 4.2 Plan view of prototype wall (a) dimensions (b) identification of segments

(a)

(b)

Figure 4.3 3D view of the specimens (a) control specimen (b) FRP wrapped specimen

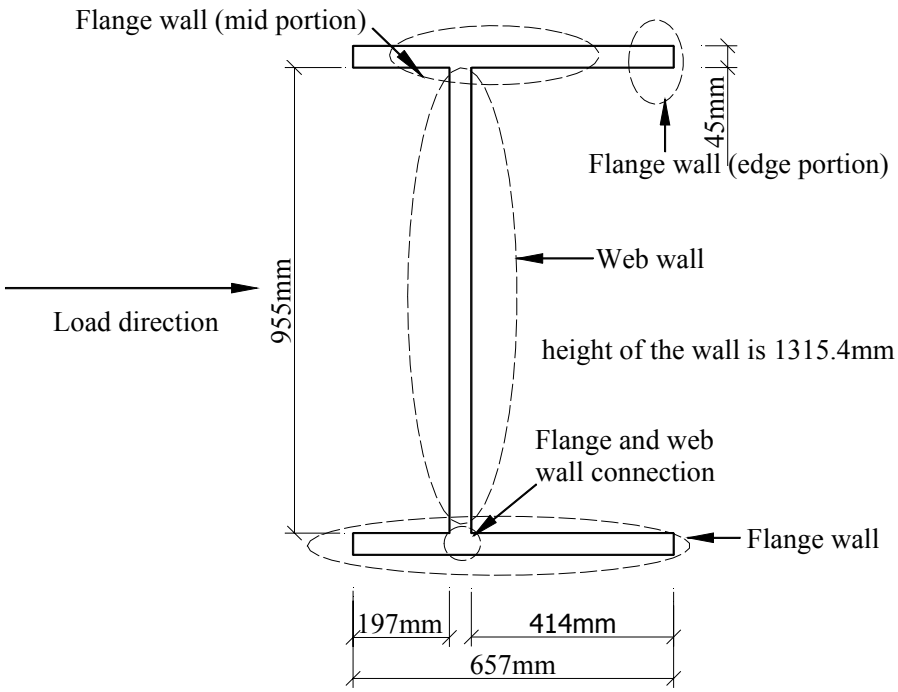

Figure 4.4 Plan view and geometry of the test model

Figure 4.5 Overall 3D view of the rebar in the wall specimen

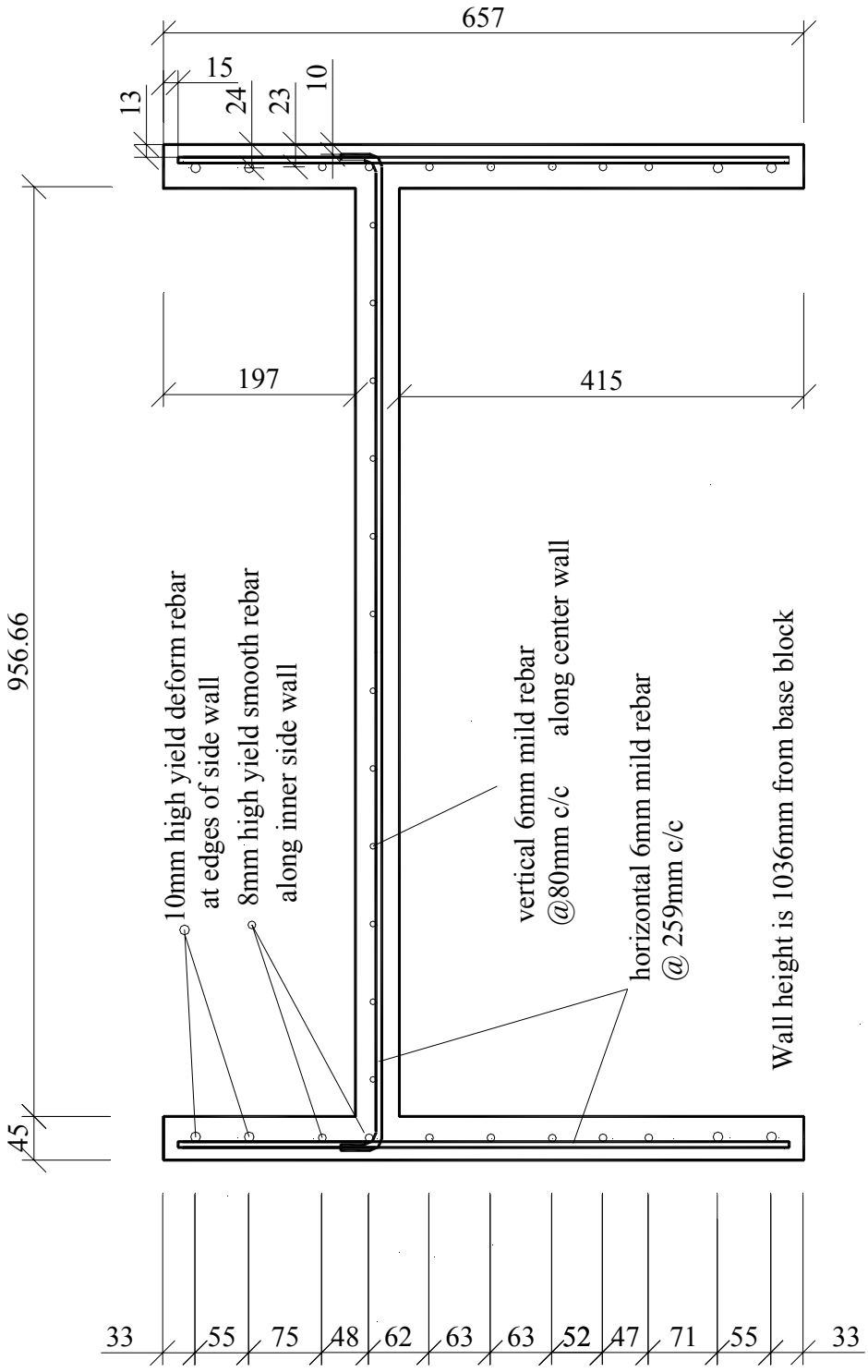

Figure 4.6 Plan view of the reinforcing bar geometry

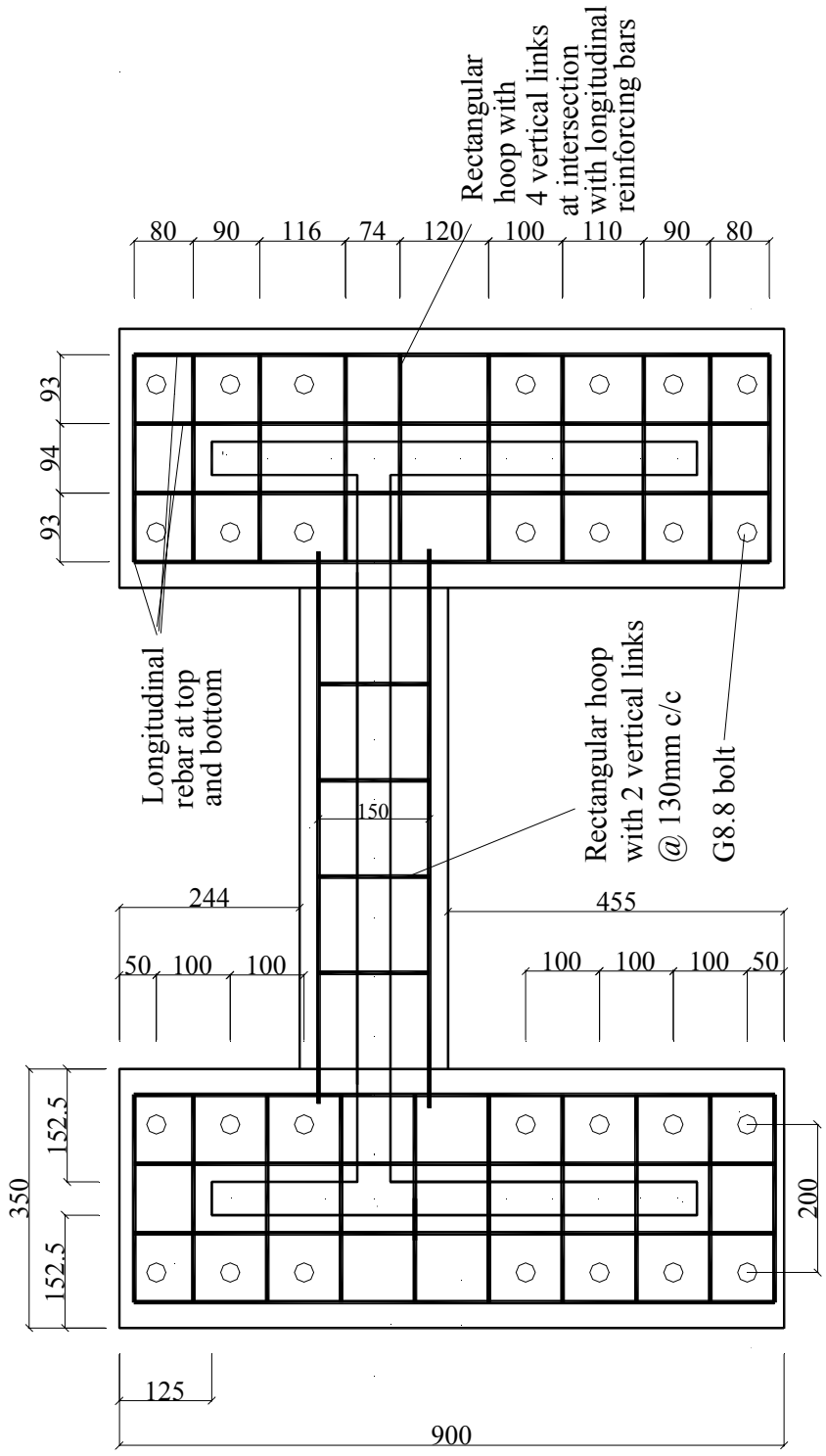

Figure 4.7 Details of reinforcing bars in the base block reinforcing bars

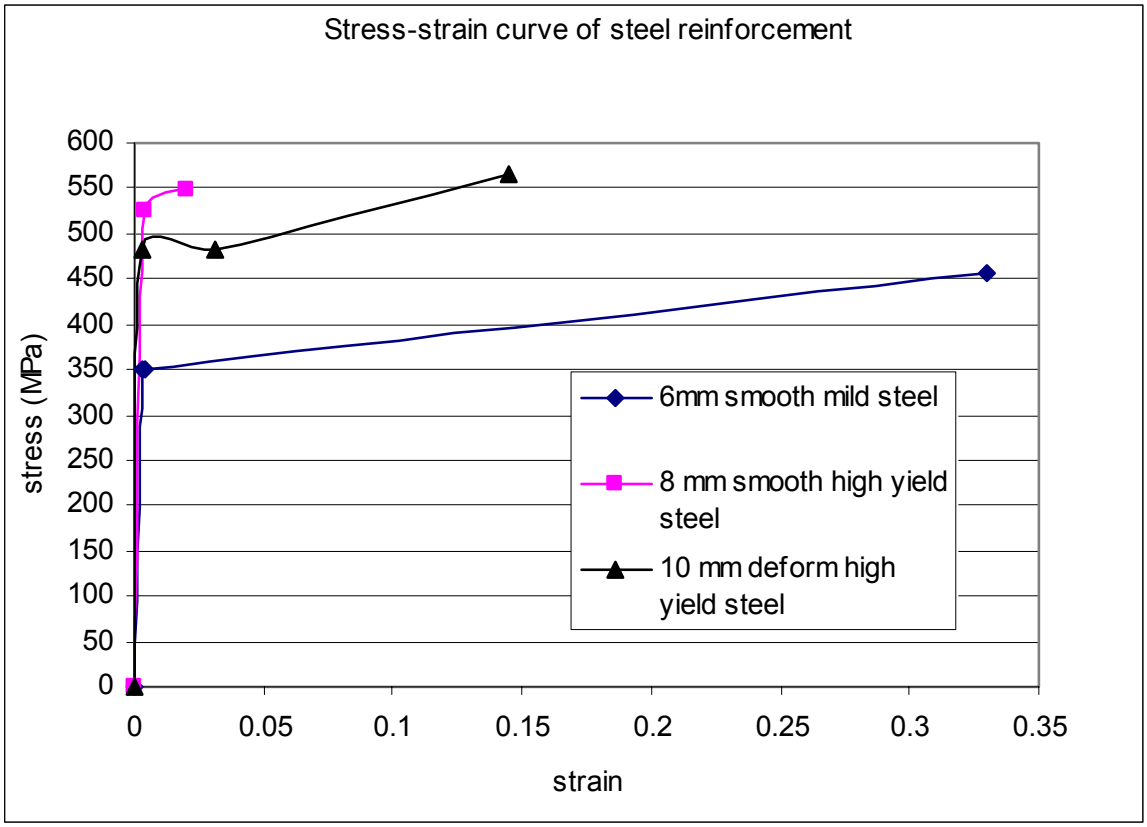

Figure 4.8 Average stress- strain curves of steel reinforcement used in model

Figure 4.9 Concrete casting in the lab

Figure 4.10 Wall after the application of MBT primer (Note the rounded edge of the wall)

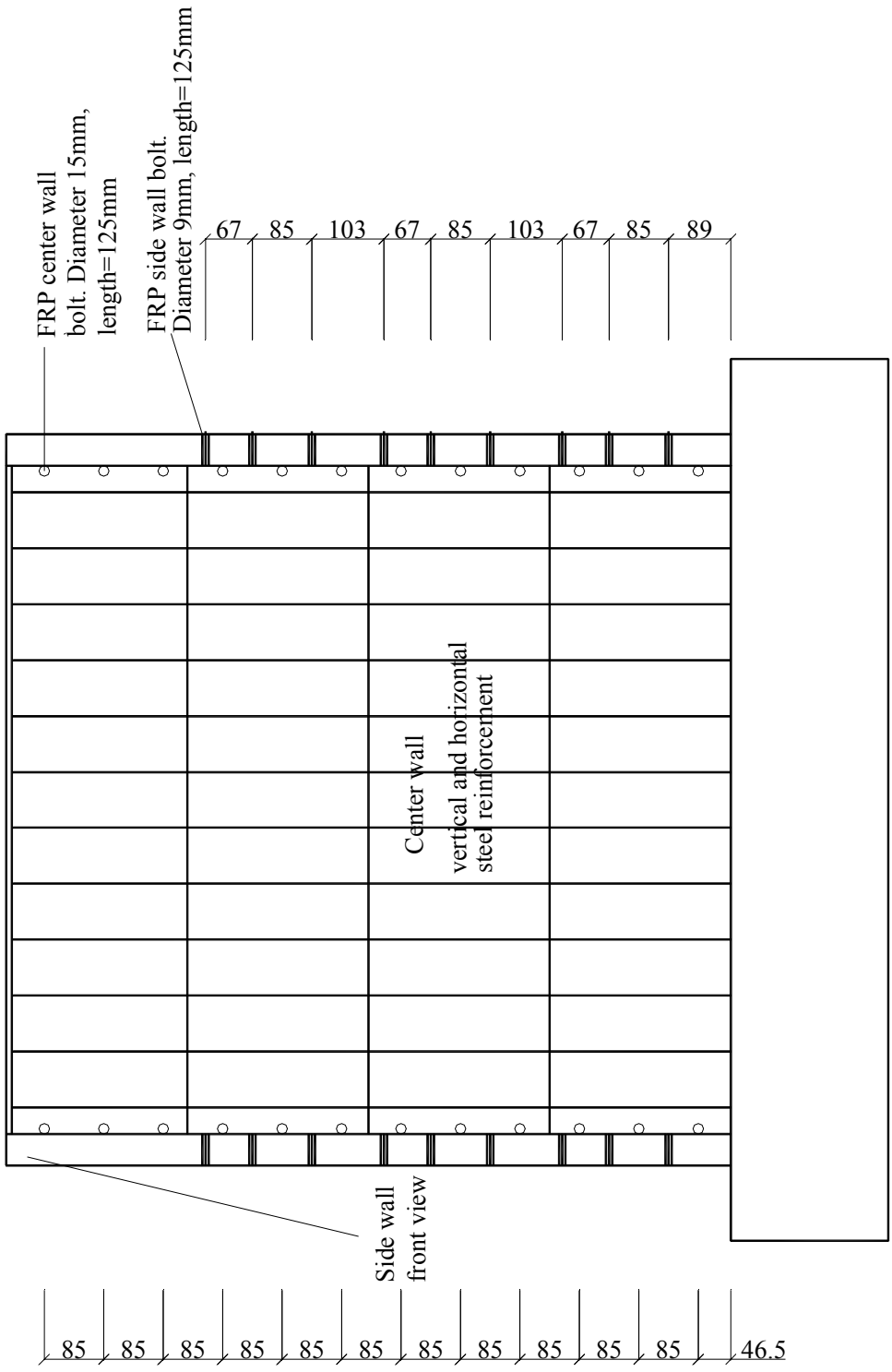

Figure 4.11 Locations of FRP bolts (front view)

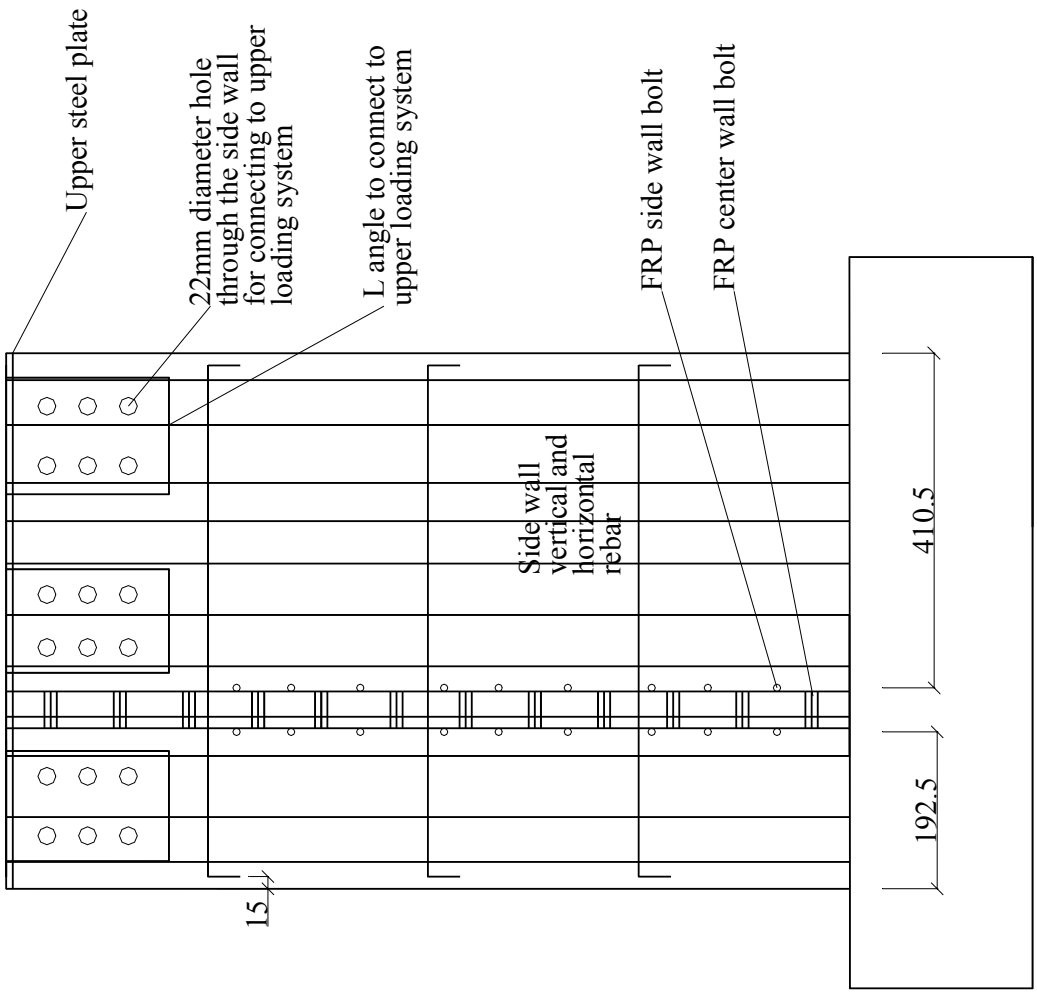

Figure 4.12 Locations of FRP bolts (side view)

Figure 4.13 3D view of the overall test setup for the control wall (specimen S1)

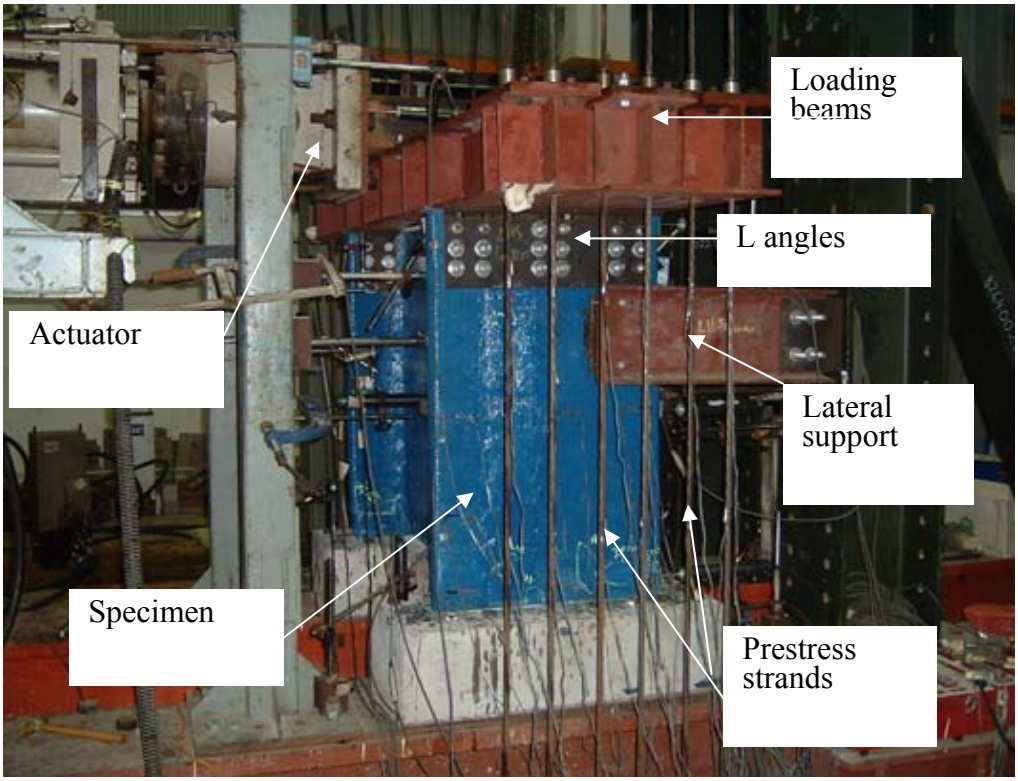

Figure 4.14 3D view of test setup for FRP wrapped wall (specimen S2)

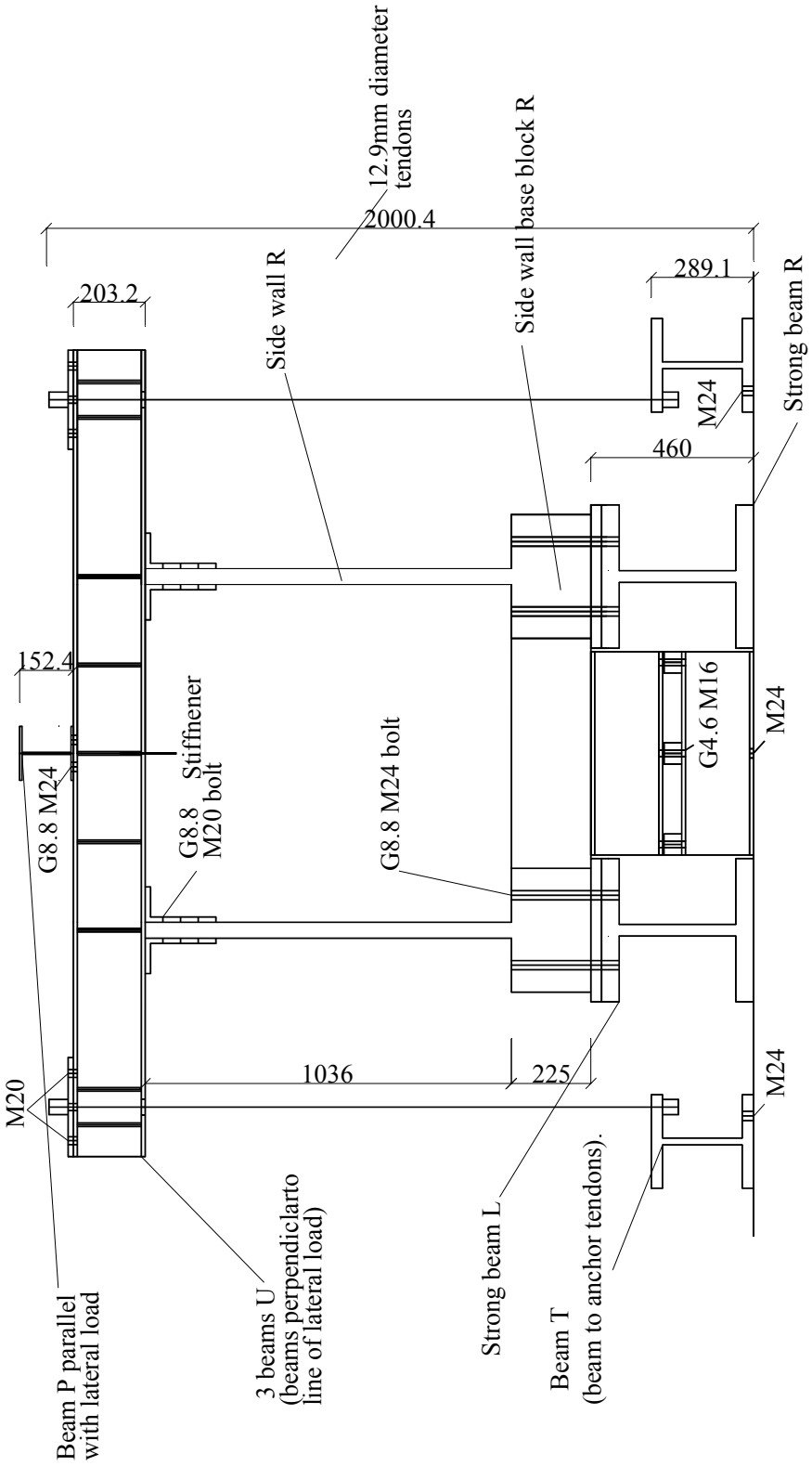

Figure 4.15 Front view of the overall set-up

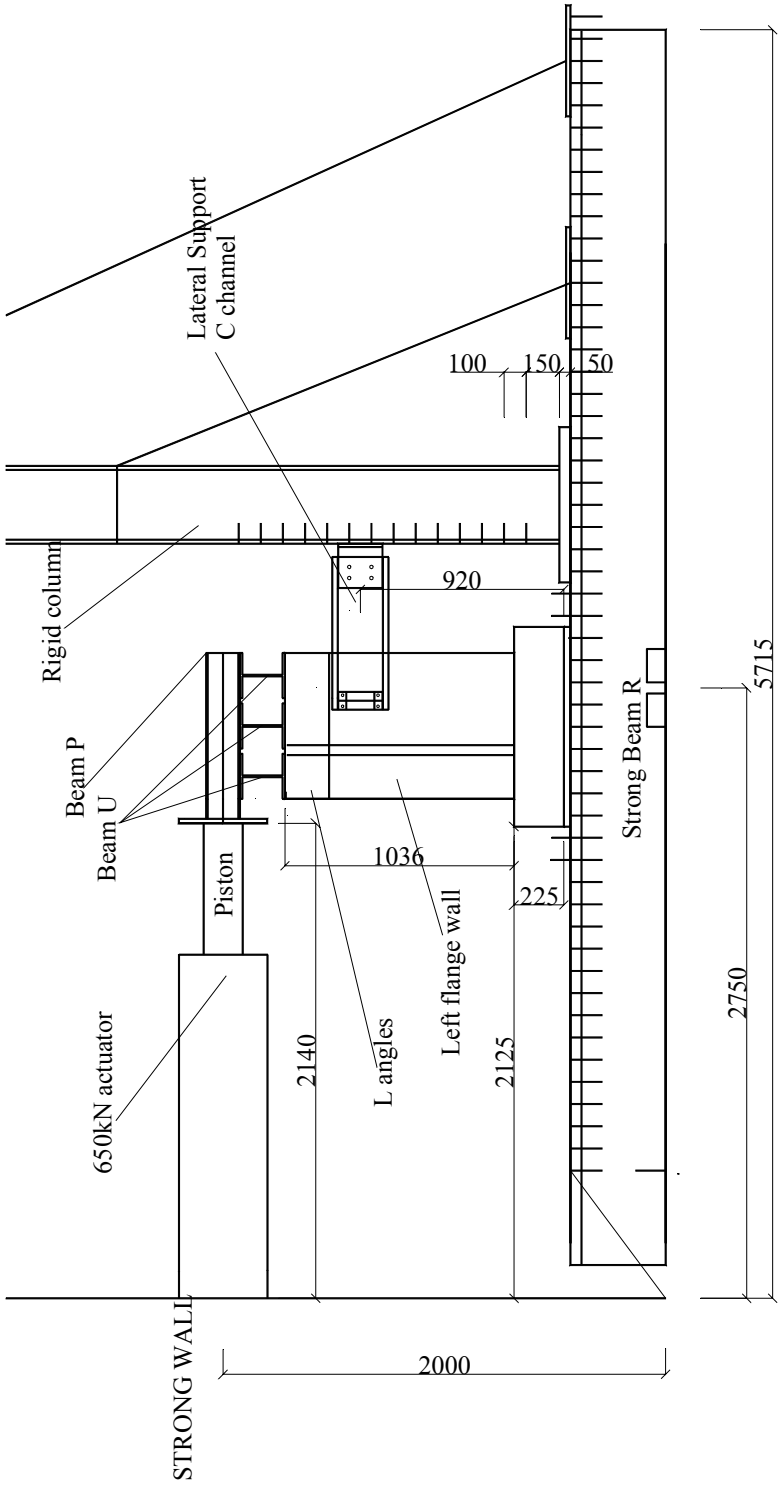

Figure 4.16 Side view of the overall set-up

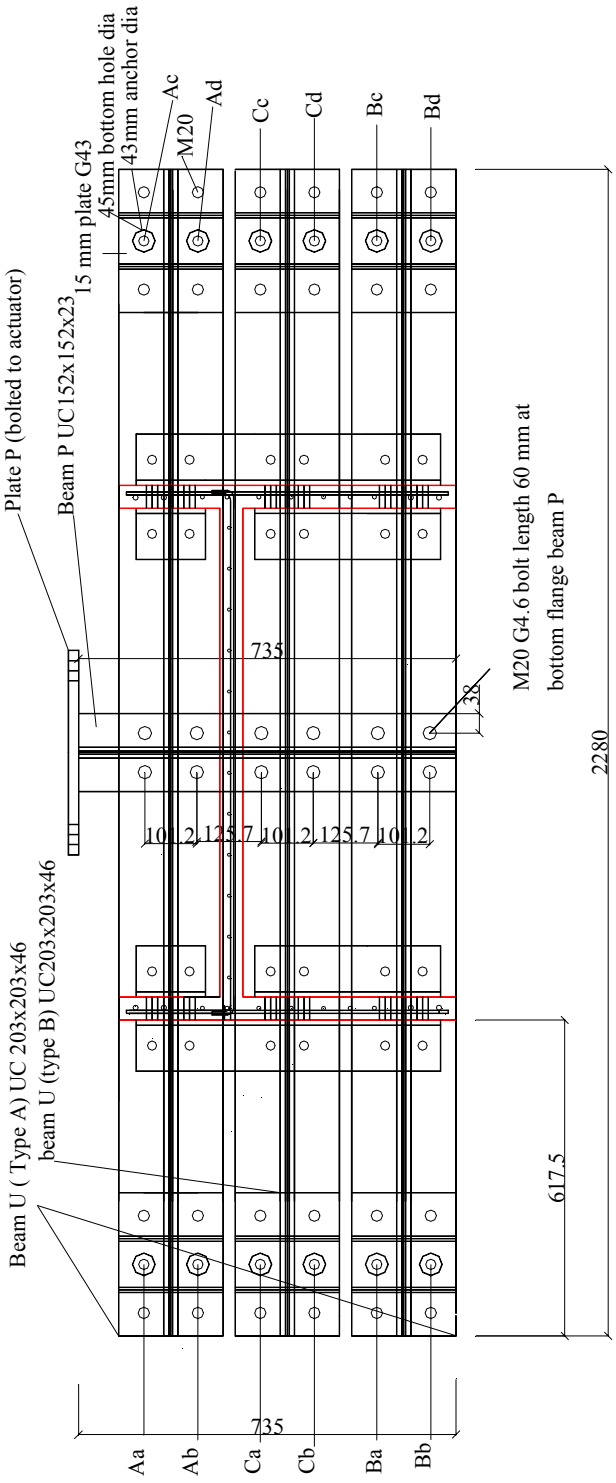

Figure 4.17 Plane view of the loading system

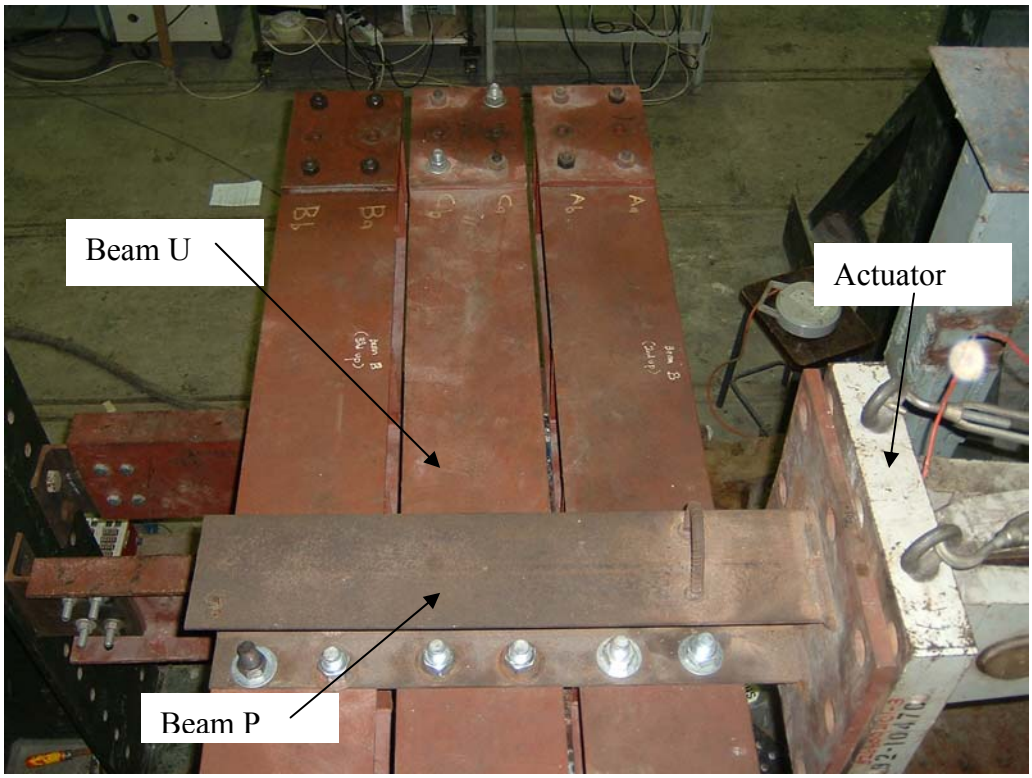

Figure 4.18 3D view of connections of actuator to P beam and P beam to U beams

Figure 4.19 3D view of connections of U beams to L angles and L angles to walls

Figure 4.20 3D view of post-tension strands anchored to the U beams

Figure 4.21 3D view of the lateral supporting system

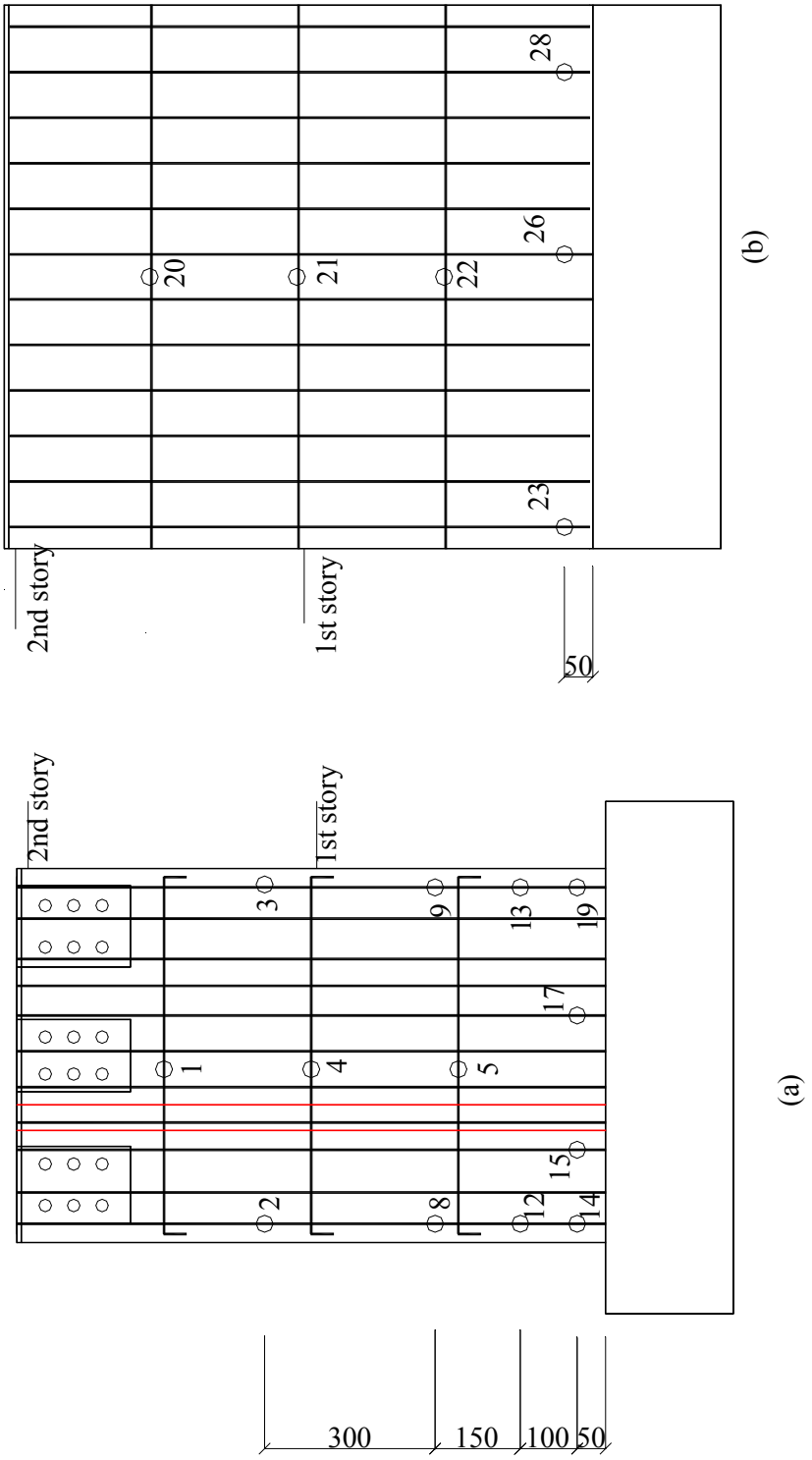

Figure 4.22 Locations of strain gauges on the reinforcing bars (a) left flange wall (b) web wall

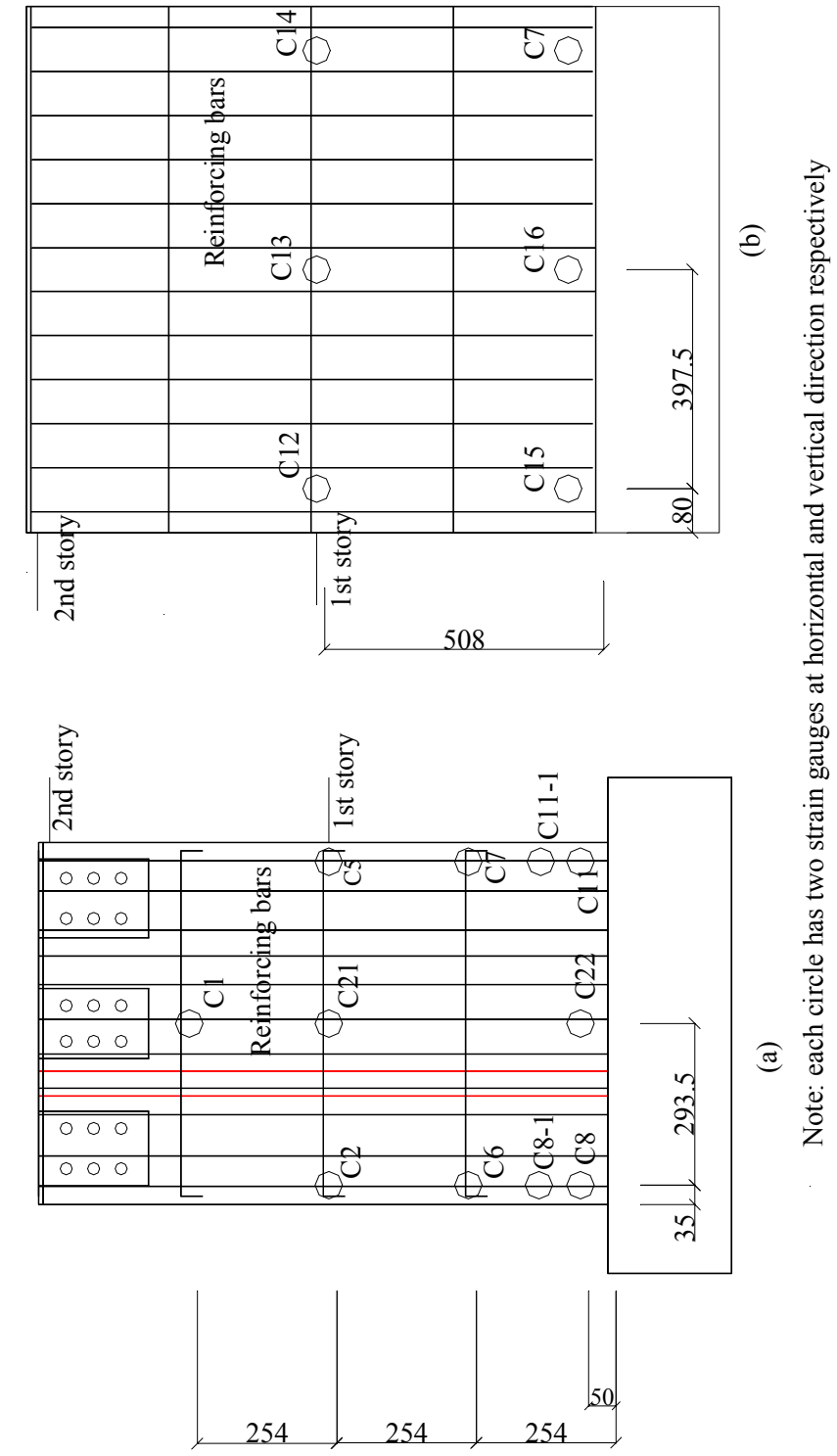

Figure 4.23 Locations of strain gauges on concrete (a) left flange wall (b) web wall

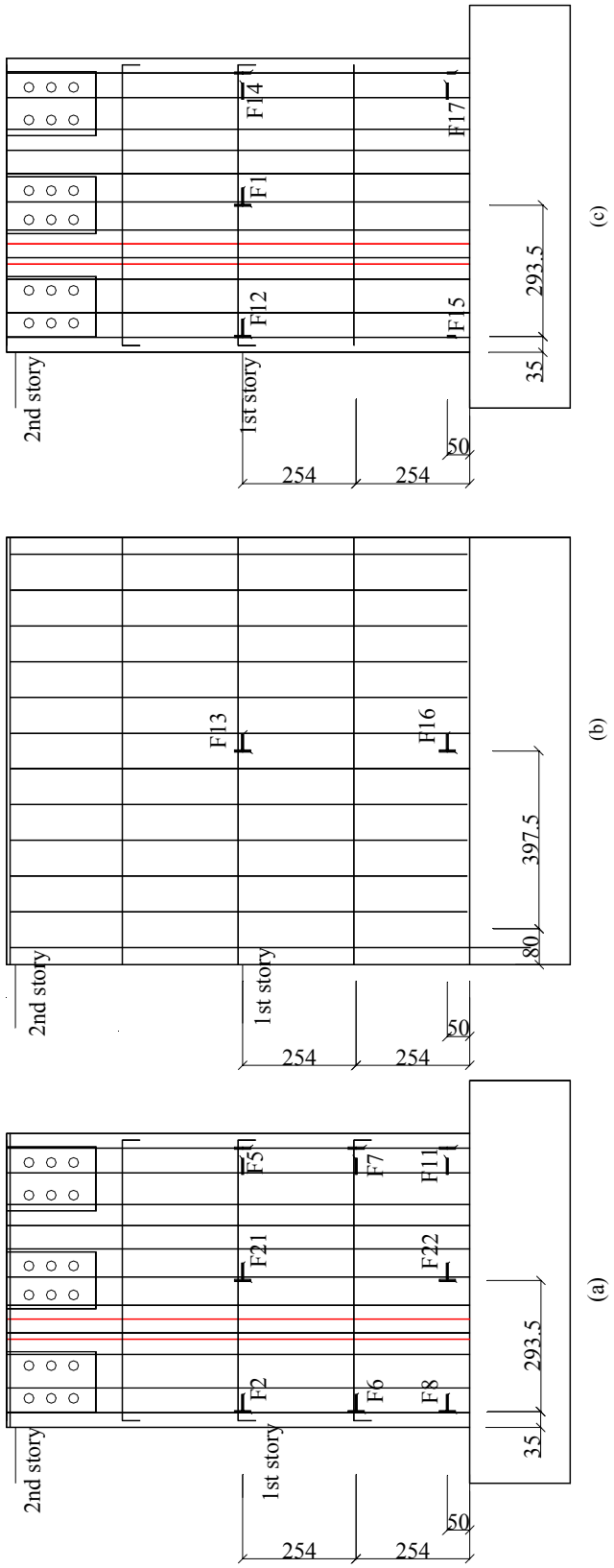

Figure 4.24 Strain gauges on the FRP of the wall (a) left flange wall (b) web wall (c) right flange wall

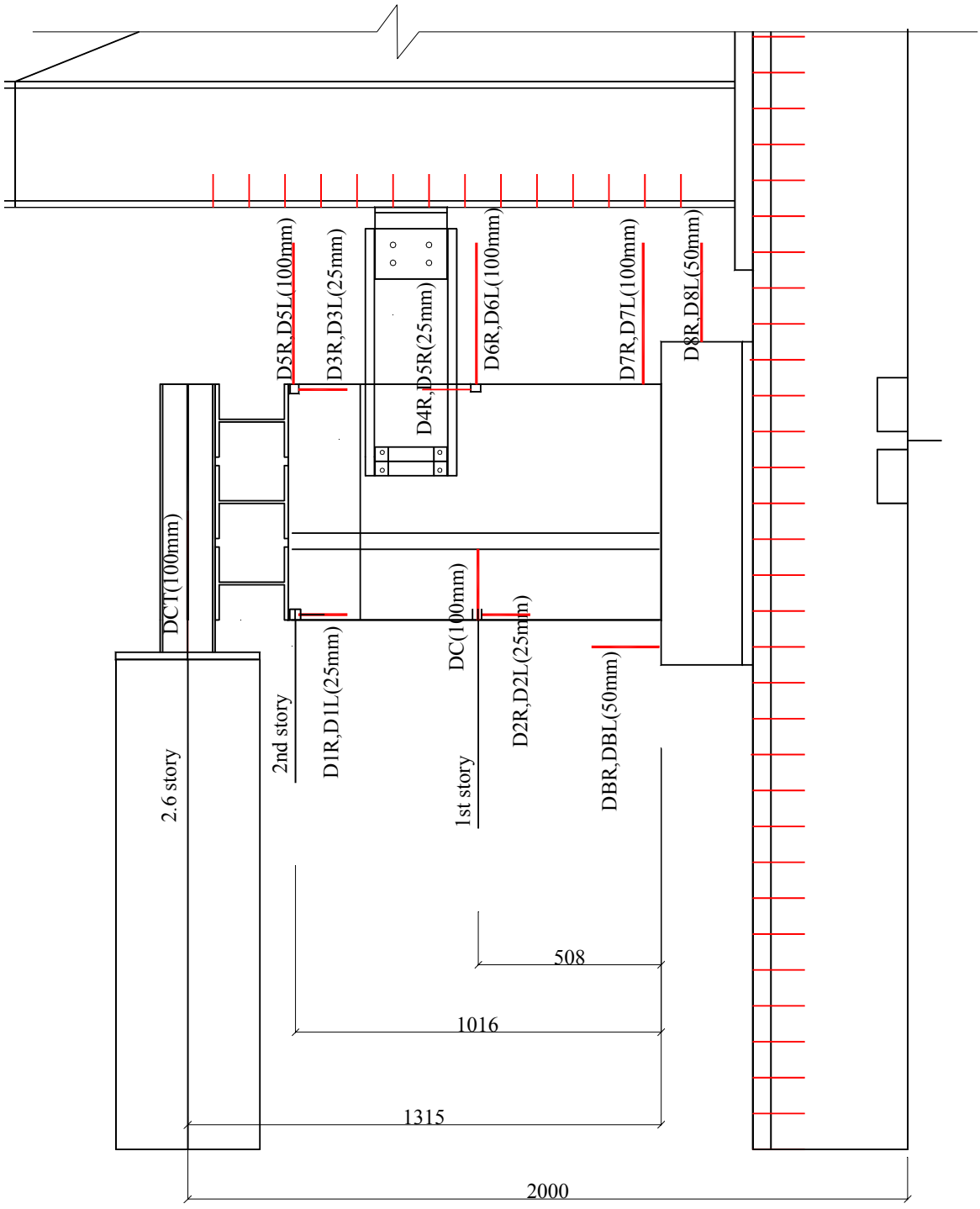

Figure 4.25 Locations and labels of displacement transducers (range of the displacement transducer is indicated within brackets)

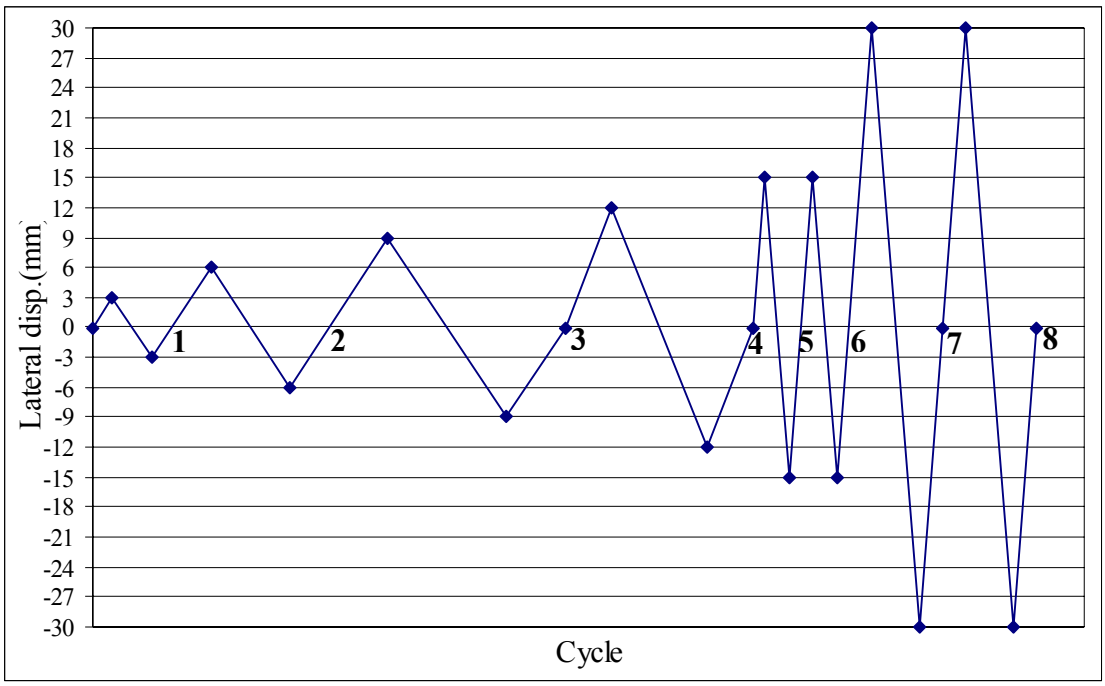

Figure 4.26 Cyclic loading history

Figure 4.27 3D view of the wall model after white wash

Figure 4.28 3D view of crack pattern of the flange wall

Figure 4.29 First spalling of the concrete of the right flange wall

Figure 4.30 Overview of the shear failure mode of the right flange wall

Figure 4.31 Spalling concrete of the upper right part of the right flange wall

Figure 4.32 Spalling of concrete of the bottom part of the right flange wall

Figure 4.33 Shear cracks on the left flange wall

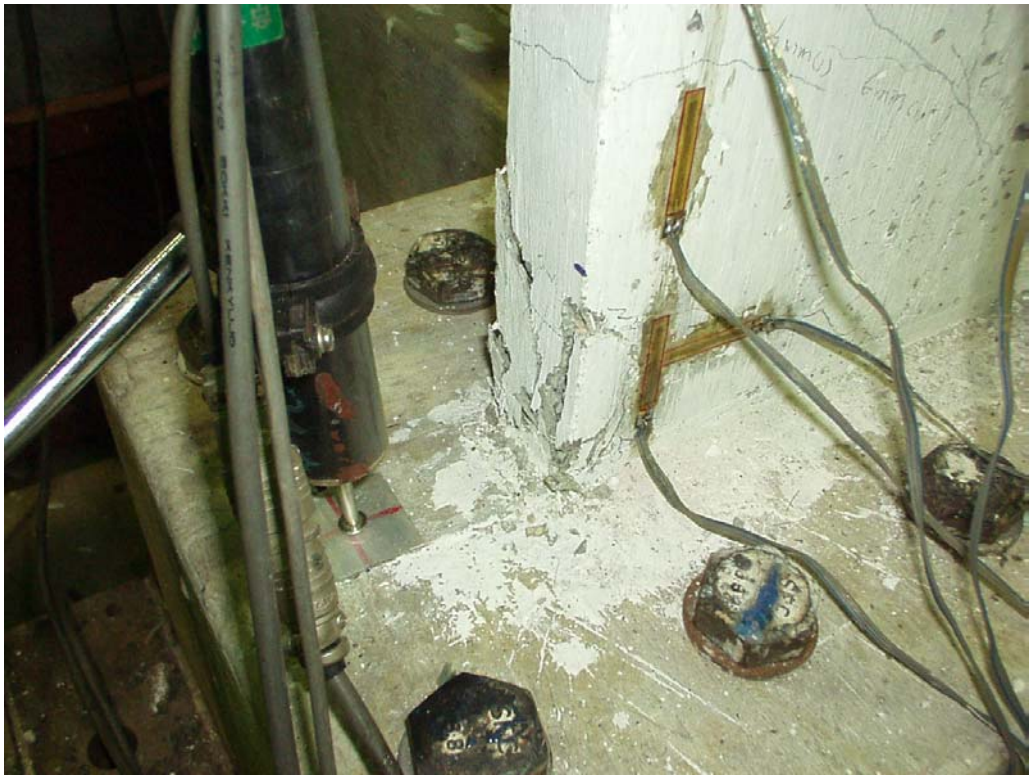

Figure 4.34 Spalling of the left flange wall corner

Figure 4.35 First FRP debonding of the left flange wall

Figure 4.36 First FRP debonding of the right flange wall

Figure 4.37 First FRP debonding of the web wall

Figure 4.38 FRP debonding of the right flange wall (the second 15 mm cycle)

Figure 4.39 Crushing of the corner of the right flange wall at 16 mm top displacement

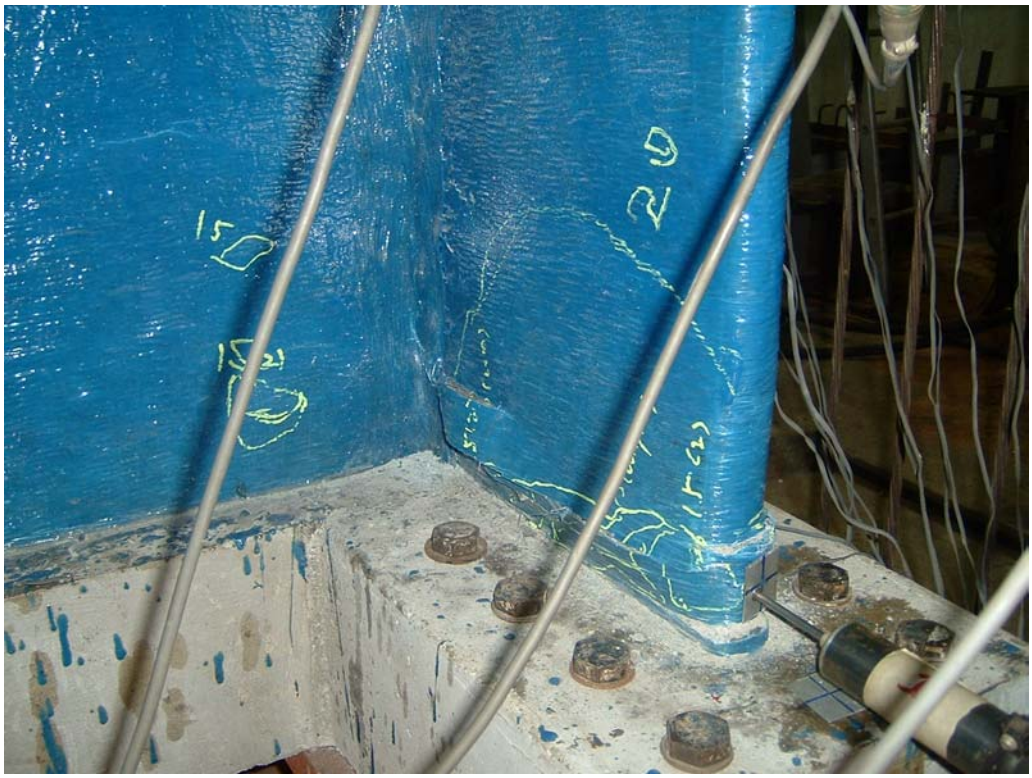

Figure 4.40 Debonding of FRP at the right flange wall corner enlarged dramatically

Figure 4.41 Crushing of the left flange wall

Figure 4.42 Crushing of the right flange wall corner at 24 mm top displacement

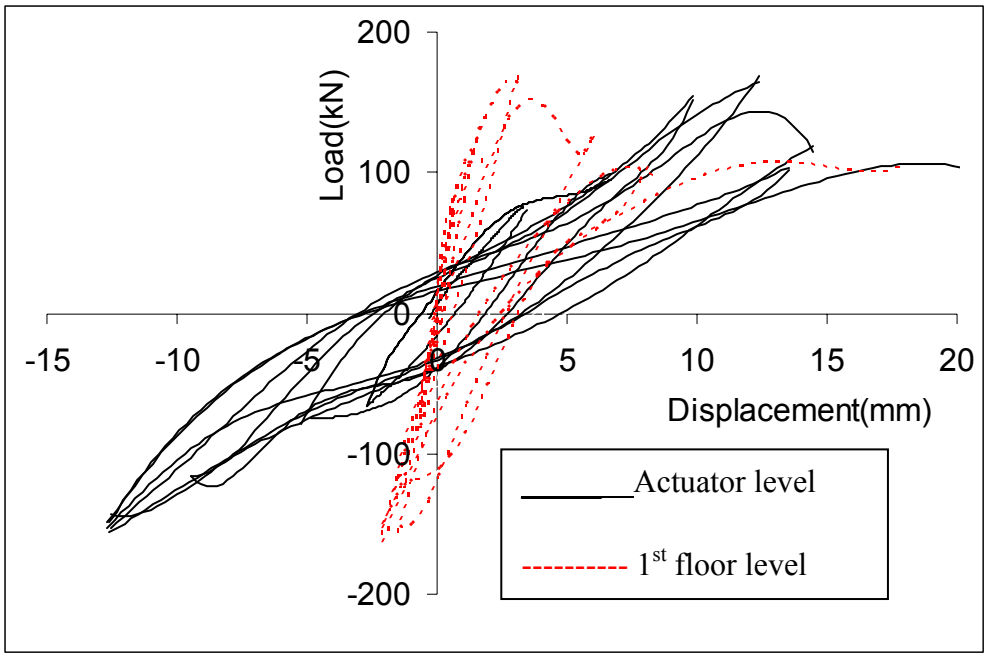

Figure 4.43 Load-displacement relationships at the top actuator level and the 1st floor level of the flange wall (control specimen S1)

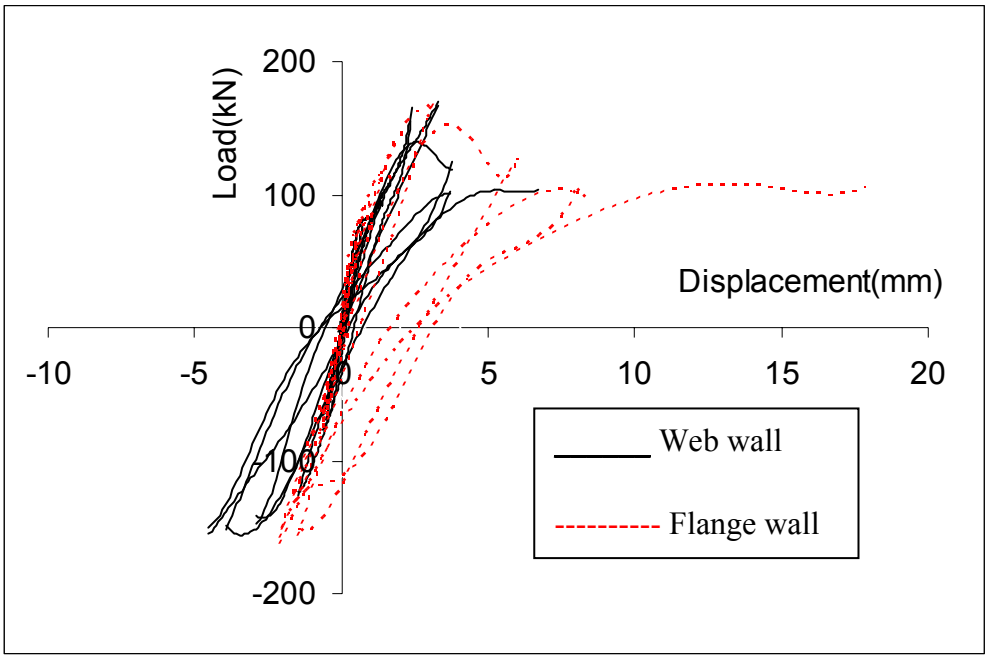

Figure 4.44 Load-displacement relationships of flange wall and web wall at the 1st floor level (control specimen S1)

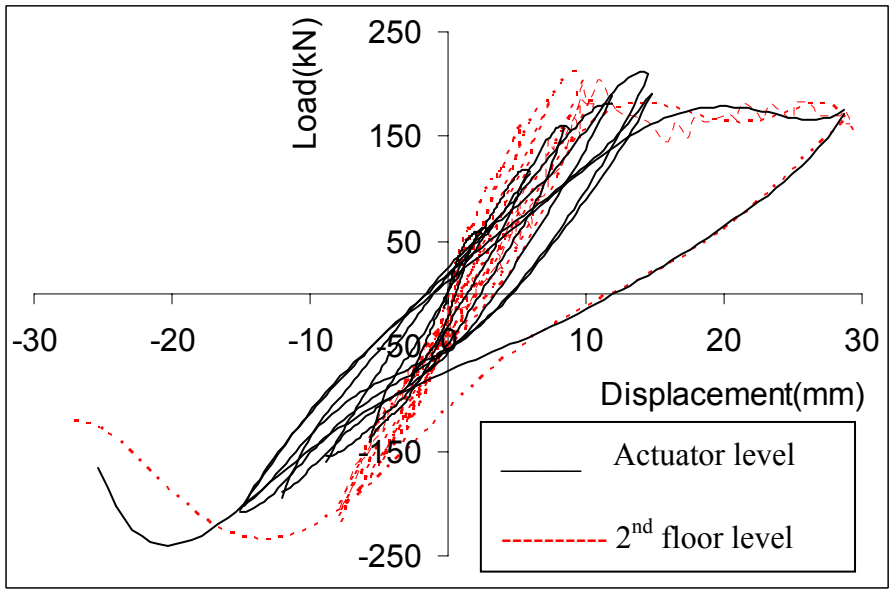

Figure 4.45 Load-displacement relationships of the top actuator level and the 2nd floor level of the flange wall (FRP wrapped specimen S2)

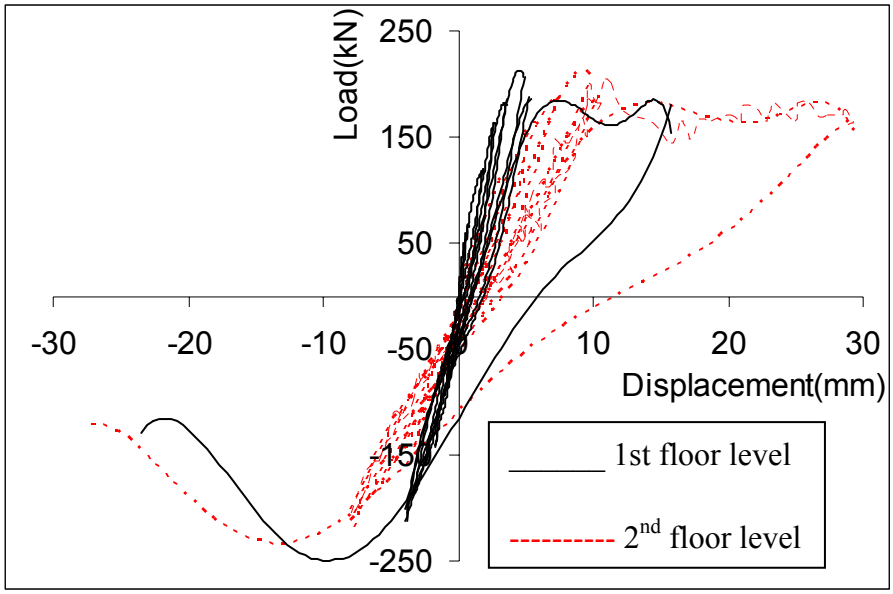

Figure 4.46 Load-displacement relationships at the 2nd and the 1st floor level of the flange wall (FRP wrapped specimen S2)

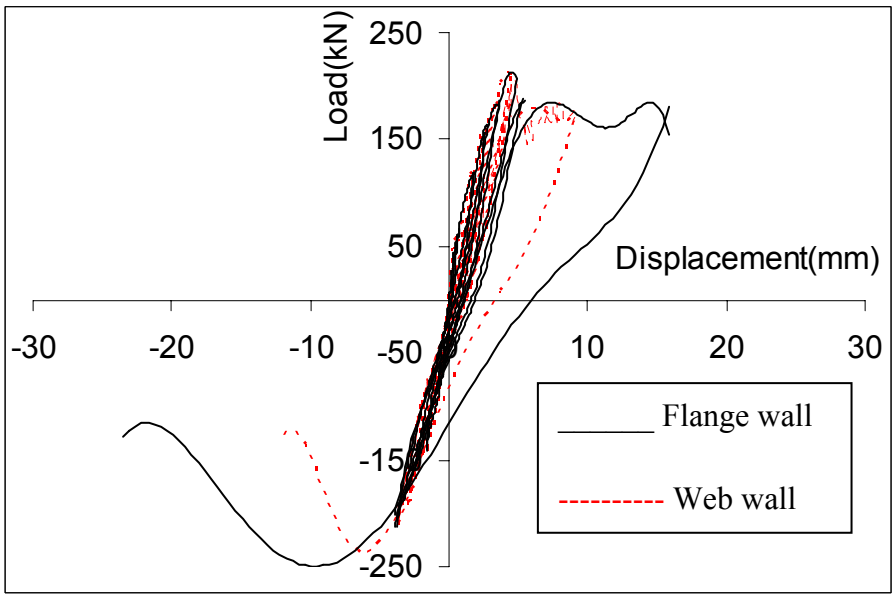

Figure 4.47 Load-displacement relationship of the FRP wrapped specimen at the 1st floor level of the flange wall and the web wall

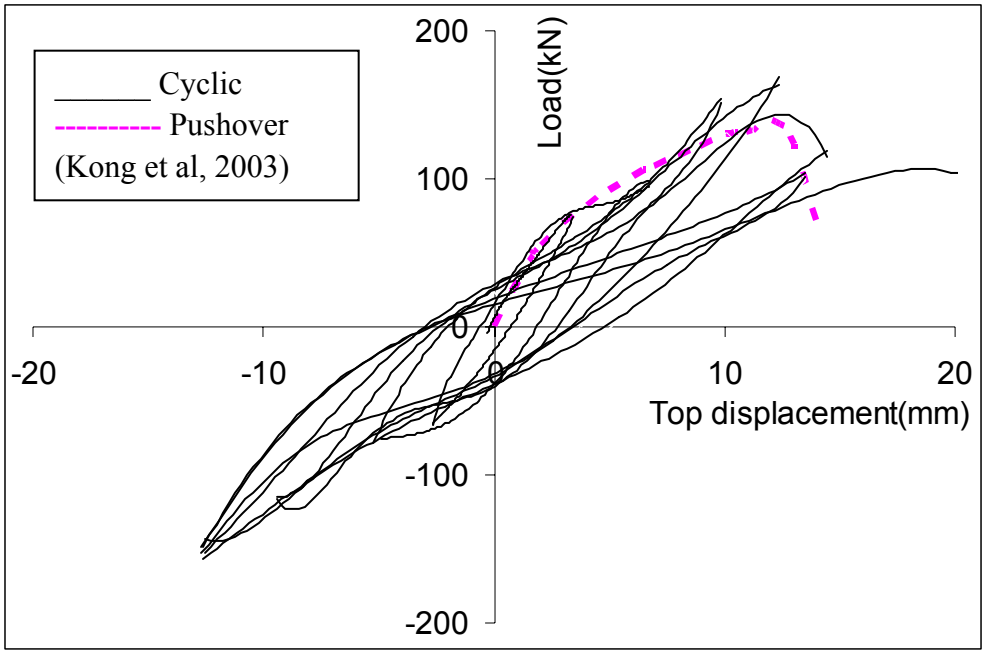

Figure 4.48 Comparison of the load- top actuator level displacement relationships between cyclic loading and pushover loading for the non-FRP specimen

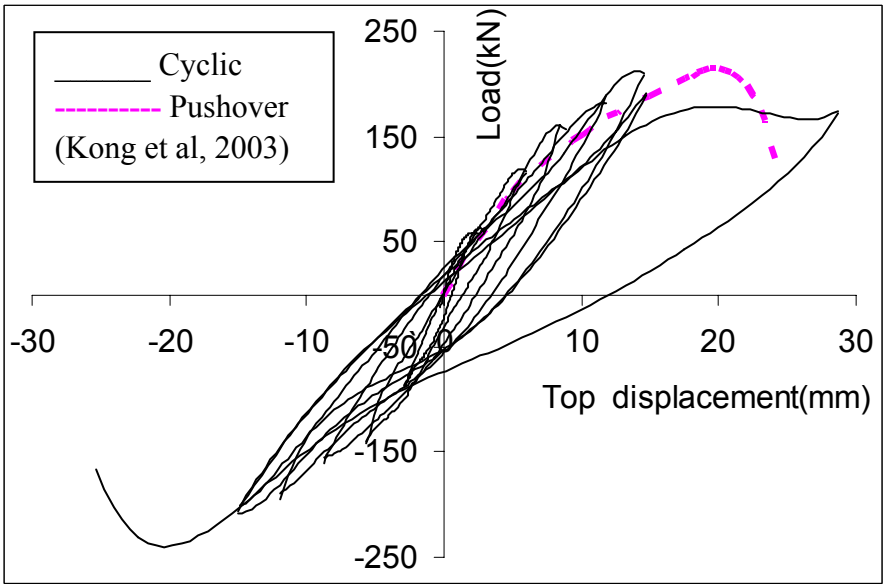

Figure 4.49 Comparison of the load-top actuator level displacement relationships between cyclic loading and pushover loading for the FRP wrapped specimen

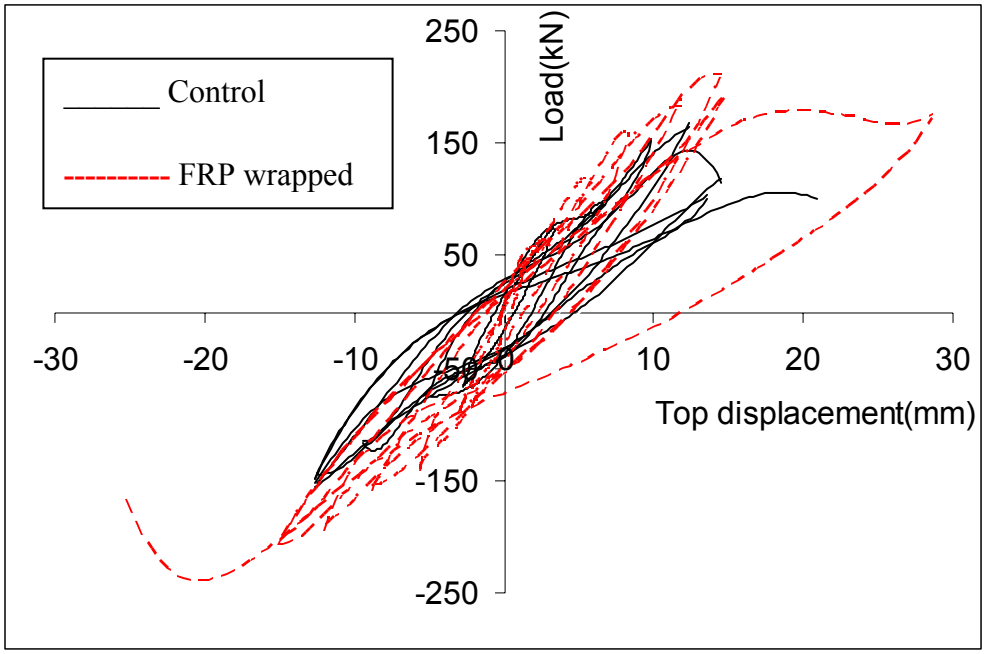

Figure 4.50 Comparison of the load-top actuator level displacement relationships between FRP wrapped specimen and control specimen under cyclic loading

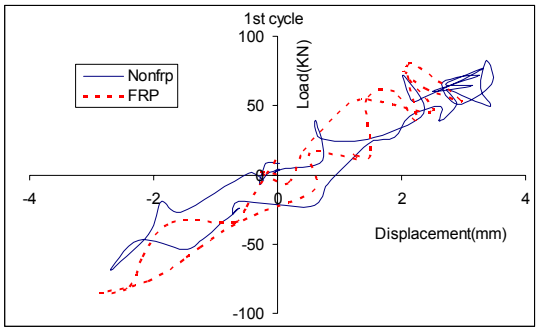

(a) 1st cycle

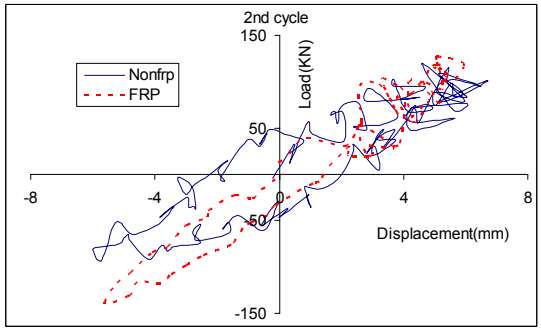

(b) 2nd cycle

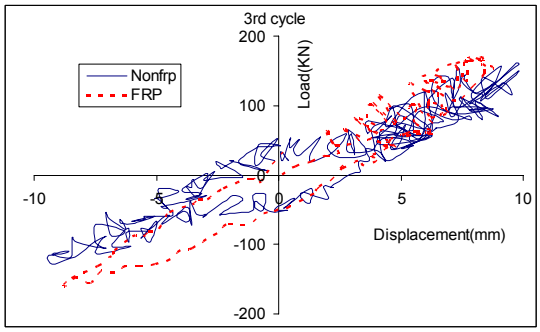

(c) 3rd cycle

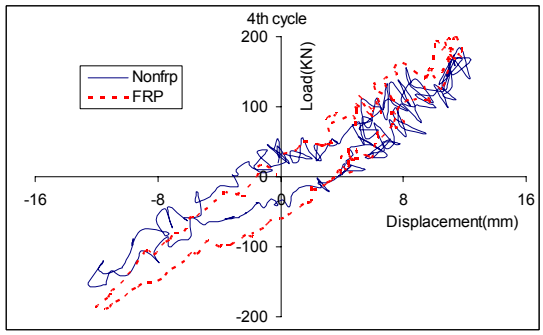

(d) 4th cycle

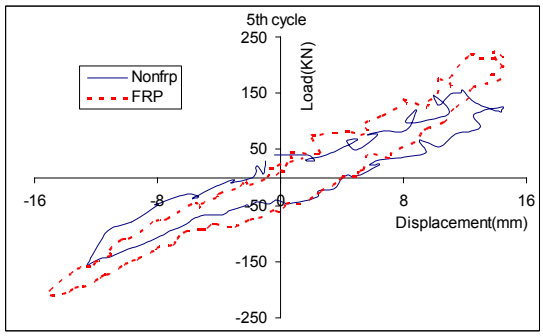

(e) 5th cycle

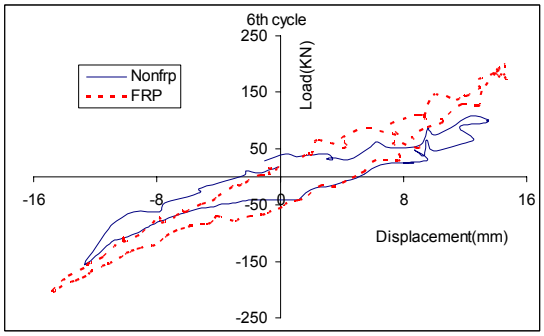

(f) 6th cycle

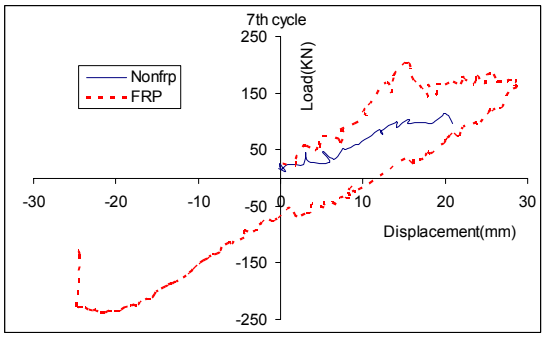

(g) 7th cycle

Figure 4.51 Comparison of the load-top actuator level displacement relationships between FRP wrapped specimen and control specimen under cyclic loading (Cycle by Cycle)

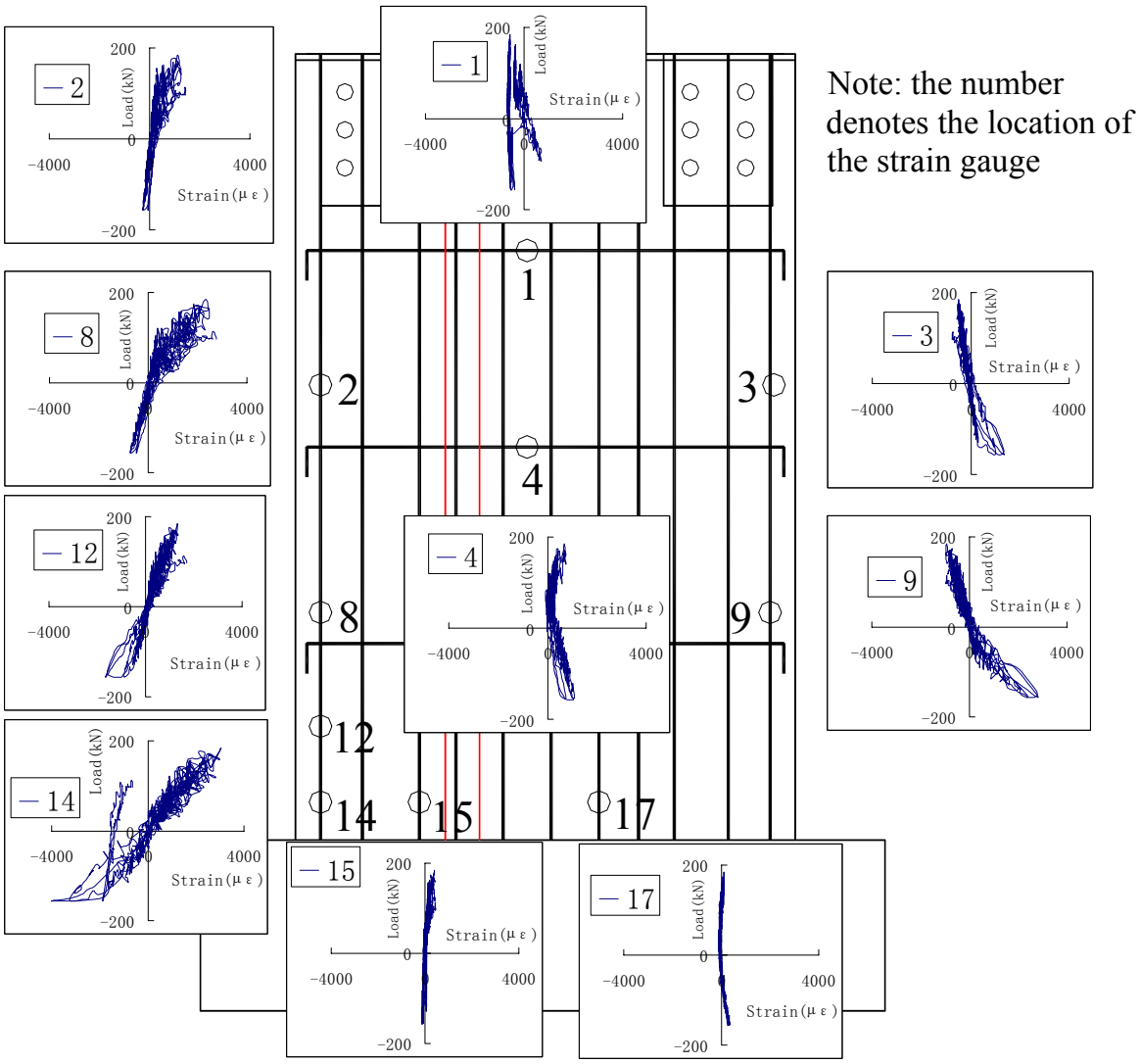

Figure 4.52 Load (kN) vs. strain in reinforcing bars (micro strain) curves at different locations (Specimen S1)

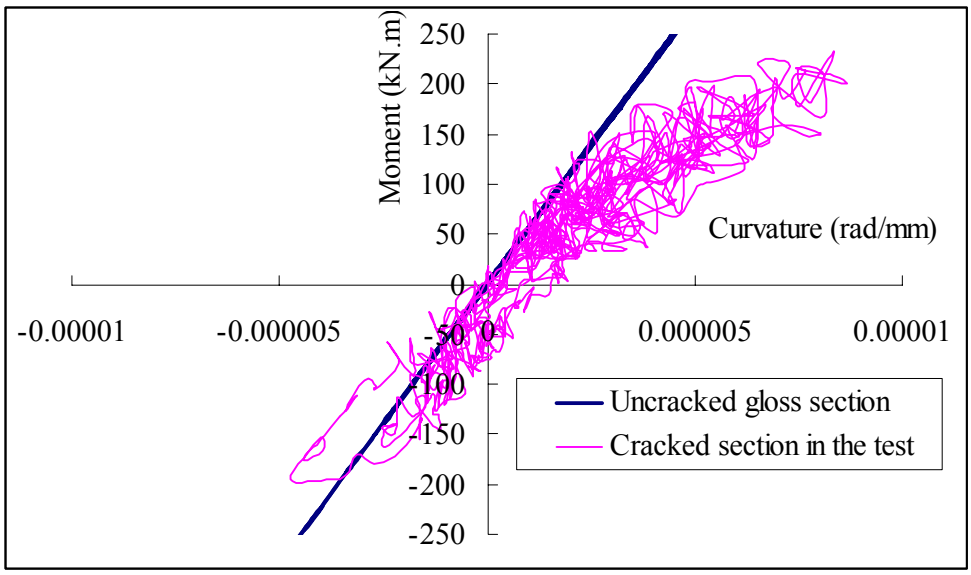

Figure 4.53 Moment-curvature curves of the control specimen (S1)

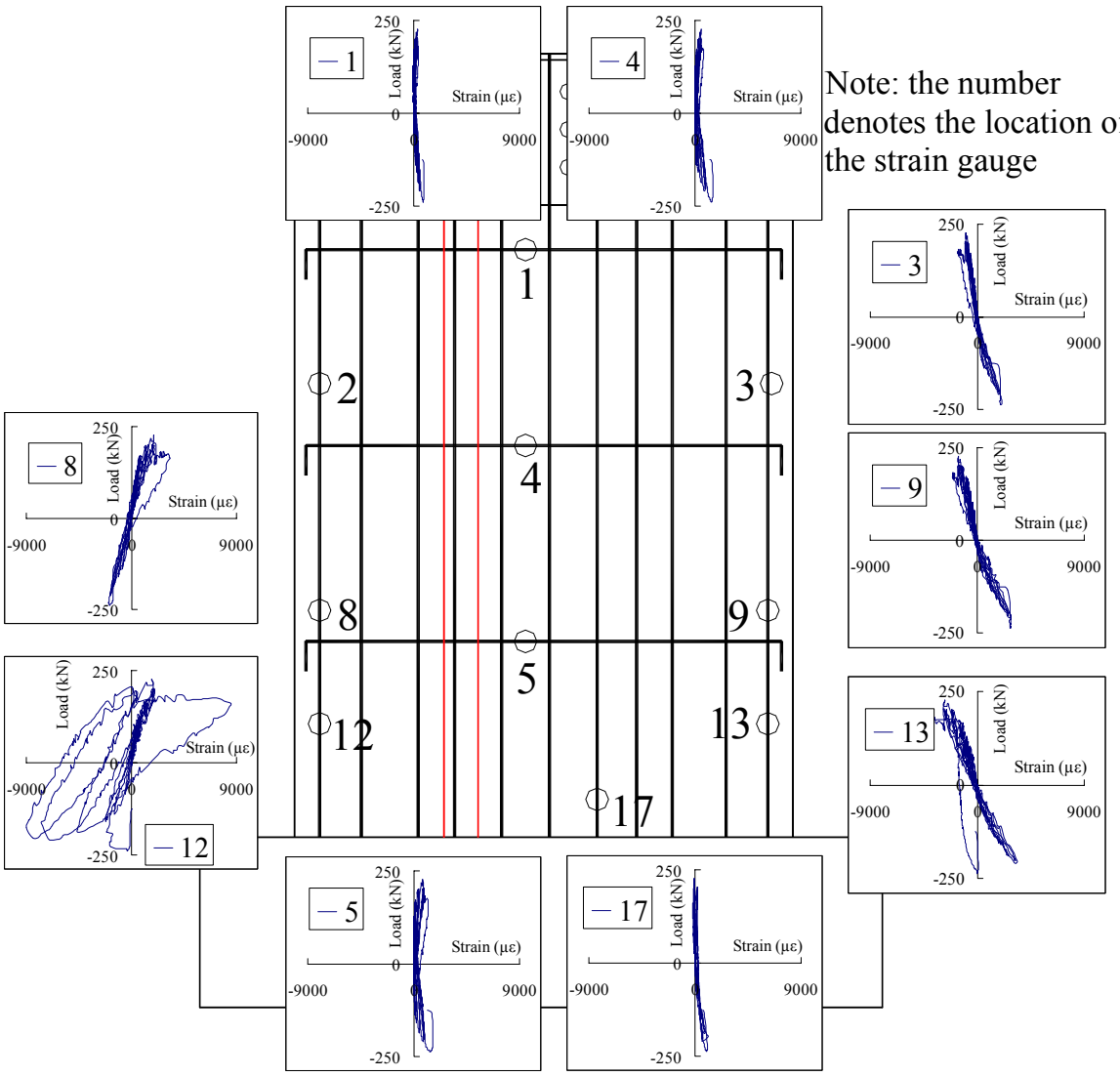

Figure 4.54 Load (kN) vs. strain in reinforcing bars (μ) curves at different locations (Specimen S2)

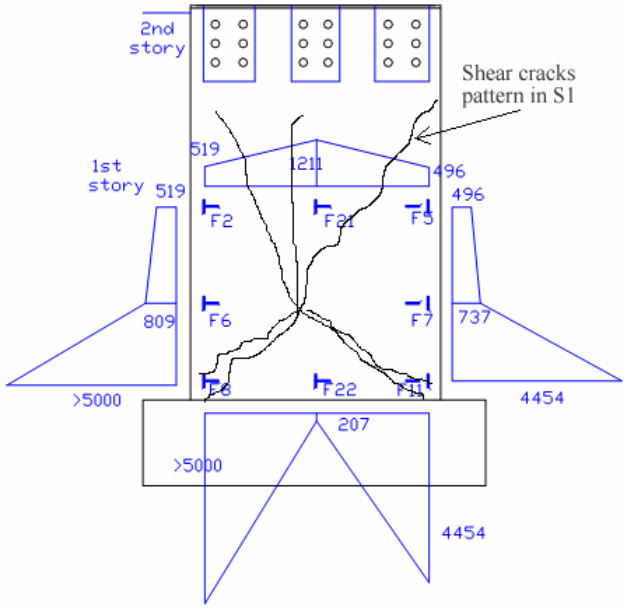

Figure 4.55 The maximum values of FRP strain gauge (micro strain) of the flange wall.

CHAPTER 5 DEVELOPMENT OF THE FEA MODELS FOR SHEAR WALLS

5.1. Introduction

With the initial stiffness reduction factor and unloading stiffness degradation parameter α and reloading stiffness degradation parameter β obtained in Chapter 4, and the bilinear factor *r* calculated according to Appendix A.5, a 2D (pushover and cyclic analysis) and a 3D (pushover analysis) nonlinear macroscopic FEA models are developed herein using RUAUMOKO for both specimens S1 and S2 (2.6-story model with height of 1.314m).

Because the current RUAUMOKO 3D version cannot perform 3D adaptive cyclic analysis, another software ABAQUS (Hibbit et al. 2003) was used to establish a 3D nonlinear microscopic FEA model for specimen S1 and S2 under cyclic loading.

5.2. FEA models using RUAUMOKO

Non-linear 2D/3D macroscopic FEA models using the computer program RUAUMOKO (Carr 2002a, 2002b) were developed to simulate the test specimens (2.6-story model with height of 1.314m) under pushover and cyclic loading. Since there is no shear wall element in the current RUAUMOKO version, the I-shape shear wall was simulated as equivalent columns connected by horizontal rigid links (as shown in Figure 5.1). The I-shape shear wall was divided into five rectangular walls: two left flange walls, two right flange walls and one web wall. Each rectangular wall

was represented by an equivalent column located at the middle. Rigid links were simulated as very rigid beams to connect the equivalent columns. For 2D modeling, the two left flange walls were combined into one equivalent column, and similarly the two right flange walls.

FRP was not simulated in the FEA model, but the enhancement of concrete due to FRP confinement was considered macroscopically, so that the section of FRP retrofitted structure has the larger yield moment and bilinear factor.

5.2.1. 2D FEA modeling

5.2.1.1. FEA meshing

Figure 5.2 shows the number of elements, nodes and sectional properties of the 2D FEA model. Three columns and four horizontal rigid links were used to simulate the I-shape shear wall in 2D (as shown in Figure 5.1). Equivalent columns were simulated using frame-type, concrete beam-column member (Elements 1-3), and rigid links were simulated using frame-type, one-component (Giberson) beam member (Elements 4-7). The inelastic flexural behavior of these two selected frame-type elements follows the concept of the Giberson one-component model, which has been discussed in Chapter 3.

5.2.1.2. Member properties

Totally four different sectional properties were defined (as shown in Figure 5.2). Sections 1 to 3 define the sectional properties of the equivalent columns and section 4 defines sectional properties of the rigid links.

Elastic (Young's) modulus of the concrete was obtained from the test (E=22.92GPa for specimen S1 and E=20.89GPa for specimen S2). Shear modulus, cross-sectional area, effective shear area were calculated according to Appendix A.1. The effective moment of inertia I was calculated by multiplying the moment of inertia of the gross section by the reduction factor obtained from the test (0.8 for shear walls). The lengths of plastic hinges were taken as 1.0h for equivalent columns as specified in Chapter 3. The input values of the elastic sectional properties for specimens S1 and S2 are listed in Tables 5.1 and 5.2, respectively.

The concrete compressive strength (31.71 MPa for specimen S1 and 27.58 MPa for specimen S2) and reinforcing bar strength (460 MPa for edge deformed bars with diameter of 10 mm, 525 MPa for BRC high strength round bars with diameter of 8 mm, and 250 MPa for transverse bars) were obtained from the test.

The contribution of reinforcing bars was through the calculation of yield moment of the sections based on ACI code (ACI318 2002). The seven parameters (*PYC*, *PB*, *MB*, *M1B*, *M2B*, *M0* and *PYT*) for specimen S1 to define the axial load-moment interaction yield surface of columns were calculated according to Appendix A.2. And the corresponding parameters for specimen S2 were based on Appendix A.2 and A.6. Values of these parameters for specimen S1 and S2 are listed

in Tables 5.3 and 5.4, respectively. For the rigid link element (section 4), a very large yield moment (like 1000 kN.m) was used, because the function of the horizontal rigid links is to transfer forces among equivalent columns, and thus should not be subjected to any flexural failure.

The stiffness degradation was considered by defining hysteresis rules. The Modified Takeda Hysteresis model was adopted here, and the parameters $\alpha = 0.5, \beta = 0.7$ of this hysteresis rule were obtained from the shear wall test as specified in Chapter 4. The bilinear factor *r* for each section of specimen S1 was calculated according to Appendix A.5 and listed in Table 5.1. The procedure to calculate bilinear factor *r* for FRP-wrapped section, which is given in Appendix A.5 and A.6, has some difference from that for non-FRP-wrapped section, because it consider the improvement of concrete due to FRP confinement. The calculated *r* values for each section of specimen S2 are listed in Table 5.2.

5.2.1.3. Boundary condition

The boundary condition of the base of columns (Nodes 1-3) was simulated as fixed ends. The nodes on the top (actuator height or 2.6 floor level) were slaved for x translation (Nodes 4, 5, 7 and 8 were slaved to master Node 6).

5.2.1.4. Vertical and lateral loads

Vertical prestressing loads on the top of the shear wall were considered as the initial prestress concentrate loads in Elements 1-3, when member properties were defined. The initial force is -118.48 kN in section 1, -259.17 kN in section 2 and -236.80 kN in section 3. The vertical gravity loads were input as node loads in LOAD option. Mass was input in WEIGHT option as a lump mass at master Node 6.

Lateral load was applied at master Node 6. For pushover test, adaptive pushover analysis was performed and the lateral loads were increased step by step, until the displacement at node 6 reached the measured displacement corresponding to the maximum applied load in the test. For cyclic test, adaptive cyclic analysis was performed, and lateral loads were applied in the form of displacement control. This control displacement history was input in EQUAKE option. In order to consider the P-Δ effect induced by the gravity load and lateral load, large displacement option was used.

5.2.2. 3D FEA modeling

5.2.2.1. FEA meshing

Only the adaptive pushover FEA analysis has been conducted because the current RUAUMOKO 3D version cannot perform 3D adaptive cyclic analysis. Figure 5.3 shows the number of elements, nodes and sectional properties of the 3D FEA model. Five equivalent columns and ten horizontal rigid links were used to simulate

the I-shape shear wall in 3D (as shown in Figure 5.1). Two 3D frame-type elements (as shown in Figure 5.4) were used: concrete beam-column member and one-component beam member (Carr 2002b). The inelastic flexural behavior of these two frame-type elements follows the concept of the Giberson one-component model as discussed in Chapter 3. Equivalent columns were simulated using frame-type, concrete beam-column member (Elements 1-5), and rigid links were simulated using frame-type, one-component (Giberson) beam member (Elements 6-15).

According to the details of members, four different sectional properties were defined. The number of sectional properties is also shown with the corresponding elements in Figure 5.3. Sections 1-3 define the sectional properties of equivalent columns, and section 4 defines the sectional properties of rigid links. In the next section, parameters of the sectional properties in 3D dimension will be described in detail.

5.2.2.2. Member properties

The definition of a cross section in 3D dimension involves elastic section properties (elastic Young modulus, shear modulus, cross-sectional area, initial effective moment of inertia, and weight of the member), initial force (prestressed load or self-weight), yield surfaces and hysteresis rules. The details of the input values are as follows:

Elastic sectional properties

Elastic (Young's) modulus of the concrete was obtained from the test, and shear modulus, cross-sectional area, effective shear area were calculated using the formula given in Appendix C. The torsional 2nd moment of area of section in the x-x direction J_{xx}, moment of inertia in the z-z direction I_{zz}, and moment of inertia in the y-y direction I_{yy} were calculated by multiplying the corresponding value of the gross section by the reduction factor obtained from the test (0.8 for shear walls). The effective shear areas in y and z direction were calculated based on Appendix A.1. The weight/unit length (WGT) was taken as 0, and the contribution of distributed weight was considered as the corresponding node weight. Values of the elastic sectional properties of specimen S1 and specimen S2 are listed in Tables 5.5 and 5.6, respectively. Moment of inertia of the rigid links (section 4) was taken as a large value, for example 1, to keep the rigidity of such links.

End condition

The end conditions of all members were assumed as 'built-in to joint'. In other words, the rotations of members at the joint region were assumed to be equal to the adjoining members. The lengths of plastic hinges were taken as 1.0h for columns and 0.5h for beams as discussed in Chapter 3.

Yield surface of the members

The properties of concrete and steel reinforcing bar were obtained from the test, as specified in the above mentioned 2D FEA modeling. The contribution of reinforcing bars was through the calculation of yield moment of the sections. The parameters to define the 3D axial load-moment interaction yield surface for columns are different from the 2D yield surface. The method to calculate the five parameters (*PC*, *PB*, *MBz*, *MBy* and *PT*) used to define the interaction yield surface for specimen S1 is given in Appendix C.2. Values of these parameters for specimen S1 are listed in Tables 5.7. For the rigid links (section 4), a large yield moment (like 1000 kN.m) was used.

The method to calculate the yield surface for FRP-wrapped specimen S2 has some difference with that for control specimen S1, because the enhancement of yield moment and bilinear factors due to FRP confinement was accounted for. The parameters for specimen S2 were calculated according to Appendix A.6 and Appendix C.2. Values of these parameters for specimen S2 are listed in Tables 5.8.

Hysteresis rule

The stiffness degradation was considered by defining hysteresis rules. The Modified Takeda Hysteresis model (as shown in Figure 1.3) was adopted, and the unloading stiffness degradation parameter $\alpha = 0.5$ and reloading stiffness degradation parameter $\beta = 0.7$ for this hysteresis rule were obtained from the test. The bilinear factor *r* for each section of specimen S1 was calculated according to Appendix A.5 and listed in Table 5.5. And *r* for each section of specimen S2 was

calculated according to Appendix A.5 and A.6 and listed in Table 5.6, by accounting for the enhancement of concrete due to FRP confinement.

5.2.2.3. Boundary condition

Boundary conditions of the base of columns (Nodes 1-5) were simulated as fixed ends. Nodes on the top (actuator height or 2.6 floor level) were slaved for x direction translation ,y direction translation and about z-z rotation to master Node 17, which is located at the center of mass (CM) of the I-shape wall at the top plane.

5.2.2.4. Vertical and lateral loads

Vertical prestressing loads on the top of the shear wall were considered as the initial concentrate loads in Elements 1-5 when member properties were defined. Mass was applied as a concentrated mass at the master Node 17, and the vertical gravity loads were applied on columns at Nodes 1-5. Lateral load was applied at master Node 17. For the pushover test, adaptive pushover analysis was performed and pushing lateral loads were increased step by step, until the displacement at node 17 reached the measured displacement corresponding to the maximum applied load in the test.

5.2.3. Comparison of FEA results using RUAUMOKO with experimental results

5.2.3.1. Load-displacement curves for control specimen S1

Figure 5.5 compares the load- top displacement (actuator level) curves between test and the 2D and 3D pushover analysis using RUAUMOKO. As can be seen from Figure 5.5, the results of the FEA form the backbone of the hysteresis curves of the test, and the 2D FEA curve matches well with the 3D FEA curve. This means the proposed 2D and 3D FEA model is able to predict well the load-displacement behavior of the control specimen test with the same accuracy.

Figure 5.6 compares the load- top displacement (actuator level) curves between the test and the 2D pushover and cyclic FEA results. As can be seen from Figure 5.6, the 2D FEA pushover curve represents the backbone of 2D FEA cyclic curve quite well, and the FEA results match the test results well. Figure 5.7 shows the cycle by cycle comparison of load-displacement curves between the test and the 2D cyclic FEA. Good match between the test results and the 2D FEA cyclic model confirms that the proposed 2D FEA cyclic model is reliable for predicting the hysteresis performance of the control specimen under cyclic loading.

5.2.3.2. Load-displacement curves for FRP retrofitted specimen S2

Figure 5.8 compares the load- top displacement (actuator level) curves between test and the 2D and 3D pushover analysis using RUAUMOKO. As can be seen from

Figure 5.8, the results of the FEA form the backbone of the hysteresis curves of the test, and the 2D FEA curve matches well with the 3D FEA curve. This means the proposed 2D and 3D FEA model is able to predict well the load-displacement behavior of the FRP retrofitted specimen test with the same accuracy.

Figure 5.9 compares the load- top displacement (actuator level) curves between the test and the 2D pushover and cyclic FEA results. As can be seen from Figure 5.9, the 2D FEA pushover curve represents the backbone of 2D FEA cyclic curve quite well, and the FEA results match the test results well. Figure 5.10 shows the cycle by cycle comparison of load-displacement curves between the test and the 2D cyclic FEA. Good match between the test results and the 2D FEA cyclic model confirms that the proposed 2D FEA cyclic model is reliable for predicting the hysteresis performance of the FRP retrofitted specimen under cyclic loading.

5.3. FEA modeling using ABAQUS

Due to the limitation of RUAUMOKO, the 3D FEA model under cyclic loading could not be established. As an alternative, another software ABAQUS (Hibbit et al. 2003) was used to establish a 3D nonlinear microscopic FEA model for specimen S1 and S2 under cyclic loading.

In the following section, non-linear 3D FEA models using ABAQUS are described. A damaged plasticity-based concrete model was used to capture the behavior of concrete under cyclic loading. A method to identify shear failure of RC shear wall was proposed. In the FEA model of FRP retrofitted specimen S2, SPRING

element was used to simulate the constraint deformation due to FRP system, and an improved concrete stress-strain curve was considered to account for the enhancement in concrete strength and ductility under FRP confinement. The proposed model is able to predict reasonably well, the shear failure and cyclic hysteresis behavior of RC shear wall with and without FRP retrofitting.

5.3.1. FEA modeling of the control specimen (S1) test

A total of 220 elements of C3D8R type (8 node solid brick elements with one Gaussian integration point) were used to model the test wall. The 3D view of the meshing of the RC wall is shown in Figure 5.11. Steel reinforcing bars in the concrete wall were modeled as one-directional strain elements (rods) and were simulated by REBAR option. In ABAQUS, when REBAR option is used, the steel reinforcing bars will be superposed on a mesh of standard element types, like C3D8R type element. The behavior of concrete is considered independent of the reinforcing bars. The effects associated with the reinforcing bar-concrete interface, like bond slip and dowel action, are normally modeled approximately by introducing some “tension stiffening” into the concrete modeling. The reinforcing bars were superimposed onto the wall.

The boundary condition of the base of the wall was simulated as fixed end. In order to prevent out-of-plane displacement, roller supports were placed at the surface of 4 brick elements which represent the locations of the lateral supports in the test. A vertical pressure load was applied on the flange and web of the top elements to simulate the vertical load. Lateral concentrated point loads were applied on each of the

top node (actuator height or 2.6 floor level) on the flange walls to simulate the lateral cyclic displacement (the cyclic displacement history is shown in Figure 4.26).

Steel reinforcing bars were considered as elastic perfectly plastic material in both tension and compression. The uniaxial stress-strain curve of the steel bars is shown in Figure 5.12. Parameters of the steel material like yield strength, Young's modulus and ultimate strength were obtained from the test.

A new concrete model (Concrete Damaged Plasticity model) available in ABAQUS version 6.3 was used to simulate the behavior of concrete of the walls. This is a continuum, plasticity-based damage model for concrete. It assumes that the two main failure mechanisms are tensile cracking and compressive crushing of the concrete material, and that the uniaxial tensile and compressive response of concrete is characterized by damaged plasticity.

Under uniaxial tension, the stress-strain response follows a linear elastic relationship until the failure stress σ_{t0}, which represents the onset of micro-cracking in the concrete material. Beyond this failure stress, the formation of micro-cracks is represented macroscopically with a softening stress-strain response. On the other hand, under uniaxial compression the response is linear until the value of initial yield, σ_{c0}. In the plastic regime the response is typically characterized by stress hardening followed by strain softening beyond the ultimate stress, σ_{cu}. When the concrete specimen is unloaded from any point on the strain softening branch of the stress-strain curves, the unloading response is weakened and the elastic stiffness of the material is damaged.

The degradation of the elastic stiffness is characterized by two damage variables, d_t and d_c ($0 \le d_{t,} d_c \le 1$). Under cyclic loading conditions, the degradation mechanisms are quite complex, involving the opening and closing of previously formed micro-cracks and their interaction. The stiffness recovery effect, namely some recovery of the elastic stiffness as the load changes sign in cyclic test, is considered. The weight factors, w_t and w_c, control the recovery of the tensile and compressive stiffness upon load reversal, respectively. The factor w_c, which results in the recovery of the compressive stiffness, is more important because when the load changes from tension to compression, tensile cracks will close.

The whole model described above is shown in Figure 5.13. The stiffness recovery factors were chosen as the default values: $w_t = 0$ and $w_c = 1$. For the tension stiffening effect, CONRETE TENSION STIFFENING TYPE=STRAIN option (more suitable for concrete with reinforcement) was used and the reduction of concrete tensile strength to zero is assumed to occur at 10 times the strain at failure. Concrete compressive behavior is assumed to follow the Hognestad curve (Macgregor 2005). The parameters of concrete used in the FEA model like Young's module, compressive strength, were obtained from the test.

5.3.2. FEA modeling of the FRP wrapped specimen (S2)

SPRING element was used to model the constraint on deformation provided by wrapping FRP. A total of 525 SPRING elements were used. The stiffness of the

SPRING element was equal to that of the GFRP material (69.65GPa). The 3D view of the meshing of the wall is shown in Figure 5.14.

Since the concrete model in ABAQUS does not account for the enhancement of concrete due to the lateral confinement, the compression stress-strain curve of concrete proposed by Teng et. al. (2001), which considers the improvement of concrete strength and strain due to GFRP confinement, was adopted herein. The improved concrete stress-strain curve proposed by Teng et. al. (2001) is shown in Figure 5.15.

This improved stress-strain relationship (the parameters are denoted in Figure 5.15) is:

$$\begin{cases} \sigma_c = E_c\varepsilon_c - \dfrac{(E_c - E_2)^2}{4f_{co}'}\varepsilon_c^{\,2} & (0 \le \varepsilon_c \le \varepsilon_t) \\ \sigma_c = f_{co}' + E_2\varepsilon_c & (\varepsilon_t \le \varepsilon_c \le \varepsilon_{cc}) \end{cases} \tag{5.1}$$

Where

$$\varepsilon_t = \frac{2f_{co}'}{(E_c - E_2)}$$

$$E_2 = \frac{f_{cc}' - f_{co}'}{\varepsilon_{cc}}$$

$$\frac{\varepsilon_{cc}}{\varepsilon_{co}} = 2 + k_2\frac{f_l}{f_{co}'} \quad \text{(For E-glass FRP, } k_2 = 26.7\text{)}$$

$$f_l = \frac{2f_{frp}t_{frp}}{\sqrt{h^2 + b^2}}$$

$$\frac{f_{cc}'}{f_{co}'} = 1 + k_1k_s\frac{f_l'}{f_{co}'} \quad k_1 = 2 \quad \text{(Confinement effectiveness coefficient)}$$

$$f_l' = k_s f_l,$$

$$k_s = \frac{b}{h}\frac{A_e}{A_c}$$

$$\frac{A_e}{A_c} = \frac{1-[(b/h)(h-2R_c)^2+(h/b)(b-2R_c)^2]/(3A_g)-\rho_{sc}}{1-\rho_{sc}}$$

ρ_{sc} = Reinforcement bar ratio

R_c =20 mm, the corner radius in a rectangular column with rounded corners

b =Width of the rectangular concrete core

h =Height of the rectangular concrete core

According to Tan (2002), the whole concrete can be divided into several regions of concrete core separated by the internal transverse links, because the internal links provide additional anchor points and help in restraining the concrete from bulging out. Since the shear wall under investigation is an I-shape wall, FRP bolts were used to anchor the flange wall-web wall joints. Thus, FRP bolts can be considered as the internal transverse links, and I-shape wall can be divided into 4 rectangular regions as shown in Figure 5.16. Equation (5.1) was used to calculate the improved strength stress-strain curve for concrete of each region, for different region had different width and height. The calculated compression stress-strain curves of these four-region concrete are shown in Figure 5.17.

5.3.3. Parameters to identify failure in FEA study

The equations for shear given in ACI 318 code (2002) were used to identify the shear failure of the RC shear wall. Here, equations for shear capacity (shear force per area or shear pressure) are introduced.

For members subjected to additional axial compression force, the shear capacity of concrete is:

$$v_c = (1 + \frac{N_u}{14A_g})(\frac{\sqrt{f_c'}}{6}) \text{ MPa} \quad (5.2)$$

Where,

N_u = the axial compression force

A_g =the area of the cross section

The shear capacity provided by the transverse reinforcement is:

$$v_s = \frac{A_v f_y d}{s_2 A_s} \text{ MPa} \quad (5.3)$$

Where,

A_v=the area of transverse reinforcement within a vertical distance s_2 and horizontal distance d

A_s=the area of shear surface

The equation of shear capacity of FRP wrap derived by Triantafillou and Antonopoulos (2000) is:

$$v_f = 0.8 E_f \varepsilon_f \rho_f \text{ MPa} \quad (5.4)$$

Where,

E_f = Young's modulus of fiber

ε_f =effective FRP strain at failure which is calculated as 0.0025(FRP rupture) and 0.002(FRP debonding) (Kong 2004)

ρ_f =FRP shear reinforcement ratio, which is $\frac{2t_f}{t}$ for continuously bonded shear reinforcement with thickness t_f.

t_f =thickness of the fiber.

t =thickness of flange wall.

Thus, the shear capacity of reinforced concrete without FRP retrofitting can be calculated using:

$$v = v_c + v_s = (1 + \frac{N_u}{14A_g})(\frac{\sqrt{f_c'}}{6}) + \frac{A_v f_y d}{s_2 A_s} \tag{5.5}$$

The shear capacity of RC shear wall retrofitted using FRP can be calculated using

$$v = v_c + v_s + v_f = (1 + \frac{N_u}{14A_g})(\frac{\sqrt{f_c'}}{6}) + \frac{A_v f_y d}{s_2 A_s} + 0.8E_f \varepsilon_f \rho_f \tag{5.6}$$

For the control specimen (S1), the shear capacity of the RC flange wall was calculated as 1.80 MPa; for the FRP wrapped specimen (S2), the shear capacity of the RC flange wall was calculated as 1.74 MPa and the shear capacity before FRP debonding and FRP rupture were 3.49 MPa and 3.93 MPa, respectively. The details of shear capacity are listed in Table 5.9.

5.3.4. Correlation of FEA and experimental results

5.3.4.1. Stages of behavior

The behavior of test walls predicted by FEA at different load stages is described as follows and the comparison of FEA and test results are listed in Table 5.10.

For the control specimen (S1), the 1st shear crack (shear stress> shear capacity of reinforced concrete=1.80 MPa) occurred at 53.4 kN with a 0.71 mm displacement (the

1st cycle). The initial shear failure occurred in the flange wall is shown in Figure 5.18. As can be seen from Figure 5.18, the distribution of the shear stress corresponds to the formation of inclined shear failure cracks as observed in the test. The final shear failure of the wall occurred at 113.9 kN with a 1.73 mm displacement (in the 4th cycle) as shown in Figure 5.19, from which the shear failure region can be seen to have enlarged. The wall corner under compression was in the shear failure region, and at the same time this corner region had the maximum compressive stress as shown in Figure 5.20. The wall corner under compression would crush and fail in shear, under the high level of shear and compressive stress. This phenomenon matches well with the observation in the test: the concrete at wall corner crushed. There was no yielding of steel reinforcement observed in the ABAQUS analysis. However, in the test, there was only one yield point at 10 mm deform bar, when the top displacement was 11.23 mm and the corresponding load was 163.1 kN. This occurs very near to the failure load and that is the reason why ABAQUS did not predict any steel yielding.

For the FRP wrapped specimen (S2), the 1st shear crack (shear stress> shear capacity of reinforced concrete=1.74 MPa) occurred at 53.6 kN when the top lateral displacement was 0.75 mm (1st cycle). As shown in Figure 5.21, at this stage, the shear stress of some of the critical regions in the flange wall started to exceed the shear capacity of reinforced concrete, and the additional shear force would be sustained by FRP reinforcement. As shown in Figure 5.22, the first debonding of FRP (shear stress> shear capacity due to FRP debonding 3.49 MPa) occurred at the corner region of the shorter flange wall in the 3rd cycle (9 mm displacement cycle). However, the

debonding region was very small in the 3rd and 4th cycles (9 mm and 12 mm displacement cycles), this is why in the test no FRP debonding was observed until the 5th cycle (15 mm displacement cycle). In the 5th and 6th cycles (twice 15 mm displacement cycle), the regions of debonding developed dramatically as shown in Figure 5.23. As can be seen from Figure 5.23, the regions of debonding are mainly at the corner of the flange wall and the nearby regions, which matches well with the regions of debonding in the test. The final shear failure due to FRP rupture in the 7th cycle (30 mm displacement cycle) (shear stress> shear capacity due to FRP rupture 3.93 MPa) is shown in Figure 5.24. As can be seen from Figure 5.24, the FRP rupture regions are concentrated at the corners of flange wall and the nearby regions as what had been observed in the test. Thus, the proposed FEA model can predict well the shear failure of the test shear wall.

5.3.4.2. Global response

In the test shear wall specimen, micro-cracks exist due to shrinkage effects of concrete. Such micro-cracks will reduce the stiffness, including the initial stiffness and the stiffness in the process of loading, of the test specimen. As discussed in the previous chapters, the initial stiffness of the test specimen may be less than the uncracked theoretical section. In FEA using RUAUMOKO, such initial stiffness reduction is accounted for by reducing the input initial stiffness. However, in ABAQUS, initial stiffness is not a parameter for input and the initial stiffness of the uncracked theoretical section is used. Thus, such influence due to micro-cracks cannot

be simulated in FEA using ABAQUS. To justify this assumption, a comparison has been carried out, between the FEA using ABAQUS and the 3D FEA using RUAUMOKO without incorporating the initial stiffness reduction. As shown in Figure 5.25, the stiffness of the FEA result using ABAQUS is roughly the same with the FEA result using RUAUMOKO with the initial stiffness of the uncracked sections. This means that the initial stiffness in ABAQUS is for the uncracked section and the above assumption is justified. Therefore, when comparing the FEA results with the test results, the influence of the micro-cracks to the initial stiffness and resulted ultimate stiffness should be accounted for. For this purpose, the displacement of FEA needs to be amplified by a factor of 4, which was obtained by dividing the ultimate stiffness of test results by that of the FEA analysis.

The cycle by cycle comparison of load- top displacement (actuator height or 2.6 floor level) curves between the test and FEA for specimens S1 and S2 are shown in Figures 5.26 and 5.27, respectively. As can be seen from Figures 5.26 and 5.27, FEA modeling could predict the shape of the hysteresis force-displacement curves in a reasonable range. It is noted that the proposed FEA modeling underestimated the lateral force to some extent. However, considering the variation of materials in the test, such error is acceptable.

5.4. Summary

A 2D (pushover and cyclic analysis) and a 3D (pushover analysis) FEA macroscopic models using RUAUMOKO were developed for shear wall specimens

with and without FRP retrofitting. The FEA models were validated using the test results, to obtain a reliable FEA model for analysis of the full scale shear wall structures. It is shown that the FEA models for control specimen S1 could predict well the global and cyclic hesteresis behaviors. And the FEA models for FRP-wrapped specimen S2, by considering FRP confinement macroscopically, could predict well the global and cyclic hesteresis behavior of the shear wall structure retrofitted by FRP, and thus can be used for retrofitting projects primarily through wrapping FPR around columns or shear walls.

The initial stiffness reduction factor 0.8 was suggested for GLD shear wall structures. Unloading stiffness degradation parameter α and reloading stiffness degradation parameter β for the Modified Takeda Hysteresis model are suggested as: $\alpha = 0.5, \beta = 0.7$ for shear walls. The procedures of calculating bilinear factor *r* were validated by the test results. All these factors and parameters will be used in Chapter 6 to develop FEA models for full scale structures.

Furthermore, a 3D nonlinear microscopic FEA model using ABAQUS was developed for both specimens under cyclic loading. It is shown this model could predict the failure mode and the overall hysterestic behavior of GLD shear wall structures with and without FRP retrofitting, with reasonable accuracy. It provides a reasonable simulation method for FRP modeling and FEA modeling of concrete behavior, under cyclic loading.

Table 5.1 Parameters of elastic section properties and bilinear factor *r* (specimen S1, 2D FEA)

Section	E(kN/m^2)	G(kN/m^2)	A(m^2)	As(m^2)	I(m^4)	r
Section 1	2.29E+07	9.55E+06	1.98E-02	1.65E-02	6.35E-05	0.114
Section 2	2.29E+07	9.55E+06	4.30E-02	3.59E-02	5.81E-06	0.020
Section 3	2.29E+07	9.55E+06	3.94E-02	3.28E-02	5.02E-04	0.183

Table 5.2 Parameters of elastic section properties and bilinear factor *r* (specimen S2, 2D FEA)

Section	E(kN/m^2)	G(kN/m^2)	A(m^2)	As(m^2)	I(m^4)	r
Section 1	2.09E+07	8.70E+06	1.98E-02	1.65E-02	6.35E-05	0.199
Section 2	2.09E+07	8.70E+06	4.30E-02	3.59E-02	5.81E-06	2.13E-05
Section 3	2.09E+07	8.70E+06	3.94E-02	3.28E-02	5.02E-04	0.217

Table 5.3 Parameters to define the axial load-moment interaction yield surface (specimen S1, 2D FEA)

Section	*PYC*	*PB*	*MB*	*M1B*	*M2B*	*M0*	*PYT*
Section 1	-671.41	-443.81	16.39	21.68	24.28	17.08	256.54
Section 2	-1005.74	-394.52	5.10	4.60	3.74	1.69	84.78
Section 3	-1246.23	-898.82	51.88	72.60	69.38	40.18	414.79

Note: the unit for *PYC*, *PB* and *PYT* is kN, and for *MB*, *M1B*, *M2B* and *M0* is kN.m.
Compressive force is negative while tensile force is positive

Table 5.4 Parameters to define the axial load-moment interaction yield surface (specimen S2, 2D FEA)

Section	*PYC*	*PB*	*MB*	*M1B*	*M2B*	*M0*	*PYT*
Section 1	-734.59	-628.95	16.17	27.36	27.51	16.88	256.54
Section 2	-1088.93	-512.58	6.50	5.96	4.44	1.68	84.78
Section 3	-1331.62	-1203.57	51.45	90.25	81.18	39.09	414.79

Table 5.5 Parameters of elastic section properties and bilinear factor *r* (specimen S1, 3D FEA)

Section	E(kN/m^2)	G(kN/m^2)	A(m^2)	J_{xx}(m^4)	I_{zz}(m^4)	I_{yy}(m^4)	r
Section1	2.29E+07	9.55E+06	0.0099	4.57E-06	3.17E-05	1.33E-06	0.114
Section2	2.29E+07	9.55E+06	0.0197	9.97E-06	2.51E-04	2.66E-06	0.183
Section3	2.29E+07	9.55E+06	0.0430	2.32E-05	5.81E-06	2.63E-03	0.020

Table 5.6 Parameters of elastic section properties and bilinear factor *r* (specimen S2, 3D FEA)

Section	E(kN/m^2)	G(kN/m^2)	A(m^2)	J_{xx}(m^4)	I_{zz}(m^4)	I_{yy}(m^4)	r
Section1	2.09E+07	8.70E+06	0.0099	4.57E-06	3.17E-05	1.33E-06	0.173
Section2	2.09E+07	8.70E+06	0.0197	9.97E-06	2.51E-04	2.66E-06	0.241
Section3	2.09E+07	8.70E+06	0.0430	2.32E-05	5.81E-06	2.63E-03	0.001

Table 5.7 Parameters to define the axial load-moment interaction yield surface (specimen S1, 3D FEA)

Section	*PC* (kN)	*PB* (kN)	*MBz*(kN.m)	*MBy*(kN.m)	*PT* (kN)
Section 1	-335.70	-84.61	12.38	0.89	128.27
Section 2	-623.11	-222.18	38.88	1.77	207.40
Section 3	-1005.74	-488.70	4.07	127.02	84.78

Note: Compressive force is negative while tensile force is positive

Table 5.8 Parameters to define the axial load-moment interaction yield surface (specimen S2, 3D FEA)

Section	*PC* (kN)	*PB* (kN)	*MBz*(kN.m)	*MBy*(kN.m)	*PT* (kN)
Section 1	-367.29	-125.28	14.14	1.26	128.27
Section 2	-665.81	-291.20	39.62	2.38	207.40
Section 3	-1088.93	-630.03	5.23	156.24	84.78

Table 5.9 Shear capacity of the shear wall

Specimen and location		Shear capacity(MPa)
Reinforced Concrete(S1)	Web wall	1.23
	Flange wall	1.8
Reinforced Concrete(S2)	Web wall	1.16
	Flange wall	1.74
FRP rupture (S2)	Web wall	3.35
	Flange wall	3.93
FRP debonding (S2)	Web wall	2.91
	Flange wall	3.49

Table 5.10 Comparison between experiment and FEA

Specimen	Parameters	Test	FEA	FEA/Test
Control specimen (S1)	1st crack load	69.3kN (1st cycle)	54.4kN (1st cycle)	0.79
	1st yield load	163.04kN	-	-
	Ultimate load	183.96kN (4th cycle)	113.9kN (4th cycle)	0.62
	Stiffness at ultimate load	183.96/11.64 =15.8kN/mm	113.9/1.733 =65.72kN/mm	4.16
	Stiffness at 1st crack	69.3/3 =23.1kN/mm	54.4/0.71 =76.64kN/mm	3.32
	Failure mode	Diagonal shear failure along flange wall	Diagonal shear failure along flange wall	-
FRP wrapped specimen (S2)	1st crack load	N.A.	53.6kN(1st cycle)	-
	1st yield load	192.52kN	-	-
	Ultimate load	238.38kN (7th cycle)	145. 8kN (5th cycle)	0.61
	Stiffness at ultimate load	238.38/21.35 =11.17kN/mm	145. 8/3.74 =38.98kN/mm	3.49
	Stiffness at 1st crack	N.A.	54.4/0.75 =72.56kN/mm	-
	Failure mode	Shear failure with FRP debonding followed by FRP rupture	Shear failure with FRP debonding followed by FRP rupture	-

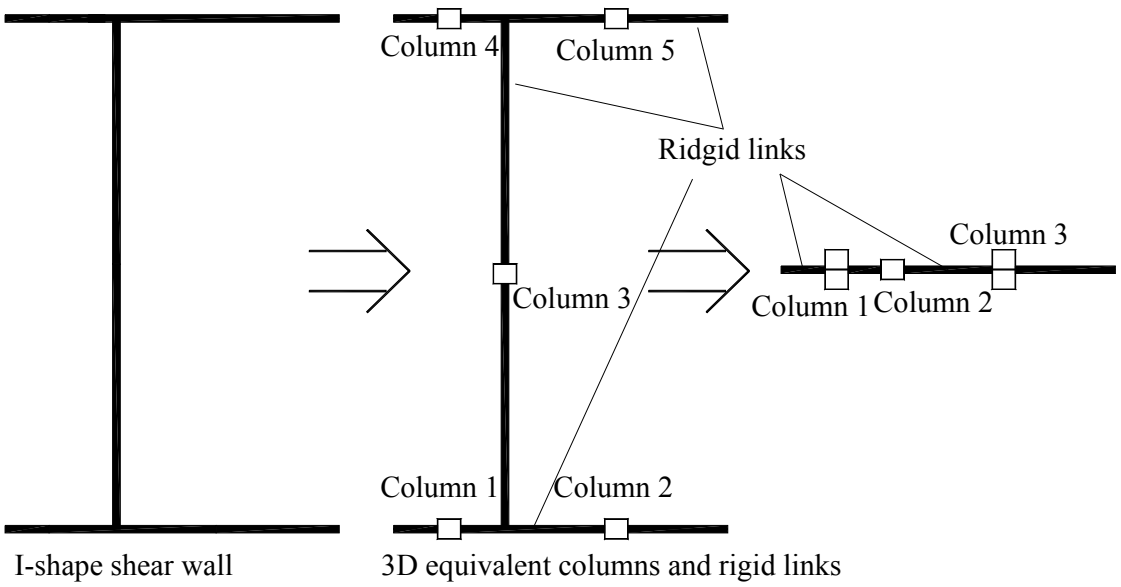

Figure 5.1 Representation of the I-shape shear wall using columns and rigid links in 3D and 2D dimension (plane view)

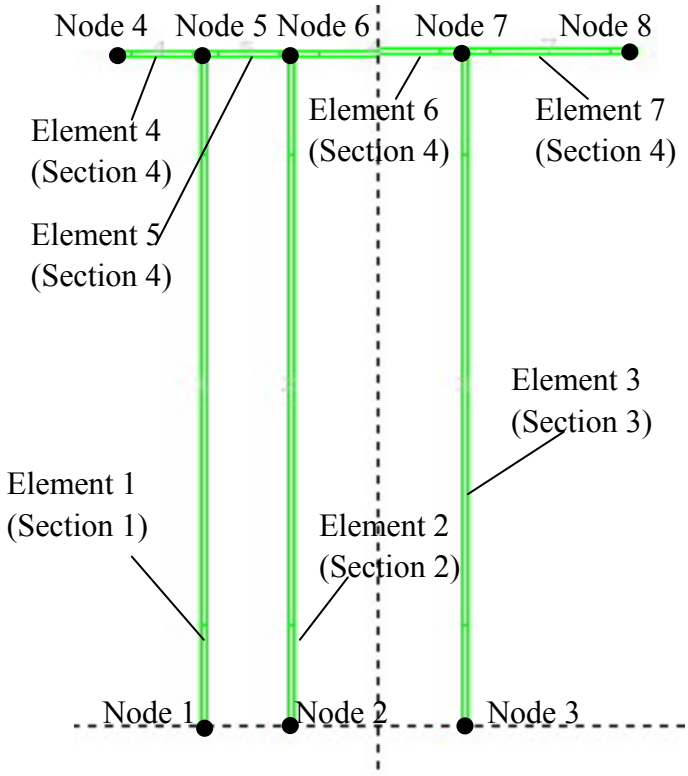

Figure 5.2 Nodes, elements and sectional properties of the 2D FEA modeling (elevate view)

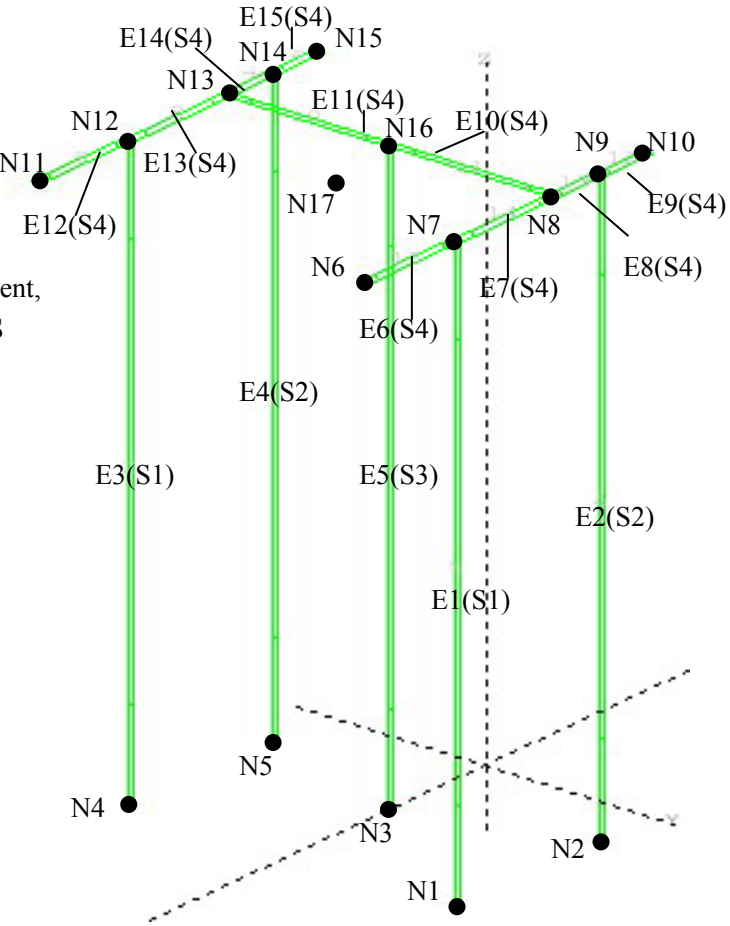

Note: E denotes element, N denotes node and S denotes the sectional property

Figure 5.3 Nodes, elements and sectional properties of the 3D FEA modeling

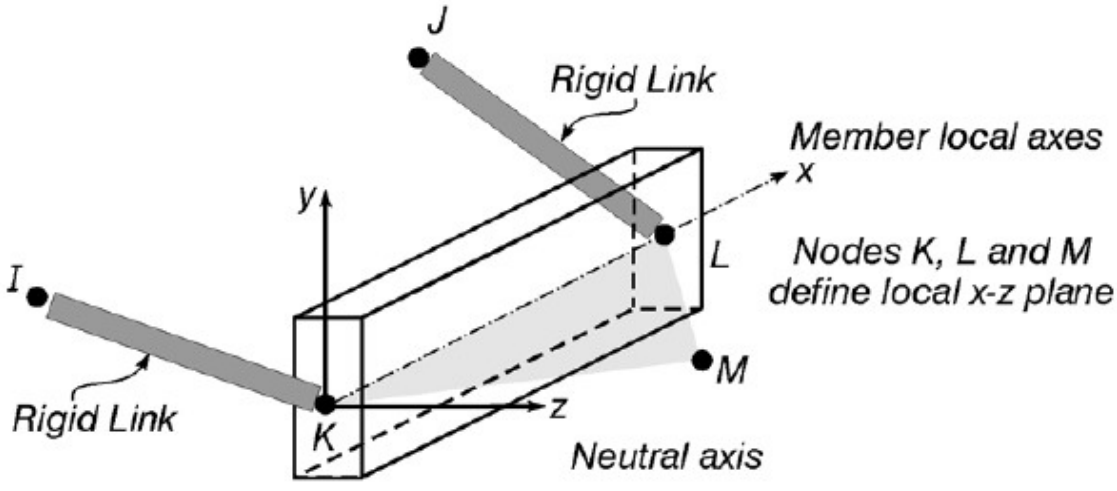

Figure 5.4 The frame element in RUAUMOKO 3D versionc(Carr 2002b)

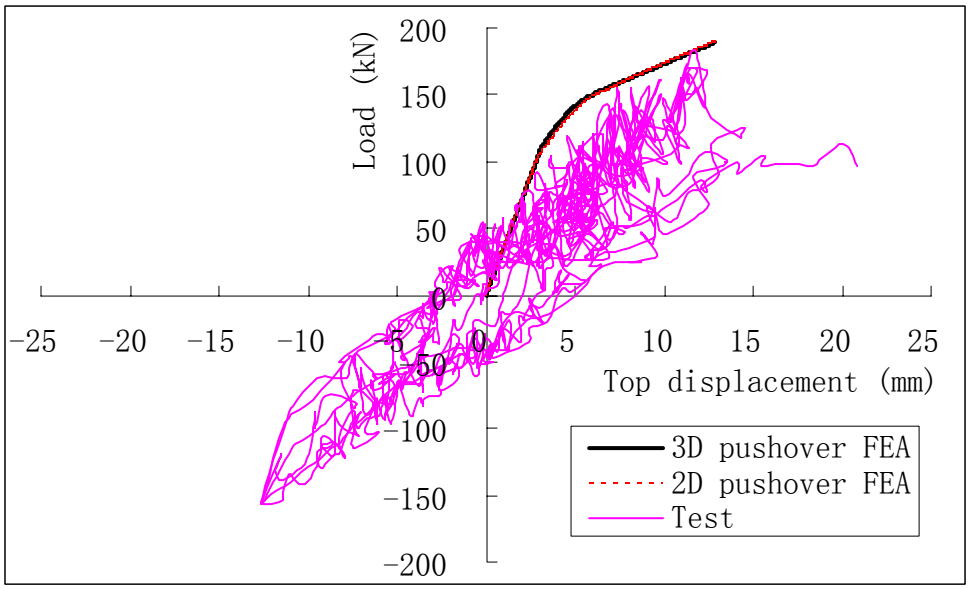

Figure 5.5 Comparison of results for specimen S1 between the pushover FEA using RUAUMOKO (2D and 3D) and the cyclic test

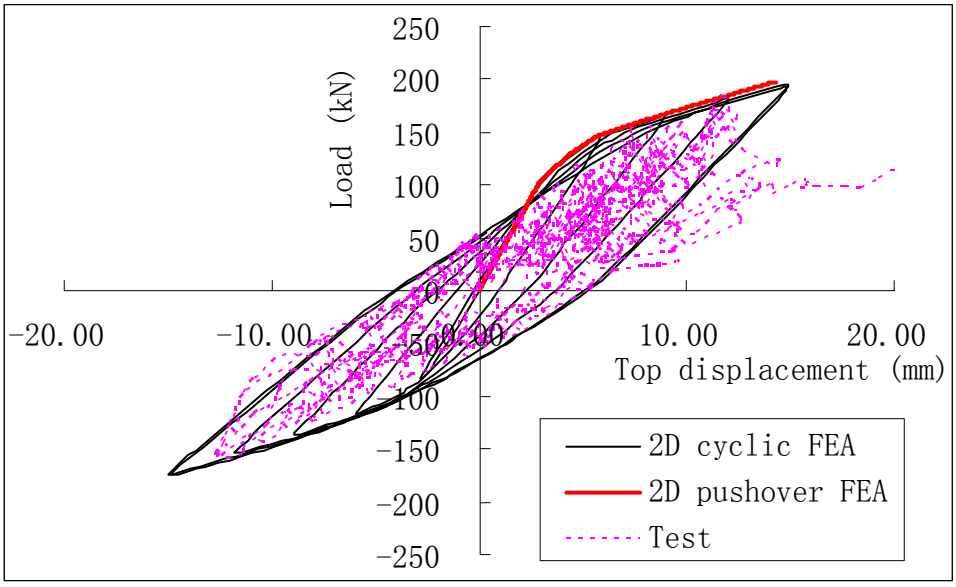

Figure 5.6 Comparison of results for specimen S1 between the test and the FEA using RUAUMOKO (2D pushover and cyclic analysis)

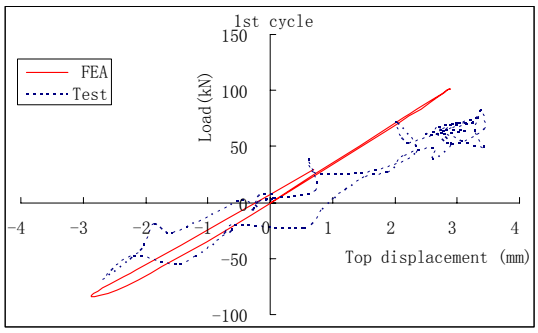

(a)1st cycle

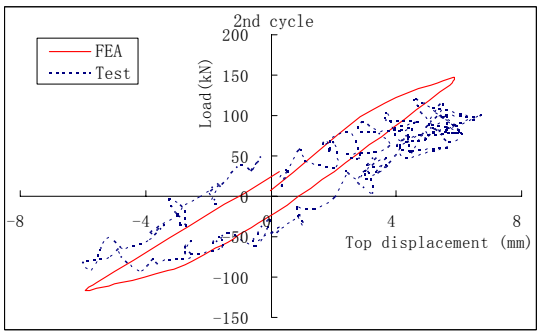

(b)2nd cycle

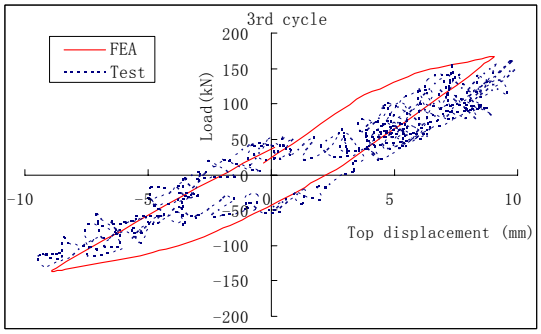

(c)3rd cycle

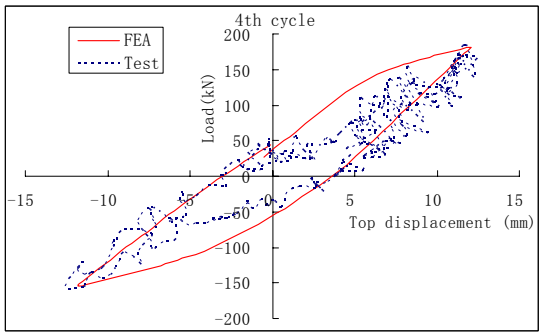

(d)4th cycle

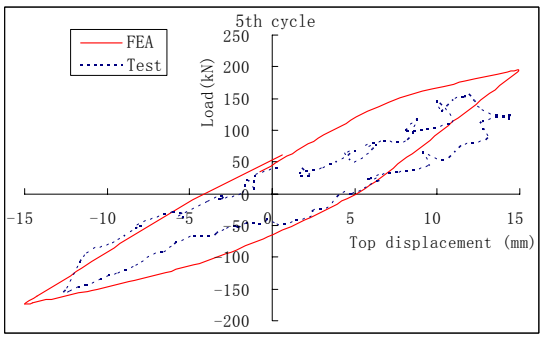

(e)5th cycle

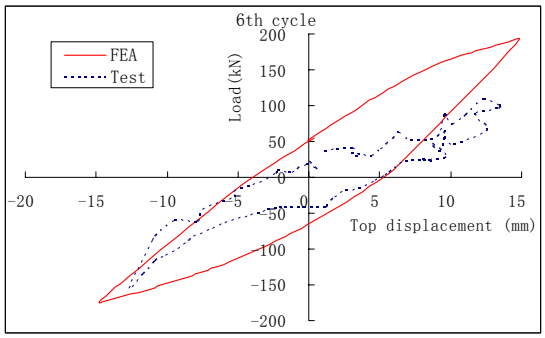

(f)6th cycle

Figure 5.7 Cycle by cycle comparison between the test and 2D cyclic FEA using RUAUMOKO for specimen S1

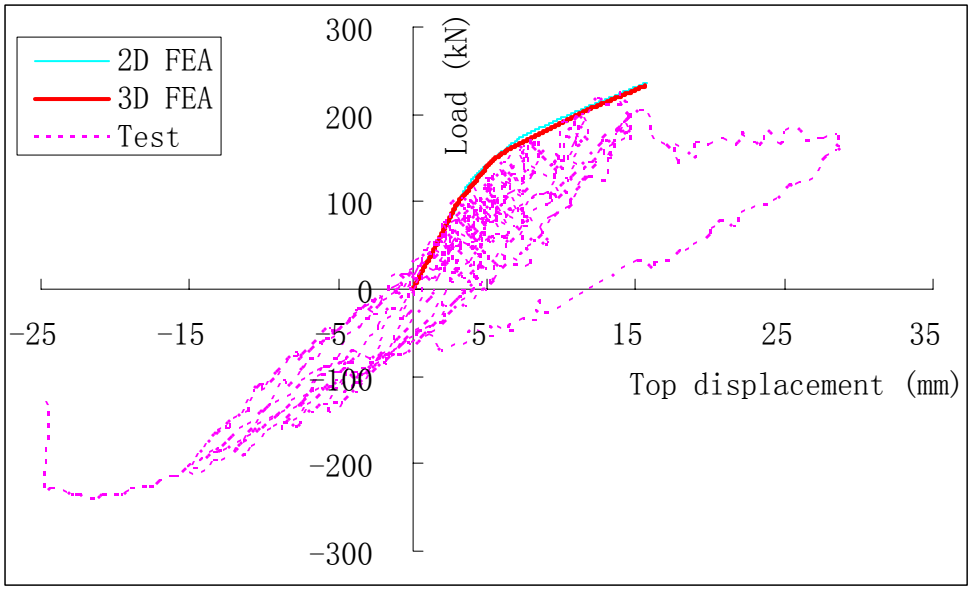

Figure 5.8 Comparison of results for FRP retrofitted specimen S2 between the pushover FEA using RUAUMOKO (2D and 3D) and the cyclic test.

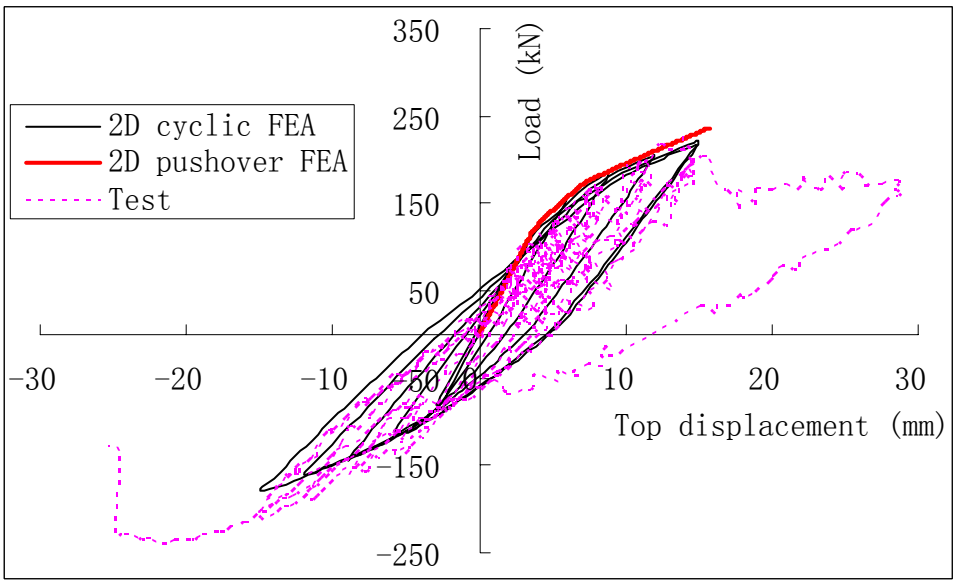

Figure 5.9 Comparison of results for specimen S2 between the test and the FEA using RUAUMOKO (2D pushover and cyclic analysis).

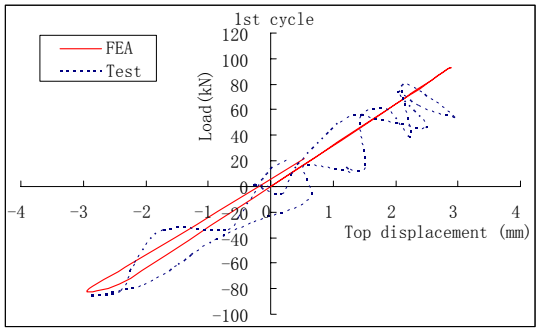

(a)1st cycle

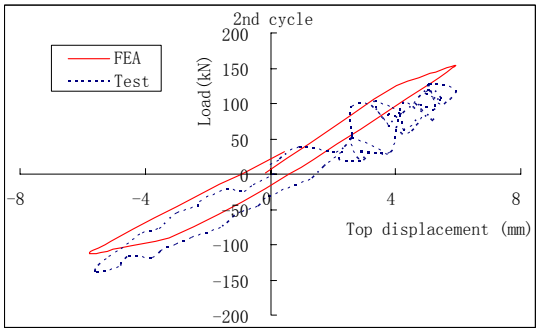

(b)2nd cycle

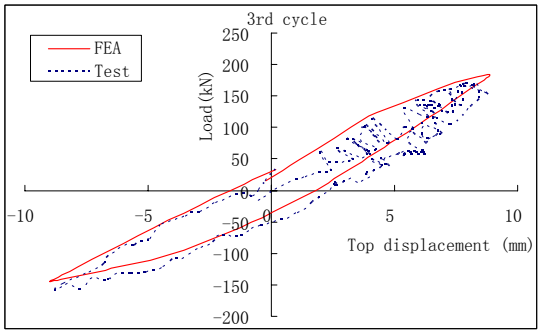

(c)3rd cycle

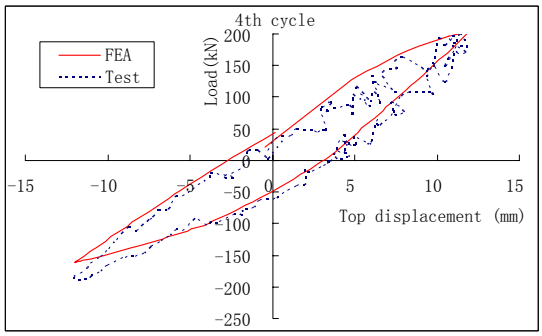

(d)4th cycle

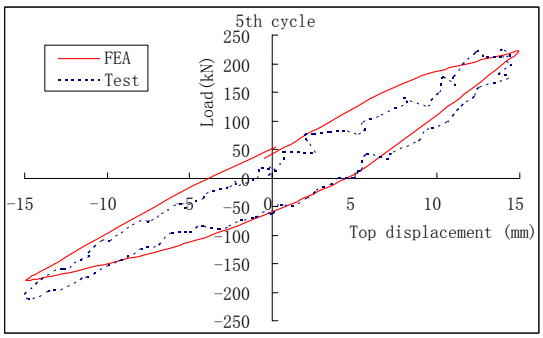

(e)5th cycle

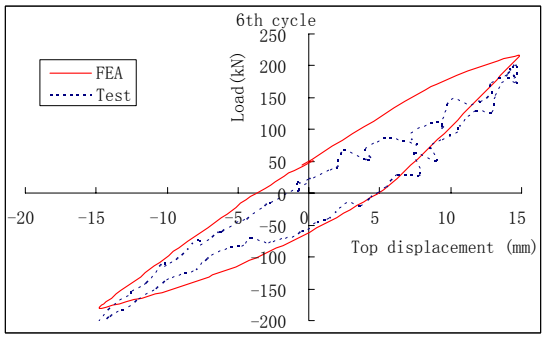

(f)6th cycle

Figure 5.10 Cycle by cycle comparison between the test and 2D cyclic FEA using RUAUMOKO for the specimen S2

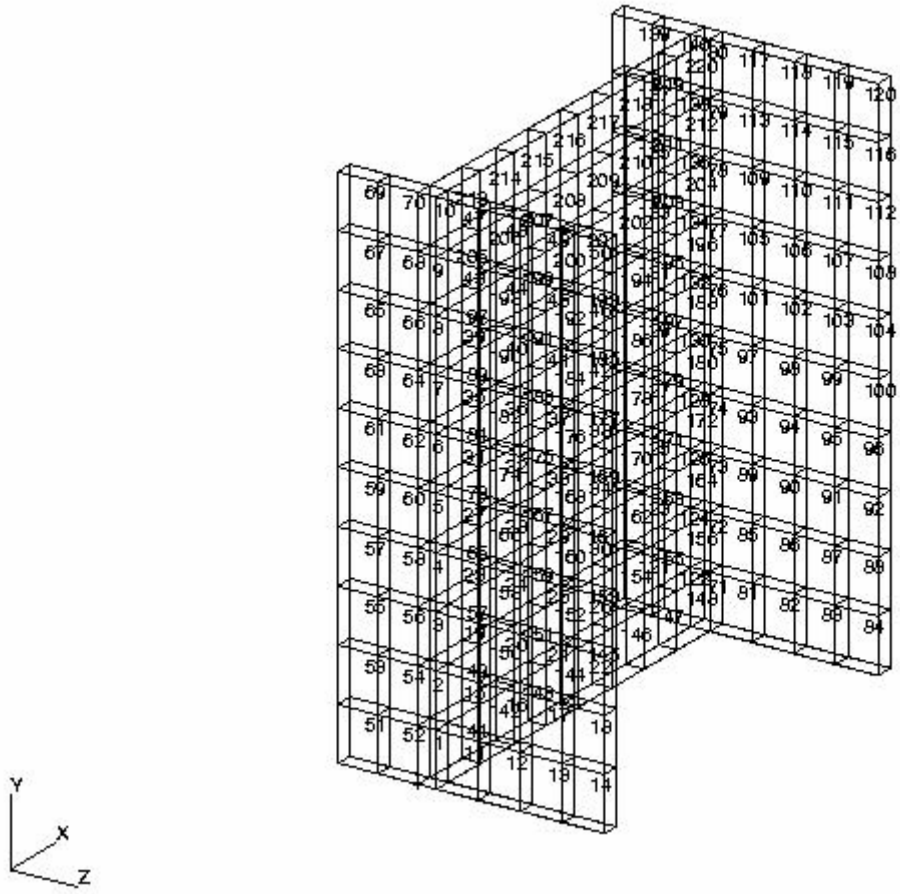

Figure 5.11 3D view of the modeling of the control wall (S1)

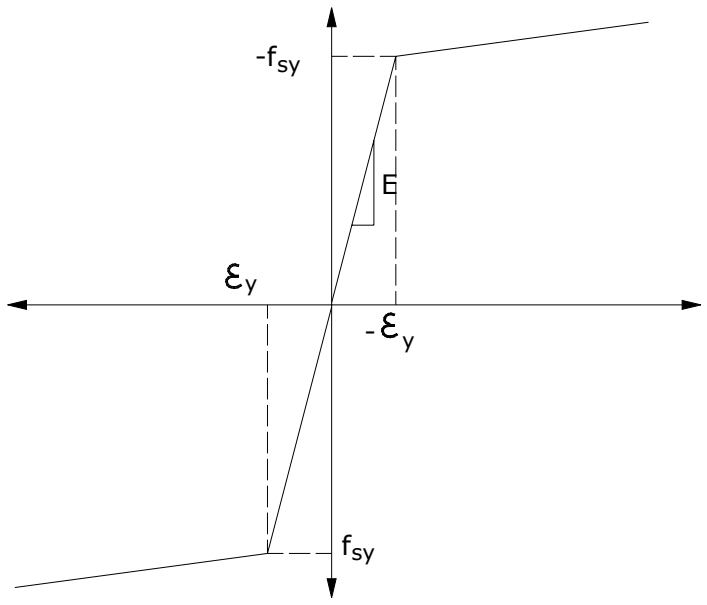

Figure 5.12 The stress-strain curve for steel used in ABAQUS

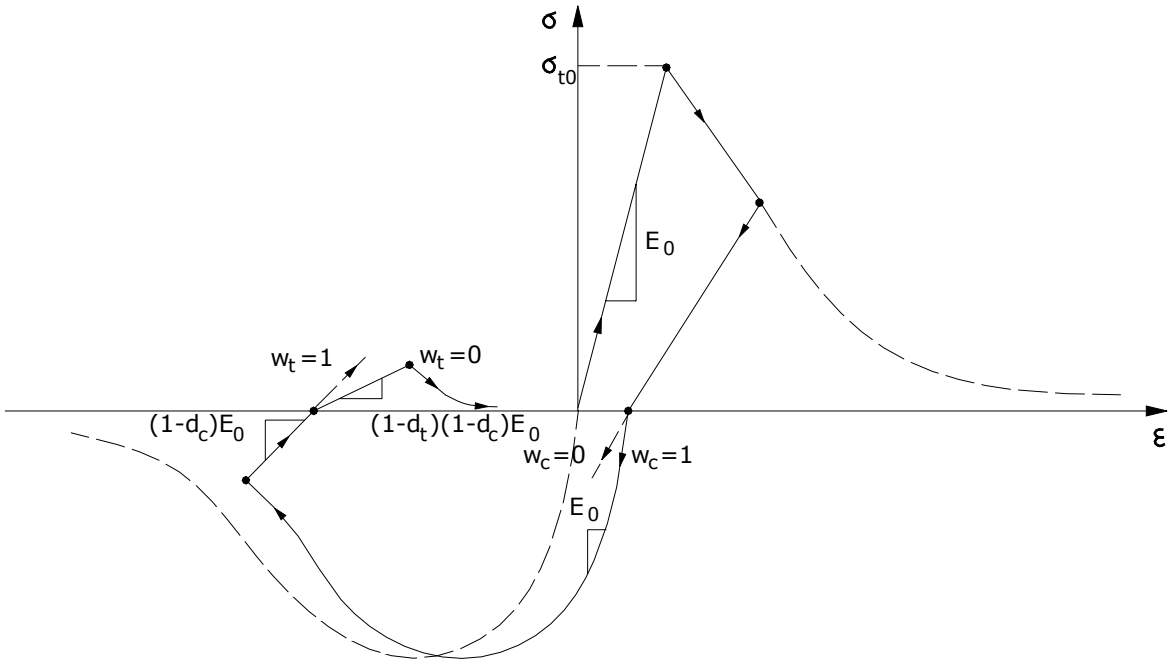

Figure 5.13 The stress-strain curve of concrete damaged plasticity model used in ABAQUS

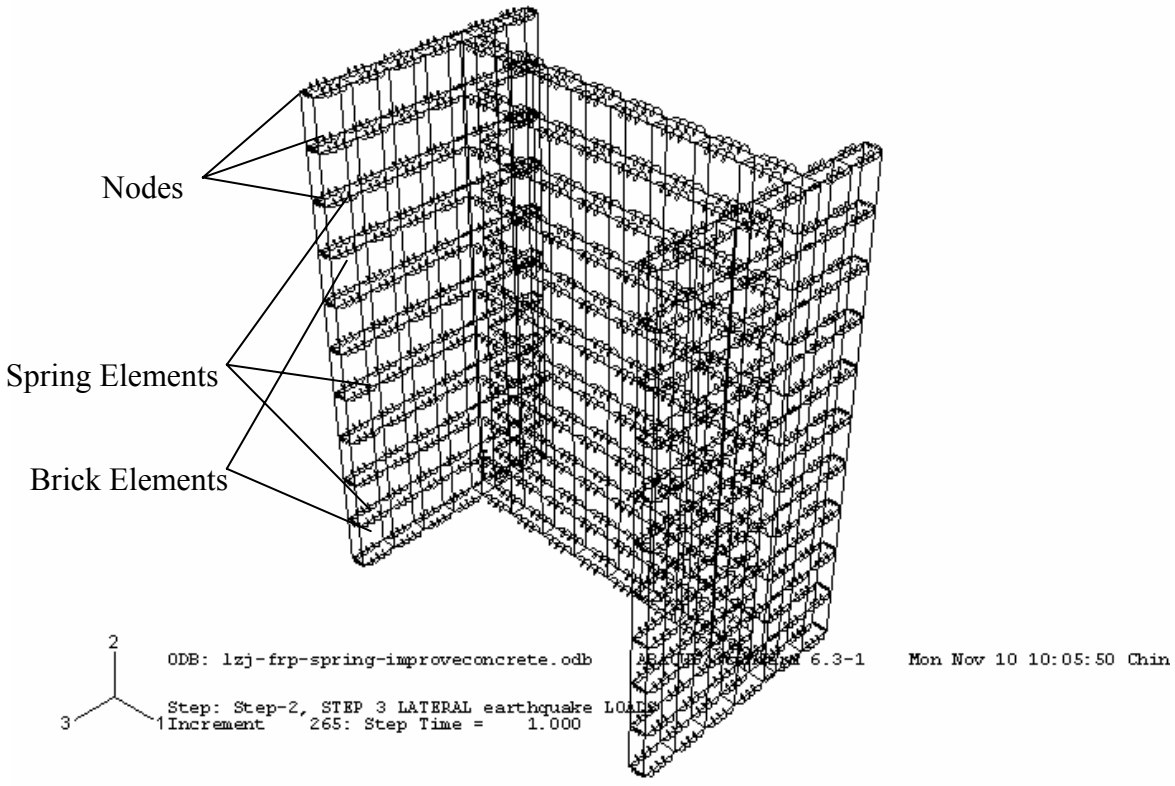

Figure 5.14 3D view of the modeling of the FRP wrapped specimen (S2)

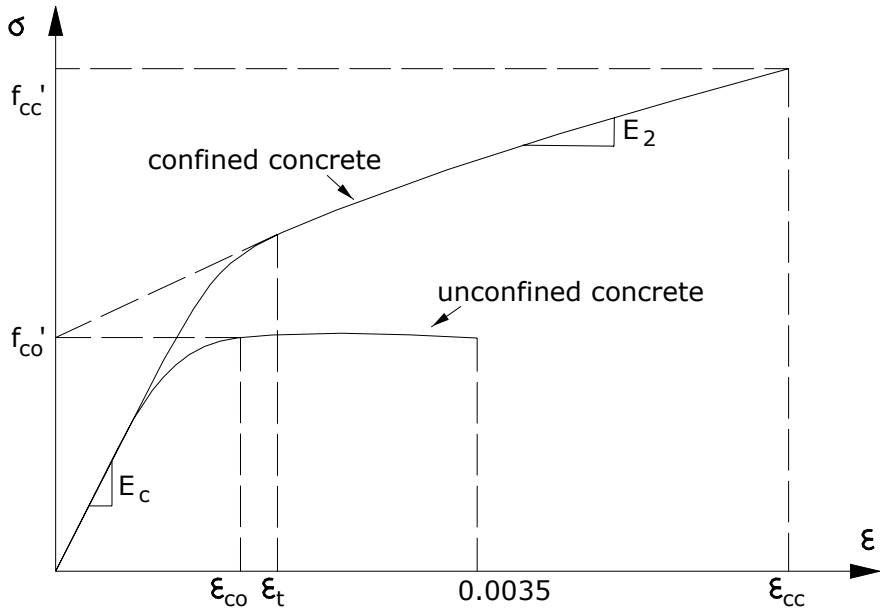

Figure 5.15 The stress-strain curve of the confined concrete (Teng 2001)

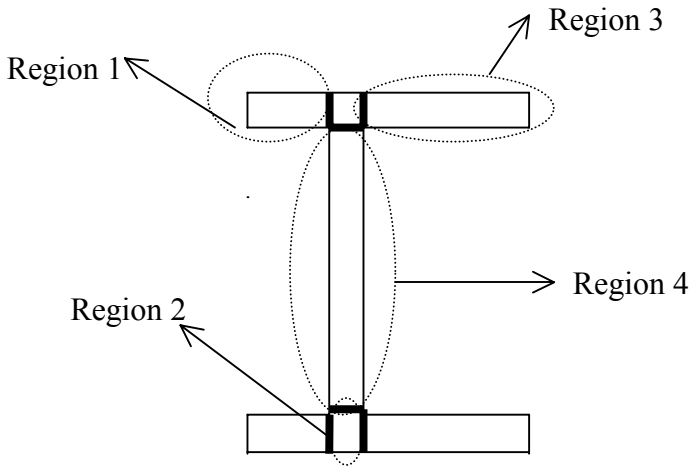

Figure 5.16 Wall divided into regions.

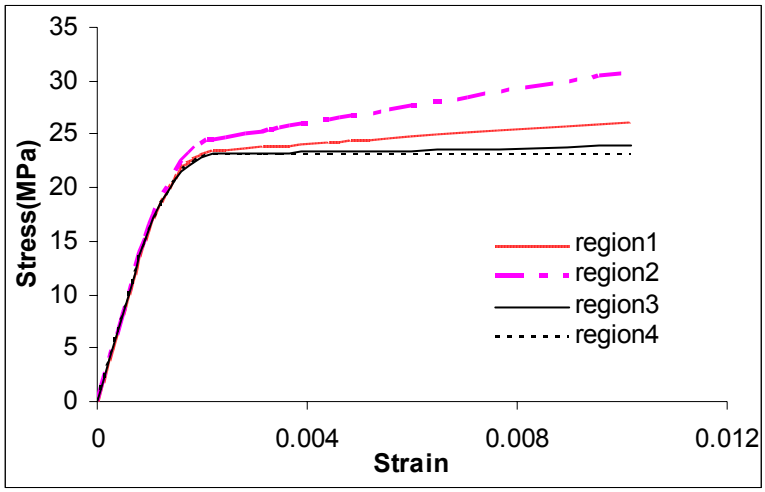

Figure 5.17 The stress-strain curves for the confined concrete at different regions

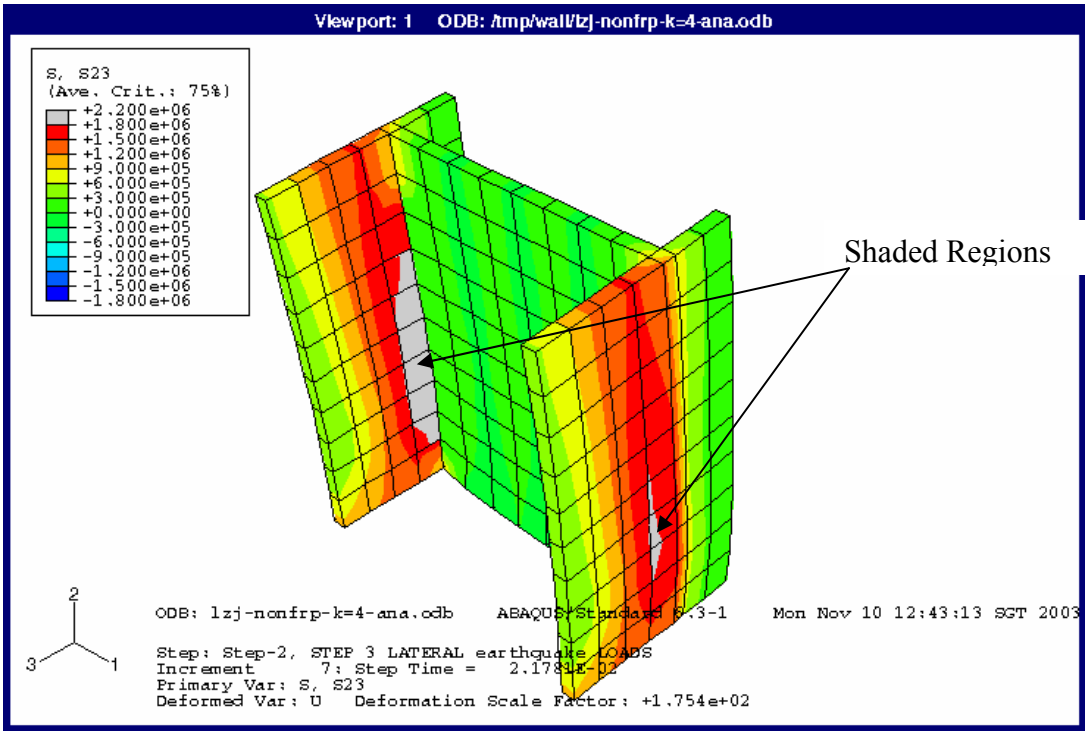

Figure 5.18 Initial shear failure in reinforced concrete flange walls of the control specimen (S1) at 54.4 kN

Note: shaded region has a shear stress >1.80 MPa (shear capacity of reinforced concrete)

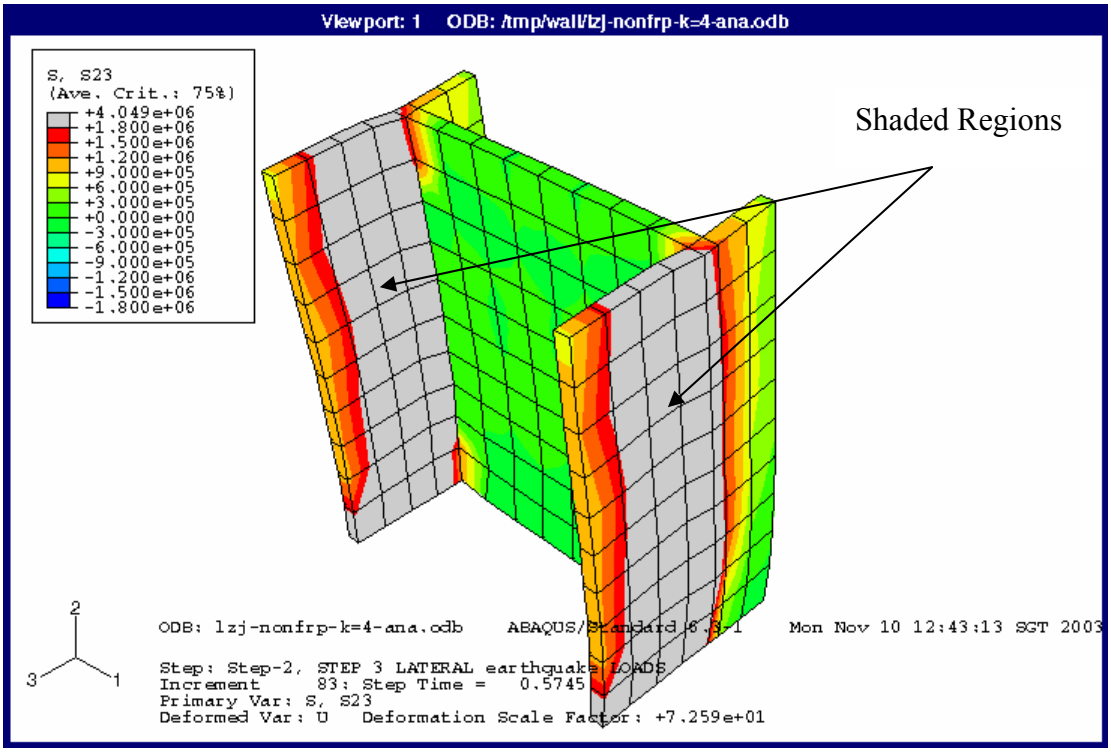

Figure 5.19 Final shear failure in the control specimen (S1) at 113.9 kN

Note: shaded region has shear stress >1.80 MPa (shear capacity of reinforced concrete)

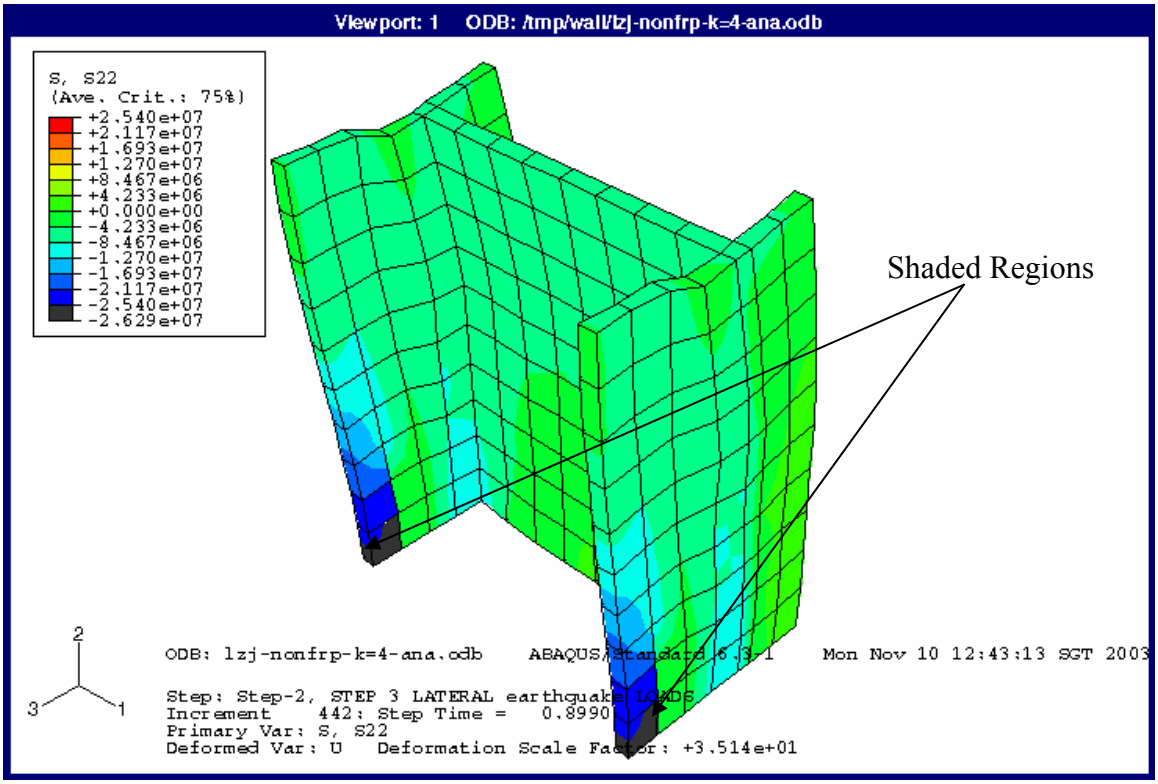

Figure 5.20 Axial compressive stress in the control specimen (S1).

Note: shade region at compressive base tip has stress > 30Mpa (f_{cu})

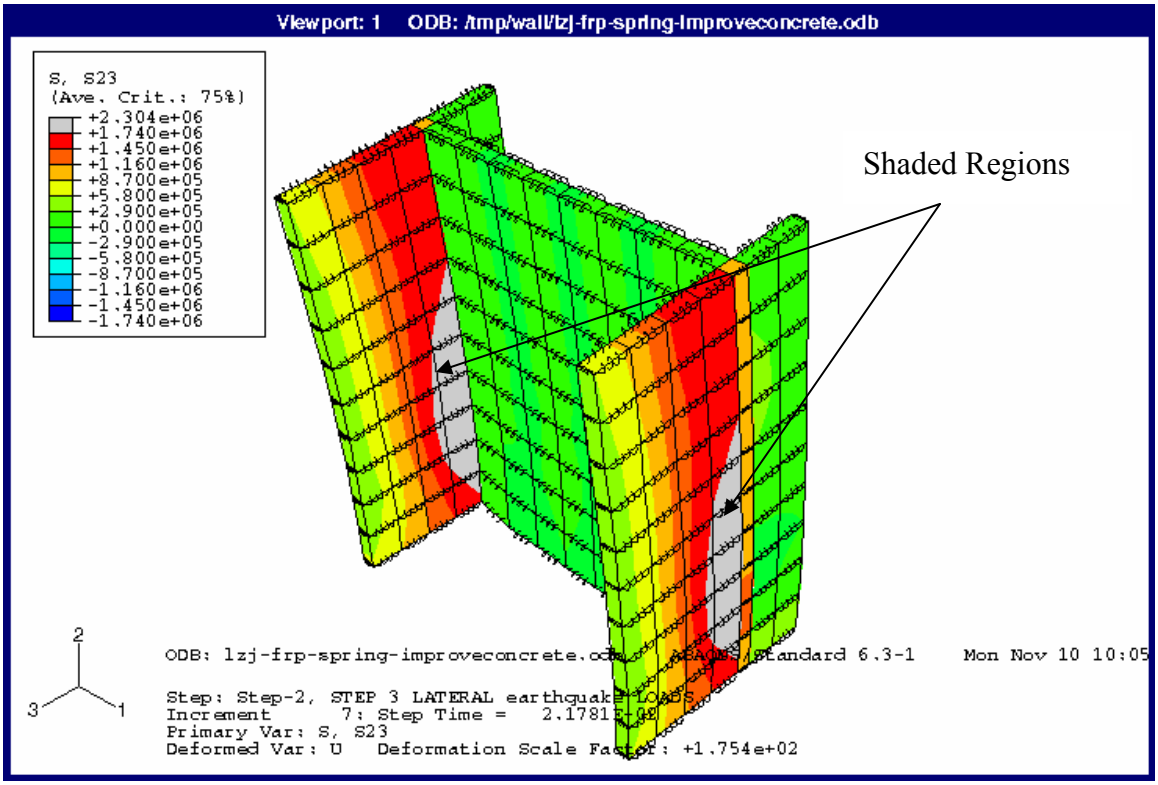

Figure 5.21 Initial shear failure in reinforced concrete flange wall of FRP wrapped specimen (S2) at 53.6kN

Note: shade region has shear stress >1.74 MPa (shear capacity of reinforced concrete)

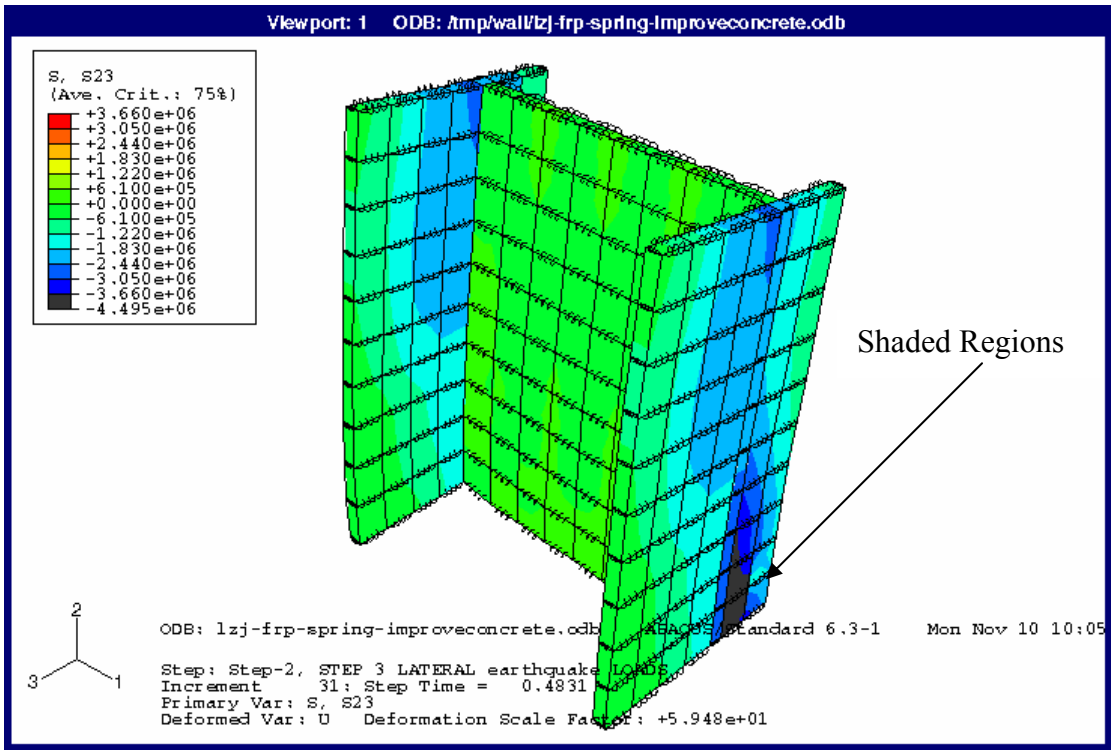

Figure 5.22 Initial shear failure of FRP wrapped specimen (S2) due to FRP debonding at the 3rd cycle

Note: shade region has shear stress > 3.49 MPa (FRP debonding shear capacity)

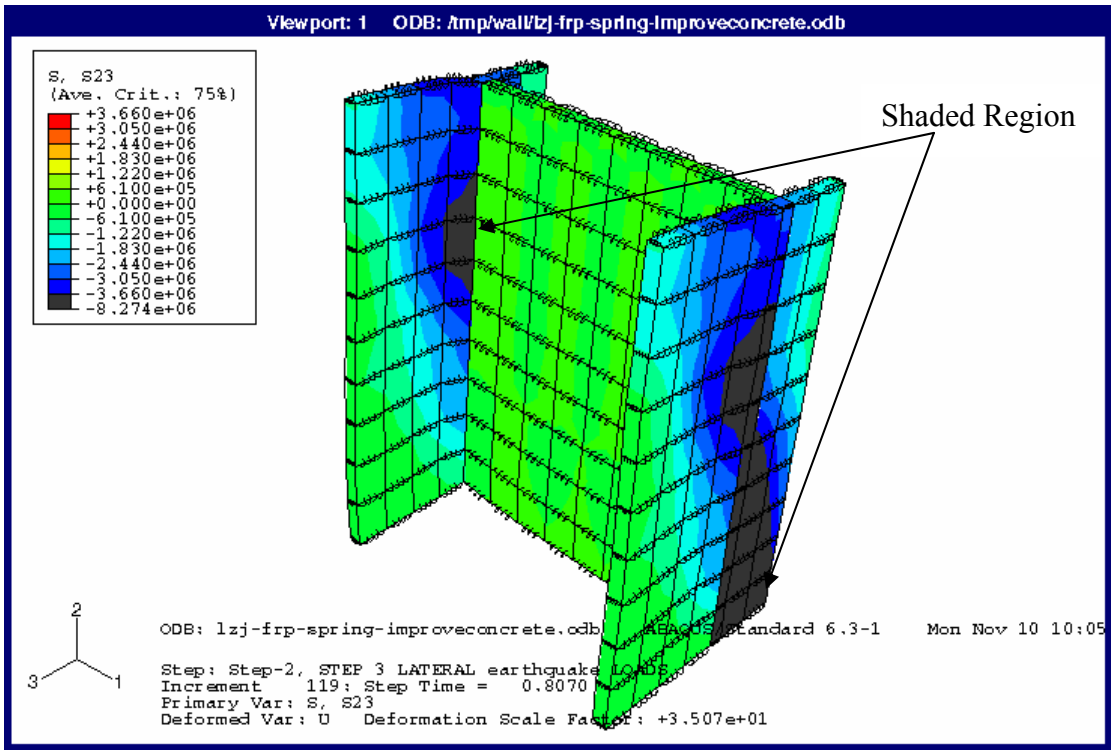

Figure 5.23 Shear failure of FRP wrapped specimen (S2) due to FRP debonding at the 5th cycle

Note: shade region has shear stress > 3.49 MPa (FRP debonding shear capacity)

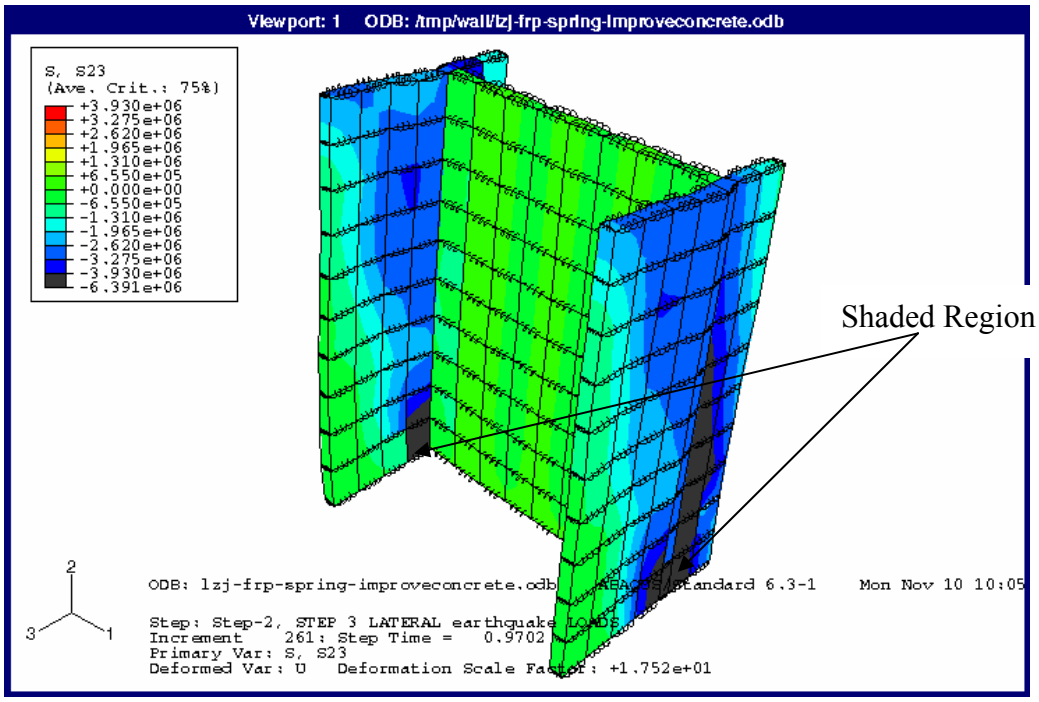

Figure 5.24 Shear failure of FRP wrapped specimen (S2) due to FRP rupture (At the end of the 7th cycle, lateral force was 151.78kN)

Note: shade region has shear stress > 3.93 MPa (FRP rupture shear capacity)

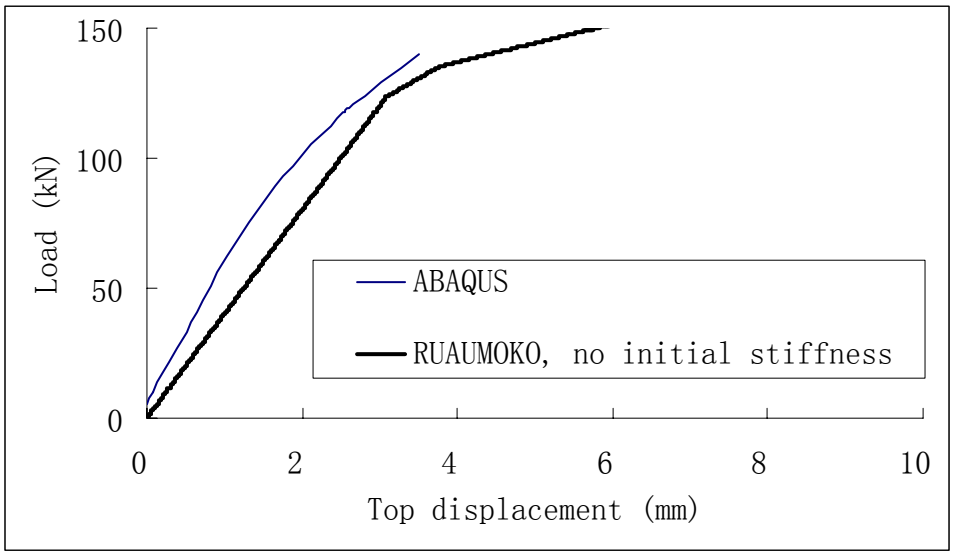

Figure 5.25 Comparison of pushover FEA using ABAQUS and 3D FEA using RUAUMOKO without consider the initial stiffness reduction for specimen S1

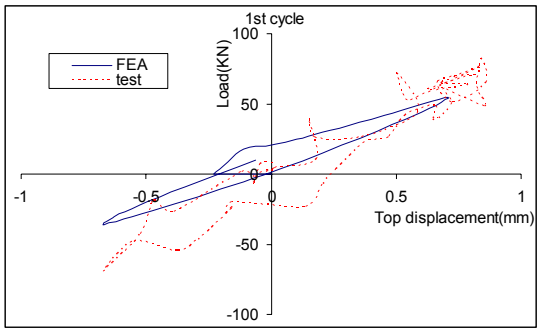

(a)1st cycle

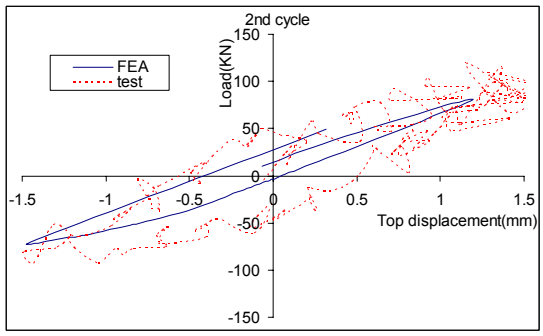

(b)2nd cycle

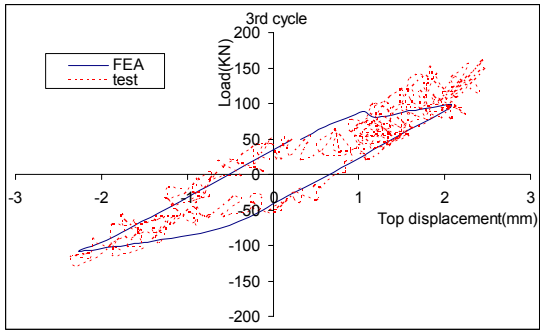

(c)3rd cycle

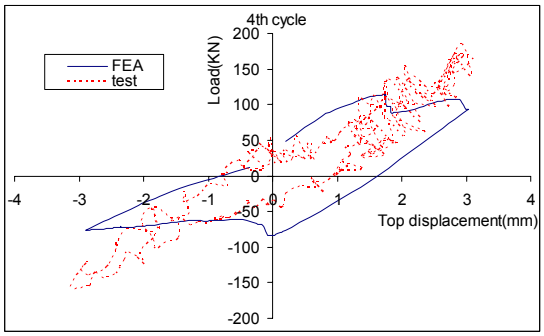

(d)4th cycle

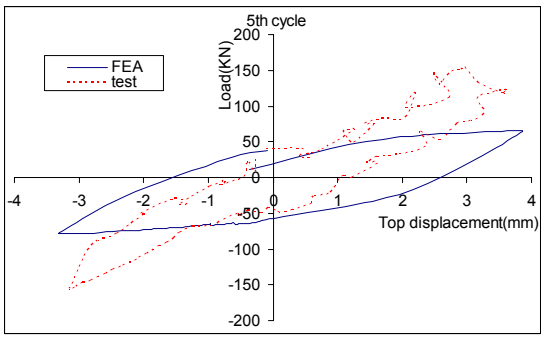

(e)5th cycle

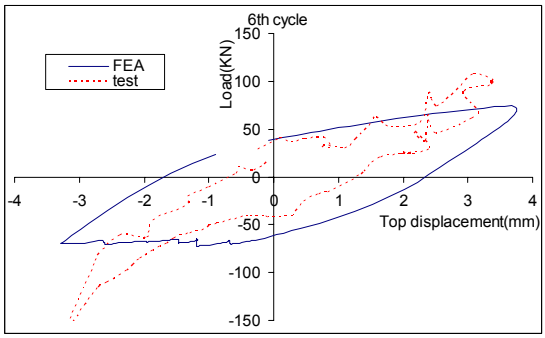

(f)6th cycle

Figure 5.26 Cycle by cycle comparison between experiment and finite element analysis for Control specimen S1

Note; displacement of FEA amplified by a factor of 4 to consider size effect

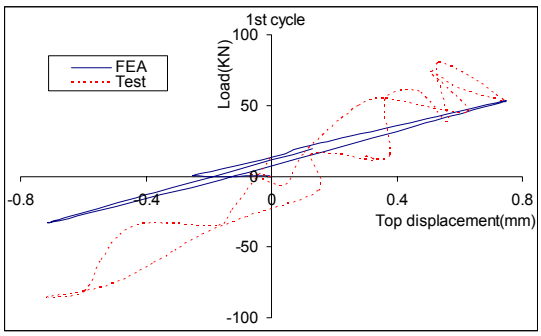

(a)1st cycle

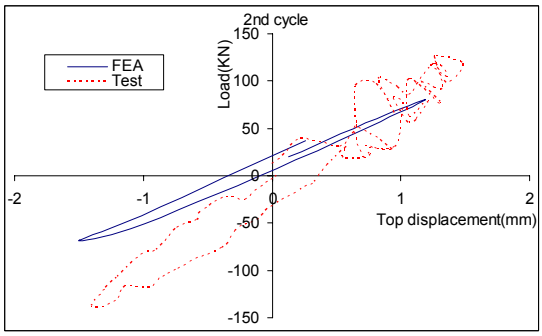

(b)2nd cycle

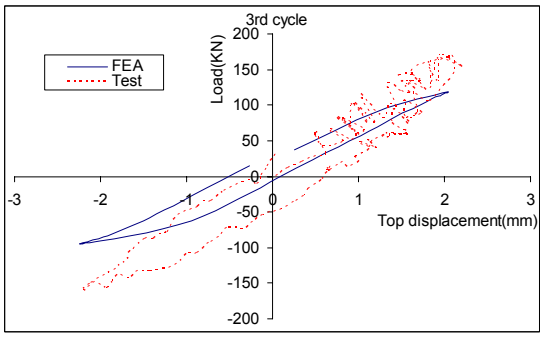

(c)3rd cycle

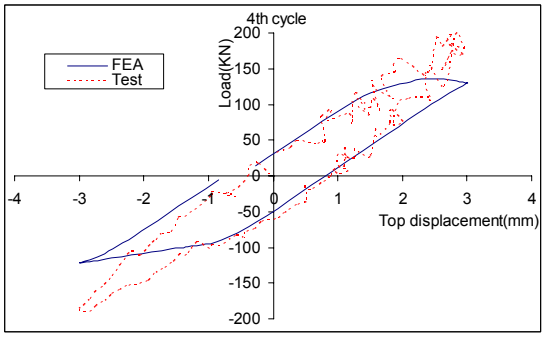

(d)4th cycle

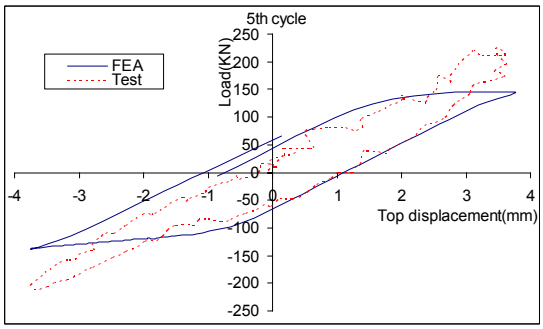

(e)5th cycle

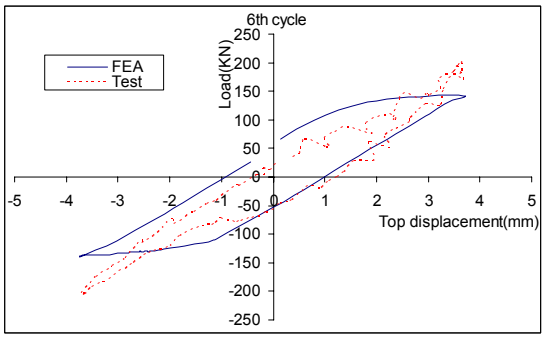

(f)6th cycle

Figure 5.27 Cycle by cycle comparison between experiment and finite element analysis for FRP wrapped specimen S2

Note: displacement of FEA amplified by a factor of 4 to consider size effect

CHAPTER 6 SEISMIC DEMAND AND CAPACITY

6.1. Introduction

In Chapters 3 and 5, FEA models using RUAUMOKO for frame and shear wall structures were established and validated using the test results as specified in Chapters 2 and 4. Based on the FEA models established in the previous chapters, FEA models for a 25-story shear wall-frame building and a 4-story sub-frame were developed to determine the capacities of these buildings.

In order to evaluate seismic adequacy of the buildings, the seismic demand for these buildings needs to be found first. Thus, in the first section of this chapter, the worst earthquake scenario in Sumatra (design earthquake) and the selected soil sites are introduced. Then the process of obtaining the seismic demand curves, based on the accelerograms of bedrock motions due to the design earthquake and soil profiles of the selected sites, is addressed in detail. After that, the pushover and dynamic collapse analyses of a 25-story shear wall-frame structure and a 4-story sub-frame are described in determining the capacity of the buildings. Finally, comparison between the seismic demand curves and the strength capacity curves is carried out, and the seismic adequacy of these two buildings is evaluated.

6.2. Seismic demand

6.2.1. Accelerations and response spectra of two recent strong earthquakes

In the recent two years (year 2004 and 2005), several strong earthquakes occurred at Sumatra, and tremors due to these earthquakes were widely reported in Singapore. Among these earthquakes, the strongest earthquake is the Aceh earthquake, with Moment Magnitude of 9.3, occurred along Northern Sumatra, 950 km away from Singapore, on Dec 26 2004. This earthquake is among the top 10 earthquakes in the last 100 years, and sparked the deadly tsunami waves that killed more than 200,000 people. The next strongest earthquake is the Nias earthquake, with Moment Magnitude of 8.7, occurred along Northern Sumatra, 600 km northwest of Singapore, on March 28 2005. The locations of these two earthquakes are shown in Figure 6.1.

The acceleration data at the ground surface, 17m depth, 50m depth and bedrock level were recorded during these two earthquakes. The recorded peak accelerations on bedrock (PRA) are 2.96×10^{-3} m/s^2 for the Aceh earthquake, and 2.57×10^{-2} m/s^2 for the Nias earthquake. Although the moment magnitude of the Aceh earthquake was larger than that of the Nias earthquake, the peak accelerations of the former was smaller than the latter, which occurred nearer (350 km nearer) to Singapore.

Based on the recorded data, acceleration and velocity response spectra were calculated (assuming a damping ratio of 5%). The method and the program for response spectra calculation, according to the Direct Integration Method introduced by Paz and Leigh (2005), are given in Appendix D.

Figures 6.2 -6.7 show the acceleration and velocity response spectra of the Aceh earthquake in three directions (east-west, north-south and vertical direction). As can be seen from Figure 6.2, the peak acceleration of the east-west direction bedrock motion occurs at a period of 5.52 s, and the peak value of the surface east-west motion, which is 4.3 times larger than that of the bedrock motion, occurs at a period of 0.84s. The same observations can also be found from Figures 6.3 and 6.4 in north-south and vertical direction. These observations show that the bedrock motions reached Singapore due to the Aceh earthquake are rich in long period seismic waves, and that the site period at the measuring location is around 0.84s.

Figures 6.8 -6.13 show the response spectra curves of the Nias earthquake. From Figures 6.8-6.10, the same phenomenon regarding the period as mentioned above is observed. The comparison of the motions due to these two earthquakes is listed in Table 6.1. The following observations can be gained from Table 6.1:

1. The peak acceleration values of motions at bedrock and surface due to the Nias earthquake are much larger than those due to the Aceh earthquake. Also, the predominate periods of the motions at bedrock and surface due to the Nias earthquake are less than those due to the Aceh earthquake. This is reasonable because the epicenter of the Nias earthquake is much nearer to Singapore than the Aceh one.
2. The peak surface acceleration occurred at the site period of 0.84s due to the amplification effect of the soil. The maximum amplification factors, the ratios of the acceleration at surface to the corresponding acceleration at bedrock, are about

or more than 10 for both earthquakes. This means the amplification effect of soil profiles in Singapore is quite large due to linear behavior of soil under low intensity ground motions.

6.2.2. Maximum possible earthquake that could affect Singapore

The acceleration records and the response spectra of the above two latest earthquakes were used to enlarge the database for establishing and verifying the F-crust component attenuation model (CAM) proposed by Balendra et. al. (2002) for Singapore. And then the synthetic random phase-angle bedrock accelerograms of the maximum possible earthquake (magnitude-distance design earthquake) are generated using program GENQKE (Lam 1999).

The expressions of the F-crust CAM (Balendra et al. 2002) to predict the peak rock acceleration (PRA) are:

$$\mathbf{PRA}(\boldsymbol{g}) = \alpha G \beta \gamma \tag{6. 1}$$

$$\alpha = 0.192g[0.40 + 0.60(M_w - 5)^{1.5}] \tag{6. 2}$$

$$G = \frac{2}{3}\left(\frac{75}{R}\right)^{0.5} ; R > 75 \text{ km} \tag{6. 3}$$

$$\beta = \left(\frac{30}{R}\right)^{C} \tag{6. 4}$$

$$C = 0.009[9.9 - 1.28(M_w - 6)]R^{0.48} \tag{6. 5}$$

$$\gamma = 0.585 \tag{6. 6}$$

Where,

PRA(*g*)=peak acceleration on bedrock (in units of gravitational acceleration)

α =source factor

G =cylindrical attenuation factor which accounts for energy dissipation

R =epicentral distance in km

β =anelastic attenuation factor which accounts for energy dissipation

γ =factor combining the effects of the mid-crust and upper-crust modifications

The verification of the above equations have been carried out by comparing the peak ground accelerations calculated with the recorded data from seven earthquakes (including the latest two) originated from the subduction region of the Indonesian Arc and the Burmese Arc. Results of the comparison are listed in Table 6.2. It is noted that the predicted PRA of the Nias earthquake is very close to the measured value. This means that the accuracy of the CAM is high to predict the strong earthquake at a distance 600 km away from Singapore.

The 2004 Aceh earthquake and 2005 Nias earthquake both occurred at the Sumatra sub-duction fault, of which the closest epicentral distance is 600 km away from Singapore. The highest earthquake magnitude ever recorded in history is the magnitude 9.5 Chilean earthquake, and the possibility of having earthquakes of this size at this fault was suggested prior to the Aceh earthquake (Zachriasen et al. 1999). Therefore, an earthquake with Moment Magnitude of 9.5, occurred at 600 km away from Singapore has been identified as the worst scenario (design earthquake).

Based on the verified CAM F-crust model, twelve synthetic bedrock accelerograms (as shown in Appendix E) for this design earthquake, were generated using a stochastic simulation program named GENQKE (Lam 1999). The average

acceleration response spectra at bedrock for the design earthquake (assuming 5% structural damping ratio) are shown in Figures 6.14. Since structures are subjected to the seismic motions at the surface, which propagate upward through the soil layers from the bedrock, appropriate sites for study need to be selected first.

6.2.3. Selected sites

The seismic waves at the bedrock can be significantly amplified when they propagate upward through the sedimentary or reclamation soft soil layers (a good example is the large soil amplification factors as listed in Table 6.1), especially when the natural period of the soft soil is close to the predominant natural period of the bedrock motions. This amplification can be further enlarged if the building founded on the soft soil site possesses a natural period which is close to the period of the site. Therefore, for worse situations, the predominant period of the bedrock motions, the period of the site and the period of the building must coincide. Thus, a careful selection of the soil sites for investigation should be carried out. Because the natural period of typical buildings in Singapore (15-25 story) have been found to be in the range of 0.7s to 1.8s (Balendra et al. 2002), and the predominate period of average peak bedrock acceleration due to the design earthquake is about 1.6s (as shown in Figure 6.14), the sites that possess natural periods from 0.7s to 1.8s could be considered. As a result, three sites in the Kallang formation on the eastern part of Singapore, located at Marine Parade (MP) with site period of 0.76s, Katong Park (KAP) with site period of 1.6s and

the Katong area (KAT) with site period of 1.85s, were selected. Tables 6.3-6.5 list the borehole data for each of these selected sites.

6.2.4. Surface motions and amplification factors

With soil profiles of the selected sites and the bedrock accelerograms as shown in Appendix E, a computer program SHAKE91(1992) is used to calculate the surface motions, acceleration response spectra at surface and amplification factors. This program is based on equivalent linear seismic response analyses of horizontally layered soil deposits. It is modified based on the original SHAKE program published by Schnabel, Lysmer and Seed (1972). In SHAKE91, the soil profile is idealized as a system of homogeneous, visco-elastic sublayers of infinite horizontal extent. The response of this system is calculated by considering vertically propagating shear waves. An equivalent linear procedure is used to account for the nonlinearity of the soil using an iterative procedure to obtain values for modulus and damping, which are compatible with the equivalent uniform strain induced in each sublayer.

The assumptions of the analysis are:

1. Each sublayer is completely defined by its shear modulus, damping ratio, total unit weight and thickness, which are independent of frequency
2. Responses in the soil profile are caused by the upward propagation of shear waves, which are specified as acceleration ordinates at equally spaced time intervals, from the underlying rock half-space.

The shear modulus and damping relationship of the soil profiles at the selected sites is calculated according to equation (6.7)(Hardin and Drnevich 1972) , and equation (6. 8) (Poulos 1991), and the results are shown in Figures 6.15 and 6.16

$$\frac{G}{G_{\max}} = \frac{1}{(1+\gamma/\gamma_r)} \tag{6.7}$$

$$\zeta_\gamma = \zeta_i + \frac{\zeta_{\max}(\gamma/\gamma_r)}{(1+\gamma/\gamma_r)} \tag{6.8}$$

Where,

G= instantaneous shear modulus at a given strain γ

$G_{\max}$ =initial shear modulus

γ_r =reference shear strain which in dependant on plasticity, values suggested by Lam and Wilson (1999) are γ_r =0.025 for sand and γ_r =0.02 for clay

ζ_γ = instantaneous damping at a given strain γ

$\zeta_i = 0.01 + 0.039(PI\%)$ (Lam and Wilson 1999)

$\zeta_{\max} = 0.16 - 0.001(PI\%)$ (Lam and Wilson 1999)

PI =plasticity index for the soil, the values are PI =0% for sand and PI =50% for clay

$G_{\max} = 14N_{spt}^{0.68}$ (Imai and Tonouchi 1982)

Figures 6.17 to 6.19 show one of the twelve surface accelerograms for the selected MP, KAP and KAT sites, respectively. The resulting maximum surface motion accelerations for MP, KAP and KAT sites are -1.45 x10^{-2} (g), -2.31 x10^{-2} (g) and 1.95x10^{-2} (g) respectively. Figure 6.20 shows the average surface acceleration response spectra (structural damping ratio of 5%) due to the design earthquake at

bedrock. The periods corresponding to the peak of the acceleration spectra at MP, KAP and KAT sites are 0.76s, 1.6s and 1.85s respectively.

Figure 6.21 shows the soil amplification factors of the selected sites (structural damping ratio of 5%) due to the design earthquake at bedrock. The maximum amplification factors are 11.2 (corresponding period of 0.74s) for MP site, 10.1 (period of 1.54s) for KAP site, and 10.8 (period of 1.82s) for KAT site. Since the period of KAP site is closest to the natural period (1.6s) of the bedrock motions, the surface peak acceleration of the KAP site is the largest (-2.31 $x10^{-2}$ g) among the three selected sites due to the resonance effect of soil.

Figure 6.22 shows the spectral acceleration vs. spectral displacement relationship for MP, KAP and KAT sites (structural damping ratio of 5%) due to the design earthquake at bedrock. The curves in Figure 6.22 are the demand curves for the structures located on the selected sites due to the design earthquake. These curves will be compared with the capacity curves of the structures obtained from the FEA modeling using RUAUMOKO, to evaluate their seismic adequacy.

6.3. Methods of analysis and failure identification

6.3.1. Methods of analysis

To obtain the strength capacity of the structure, the pushover analysis and dynamic collapse time-history analysis were conducted using RUAUMOKO. Dynamic collapse time-history analysis is a stepwise solution of the multi-degree of freedom

equations of motion in the time domain. It is a powerful tool for the study of structural seismic response. A set of carefully selected ground motion records can give an accurate evaluation of the anticipated seismic performance of structures. However, it needs significant computational efforts.

As an alternative, the inelastic static pushover analysis is a simple option for estimating the strength capacity in the post-elastic range, and can also be used to highlight potential weak areas in the structure. This procedure involves applying a predefined lateral load pattern which is distributed along the building height. The lateral forces are then monotonically increased in constant proportion with a displacement control at the top of the building, until the failure of the structure (Mwafy and Elnashai 2001). The assumption of the pushover analysis is that the response of the structure can be related to the response of an equivalent single degree of freedom system. This implies that the response is controlled by a single mode, and that the shape of this mode remains constant throughout the time history response (Krawinkler and Seneviratna 1998).

Before the pushover analysis or dynamic collapse analysis, a modal analysis is performed. The modal analysis yields the natural frequencies and mode shapes of the structure, which are used respectively for selecting the base accelerogram in the dynamic collapse analysis and determining the lateral load distribution in the pushover analysis. Rayleigh damping model was used in the analysis and the damping matrix is given by

$$C = \alpha M + \beta K \tag{6.9}$$

Since the damping of higher modes is unpredictable, the damping is assumed to be proportional to initial stiffness (K) only. Thus α is taken as zero and β is calculated by the program to give 5% critical damping in the first mode of the structure.

In the pushover analysis, lateral loads are applied in one direction at the master nodes of the floor levels, and are increased until the failure of the structure. The distribution of loading in the vertical direction, which is incorporated in the SHAPE option of RUAUMOKO, is calculated according to the Australian standard (AS1170.4 1993). The lateral load applied at each level is:

$$F_x = \frac{G_{gx} h_x{}^k}{\sum_i G_{gi} h_i{}^k} V_b \tag{6.10}$$

Where,

G_{gx} = the gravity load at story x

h_x = the gravity load at story x

G_{gi} = the gravity load at story i

h_i = the gravity load at story i

V_b =total base shear

$$k = \begin{cases} 1.0 & when\ period\ T \le 0.5s \\ 1.0 + 0.5(T - 0.5) & 0.5s < T < 2.5s \\ 2.0 & T \ge 2.5s \end{cases}$$

Based on the fundamental periods calculated in the modal analysis and equation (6.10), the loading shape for the pushover analysis was calculated. Then the predefined lateral loads were increased in steps. It is recommended in RUAUMOKO that the time step be smaller than one tenth of the period of the highest mode of vibration that contributed significantly to the response of the structure. A small time step of 0.01s

was selected to make sure that the loading rate was slow enough that inertia forces were insignificant. This time step was verified by the running of several analyses with different time steps, to check for convergence of the results.

In the dynamic collapse analysis, one set of the input ground accelerogram generated from an earthquake can only generate one value of the maximum displacement and maximum base shear. In order to determine the capacity of the structures, the input base motion has to be scaled to simulate varying intensity of the ground motions, and a series of maximum responses were generated from the analysis. This scaling method involves multiplying the base acceleration by a factor, while keeping the time step the same. An iteration time step of 0.005s was selected in dynamic collapse analysis, which was verified by the running of several analyses with different time steps, to check for convergence of the results

6.3.2. Failure identification

Identification of the failure mode/failure point is important to estimate the capacity. To avoid both global and local failures, the following failure criteria were used:

1. A mechanism due to formation of plastic hinges that lead to unstable structure (for example, soft story collapse mechanism), which is a global flexural failure (as shown in Appendix G.1). Since the formation of plastic hinges can be observed from the post-process of RUAUMOKO results, the locations and numbers of plastic hinges may be used to judge whether a collapse mechanism occurs.

2. Overall or inter-story drift exceeds a limit of 2% (global failure).
3. Local shear failure occurs in any member. The identification of the local shear failure in members is performed by manual checking. In the output files, the shear envelope in each member is given, which is compared with the shear capacity calculated as shown in Appendix B.
4. Local flexural failure occurs in any member. The identification of the local flexural failure in members is performed by manual checking. In the output files, the moment envelope and the corresponding axial load in each member is given, and the moment capacity of the member is calculated based on Appendix A.4. By comparing the moment demand and calculated capacity in a member, the local flexural failure is checked.

Programs can be written using Fortran to draw out the envelope values of shear and moment, and values of axial loads corresponding to the maximum moment Comparisons between the shear/moment demands and capacities, to identify local failures, can also be carried out by Fortran programs. When a local shear or local moment failure is identified, the time at which such failure occurred is identified from the time history results. The corresponding roof displacement and base shear values are used to identify the point of failure.

In the following sections, FEA modeling and the procedure to evaluate seismic adequacy of high-rise structures and low-rise structures will be described in detail using two case studies

6.4. Case study 1: a 25-story reinforced concrete HDB point block

The prototype 25-story reinforced concrete HDB point block mentioned in Chapter 4 represents the high-rise buildings in Singapore, and thus was chosen as a case study for evaluation. In this section, details of FEA modeling are described and the analysis results are presented. Then the seismic adequacy of this building is evaluated and the retrofitting scheme is proposed.

6.4.1. FEA modeling

6.4.1.1. Building under study and model layout

The plan view of the 25-story building is shown in Figure 4.1. Total dimension of the building is 24.4m by 19.81m and the total height is 64.77m (with each story height being 2.59m).

The structure comprises of moment-resisting frames, two I-shape shear walls located in the center and four L-shape shear walls located at the corners. Details of the floors and beams are identical for all stories, but the dimensions and details of columns and shear walls vary with the height. Slab thickness is 100 mm and the typical dimensions of beams and columns are 230 mm x 450 mm and 300 mm x 1200 mm, respectively. Typical thickness of shear walls is 230 mm. Longitudinal reinforcing bars in members have design yield strength of 460 MPa, and transverse reinforcing bars in members have design yield strength of 250 MPa. As the building was designed in the late 1970s, the concrete cube compressive strength of the buildings at that period

varied between 20 MPa to 30 MPa. in order to see the influence of concrete strength to the structural performance, concrete cube compressive strength of 20 MPa and 30 MPa were considered in the FEA models.

Since different combination of dead load and live load may have different influence on the structure, two loading cases of the vertical loads were considered in the study, viz, (1) ultimate loading case: 1.2 dead load+1.2 live load; and (2) common loading case: 1.0 dead load +0.4 live load. Dead load due to finishes and the partition is assumed to be 1.2 kN/m^2 and 1.0 kN/m^2, and the density of concrete is assumed to be 24kN/m^3, thus unfactored dead loads calculated for the typical floors and the roof floor (no partition on the roof floor) are 4.6 kN/m^2 and 3.6 kN/m^2, respectively. Unfactored live load is taken as 1.5 kN/m^2.

The structure was modeled using 3D RUAUMOKO (Carr 2002b). The model was aimed to represent the actual situation as far as possible, but some small details and uncertain influence were conservatively simplified. In the FEA modeling, to be conservative, infill walls were not included, although masonry infill walls could be beneficial in minor to moderate seismic regions as they increase the strength of the global structure (Lee and Woo 2002a). It was assumed that the foundation would not govern the failure in an earthquake, so in the study herein, boundary conditions of the bases of columns and shear walls were assumed as fixed end.

The contribution of slabs to the stiffness of the structure was considered by incorporating the effective flanges into the calculation of the area and stiffness of the corresponding beams. According to ACI code (1989) Section 8.10, the effective flange

width of T-beam (with slabs at both sides) was taken as the smallest of $L/4$, $b+8h_f$ and $b+S/2$, and that of inverted L beam (only with slab at one side) was taken as the smallest of $b+L/12$, $b+6h_f$ and $b+S/2$, where, L is the span length of the beam, b is the width of the rectangular beam, h_f is the thickness of the slab and S is the clear distance to the adjacent web.

Since the point block structure is symmetrical in two directions in the plane, only the left half of the structure was analyzed. Figure 6.23 shows the typical story layout of the half structure. Boundary conditions of the nodes on the symmetric plane were modeled as roller supports to make sure that the out of plane displacements and rotations were zero. Because the dimensions in x and y directions are similar, and thus there are no obvious weaker direction, the analysis for both directions were carried out.

As described in Chapter 5, shear walls were treated as equivalent columns connected by horizontal rigid links. The L-shape shear walls at the corners were simulated by two equivalent columns W1 and W2 located at the center of the two separated rectangular wall (shown as the two black solid points in Figure 6.23). The I-shape shear walls at the center of the structure were simulated by three equivalent columns W3, W4 and W5. Rigid links, used to connect these equivalent columns together or to adjoining members, were modeled using frame-type one-component beam element with very large stiffness and moment capacity. Equivalent columns or frame columns, and beams were modeled with frame-type RC beam-column element and one component beam element respectively, with the appropriate reduced stiffness.

The stiffness reduction for equivalent columns, frame columns and beams are 0.8, 0.58 and 0.35.

Serial numbers denoting beams are shown in Figure 6.23. The reinforcement details at the beam ends may be different from those in the middle because of the curtailment of reinforcement beyond the anchorage regions. Therefore, in Figure 6.23, some beams may have different sectional properties due to different detailing. For example, beam B1 has two sections and is denoted as B1-1 and B1-2. The shapes of the rectangular frame columns are also shown in Figure 6.23. It is noted that column C5 is different from other columns in the direction of the longer side.

As described previously, two concrete compressive strengths (f_{cu} =20 MPa and f_{cu} =30 MPa) and two loading cases (ultimate loading case and common loading case) were considered. In the following sections, only one case (f_{cu} =20 MPa and ultimate loading) will be described in detail for demonstration of the FEA model, but the results of all cases will be presented.

6.4.1.2. FEA meshing

Figure 6.24 shows the 3D view of the mesh. There are 2071 nodes, 2975 elements and 101 sectional properties in the FEA model. Among the 2071 nodes, nodes 2047- 2071 are master nodes of story 1-25, which are located at the center of mass (CM) of the corresponding floor plane (as shown in Figure 6.23). Among the 2975 elements, elements 1-300 are used to model frame columns, elements 301-2300 are used to model beams (at one floor level, there are 80 beam elements), elements

2301-2500 are used to model the rigid links for L-shape shear walls, elements 2501-2750 are used to model the rigid links for I-shape shear walls, elements 2751-2850 are used to model equivalent columns of the L-shape shear walls and elements 2851-2975 are used to model equivalent columns of the I-shape shear walls. Among the 101 sectional properties, sections 1-26 are for beams, sections 27-72 are for frame columns, sections 73-100 are for equivalent columns of shear walls, and section 101 are rigid links of the shear walls. The relationship between members and element sections is listed Table H.1 in Appendix H.

6.4.1.3. Member properties

The definition of a cross section in 3D dimension involved elastic section properties (elastic Young modulus, shear modulus, cross-sectional area, effective moment of inertia, and weight of the member), initial force (distributed self-weight), section strength properties, yield surfaces and hysteresis rules. The details are as follows.

Elastic sectional properties

Elastic (Young's) modulus of the concrete (E), shear modulus (G), cross-sectional area (A), effective shear area (A_s) were calculated using the equations given in Appendix C. For the case of f_{cu} =20 MPa, E =19.92GPa and G =7.88GPa, and for the case of f_{cu} =30 MPa, E =23.17GPa and G =9.66GPa. Torsional second moment of area of section in the x-x direction J_{xx}, moment of inertia in the z-z direction I_{zz} ,and

moment of inertia in the y-y direction I_{yy}, were calculated by multiplying the corresponding values of the gross section by the reduction factors obtained from the tests (that is, 0.58 for frame columns, 0.8 for shear walls and 0.35 for beams). Weight/unit length (WGT) was taken as 0, and the input of mass was incorporated as nodal lump weight. Input values of the elastic sectional properties are listed in Table H.2 in Appendix H.

End condition

The end condition of all members was assumed as 'built-in to joint'. In other words, the rotations of the members at the joint region were assumed to be equal to the adjoining members. The lengths of plastic hinges were taken as 1.0h for columns and 0.5h for beams as discussed in Chapter 3.

Yield surface of the members

The contributions of reinforcing bars were through the calculation of yield moment surface. The method to calculate the five parameters (*PC*, *PB*, *MBz*, *MBy* and *PT*) used to define the interaction yield surface is given in Appendix C.2. For the beam, the interaction between axial load and moment is neglected, so that only the yield moment, calculated as shown in Appendix C.3, is needed for input. The values of these parameters used for the case of $f_{cu} = 20$ MPa and ultimate loading are listed in Table H.3 in Appendix H. For rigid links, a large moment capacity (like 10^9kN.m) was taken.

Hysteresis rule

The stiffness degradation was considered by defining hysteresis rules. The Modified Takeda Hysteresis model (as shown in Figure 1.3) was adopted, and the unloading stiffness degradation parameter α and reloading stiffness degradation parameter β obtained from the tests (as described in Chapter 2 and Chapter 4) were used: $\alpha = 0.5, \beta = 0.1$ for frame columns, $\alpha = 0.4, \beta = 0.1$ for frame beams and $\alpha = 0.5, \beta = 0.7$ for shear walls (equivalent columns). The bilinear factor *r* was calculated according to Appendix A.5. As an example, the calculated values of *r* for the case of f_{cu}=20 MPa and ultimate loading are listed in Table H.3 in Appendix H.

6.4.1.4. Boundary conditions

Boundary conditions of the base of columns and shear walls were simulated as fixed ends. To simulate the diaphragm effects of slabs, nodes on each floor were slaved to the master node in that floor. The slaved degrees of freedoms were x direction translation, y direction translation and rotation about z-z.

6.4.1.5. Vertical and lateral loads

Vertical loads and masses were input in RUAUMOKO separately, because the input vertical loads were used in the static analysis, while the input masses were used to calculate inertia forces in the dynamic analysis. The self-weight of members and distributed loads on the beams were considered as the initial uniform distributed loads

when sectional properties were defined. Initial loads (ultimate loading case) in members are listed in Table H.2 in Appendix H. Since all gravity loads were input as initial distributed loads in members, the input of nodal gravity loads were taken as zero. There may be initial displacements or shear forces in members due to gravity loads in the static analysis. Therefore, when dealing with the data of displacements and shear forces due to the lateral load, the corresponding initial values should be deduced.

Mass of the structure is input in the form of weights, and internally converted by the program to mass units, by dividing the weights by the acceleration of gravity. Mass can be provided by specifying nodal weights in WEIGHT option or values of member weight/unit length in sectional properties. In the study herein, weights were applied as nodal weights.

Based on the fundamental periods calculated in the modal analysis (as listed in Table 6.6) and equation (6.10), the loading shape for pushover analysis was calculated. As an example, the lateral loads (for the case f_{cu}=20 MPa, ultimate loading) corresponding to a base shear demand of 1% of the total gravity load (unfactored dead loads of the structure) are shown in Figure 6.25. And values for all cases are listed in Table 6.7.

In the dynamic collapse analysis, the surface accelerograms due to the design earthquake (M_w=9.5, 600 km away from Singapore) was used as the input base motions. As shown in Figure 6.20, the predominant period of the surface acceleration response spectra of KAT site is 1.85s, which is close to the period of the 25-story

building obtained from the modal analysis. Thus, one of the surface accelerograms of KAT site was selected as the input base motion.

6.4.2. FEA results and interpretation

There are four different cases considered: (1) f_{cu} =20 MPa, ultimate loading case; (2) f_{cu} =20 MPa, common loading case; (3) f_{cu} =30 MPa, ultimate loading case; (4) f_{cu} =30 MPa, common loading case. For each case, x and y directions as shown in Figure 6.23, were considered. The results for f_{cu} =30 MPa under ultimate loading will be described in detail for demonstration, and results of all cases will be listed in a table and shown in figures.

6.4.2.1. FEA results for the case of f_{cu}=30 MPa, ultimate loading case in x direction

Total base shear demand V_b / gravity load W_g vs. overall drift (Δ / H) curve for the case of f_{cu} =30 MPa and ultimate loading in x direction, obtained from the pushover analysis, is shown in Figure 6.26, in which, the total base shear demand is the sum of all the shear forces in base members in x direction, W_g = 38866.12kN is the total unfactored dead load of the left half symmetric side of the 25-story building under study, Δ is the roof displacement and H=64.75m is the total height of the building. The maximum overall drift Δ / H is less than 2%, hence, the failure is not due to excessive lateral displacement. In Figure 6.26, the point corresponding to the 1st shear failure (where the shear demand exceeds the shear capacity) in members is shown.

This first shear failure occurred at the 1st story I-shape flange wall (I3), when V_b/W_g=5.52% and Δ/H=0.413%. Since there are no shear failure at columns and beams and there are no local flexural failure prior to this failure point, the pushover capacity curve was terminated and the capacity of the structure is taken as corresponding to this point.

Results of maximum V_b/W_g and maximum Δ/H, corresponding to different scaling factors in the dynamic collapse analysis, are also shown in Figure 6.26 for comparison. From Figure 6.26, it is observed that points from the dynamic collapse analysis match well with the curve of the pushover analysis. In order to find out the local shear failure point in the dynamic collapse analysis, the relationship between V_b/W_g and shear forces in the critical member (1st story I-shape flange wall, I3) is shown in Figure 6.27. The ordinate is in the form of percentage of the shear capacity of member I3, so the point corresponding to 100 percent in the ordinate is the local shear failure point. As can be seen from Figure 6.27, the value of V_b/W_g corresponding to the local shear failure in the dynamic collapse analysis is 5.40%, which is quite close to the corresponding value of 5.52% in the pushover analysis. Therefore, the pushover analysis agrees well with the dynamic collapse analysis, and it is reasonable to use results of the pushover analysis as the capacity curves of the structure.

It is worthwhile noting that when scaling factor equal to 1, the corresponding values are V_b/W_g=2.24% and Δ/H=0.143% (as listed in Table 6.8). These values are less than the values corresponding to the failure. Therefore, the structure is safe in a scenario of the design earthquake. In order to find out to which scale of the design

earthquake that the structure can sustain without any failure, the relationship between scaling factors and shear forces in the critical member is plotted and shown in Figure 6.28. As can be seen from Figure 6.28, the scaling factor corresponding to the local shear failure is 3.51.

6.4.2.2. FEA results for the case of f_{cu}=30 MPa, ultimate loading case in y direction

The V_b/W_g vs. Δ/H curve for the case of f_{cu} =30 MPa and ultimate loading in y direction, obtained from the pushover analysis, is shown in Figure 6.29. The maximum overall drift Δ/H is less than 2%, so the failure is not due to excessive lateral displacement. In the same figure, the point corresponding to the 1st shear failure is also shown. This first shear failure occurred at the 1st story I-shape web wall (I1), when V_b/W_g =3.81% and Δ/H =0.126%. Since there are no shear failure at columns and beams and there are no local flexural failure prior to this failure point, the pushover capacity curve was terminated and the capacity of the structure is taken as corresponding to this point.

Results of the maximum response in the dynamic collapse analysis are also shown in Figure 6.29 for comparison. It can be observed from Figure 6.29 that points from the dynamic collapse analysis match well with the curve of the pushover analysis. The relationship between V_b/W_g and shear forces in the critical member (1st story I-shape web wall, I1) is shown in Figure 6.30. As can be seen from Figure 6.30, the value of V_b/W_g corresponding to the local shear failure is 3.72%, which is quite close

to the value of 3.81% in the pushover analysis. Therefore, it is reasonable to use the results of pushover analysis as the capacity curves of the structure.

It is worthwhile noting that when scaling factor equal to 1, the corresponding values are V_b/W_g=5.20% and Δ/H=0.157% (as listed in Table 6.8). These values are larger than those at failure. Therefore, the structure will be subjected to local shear failure at the 1st story I-shape web wall due to the design earthquake. In order to find out to which scale of the design earthquake that the structure can survive without any failure, the relationship between scaling factors and shear forces in the critical member is plotted and shown in Figure 6.31. As can be seen from Figure 6.31, the scaling factor corresponding to the local shear failure is 0.79.

6.4.2.3. FEA results for other cases

Results of all cases are listed in Table 6.8. From this table, it is observed that the results from the pushover analysis match with those obtained from the dynamic collapse analysis in a reasonable range (for y direction loading, errors are within 5%; for x direction loading, errors are larger, but still within 15%, due to the influence of higher mode effects). Thus, it is reasonable to use the pushover analysis as a simplified method to obtain the seismic capacity curves of the structure (as shown in Figures 6.32 and 6.33). It should be noted that the assumption of the pushover analysis is that the response of the structure is controlled by the first mode and the shape of this mode remains constant throughout. If the period of the structure is large (for example, larger than 2s) and the influence of higher mode cannot be ignored, the pushover analysis

may not represent the response of the structure. In this case, the dynamic collapse analysis should be used to obtain the capacity curves.

The influence of concrete strength and loading combination can be observed from the figures. The ultimate vertical loading cases have higher ultimate strength capacities and overall drifts than the common loading cases. This shows that higher axial loads in columns or shear walls may enhance the seismic performance. The cases with larger concrete strength have higher ultimate strength capacities, but lower overall drifts. This observation indicates that increasing concrete strength can increase the strength of a structure, but may reduce its overall drift.

6.4.3. Evaluation of seismic adequacy of the 25-story building

The seismic demand curves obtained from Section 6.2 are in spectra acceleration S_a -spectra displacement S_d format (A-D format), for a single-degree-of-freedom (SDOF) system, while the capacity curves obtained from the pushover analysis in Section 6.4.2 are for a multi-degree-of-freedom (MDOF) system. Thus, in order to compare the curves of demands and capacities, the capacity curves (V_b-Δ format, as shown in Figures 6.32 and 6.33) should be converted into the A-D format for an equivalent single-degree-of-freedom (SDOF) system. The procedure of such conversion is described as follows (Freeman et al. 1975; Freeman 1978; Kong 2004).

1. Conversion of the capacity curve from MDOF system to equivalent SDOF system

The equation of motion for a MDOF system is (damping is not involved for simplicity):

$$M\ddot{U} + F = M[1]\ddot{u}_g(t) \tag{6.11}$$

Where,

$\ddot{U}$ =acceleration vector

M=mass vector

F=internal forces vector

[1]=a unit vector

$\ddot{u}_g(t)$ =ground acceleration in terms of time

From equation (6.11), the force (F^*) and displacement (D^*) of an equivalent SDOF system can be derived as:

$$F^* = V_b / \Gamma \tag{6.12}$$

$$D^* = \Delta / \Gamma \tag{6.13}$$

$$\Gamma = \frac{\sum_j m_j \phi_j}{\sum_j m_j \phi_j{}^2} \tag{6.14}$$

Where,

Γ =the modal participation factor

m_j =story mass at level j

ϕ_j =displacement shape at level j, which can be taken as the 1st modal displacement of the master node at level j.

2. Conversion of the capacity curve for an equivalent SDOF system from F^*-D^* format to acceleration-displacement format (A-D format)

For a SDOF system, the acceleration is obtained by dividing the force F^* by the equivalent mass m*, so that the values in A-D format are:

$$S_a = F^* / m^* \tag{6.15}$$

$$S_d = D^* \tag{6.16}$$

Where,

$m^* = \sum_j m_j \phi_j$

After the capacity curve is converted into A-D format, it is superimposed with the demand curve. If the capacity curve intersects the demand curve, it means that the ultimate capacity of the building exceeds or meets the seismic demand, and thus the seismic adequacy is sufficient. On the contrary, if the capacity curve does not intersect with the demand curve, the seismic adequacy is insufficient. The point of the intersection is referred to as the performance point of the structure, and the last point of the capacity curve is referred to as the capacity point of the equivalent SDOF system.

Figures 6.34 and 6.35 depict the capacity and demand curves in A-D format. In these two figures, demand curves of the three selected sites KAT, KAP and MP and capacity curves of different cases are combined together for comparison. As can be seen from Figure 6.34, for the earthquake along x direction, the capacity curves of all four cases intersect the demand curves of all three sites. This indicates that for loading in x direction, the structure is strong enough to resist the design earthquake.

It can be observed from Figure 6.35 that for the earthquake along y direction, three capacity curves does not intersect the demand curves of KAT site, implying that the capacities of these three cases are insufficient to resist the base motion on KAT site

due to the design earthquake. The insufficient cases are: f_{cu} =20 MPa under common vertical loading with earthquake in y direction; f_{cu} =30 MPa under ultimate vertical loading with earthquake in y direction; and f_{cu} =30 MPa under common vertical loading with earthquake in y direction.

6.4.4. Retrofitting of the 25-story building using GFRP

It is shown in the Section 6.4.3 that three cases, when loading in y direction, do not meet the seismic demand due to the design earthquake. Since the proposed retrofitting scheme using GFRP system in Chapter 4 was proved to be effective, it will be used to retrofit the I-shape shear wall to meet the earthquake demand. The procedure is as follows:

1. The pushover curves in Figures 6.35 are extended until they meet the demand curve of the KAT site (as shown in Figure 6.36). From the intercept points, the corresponding top roof displacements (Δ) are found.
2. The adaptive pushover analysis is carried out until the roof displacements reach the values obtained in step 1. Then the members suffered from the local shear or flexural failure are identified.
3. The difference between the demands and capacities in shear or moment of these members is identified. Then the thickness of GFRP needed for compensation of the difference is calculated. If the member is subjected to local shear failure, equation (4.2) is used to calculate the GFRP needed. If the member is subjected to local flexural failure, the FEA model using RUAUMOKO for FRP retrofitted members

as specified in Chapter 5 should be carried out by assuming the thickness of GFRP used, and then the trial and error procedure is performed until no local flexural failure is observed.

It is found that at the intercept points, no local failure due to flexure occurred. The members suffered from the local shear failure, and the corresponding shear demands and capacities of these members are listed in Tables 6.9-6.11. By assuming that all these exceeded shear forces are sustained by the retrofitted GFRP sheets, the resulting shear forces resisted by GFRP sheets V_f, and the thickness and layers of GFRP sheets that are required for V_f were calculated according to equation (4.2). (Parameters of GFRP, like thickness of one layer=0.353 mm and Young modulus E=69.65Gpa, are listed in Table 4.2).

The selected layer numbers are listed in Tables 6.9-6.11. In practical implement of this retrofitting scheme, it is suggested that the whole I-shape wall is wrapped with the required layers of FRP sheets, and FRP bolts are used at the flange wall-web wall joints for anchorage.

In conclusion, old high-rise HDB buildings in Singapore may suffer damages due to far-field effects of the design earthquake in Sumatra. The proposed retrofitting scheme using GFRP is a simple and effective way to enhance the seismic capacities.

6.5. Case study 2: a sub-frame of a 4-story HDB frame building

The prototype 4-story reinforced concrete HDB frame building mentioned in Chapter 2 represents the low rise buildings built in 1970s in Singapore, and thus was

chosen as a case study for evaluation. Since this frame building is a slab block, the lateral resistant capacity of a weakest sub-frame would represent the capacity of the whole frame for conservative consideration. Therefore, in this section, the FEA model of the critical frame as shown in Figure 2.1(b) is presented, and the seismic adequacy is discussed based on the FEA results.

6.5.1. FEA modeling

6.5.1.1. Building under study and model layout

The plan view of the 4-story building is shown in Figure 2.1(a). The elevation view of the selected critical sub-frame is shown in Figure 6.37. The first story height is 3.2m and the height of other three stories is 2.7m. Design compressive strength of concrete is 20 MPa.

There are four columns: A, B, C and D in the sub-frame. Dimensions and reinforcement details of columns and beams are listed in Table 6.12. As can be seen from table 6.12, the dimensions and longitudinal reinforcing bars of columns vary with the story, while those of beams are identical. The slab thickness is 100 mm and the width of beams and columns is 200 mm. Longitudinal reinforcing bars in members have design yield strength of 460 MPa, and transverse reinforcing bars (shear links) have design yield strength of 250 MPa. The case for f_{cu} =20 MPa, under common loading is investigated herein. The dead load due to finishes and partition is assumed to be 1.2 kN/m^2 and 1.0 kN/m^2 and the density of concrete is assumed to be 24 kN/m^3.

Thus, unfactored dead loads calculated for the typical floors and the roof floor (no partition on the roof floor) are 4.6 kN/m^2 and 3.6 kN/m^2, respectively. Unfactored live load is taken as 1.5 kN/m^2.

The structure was modeled using 2D RUAUMOKO (Carr 2002a). In the FEA model, to be conservative, infill walls were not included as the structural components for simplicity. It was assumed that foundation would not govern the failure in an earthquake, so the boundary conditions of the bases of columns were assumed as fixed end. Effective stiffness reduction factors for columns and beams were taken as 0.58 and 0.35.

6.5.1.2. FEA meshing

Columns and beams were modeled with frame-type RC beam-column element and one component beam element respectively, with the appropriate reduced stiffness. Figure 6.38 shows the FEA meshing and denotation of nodes, elements and sectional properties. There are 20 nodes, 28 elements and 11 sectional properties in the FEA model. Among the 20 nodes, nodes 6, 10, 14 and 18 are master nodes of floors 1-4. Among the 28 elements, elements 1-16 are used to model columns, and elements 17-28 are used to model beams. Among the 11 element sections, sections 1-9 are for columns, section 10 is for typical story beams, and section 11 is for roof beams.

6.5.1.3. Member properties

The definition of a cross section in 2D dimension involved elastic section properties (elastic Young modulus, shear modulus, cross-sectional area, effective moment of inertia, and weight of the member), initial force (distributed self-weight), yield surfaces and hysteresis rules. The details of the input values are as follows.

Elastic sectional properties

Elastic (Young's) modulus of the concrete (E), shear modulus (G), cross-sectional area, effective shear area were calculated using the equations given in Appendix A. For the case of f_{cu} =20 MPa, E =19.92GPa and G =7.88GPa. Moment of inertia I was calculated by multiplying the value of the gross section by the reduction factors (that is, 0.58 for columns and 0.35 for beams). Weight/unit length (WGT) was taken as 0, and input of mass was incorporated as nodal lump weight in WEIGHT option. Values of the elastic sectional properties are listed in Table H.4 in Appendix H. The lengths of the plastics hinges were taken as 1.0h for columns and 0.5h for beams as specified in Chapter 3.

Yield surface of the members

The contributions of reinforcing bars were through the calculation of yield moment surfaces. The method to calculate the seven parameters (*PYC*, *PB*, *MB*, *M1B, M2B, M0* and *PYT*) used to define the interaction yield surface is given in Appendix A.2. For the beam, the interaction between axial load and moment is neglected, so that

only the yield moment, calculated as shown in Appendix A.3, is needed for input. Values of these parameters are listed in Table H.5 in Appendix H.

Hysteresis rule

The stiffness degradation was considered by defining hysteresis rules. The Modified Takeda Hysteresis model (as shown in Figure 1.3) was adopted, and the parameters of α and β obtained from the tests were used: $\alpha = 0.5, \beta = 0.1$ for columns and $\alpha = 0.4, \beta = 0.1$ for beams. The bilinear factor r was calculated according to Appendix A.5, and the results are listed in Table H.4 in Appendix H

6.5.1.4. Boundary conditions

Boundary conditions of the base of columns were simulated as fixed ends. To simulate the diaphragm effects of slabs, nodes on each floor were slaved to the corresponding master node. The slaved degrees of freedoms was x direction translation.

6.5.1.5. Vertical and lateral loads

Vertical loads and masses are input in RUAUMOKO separately. Self-weights of columns were considered as the initial axial loads in elements when member properties were defined (As listed in Table H.4 in Appendix H). Distributed loads on beams were

considered as equivalent nodal loads in the input of LOAD option. In the study herein, weights were applied as nodal weights.

Based on the fundamental periods calculated in the modal analysis (0.52 second) and equation (6.10), the loading shape for pushover analysis was calculated. The resulted lateral loads (corresponding to a base shear demand of 1% of the total gravity load) are 1.16kN for the 1st floor level, 2.02kN for the 2nd, 2.93kN for the 3rd floor levels, and 3.46kN for the 4th floor level.

As shown in Figure 6.20, the predominant period of the surface acceleration response spectra of MP site is 0.74s, which is close to the fundamental period of the structure. Thus, one of the surface accelerograms of MP site was selected as the input ground motion in the dynamic collapse analysis.

6.5.2. FEA results and seismic adequacy evaluation

The V_b / W_g vs. Δ / H curve obtained from the pushover analysis, is shown in Figure 6.39, in which, the total unfactored dead load of the sub-frame W_g = 957.44kN, and the total height of the building H=11.3m. The first local failure is a local flexural failure, which occurred at the bottom of column C (Element 3 as shown in Figure 6.39), when V_b / W_g=45.7% and Δ / H =0.601%. In Figure 6.39, the point corresponding to this 1st flexural failure is shown. The response corresponding to this point is considered as the capacity of the structure. It is noted that the capacity value of V_b / W_g is far more than the shear demand from the design earthquake, which is around

10% of the gravity load. This shows that the sub-frame under study has high lateral resistant capacity even if it was designed without any seismic provision.

Results of maximum V_b / W_g and maximum Δ / H in the dynamic collapse analysis are also compared in Figure 6.39. It is observed that points from the dynamic collapse analysis match with the curve of the pushover analysis in a reasonable range. In order to find out the local moment failure point in the dynamic collapse analysis, the relationship between V_b / W_g and moment in the critical member (Element 3) is shown in Figure 6.40. The ordinate is in the form of percentage of the moment capacity of Element 3, so the point corresponding to 100 percent in the ordinate is the local failure point. As can be seen from Figure 6.40, the value of V_b / W_g corresponding to the local moment failure in the dynamic collapse analysis is 43.7%, which is quite close to the corresponding value of 45.7% in the pushover analysis.

As shown in Figure 6.39, when scaling factor equal to 1, the corresponding values are V_b / W_g=1.71% and Δ / H=0.019%. These values are much less than the values corresponding to the local flexural failure. In order to find out to which scale of the design earthquake that the structure can survive without any failure, the relationship between scaling factors and moment in the critical member is plotted (as shown in Figure 6.41.) As can be seen from Figure 6.41, the scaling factor corresponding to the local failure is 20.7.

It is shown in the above analysis that the V_b / W_g corresponding to the failure is much larger than the shear demand, and the sub-frame can resistant up to 20.7 times

the base motions due to the design earthquake. Thus, the 4-story HDB building under study is safe enough for the design earthquake.

Because the natural periods of the low-rise buildings are quite small (often less than 0.5s), and much less than the predominant period of bedrock motions (1.6s) and the natural period of soft soils (1.6s to 1.8s) that are characteristics of far-field-effects of earthquakes, the possibility of resonance effects in the buildings and the influence of the soil amplification effect is small. Although it may not be enough for only the case study 2 to conclude that all low-rise buildings in Singapore is safe in the worst earthquake, the possibility for low-rise building in Singapore to suffer some damage is very low.

6.6. Summary

The seismic vulnerability of frame and shear wall structures in Singapore was evaluated by comparing the demand and capacity curves through two case studies: a 25-story shear wall-frame structure and a 4-story sub-frame structure.

Based on the data of recent two strong earthquakes (2004 Aceh earthquake and 2005 Nias earthquake), the worst earthquake scenario (design earthquake) was updated to Mw=9.5, 600km away from Singapore, and the corresponding seismic demand for buildings in Singapore due to the design earthquake was obtained, by consider the amplification of soft soil profiles. Reliable and elegant FEA models, validated by test results (as described in Chapter 2 to 5), were developed to determine the capacity of full scale buildings in the case studies.

Case study 1 reveals that for certain cases, high-rise buildings built in 1970s in Singapore may suffer damage due to the worst possible earthquake. For buildings that do not meet the demand, a retrofitting scheme using FRP system was proposed. The members require retrofitting and the amount of FRP laminates needed can be found by the proposed FEA analytical method. Case study 2 shows that the possibility of low-rise buildings in Singapore to suffer from damage in a scenario of the worst earthquake is low.

Table 6.1 Comparison of the motions due to the Aceh earthquake in December 2004 and the Nias earthquake in March 2005

East-west direction	Aceh	Nias
Peak acceleration at bedrock(m/s^2)	0.007	0.018
Period corresponding to the peak acc. at bedrock (s)	5.52	4.37
Peak acceleration at surface(m/s^2)	0.03	0.093
Period corresponding to the peak acc. at surface (s)	0.84	0.84
Maximum amplification factor	11.5	13.1
North-south direction	Aceh	Nias
Peak acceleration at bedrock(m/s^2)	0.011	0.04
Period corresponding to the peak acc. at bedrock (s)	4.29	3.11
Peak acceleration at surface(m/s^2)	0.034	0.118
Period corresponding to the peak acc. at surface (s)	0.84	0.84
Maximum amplification factor	10.1	6.27

Note: amplification factor is obtained by dividing the acceleration at the surface by the corresponding acceleration at the bedrock.

Table 6.2 Prediction of peak rock motion

Event	Magnitude		Distance	Peak rock motion	Peak rock motion
	M_L	M_w	(km)	(gals)(computed)	(gals)(measured)
Burma,1912		8	400	5.5	5-10
Burma,1912		8	300	12.5	11-14
Burma,1930		7.2	400	2.4	1-4
Burma,1930		7.2	300	6	2-10
Sumatra,1926	6.75		250	11.6	7-14
Sumatra,1998	6.8		600	0.42	0.31
Sumatra,2000	7.9		700	0.69	0.36
Sumatra,2004		9.3	950	1.11	0.30
Sumatra,2005		8.7	600	3.02	2.62

Note: 1gals=0.1%g, g=9.81 is the gravity of acceleration

Table 6.3 Soil data for the Marine Parade (MP) site

No.	Description	t	N_{SPT}	ρ	S	w
1	Backfill-very loose light yellowish brown clayey SAND. Ground water is 3.0m below ground	6.00	2.5	35	-	19.70
2	Soft grey marine CLAY	3.00	0*	-	14.0	16.30
3	Loose brownish-yellowish and whitish grey silty SAND	3.00	8	45	-	18.00
4	Medium dense light whitish grey silty SAND	3.00	19	60	-	19.10
5	very loose yellowish brown silty SAND	3.00	4	35	-	18.00
6	Stiff light bluish grey sandy SILT	3.00	12	-	50.0	17.70
7	Very stiff dark brown and bluish grey silty CLAY	9.00	21	-	87.5	20.30
8	Hard bluish grey silty CLAY	3.00	46	-	191.7	20.30
9	Hard reddish brown and blueish grey silty CLAY	6.45	79	-	330.6	22.00
10	Bedrock	-	100		0.0	22.00
	Total soil depth	39.45				

t= thickness (m)

N_{SPT} = N value of the standard penetration test for soil (blow/30cm)

ρ= relative density (%)

S= undrained shear strength (kN/m^2)

w= Unit weight (kN/m^3)

Note: * means a nominal value of 1 was used

Table 6.4 Soil data for the Katong Park (KAP) site

No.	Description	t	N_{SPT}	ρ	S	w
1	Fill-brownish grey. Loose clayey silt with some fine to coarse grain sand. Below ground level of 1.5m material becomes loose SAND	6.50	11	35	-	17.3
2	Upper marine CLAY-blueish grey. Very soft ,high plasticity and high water content. Ground water table is at this level	13.00	0*	-	21.6	15.6
3	CLAY-stiff brown, low water content, moderate plasticity	2.00	15	-	59.9	18.7
4	Lower marine CLAY-blueish grey. Very soft,high plasticity and high sensitive silt clay	9.00	0*	-	23.9	16.2
5	Organic CLAY-very soft, very sensitive, highwater content, lots of organic material	4.00	2	-	26.3	16.2
6	Stiff to very stiff silty CLAY-low water content, moderate plasticity	5.00	13	-	52.0	18.7
7	Slightly weathered silty SAND-very dense and stiff	5.90	75	100	-	21.1
8	Slightly weathered SILT-very stiff	1.90	100	-	400.0	22.0
9	Bedrock	-	100	-	-	22.0
	Total soil depth	47.30				

Note: * means a nominal value of 1 was used

Table 6.5 Soil data for the Katong area (KAT) site

No.	Description	t	N_{SPT}	ρ	S	w
1	Fill-loose fine SAND	7.9	5	35	-	17.1
2	Marine CLAY-very soft to medium stiff	27.9	2	-	18.7	16.2
3	CLAY-reddish brown,medium stiff with organic matter	13.2	10	-	40.2	20.3
4	CLAY-medium stiff to stiff	4.2	50	-	200.0	20.3
5	Bedrock	-	100	-		21.1
	Total soil depth	53.2				

Table 6.6 Fundamental period obtained from the modal analysis

Direction	f_{cu}=20MPa	f_{cu} =20MPa	f_{cu} =30MPa	f_{cu} =30MPa
	Ultimate load	Common load	Ultimate load	Common load
x	2.82s	2.79s	2.56s	2.52s
y	1.94s	2.02s	1.75s	1.80s

Table 6.7 Gravity loads and lateral forces (1% of the total gravity loads) applied at the story levels (unit: kN)

Story	Dead load	Force f_{cu}=20MPa ultimate load		Force f_{cu}=20Mpa common load		Force f_{cu}=30Mpa ultimate load		Force f_{cu}=30Mpa common load	
		x	y	x	y	x	y	x	y
1	1632.89	0.08	0.15	0.08	0.15	0.08	0.23	0.08	0.21
2	1632.89	0.30	0.51	0.30	0.51	0.30	0.70	0.31	0.66
3	1632.89	0.68	1.05	0.68	1.05	0.68	1.35	0.70	1.28
4	1627.11	1.21	1.73	1.21	1.73	1.21	2.15	1.23	2.05
5	1626.03	1.89	2.57	1.89	2.57	1.89	3.08	1.92	2.96
6	1620.26	2.71	3.53	2.71	3.53	2.71	4.12	2.74	3.99
7	1585.89	3.62	4.53	3.62	4.53	3.62	5.17	3.65	5.03
8	1573.74	4.69	5.68	4.69	5.68	4.69	6.36	4.72	6.22
9	1572.77	5.93	6.99	5.93	6.99	5.93	7.69	5.97	7.54
10	1560.50	7.26	8.34	7.26	8.34	7.26	9.04	7.30	8.90
11	1560.50	8.78	9.87	8.78	9.87	8.78	10.55	8.83	10.41
12	1542.46	10.33	11.37	10.33	11.37	10.33	12.00	10.38	11.87
13	1541.38	12.12	13.08	12.12	13.08	12.12	13.65	12.16	13.53
14	1535.60	14.00	14.85	14.00	14.85	14.00	15.32	14.04	15.23
15	1535.60	16.07	16.76	16.07	16.76	16.07	17.13	16.10	17.06
16	1531.27	18.24	18.73	18.24	18.73	18.24	18.96	18.26	18.91
17	1531.27	20.59	20.83	20.59	20.83	20.59	20.91	20.60	20.90
18	1531.27	23.08	23.04	23.08	23.04	23.08	22.93	23.08	22.96
19	1525.49	25.62	25.24	25.62	25.24	25.62	24.93	25.61	25.00
20	1523.33	28.35	27.59	28.35	27.59	28.35	27.04	28.32	27.16
21	1523.33	31.25	30.06	31.25	30.06	31.25	29.26	31.21	29.43
22	1522.24	34.27	32.61	34.27	32.61	34.27	31.52	34.21	31.75
23	1522.24	37.46	35.26	37.46	35.26	37.46	33.87	37.37	34.16
24	1522.24	40.79	38.00	40.79	38.00	40.79	36.28	40.68	36.64
25	1352.91	39.34	36.29	39.34	36.29	39.34	34.44	39.21	34.82

Table 6.8 Results of the RUAUMOKO pushover and dynamic collapse analysis

		f_{cu}=20MPa ultimate loading	f_{cu}=20MPa common loading	f_{cu}=30MPa ultimate load	f_{cu}=30MPa common load
Pushover analysis in y direction at failure	V_b/W_g(%)	3.31	3.29	3.81	3.76
	Δ/H(%)	0.134	0.126	0.126	0.118
	failure mode	Local shear failure	Local shear failure	Local shear failure	Local shear failure
Dynamic analysis in y direction at failure	V_b/W_g(%)	3.37	3.29	3.72	3.89
	Δ/H(%)	0.134	0.125	0.125	0.120
	failure mode	Local shear failure	Local shear failure	Local shear failure	Local shear failure
	scale	1.08	1.07	0.77	0.79
Dynamic in y direction when scale=1	V_b/W_g(%)	2.86	3.05	5.20	5.28
	Δ/H(%)	0.122	0.116	0.157	0.153
Pushover analysis in x direction at failure	V_b/W_g(%)	4.81	4.73	5.52	5.38
	Δ/H(%)	0.419	0.384	0.413	0.379
	failure mode	Local shear failure	Local shear failure	Local shear failure	Local shear failure
Dynamic analysis in x direction at failure	V_b/W_g(%)	4.76	4.93	5.40	5.11
	Δ/H(%)	0.460	0.447	0.389	0.347
	failure mode	Local shear failure	Local shear failure	Local shear failure	Local shear failure
	scale	4.00	3.90	3.51	3.30
Dynamic in x direction when scale=1	V_b/W_g(%)	1.91	2.03	2.24	2.48
	Δ/H(%)	0.138	0.127	0.143	0.148

Table 6.9 Minimum thickness requirement and layers of GFRP sheets needed for retrofitting (f_{cu}=30 MPa, ultimate loading case, in y direction)

Member	Demand (kN)	Capacity (kN)	V_f (kN)	Thickness (mm)	Layers required	Layers used
I1 1st story	1842	1250	592	0.545	1.54	2
I1 2nd story	1838	1250	588	0.541	1.53	2
I1 3rd story	1828	1250	578	0.532	1.51	2
I1 4th story	1811	1250	561	0.516	1.46	2
I1 5th story	1782	1250	532	0.489	1.39	2
I1 6th story	1775	1250	525	0.483	1.37	2
I1 7th story	1766	1250	516	0.475	1.34	2
I1 8th story	1698	1250	448	0.412	1.17	2
I1 9th story	1634	1250	384	0.353	1.00	2
I1 10th story	1577	1250	327	0.301	0.85	1
I1 11th story	1502	1250	252	0.232	0.66	1
I1 12th story	1441	1250	191	0.176	0.50	1
I1 13th story	1357	1250	107	0.098	0.28	1
I1 14th story	1276	1250	26	0.024	0.07	1

Table 6.10 Minimum thickness requirement and layers of GFRP sheets needed for retrofitting (f_{cu}=30 MPa, common loading case, in y direction)

Member	Demand (kN)	Capacity (kN)	V_f (kN)	Thickness (mm)	Layers required	Layers used
I1 1st story	1976	1250	726	0.668	1.89	2
I1 2nd story	1970	1250	720	0.662	1.88	2
I1 3rd story	1958	1250	708	0.651	1.85	2
I1 4th story	1939	1250	689	0.634	1.80	2
I1 5th story	1908	1250	658	0.605	1.71	2
I1 6th story	1899	1250	649	0.597	1.69	2
I1 7th story	1891	1250	641	0.590	1.67	2
I1 8th story	1822	1250	572	0.526	1.49	2
I1 9th story	1756	1250	506	0.466	1.32	2
I1 10th story	1698	1250	448	0.412	1.17	2
I1 11th story	1619	1250	369	0.339	0.96	1
I1 12th story	1554	1250	304	0.280	0.79	1
I1 13th story	1465	1250	215	0.198	0.56	1
I1 14th story	1379	1250	129	0.119	0.34	1
I1 15th story	1278	1250	28	0.026	0.07	1

Table 6.11 Minimum thickness requirement and layers of GFRP sheets needed for retrofitting (f_{cu}=20 MPa, common loading case, in y direction)

Member	Demand (kN)	Capacity (kN)	V_f (kN)	Thickness (mm)	Layers required	Layers used
I1 1st story	1368	1080	288	0.265	0.75	1
I1 2nd story	1365	1080	285	0.262	0.74	1
I1 3rd story	1359	1080	279	0.257	0.73	1
I1 4th story	1347	1080	267	0.246	0.70	1
I1 5th story	1326	1080	246	0.226	0.64	1
I1 6th story	1320	1080	240	0.221	0.63	1
I1 7th story	1315	1080	235	0.216	0.61	1
I1 8th story	1268	1080	188	0.173	0.49	1
I1 9th story	1222	1080	142	0.131	0.37	1
I1 10th story	1182	1080	102	0.094	0.27	1
I1 11th story	1128	1080	48	0.044	0.13	1
I1 12th story	1084	1080	4	0.004	0.01	1

Table 6.12 Dimensions and reinforcement details of members of the 4-story sub-frame

Members	Dimension	Longitudinal bars	Shear Link
Column A(1st story)	200mm x 600mm	6 x 16mm	6mm@140mm
Column A(2nd-4th story)	200mm x 600mm	6 x 13mm	6mm@140mm
Column B(1st story)	200mm x 900mm	8 x 16mm	6mm@140mm
Column B(2nd-4th story)	200mm x 900mm	8 x 13mm	6mm@140mm
Column C(1st story)	200mm x1100mm	10 x 16mm	6mm@140mm
Column C(2nd story)	200mm x 600mm	6 x 16mm	6mm@140mm
Column C(3rd-4th story)	200mm x 600mm	6 x 13mm	6mm@140mm
Column D(1st story)	200mm x 1000mm	10 x 16mm	6mm@140mm
Column D(2nd-4th story)	200mm x 1000mm	6 x 13mm	6mm@140mm
Beams	200mm x 500mm	4 x 20mm	8mm@250mm

Figure 6.1 Locations of the Aceh earthquakes occurred in 26 December 2004 and the Nias earthquake occurred in 28 March 2005

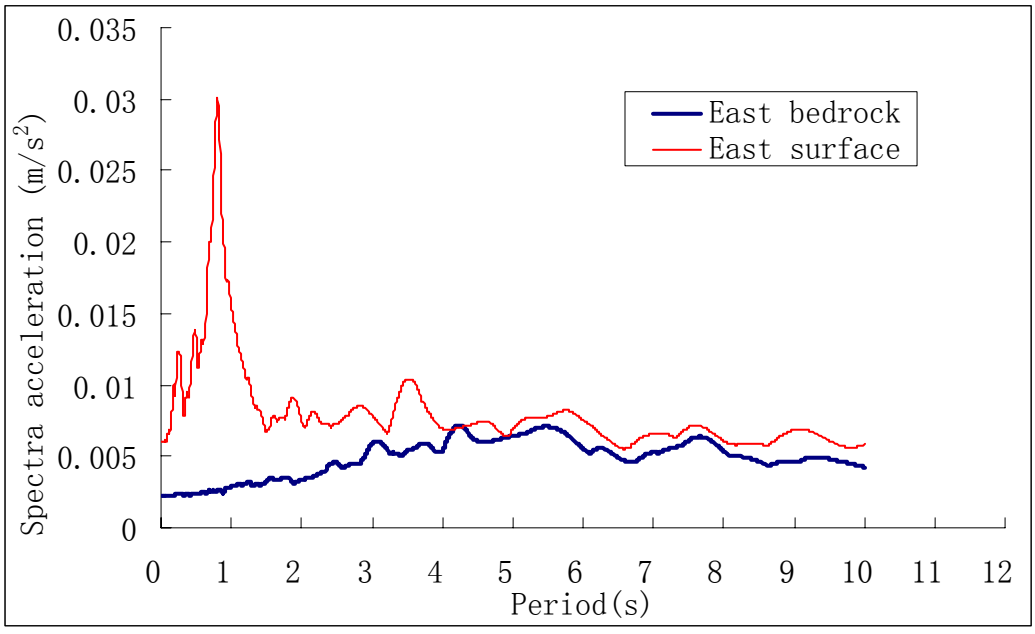

Figure 6.2 Acceleration response spectra of the Aceh earthquake (east-west direction)

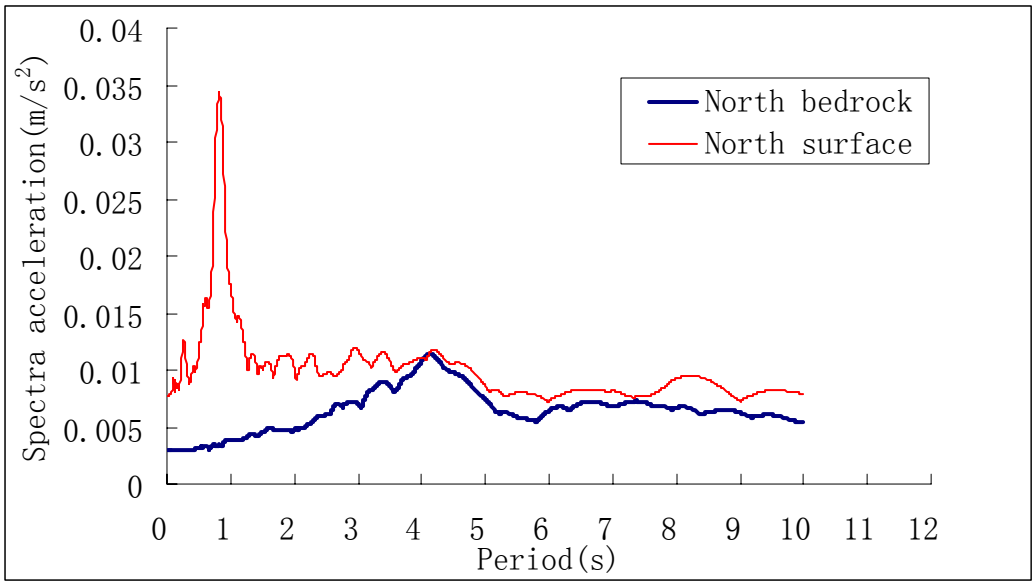

Figure 6.3 Acceleration response spectra of the Aceh earthquake (north-south direction)

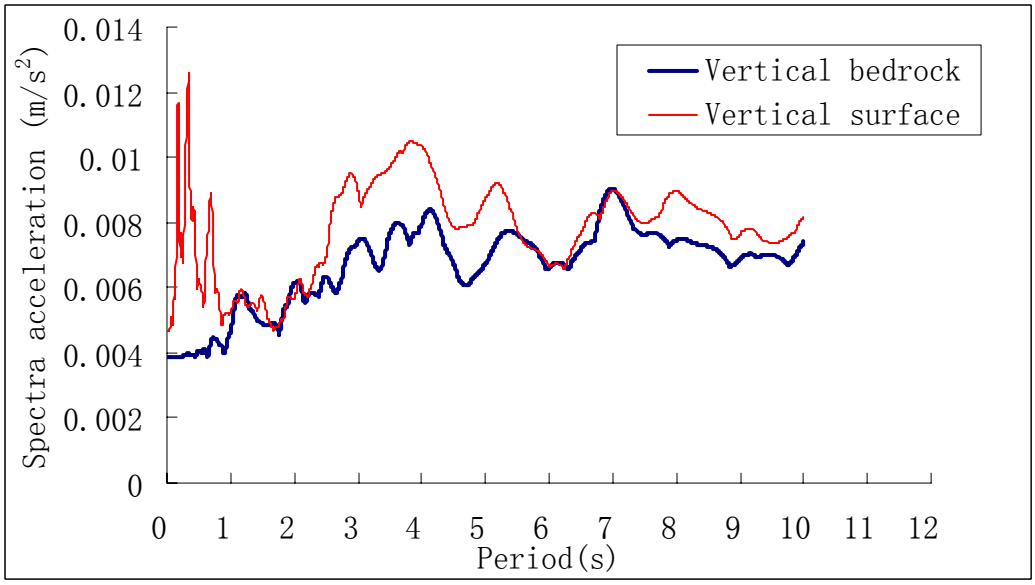

Figure 6.4 Acceleration response spectra of the Aceh earthquake (vertical direction)

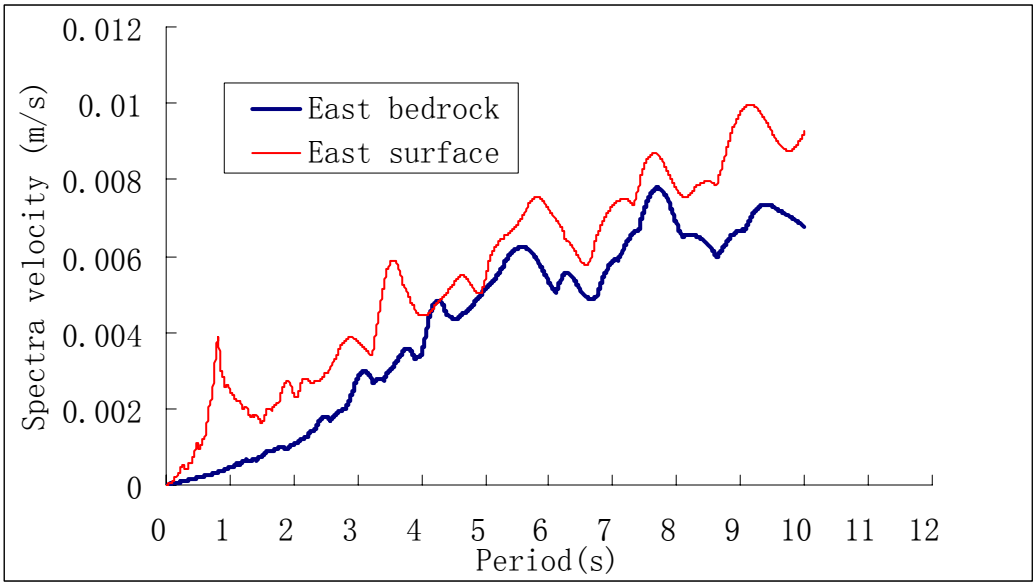

Figure 6.5 Velocity response spectra of the Aceh earthquake (east-west direction)

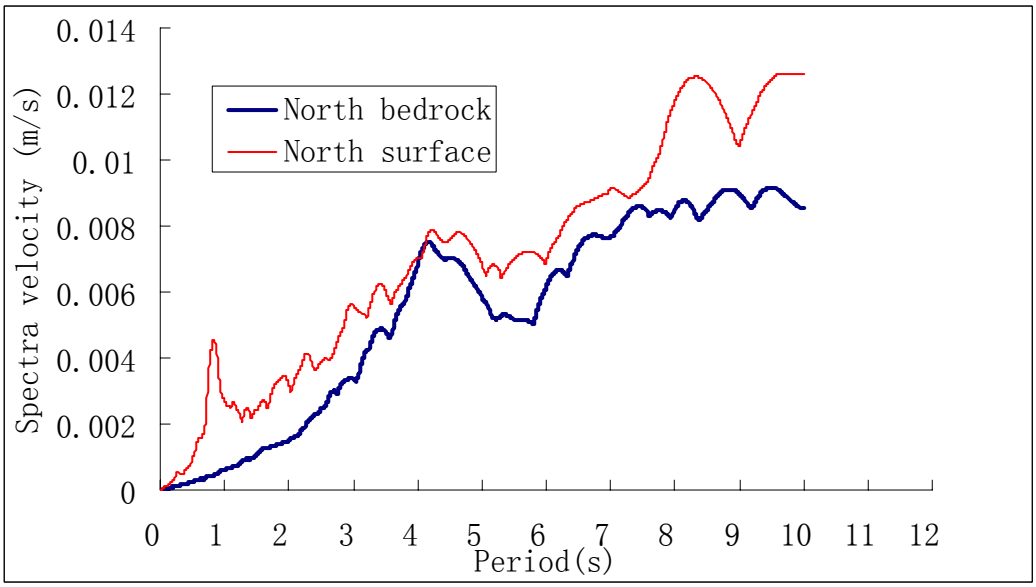

Figure 6.6 Velocity response spectra of the Aceh earthquake (north-south direction)

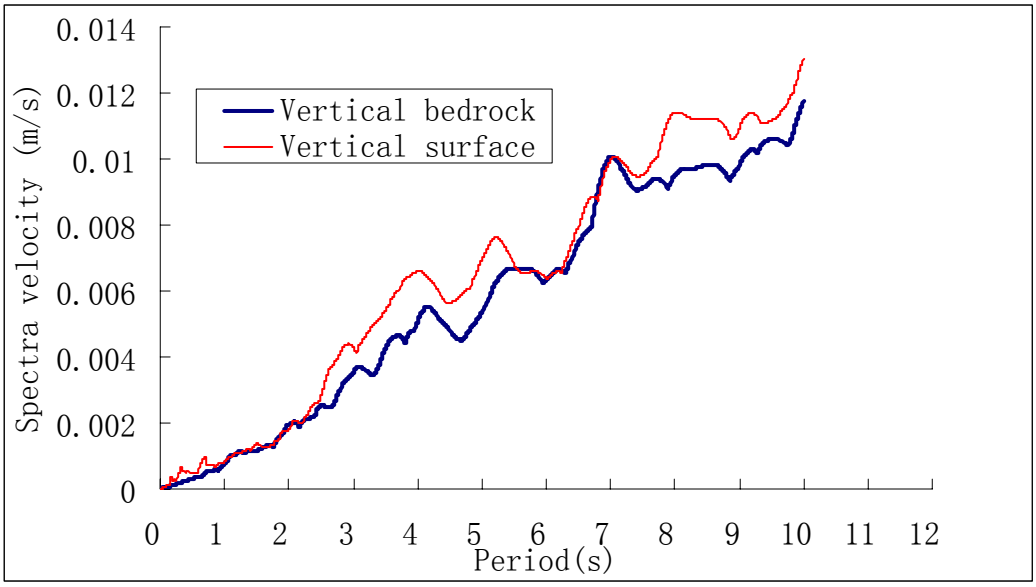

Figure 6.7 Velocity response spectra of the Aceh earthquake (vertical direction)

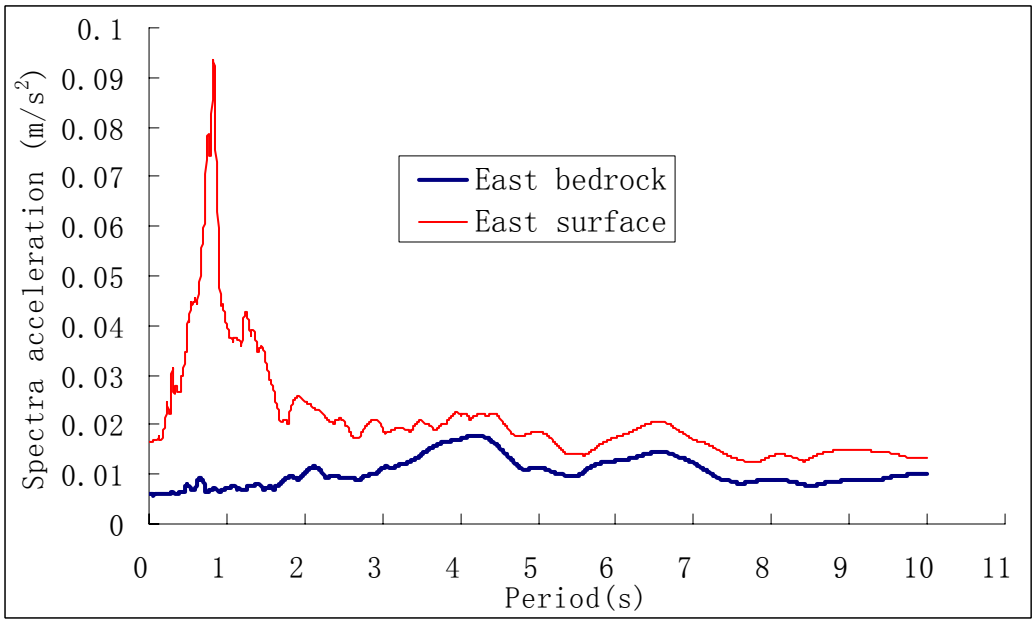

Figure 6.8 Acceleration response spectra of the Nias earthquake (east-west direction)

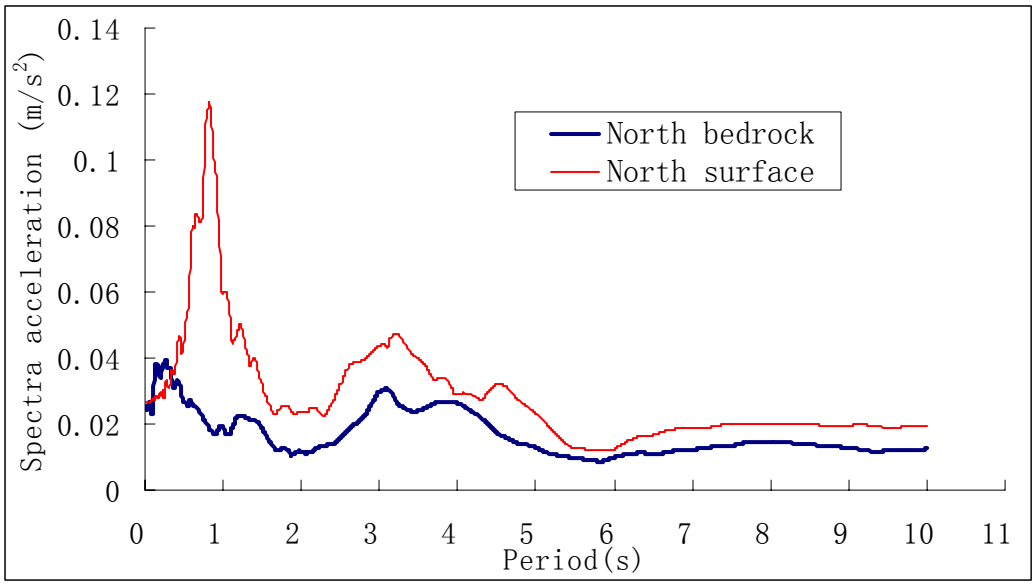

Figure 6.9 Acceleration response spectra of the Nias earthquake (north-south direction)

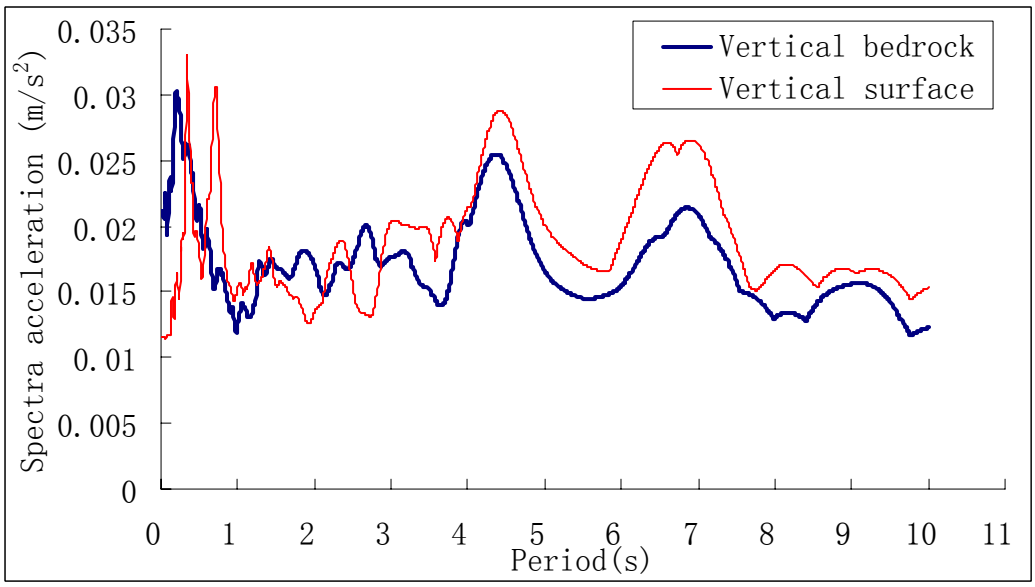

Figure 6.10 Acceleration response spectra of the Nias earthquake (vertical direction)

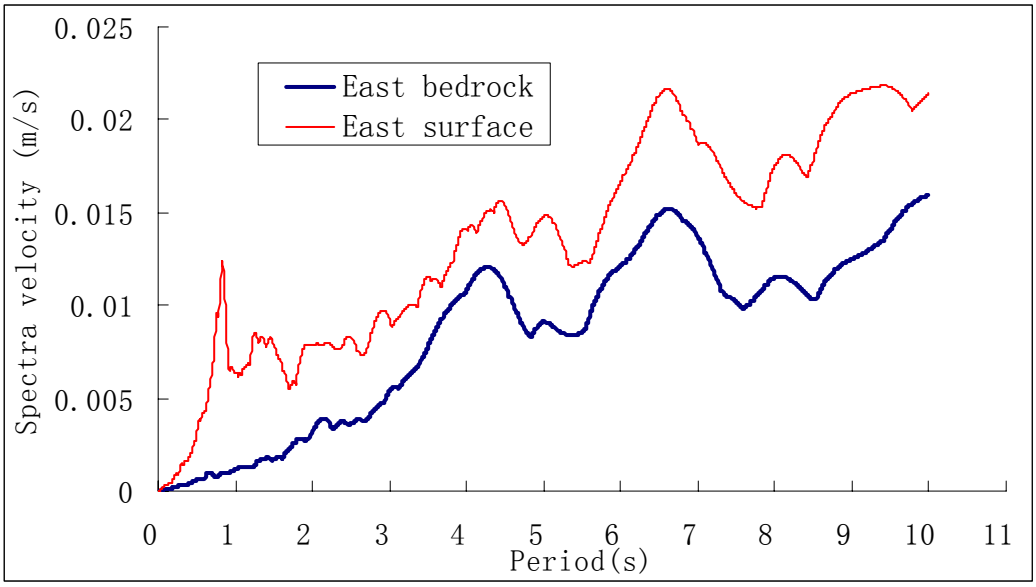

Figure 6.11 Velocity response spectra of the Nias earthquake (east-west direction)

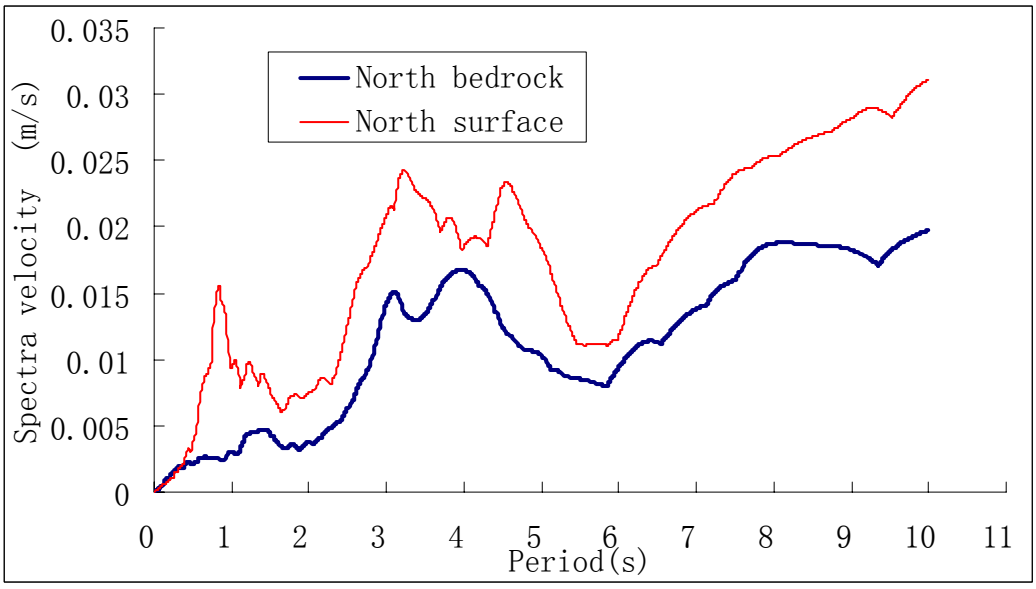

Figure 6.12 Velocity response spectra of the Nias earthquake (north-south direction)

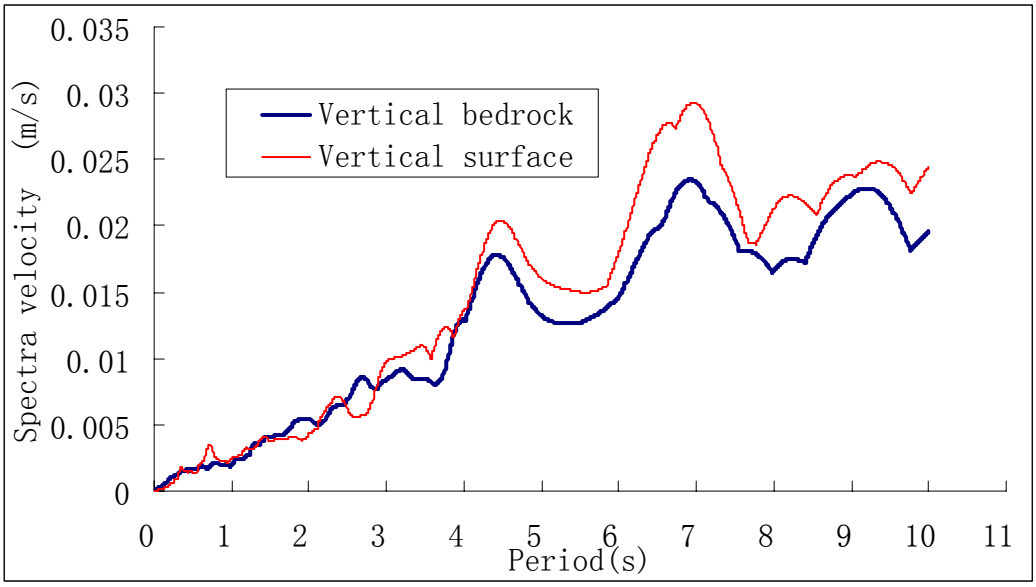

Figure 6.13 Velocity response spectra of the Nias earthquake (vertical direction)

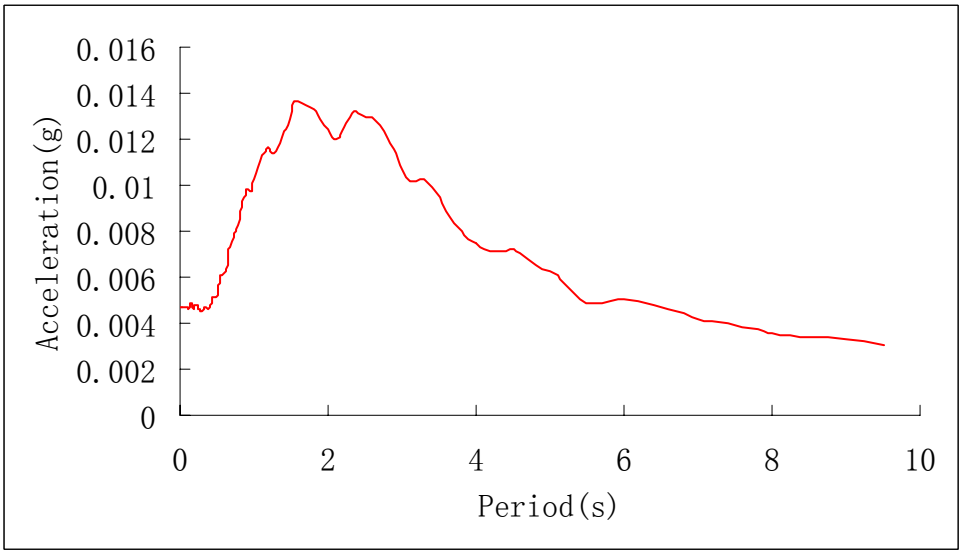

Figure 6.14 Average acceleration response spectra of the design earthquake at bedrock (M_w=9.5, 600 km away)

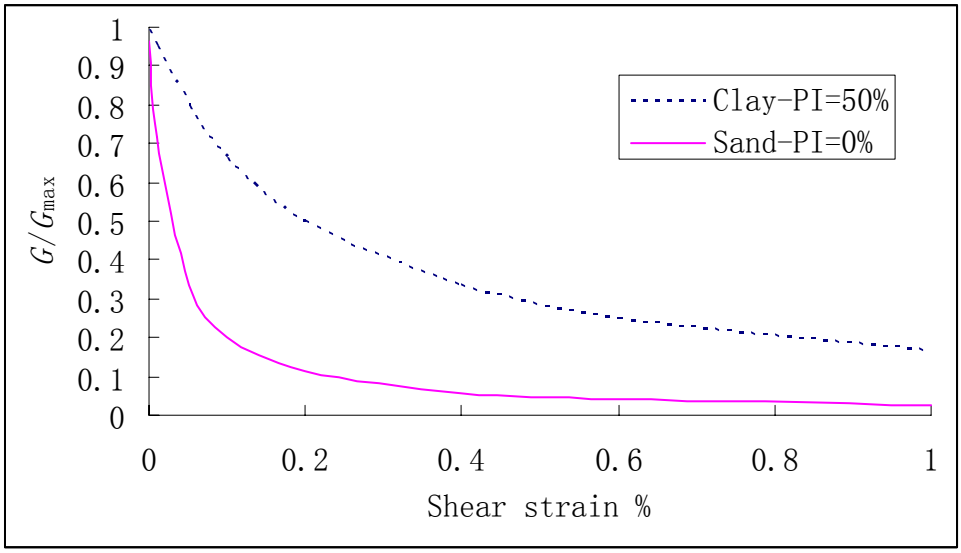

Figure 6.15 Shear modulus/ shear modulus at low strain 0.001% (G/G_{max}) vs. shear strain (%) for clay and sand

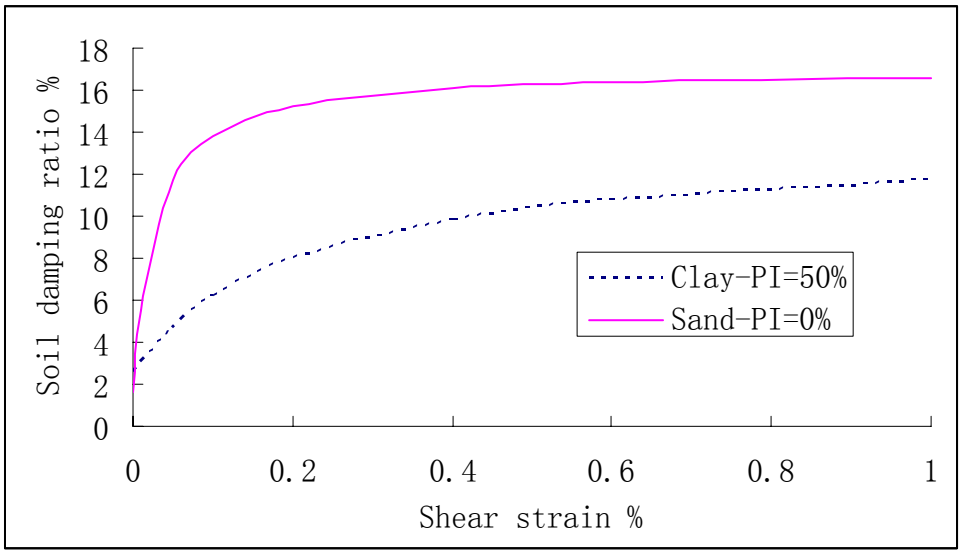

Figure 6.16 Soil damping ratio vs. shear strain(%) for clay and sand

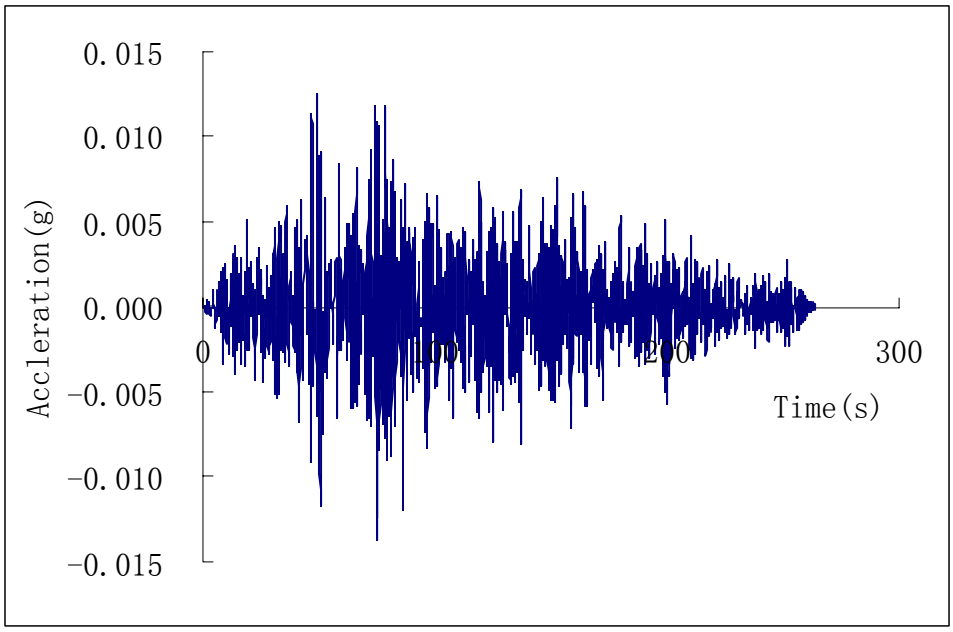

Figure 6.17 One of the twelve surface accelerograms of MP site due to design earthquake at bedrock

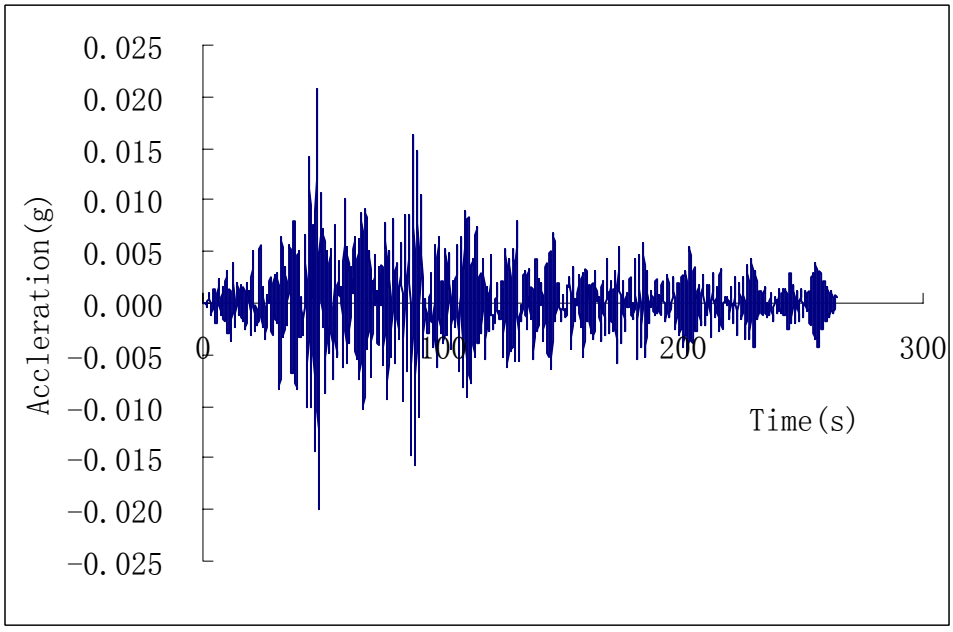

Figure 6.18 One of the twelve surface accelerograms of KAP site due to design earthquake at bedrock

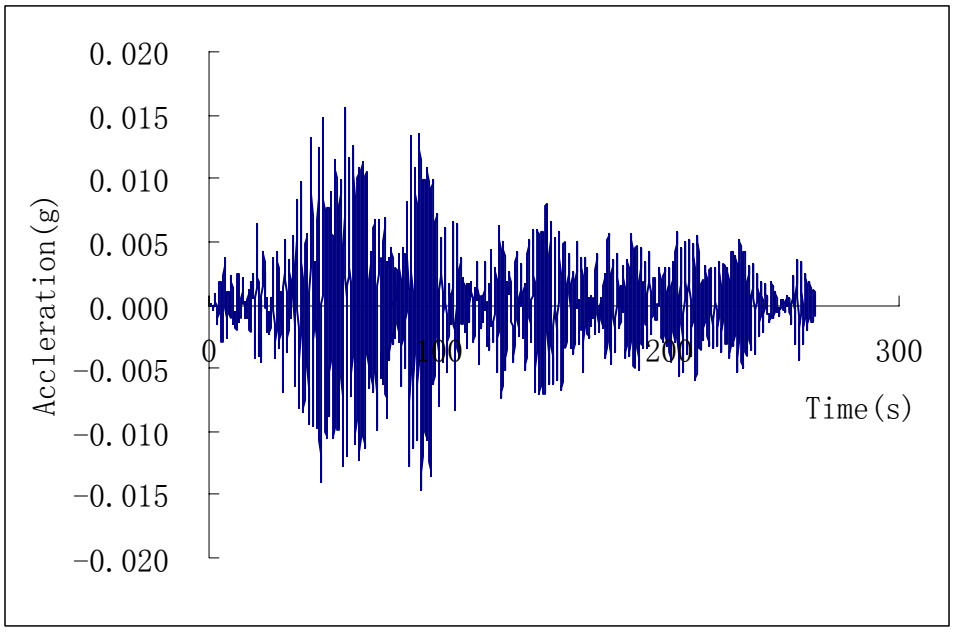

Figure 6.19 One of the twelve surface accelerograms of KAT site due to design earthquake at bedrock

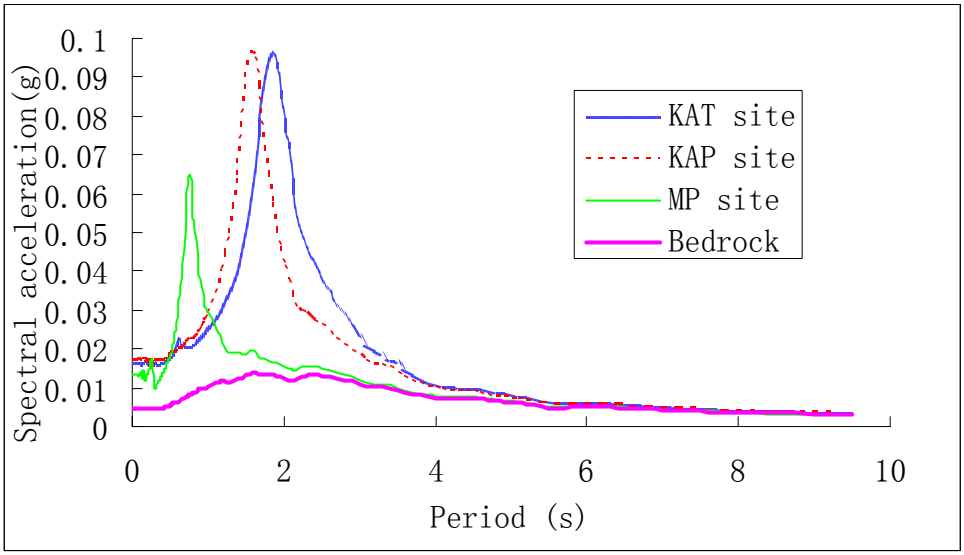

Figure 6.20 Average surface acceleration response spectra of the bedrock and selected MP, KAP and KAT sites for structural damping ratio of 5% due to the design earthquake.

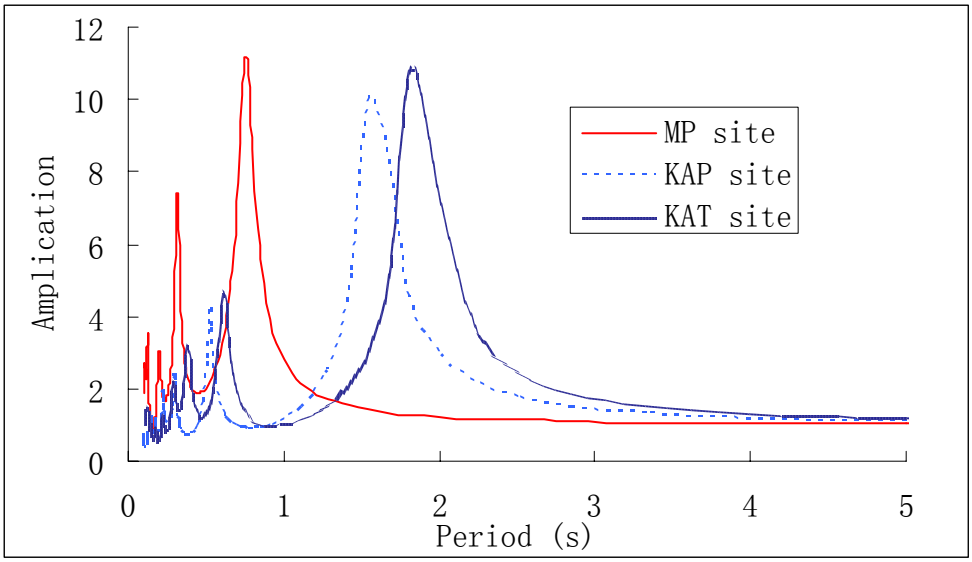

Figure 6.21 Average soil amplification factors (ratio of surface to bedrock spectral acceleration) for MP, KAP and KAT sites for structural damping ratio of 5% due to design earthquake at bedrock

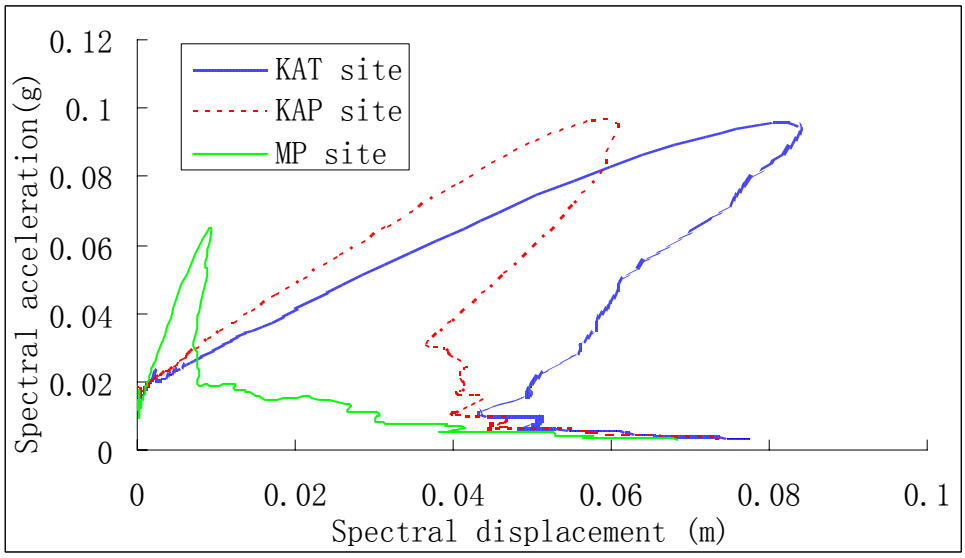

Figure 6.22 Spectral acceleration vs. spectral displacement curves for MP, KAP and KAT sites for structural damping ratio of 5% due to design earthquake at bedrock

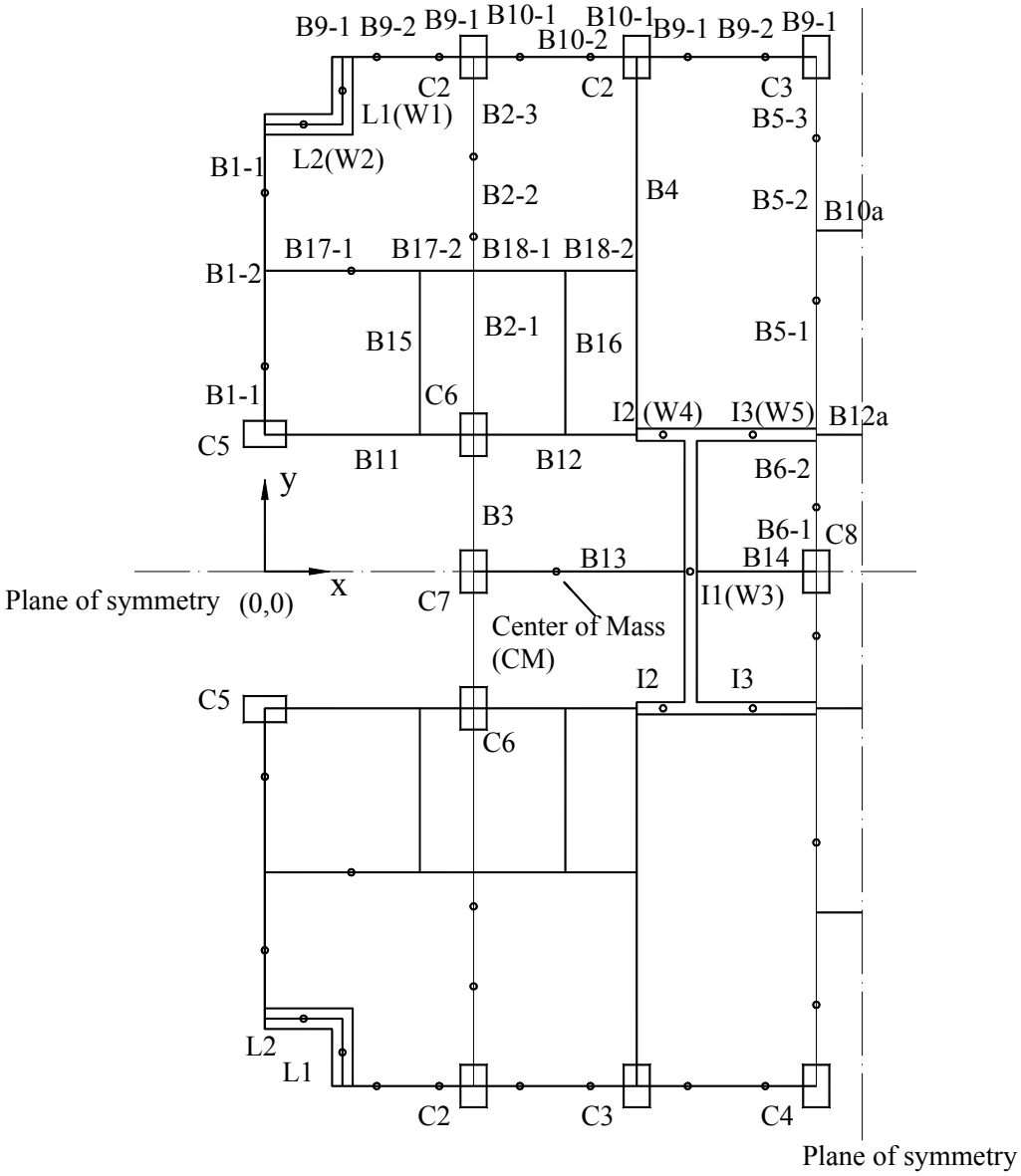

Figure 6.23 Typical story model layout of the 25-story building (plan view)

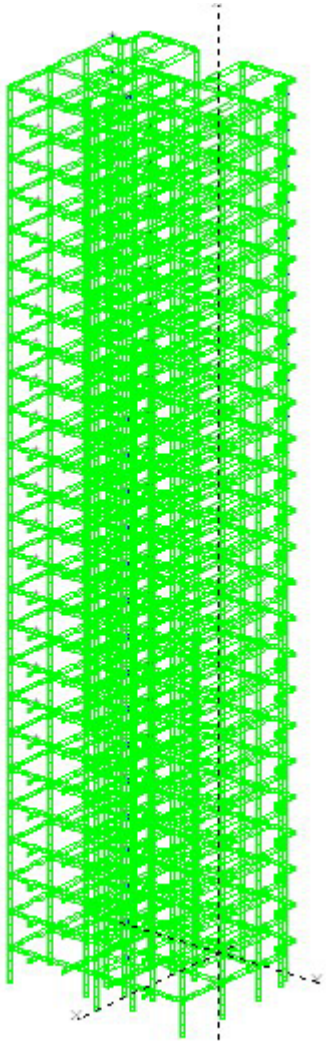

Figure 6.24 3D view of the FEA mesh of the 25-story building

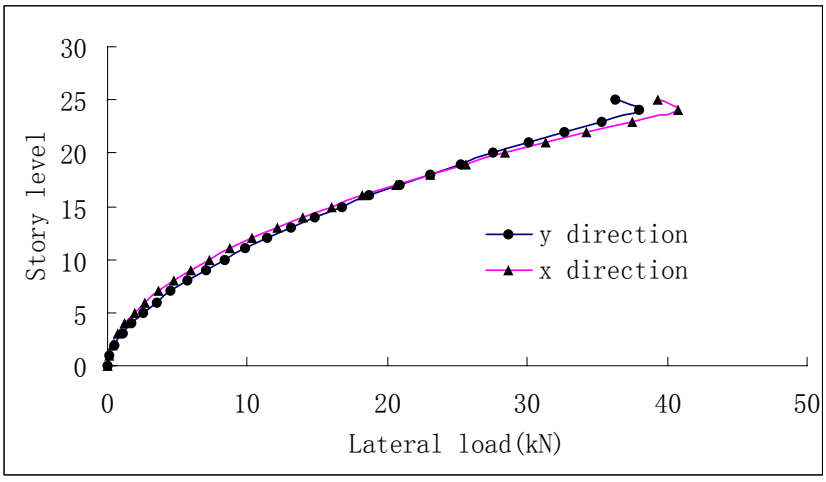

Figure 6.25 Loading shape for the pushover analysis (f_{cu} =20 MPa, ultimate loading case)

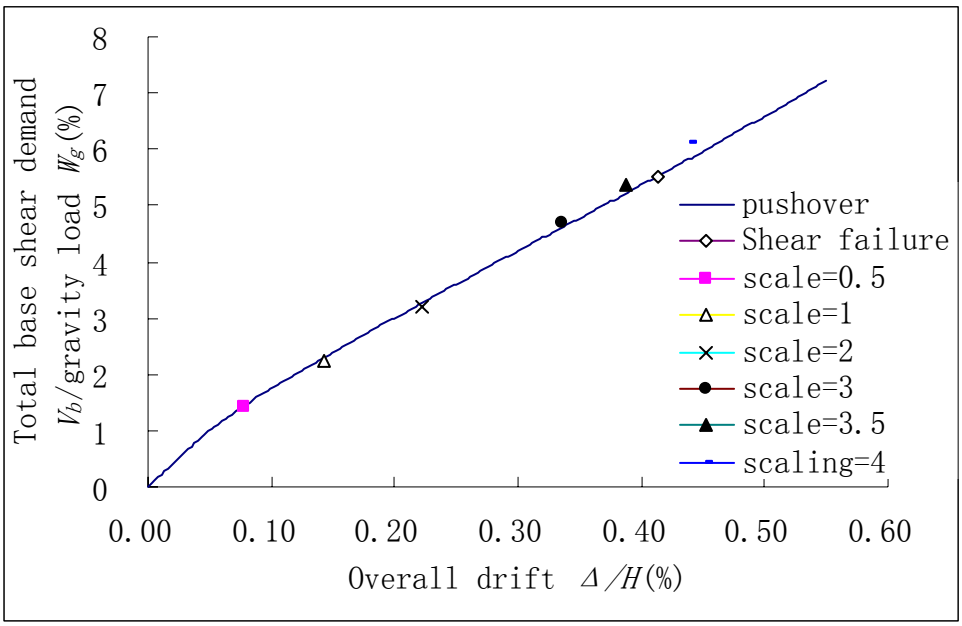

Figure 6.26 Total base shear demand V_b/ gravity load W_g vs. overall drift curve for the case of f_{cu} =30 MPa, ultimate loading, in x direction (W_g = 38866.12kN, H=64.75m)

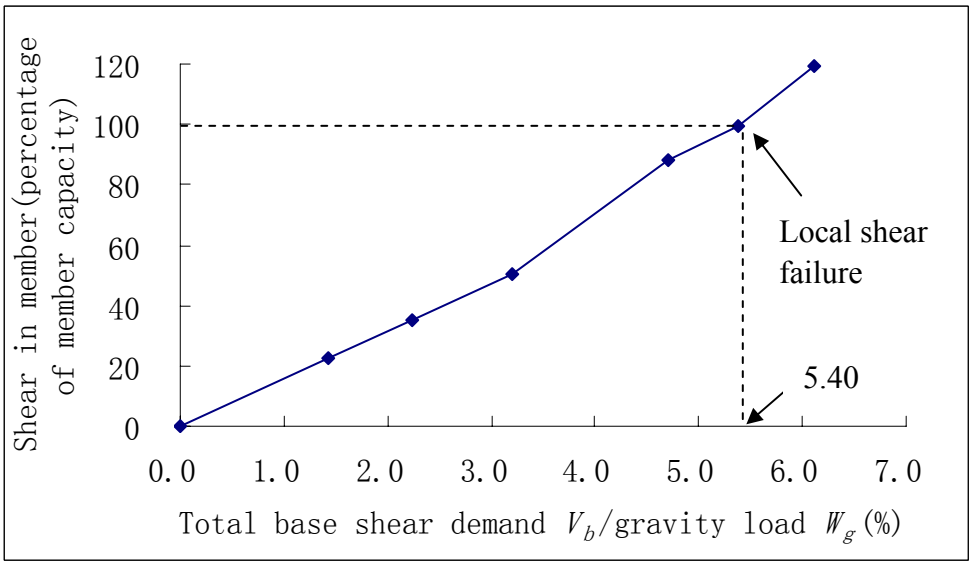

Figure 6.27 Relationship between V_b / W_g and shear forces in the critical member (1st story I-shape flange wall, I3) of the dynamic collapse analysis (f_{cu} =30 MPa, ultimate loading case, in x direction)

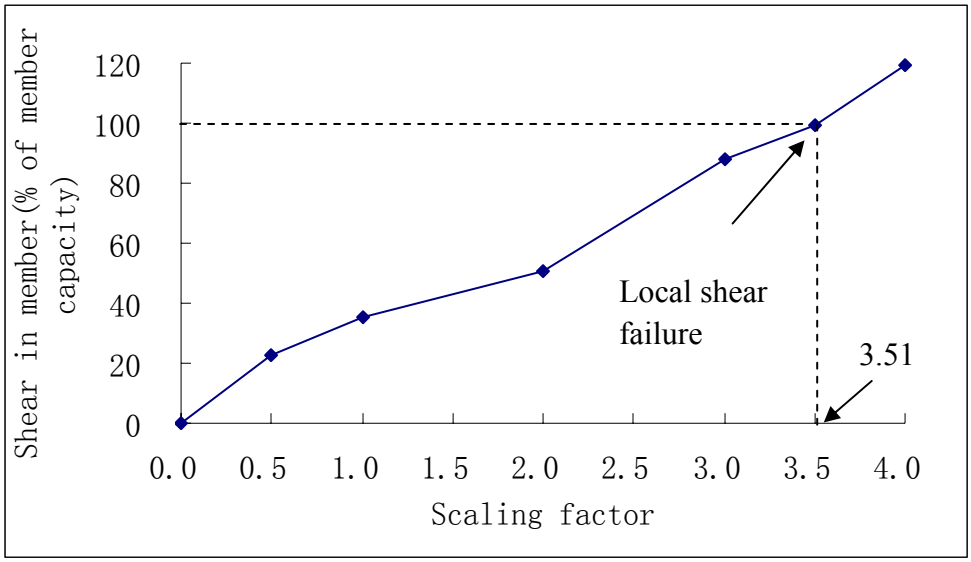

Figure 6.28 Relationship between scaling factors and shear forces in the critical member (1st story I-shape flange wall, I3) of the dynamic collapse analysis (f_{cu} =30 MPa, ultimate loading case, in x direction)

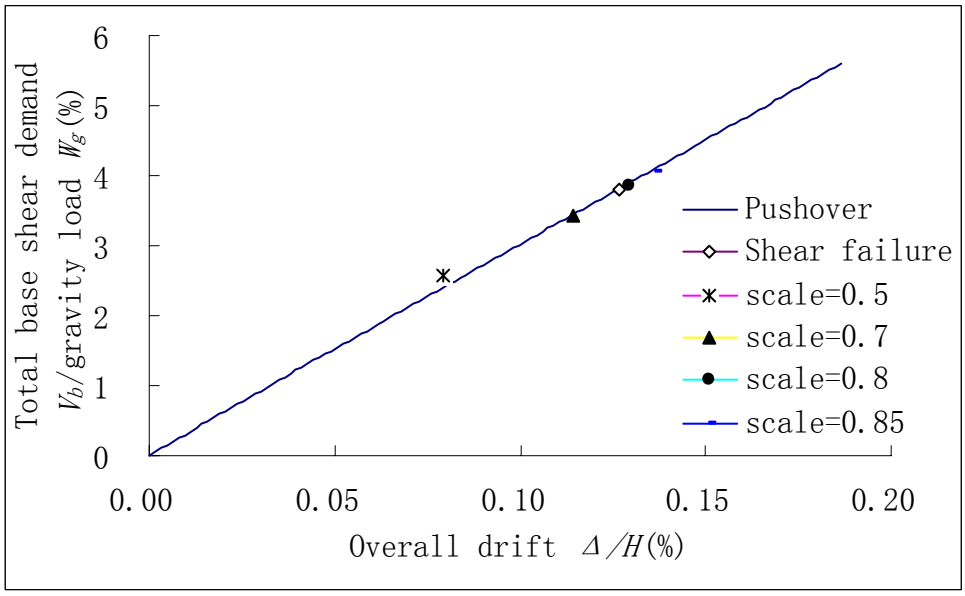

Figure 6.29 Total base shear demand V_b/ gravity load W_g vs. overall drift curve for the case of f_{cu} =30 MPa, ultimate loading, in y direction

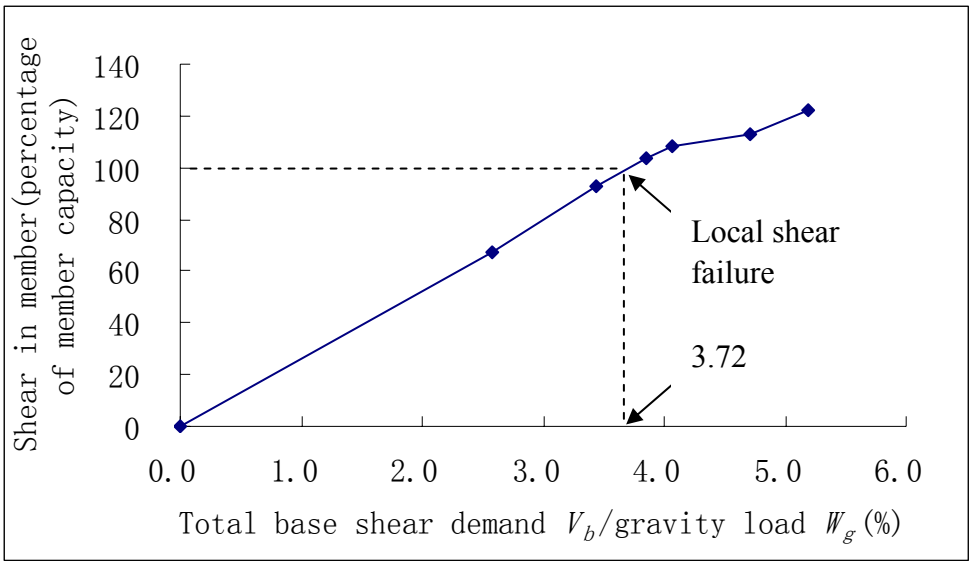

Figure 6.30 Relationship between V_b/ W_g and shear forces in the critical member (1st story I-shape web wall, I1) of the dynamic collapse analysis (f_{cu} =30 MPa, ultimate loading case, in y direction)

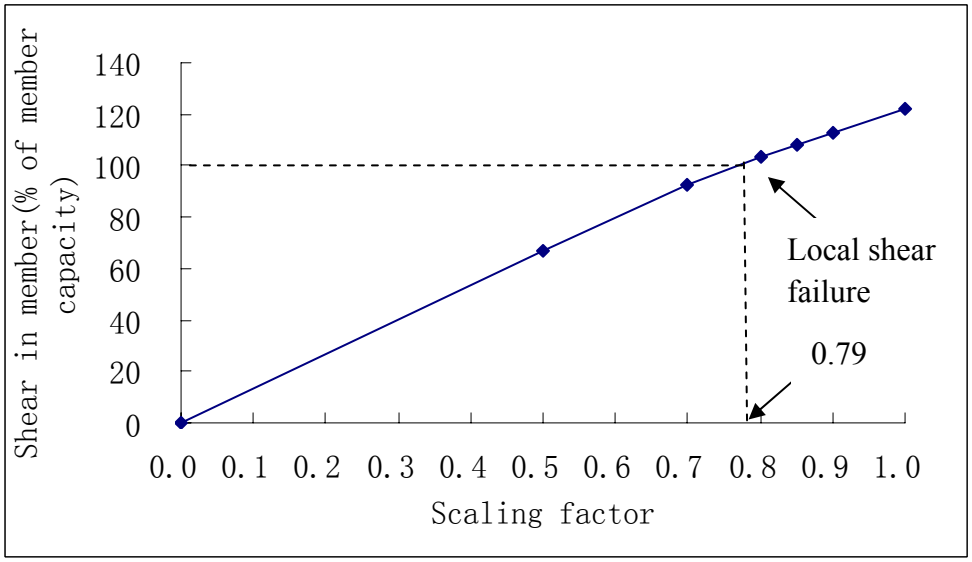

Figure 6.31 Relationship between scaling factors and shear forces in the critical member (1st story I-shape web wall, I1) of the dynamic collapse analysis (f_{cu} =30 MPa, ultimate loading case, in y direction)

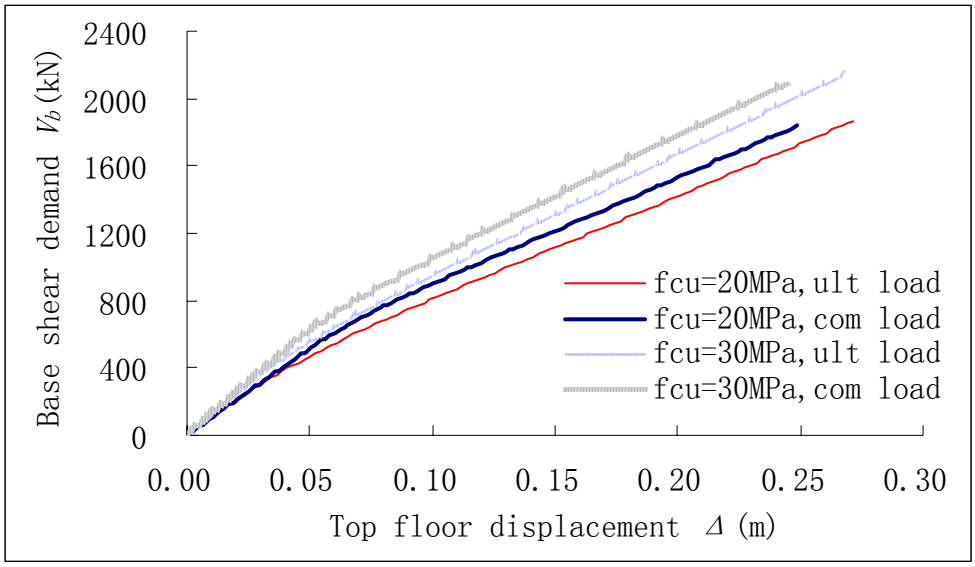

Figure 6.32 Seismic capacity curves in x direction obtained from the pushover adaptive analysis

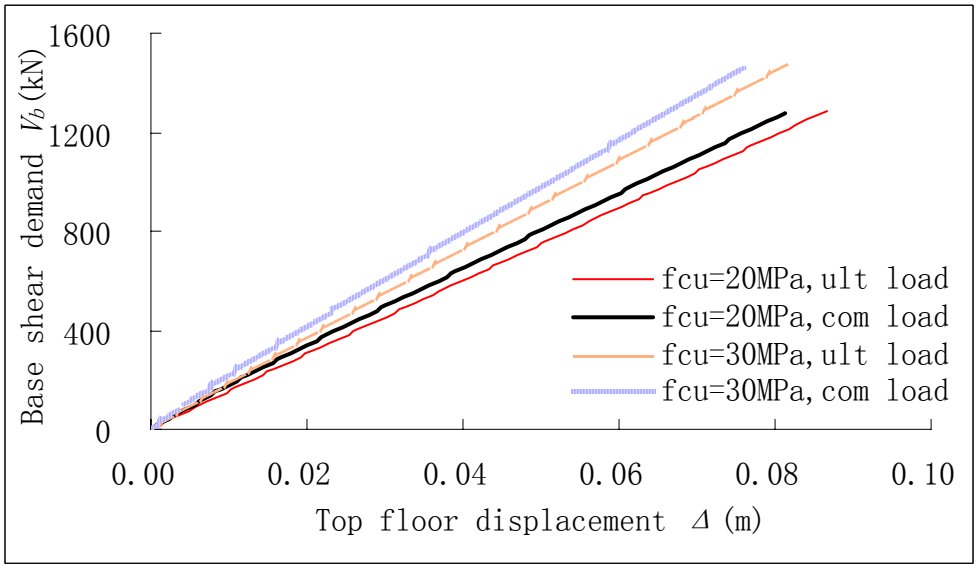

Figure 6.33 Seismic capacity curves in y direction obtained from the pushover adaptive analysis

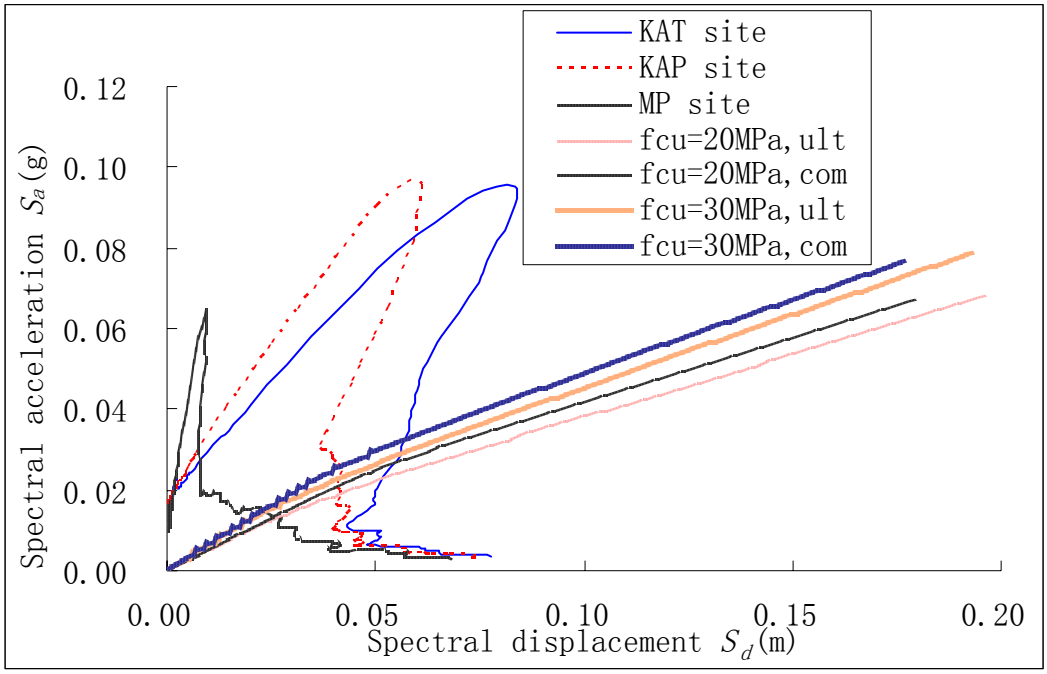

Figure 6.34 Spectra acceleration (S_a)– spectra displacement (S_d)curves in x direction of the 25-story structure (combination of capacity curves and demand curves)

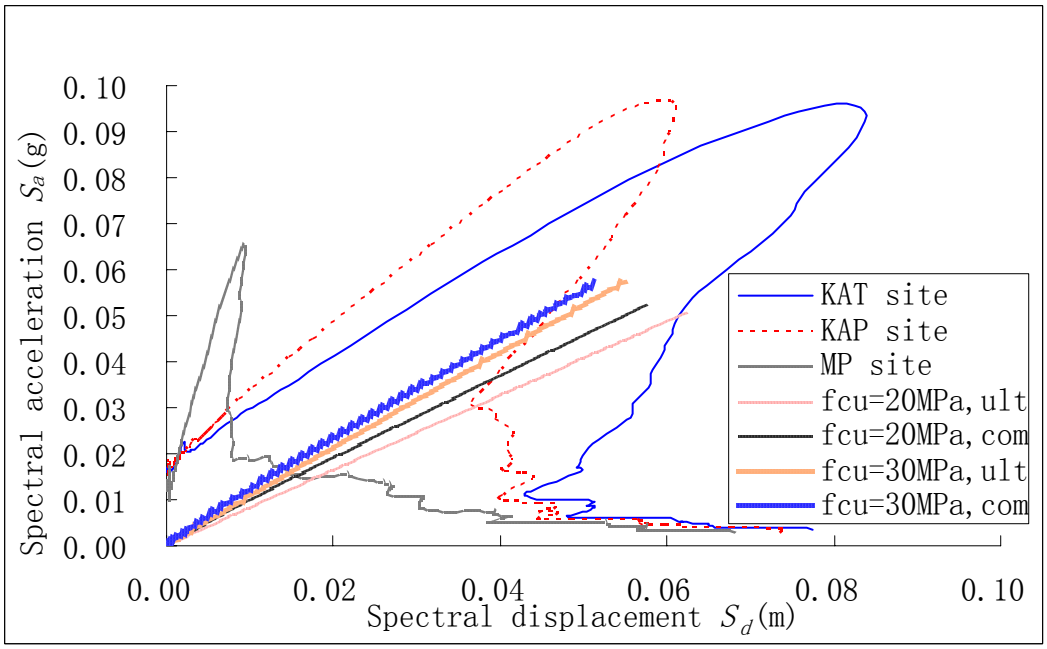

Figure 6.35 Spectra acceleration (S_a)– spectra displacement (S_d) curves in y direction of the 25-story structure (combination of capacity curves and demand curves)

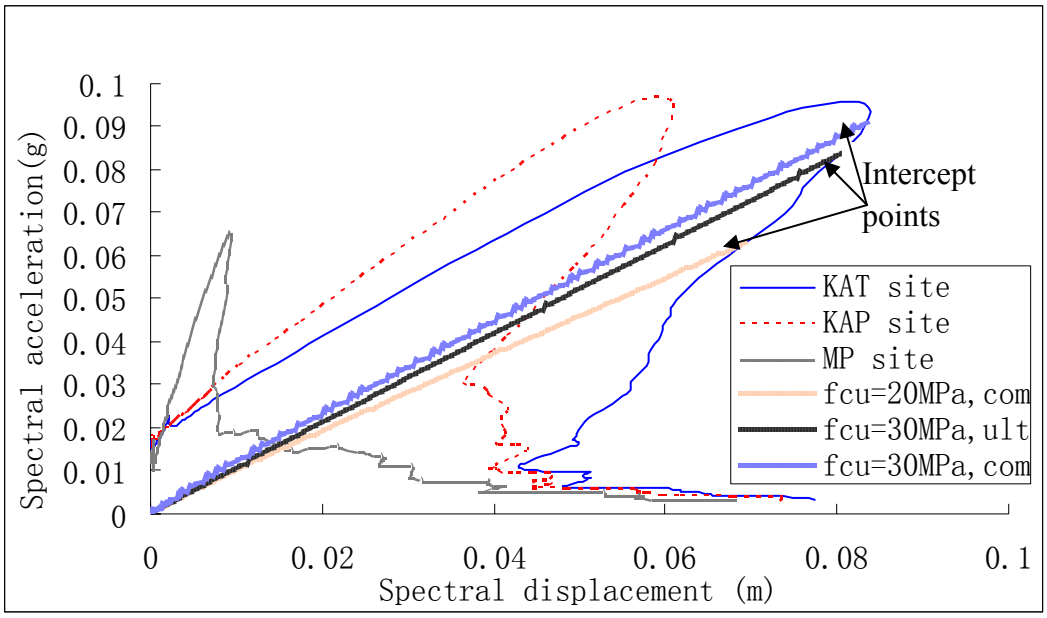

Figure 6.36 Intercept points of the three insufficient cases

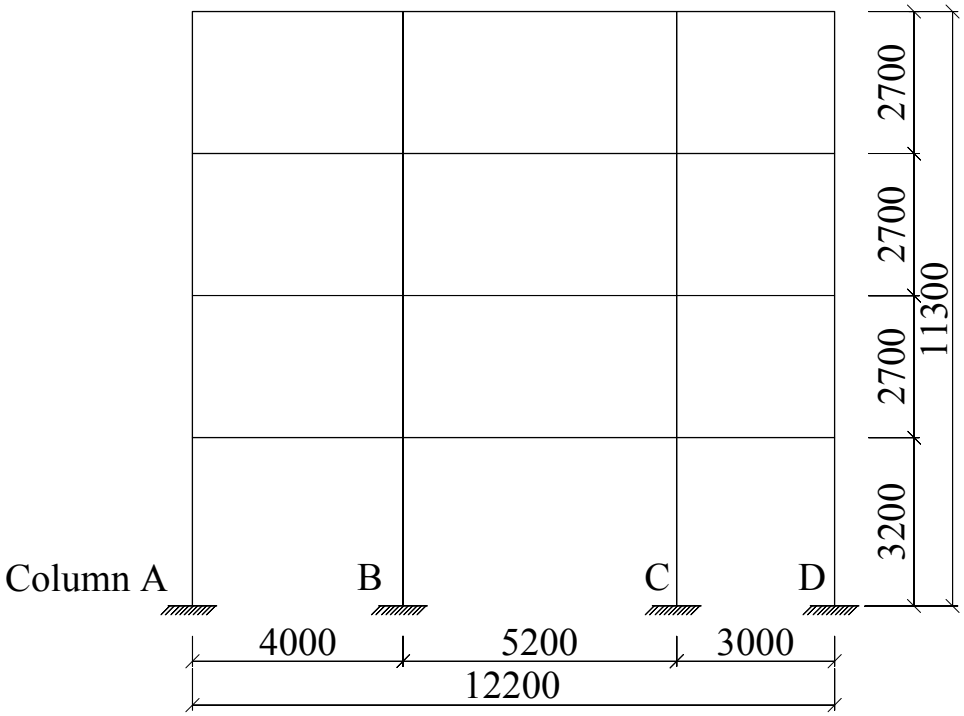

Figure 6.37 Elevation view of the 4-story sub-frame (dimension in mm)

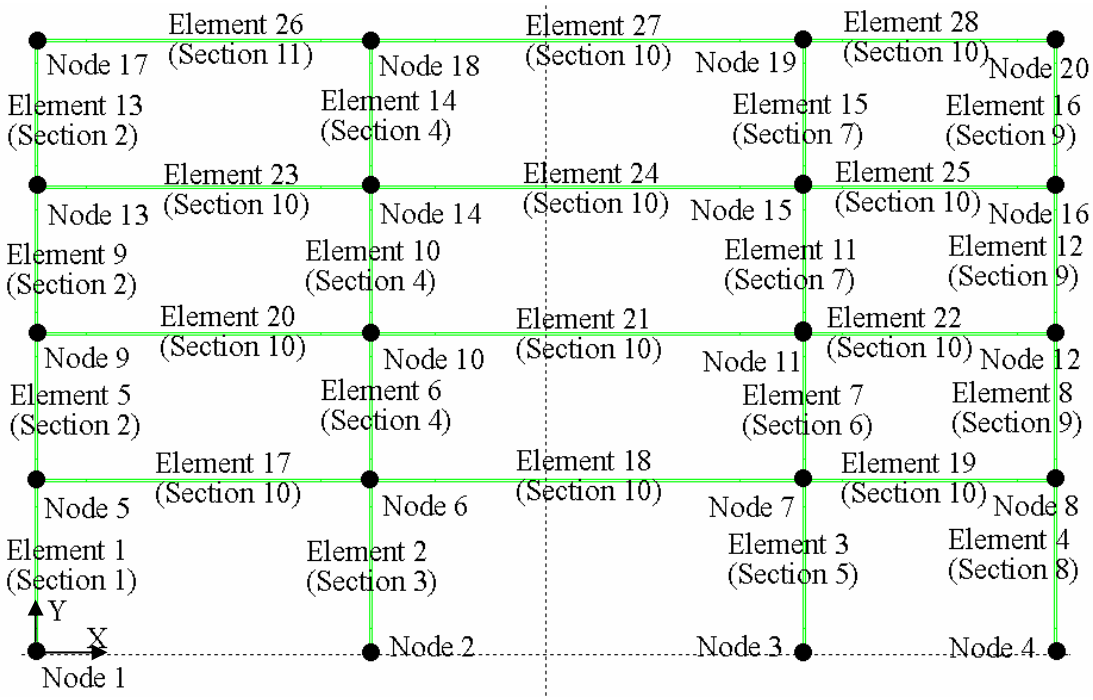

Figure 6.38 Nodes, elements and sectional properties of FEA for the 4-story sub-frame

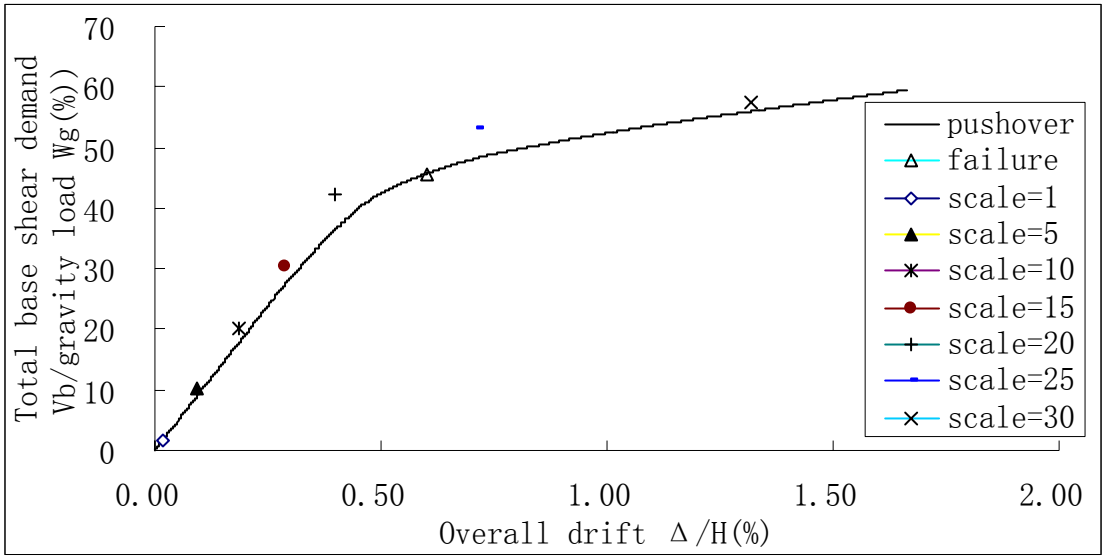

Figure 6.39 Total base shear demand V_b/ gravity load W_g vs. overall drift curve of the 4-story sub-frame (W_g = 957.44kN, H=11.3m)

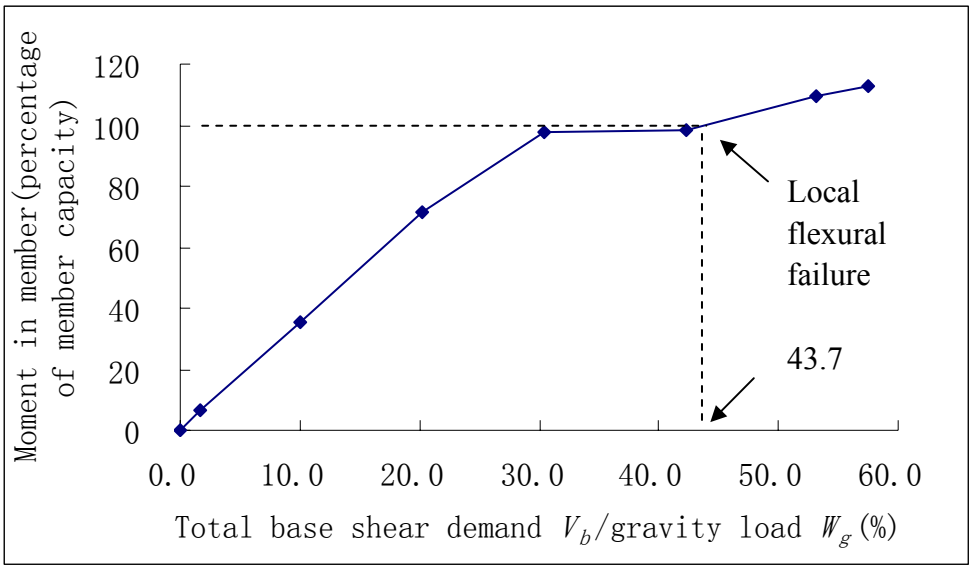

Figure 6.40 Relationship between V_b/ W_g and moment in the critical member (Element 3) of the dynamic collapse analysis

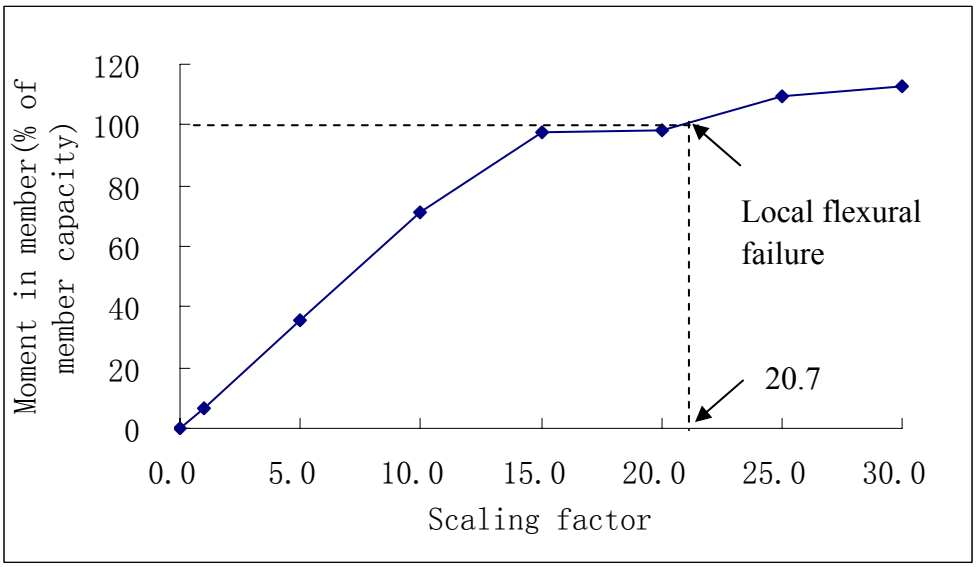

Figure 6.41 Relationship between scaling factors and moment in the critical member (Element 3) of the dynamic collapse analysis

CHAPTER 7 CONCLUSIONS AND RECOMMENDATIONS

7.1. Conclusions

The study focused on evaluating the seismic vulnerability of frame and shear wall structures in Singapore, which were designed according to BS8110(1985) without any seismic provision, when subjected to far field effects due to earthquakes occurred in Sumatra. A reliable and elegant FEA analytical model to determine the capacity of full scale buildings was established, and retrofitting scheme using FRP for the cases with insufficient seismic adequacy was proposed.

The principal conclusions from this study are as follows:

1. An experimental model of a half scale frame showed the relatively good seismic performance of the GLD low-rise buildings in Singapore: strong column-weak beam mechanism; good ductility capability with ultimate ductility factor of 3.4 and ultimate total story drift of 2.8%; failure mode which was dominated by flexural behavior instead of shear failure. The proposed FEA model using RUAUMOKO could predict the ultimate strength capacity, ultimate displacement, yield strength, and cyclic hesteresis behavior of the frame structure, with reasonably good accuracy.
2. The results of an experimental model of one fifth scale shear wall structure under cyclic loading provided useful information of cyclic behavior of such structures and could be used to evaluate their seismic adequacy. The proposed FRP

retrofitting scheme could change the brittle failure mode to a less brittle failure mode and effectively improve the seismic performance of GLD structures. The proposed FEA model could predict the failure mode and the overall hysterestic behavior of GLD shear wall structures with and without FRP retrofitting, reasonably well.

3. Comparison of the results of the cyclic loading tests and pushover loading tests showed that the pushover test could be a simple and backbone representation of the cyclic behavior of GLD frame and shear wall structures designed according to BS8110(1985).
4. From the test results, it was observed that the flexure stiffness (*EI*) obtained from the test was less than that of the ideal uncracked section due to micro-cracks. The initial stiffness reduction factors, 0.58 for columns and 0.35 for beams and 0.8 for shear walls, were suggested. The Modified Takeda Hysteresis model was adopted to simulate the stiffness degradation in FEA models. The unloading stiffness degradation parameter α and reloading stiffness degradation parameter β for the Modified Takeda Hysteresis model were obtained from the tests: α=0.5, β=0.1 for columns, α=0.4, β=0.1 for beams, and α=0.5, β=0.7 for shear walls. The bi-linear parameter *r* varied from section to section, and a procedure to calculate *r* was proposed.
5. Based on the data of recent two strong earthquakes, the worst scenario (design earthquake) corresponds to an earthquake with M_w=9.5, at 600 km away from

Singapore. The seismic demand for buildings in Singapore due to this design earthquake was found to be 9.6% for structural damping ratio of 5%.

6. The proposed FEA model, validated by the test results, is a reliable and elegant tool to determine the capacity of full scale buildings.
7. The case study revealed that for certain cases, high-rise buildings built in 1970s in Singapore may suffer from some damage due to the worst possible earthquake.
8. For buildings that do not meet the demand, a retrofitting scheme using FRP system was proposed. The members required retrofitting and the amount of FRP laminates needed could be found using the proposed FEA analytical method.

7.2. Recommendations

1. The study herein is mainly based on strength-base criteria. As a further study, experimental investigations and numerical models for seismic retrofitting using FRP may be carried out to satisfy the performance-base criteria.

2. The proposed retrofitting scheme focuses on confinement of structure members by wrapping FRP laminates. Further experimental and analytical studies for other retrofitting methods using FRP system may be carried out.

REFERENCES

ACI318. (1989). *Building code requirements for structural concrete and commentary(ACI 318-89/ACI 318R-89)*, American Concrete Institute, Detroit, Michigan.

ACI318. (2002). *Building code requirements for structural concrete and commentary*, American Concrete Institute, Detroit, Michigan.

Aktan, A. E., Bertero, V. V., and Sakino, K. (1985)."Lateral stiffness characteristics of reinforced concrete frame-wall structures." *Deflections of Concrete Structures.*, American Concrete Institute, Detroit, MI, USA, Phoenix, AZ, USA, 231-262.

Aoyama, H., and Yamamoto, Y. (1984)."Seismic strengthening of existing RC building." *Proceedings of the U.S/Japan joint seminar*, C. W. Roeder, ed., Composite and Mixed Construction, Washington,USA, 312-322.

AS1170.4. (1993). *Minimum design loads on structures. Part 4: Earthquake loads*, Standards Association of Australia.

ATC-40. (1996). "Seismic evaluation and retrofit of concrete buildings, vols. 1 and 2." *No. SSC 96-01*, Applied Technology Council, California Seismic Safety Commission.

Aycardi, L. E., Mander, J. B., and Reinhorn, A. M. (1994). "Seismic resistance of reinforced-concrete frame structures designed only for gravity loads - experimental performance of subassemblages." *ACI Structural Journal*, V91, No.5, 552-563.

Balendra, T., Lam, N. T. K., Wilson, J. L., and Kong, K. H. (2002). "Analysis of long-distance earthquake tremors and base shear demand for buildings in Singapore." *Engineering Structures*, V24, No.1, 99-108.

Balendra, T., Tan, K. H., and Kong, K. H. (2001)."Ultimate strength of a reinforced concrete frame-wall structure designed according to BS 8110." *ICCMC/IBST (International Committee on Concrete Model Code for Asia and the Vietnam Institute for Building Science and Technology)*.

Balendra, T., Tan, K. H., and Kong, S. K. (1999). "Vulnerability of reinforced concrete frames in low seismic region, when designed according to BS 8110." *Earthquake Engineering and Structural Dynamics*, V28, No.11, 1361-1381.

Balendra, T., Tan, T. S., and Lee, S. L. (1990). "An analytical model for far-field response spectra with soil amplification effects." *Engineering Structures*, V12, No.4, 263-268.

Bracci, J. M., Reinhorn, A. M., and Mander, J. B. (1995a). "Seismic resistance of reinforced-concrete frame structures designed for gravity loads - performance of structural system." *ACI Structural Journal*, V92, No.5, 597-609.

Bracci, J. M., Reinhorn, A. M., and Mander, J. B. (1995b). "Seismic retrofit of reinforced concrete buildings designed for gravity loads: Performance of structural model." *ACI Structural Journal*, V92, No.6, 711-723.

BS8110. (1985). *Structural use of concrete Parts 1, 2 and 3*, British Standards Institution.

Buyle-Bodin, F., David, E., and Ragneau, E. (2002). "Finite element modelling of flexural behaviour of externally bonded CFRP reinforced concrete structures." *Engineering Structures*, V24, No.11, 1423-1429.

Carr, A. J. (2002a). "Ruaumoko, The Maori God of Volcanoes and Earthquakes, 2-dimensional version." Department of Civil Engineering, University of Canterbury, New Zealand.

Carr, A. J. (2002b). "Ruaumoko, The Maori God of Volcanoes and Earthquakes, 3-dimensional version." Department of Civil Engineering, University of Canterbury, New Zealand.

CPCA. (1995). *Concrete design handbook*, Canadian Portland Cement Association, Ottawa, Ont.

Dhakal, R. P., Pan, T.-C., Irawan, P., Tsai, K.-C., Lin, K.-C., and Chen, C.-H. (2005). "Experimental study on the dynamic response of gravity-designed reinforced concrete connections." *Engineering Structures*, V27, No.1, 75-87.

DIANA. (2000). *User Manual-DIANA Version 7*, P.O. Box 113, 2600 AC Delft, The Netherlands.

Dolsek, M., and Fajfar, P. (2002). "Mathematical modelling of an infilled RC frame structure based on the results of pseudo-dynamic tests." *Earthquake Engineering and Structural Dynamics*, V31, No.6, 1215-1230.

Ei-Tawil, S., and Kuenzli, C. M. (2002). "Pushover of hybrid coupled walls. II: Analysis and behavior." *Journal of Structural Engineering-ASCE*, V128, No.10, 1282-1289.

ElAttar, A. G., White, R. N., and Gergely, P. (1997). "Behavior of gravity load designed reinforced concrete buildings subjected to earthquakes." *ACI Structural Journal*, V94, No.2, 133-145.

Elhassan, R. M., and Hart, G. C. (1995). "Analysis and seismic strengthening of concrete structures." *Structural Design of Tall Buildings*, V4, No.1, 71-90.

Elnashai, A. S., Pilakoutas, K., and Ambraseys, N. N. (1988)."Shake table testing of small scale structural walls." *Proceedings of the Ninth World Conference on Earthquake Engineering*, Tokyo-Kyoto, Japan.

Elnashai, A. S., Pilakoutas, K., and Ambraseys, N. N. (1990). "Experimental behaviour of reinforced concrete walls under earthquake loading." *Earthquake Engineering & Structural Dynamics*, V19, No.3, 389-407.

Eusebio, M., Palumbo, P., Lozza, F., and Manfredi, G. (2002)."Numerical modeling of masonry panels strengthened using FRPS." *Finte Elements in Civil Engineering Applications*, Hendriks and Rots, eds., Swets & Zeitlinger, Lisse, 295-303.

Filiatrault, A., Lachapelle, E., and Lamontagne, P. (1998). "Seismic performance of ductile and nominally ductile reinforced concrete moment resisting frames. II. Analytical study." *Canadian Journal of Civil Engineering*, V25, No.2, 342-352.

Freeman, S. A. (1978)."Prediction of response of concrete buildings to severe earthquake motion." *Publication SP-55, American Concrete Institute*, Detroit, Michigan, USA, 589-605.

Freeman, S. A., Nicoletti, J. P., and Tyrell, J. V. (1975)."Evaluation of existing buildings for seismic risk - a case study of Puget Sound Naval Shipyard, Bremerton, Washington." *Proceedings of 1st US National Conference on Earthquake Engineering*, Berkeley, California,USA, EERI, 113-122.

Han, S. W., Kwon, O.-S., and Lee, L.-H. (2004). "Evaluation of the seismic performance of a three-story ordinary moment-resisting concrete frame." *Earthquake Engineering and Structural Dynamics*, V33, No.6, 669-685.

Harajli, M. H. (2005). "Behavior of gravity load-designed rectangular concrete columns confined with fiber reinforced polymer sheets." *Journal of Composites for Construction*, V9, No.1, 4-14.

Harajli, M. H., and Rteil, A. A. (2004). "Effect of confinement using fiber-reinforced polymer or fiber-reinforced concrete on seismic performance of gravity load-eesigned columns." *ACI Structural Journal*, V101, No.1, 47-56.

Hardin, B. O., and Drnevich, V. P. (1972). "Shear modulus and damping in soils:measurement and parameter effects." V98, No.SM6, 603-624.

Harries, K. A., Mitchell, D., Redwood, R. G., and Cook, W. D. (1998). "Nonlinear seismic response predictions of walls coupled with steel and concrete beams." *Canadian Journal of Civil Engineering*, V25, No.5, 803-818.

Hibbit, Karlsson, and Sorense. (2003). "ABAQUS/Standard user's manual(Version 6.3)." Pawtucket, RI.

Hirosawa, M. (1975). "Past experimental results on reinforced concrete shear walls and analysis on them.(in Janpanese)." *No. 6*, Kenchiku Kenkyu Shiryo, Building Research Institute, Ministry of Construction.

IDARC-2D. (2004). "A computer program for seismic inelastic structural analysis(latest version)." http://civil.eng.buffalo.edu/idarc2d50/, State University of New York at Buffalo.

Idriss, I., and Sun, J. (1992). "User's manual for SHAKE91-A computer program for conduction equivalent linear seismic response analyses of horizontally layered soil deposits- program modified based on the original SHAKE program published in December 1972 by Schnabel,Lysmer and Seed." Centre for Geotechnical Modelling, Department of Civil and Environmental Engineering, University of California, Davis, California.

Imai, T., and Tonouchi, K. (1982)."Correlations of N value with S-wave velocity and shear modulus." *Proceedings of the 2nd European Symposium on Penetration Testing*, 24-27.

Kenneally, R. M., and Burns, J. J. J. (1986). "Experimental investigation into the seismic behavior of nuclear power plant shear wall structures." *Nuclear Engineering and Design Curr Issues Relat to Nucl Power Plant Struct, Equip and Piping-Sel Pap, Dec 10-12*, V107, No.1-2, 95-107.

Koh, X. C. (2003). "Dynamic collapse analysis of RC structures," Bachelor thesis, National University of Singapore, Singapore.

Kong, K. H. (2004). "Overstrength and ducitlity of reinforced concrete shear-wall frame buildings not designed for seismic loads," PHD thesis, National University of Singapore, Singapore.

Kong, K. H., Tan, K. H., and Balendra, T. (2003a)."Retrofitting of shear walls designed to BS 8110 for seismic loads using FRP." *Proceedings of the Sixth*

International Symposium on FRP Reinforcement for Concrete Structures (FRPRCS-6), K. H. Tan, ed., Singapore, 1127-1136.

Kong, K. H., Tan, K. H., and Balendra, T. (2003b)."Retrofitting of shear walls designed to BS 8110 for seismic loads using FRP." *Proceedings of the Sixth International Symposium on FRP Reinforcement for Concrete Strictires(FRPRCS-6)*, K. H. Tan, ed., Singapore, 1127-1136.

Kong, S. K. (2003). "A novel technique for retrofitting of RC buildings subjected to seismic loads," PHD thesis, National University of Singapore, Singapore.

Krawinkler, H., and Seneviratna, G. D. P. K. (1998). "Pros and cons of a pushover analysis of seismic performance evaluation." *Engineering Structures*, V20, No.4-6, 452-464.

Kunnath, S. K., Hoffmann, G., Reinhorn, A. M., and Mander, J. B. (1995a). "Gravity load-designed reinforced concrete buildings - Part II: evaluation of detailing enhancements." *ACI Materials Journal*, V92, No.4, 470-478.

Kunnath, S. K., Hoffmann, G., Reinhorn, A. M., and Mander, J. B. (1995b). "Gravity-load-designed reinforced concrete buildings - part I: seismic evaluation of existing construction." *ACI Structural Journal*, V92, No.3, 343-354.

Lam, N. T. K. (1999). "Program GENQKE user's guide: program for generating synthetic earthquake acceleration based on stochastic simulations of seismological models." Civil & Environmental Engineering, the University of Melbourne, Australia.

Lam, N. T. K., and Wilson, J. L. (1999). "Estimation of the site natural period from borehole records." *Australian Journal of Structural Engineering*, VSE1 (3), 179-199.

Lee, H. S., and Sung-W, W. (1998)."An experimental study on the similitude in structural behaviors for small-scale modeling of reinforced concrete structures." *Proceedings of the 6th US National Conference on Earthquake Engineering*, Oakland, CA: EERI, USA.

Lee, H. S., and Woo, S. W. (2002a). "Effect of masonry infills on seismic performance of a 3-storey R/C frame with non-seismic detailing." *Earthquake Engineering and Structural Dynamics*, V31, No.2, 353-378.

Lee, H. S., and Woo, S. W. (2002b). "Seismic performance of a 3-story RC frame in a low-seismicity region." *Engineering Structures*, V24, No.6, 719-734.

Lefas, I. D., Kotsovos, M. D., and Ambraseys, N. N. (1990). "Behavior of reinforced concrete structural walls. Strength, deformation characteristics, and failure mechanism." *ACI Structural Journal (American Concrete Institute)*, V87, No.1, 23-31.

Li, Z. J., Kong, K. H., Balendra, T., and Tan, K. H. (2004)."Behaviour of FRP retrofitted shear walls designed according to BS8110." *Developments in Mechanics of Structures & Materials*, J. D. Andrew and H. Hong, eds., Australia, 133-137.

Lombard, J. C., Lau, D. T., Humar, J. L., Cheung, M. S., and Foo, S. (1999). "Seismic repair and strengthening of reinforced concrete shear walls for flexure and shear using carbon fibre sheets." *Advanced Composite Materials in Bridges and Structures*, 645-652.

Lopes, M. S. (2001). "Experimental shear-dominated response of RC walls. Part II: Discussion of results and design implications." *Engineering Structures*, V23, No.3, 564-574.

Macgregor, J. G. (2005). "Reinforced concrete-mechanics & design." 4th edition, Prentice Hall, 35.

Megawati, K., and Pan, T.-C. (2002). "Prediction of the maximum credible ground motion in Singapore due to a great Sumatran subduction earthquake: The worst-case scenario." *Earthquake Engineering and Structural Dynamics*, V31, No.8, 1501-1523.

Megawati, K., Pan, T.-C., and Koketsu, K. (2003). "Response spectral attenuation relationships for Singapore and the Malay Peninsula due to distant Sumatran-fault earthquakes." *Earthquake Engineering and Structural Dynamics*, V32, No.14, 2241-2265.

Megawati, K., Pan, T.-C., and Koketsu, K. (2005). "Response spectral attenuation relationships for Sumatran-subduction earthquakes and the seismic hazard implications to Singapore and Kuala Lumpur." *Soil Dynamics and Earthquake Engineering*, V25, No.1, 11-25.

Meyer, C. (1984)."Earthquake analysis of structural walls." *Proceedings of the International Conference on Computer-aided Analysis and Design of Concrete Structures*, Pineridge Press, plit, Yugoslavia, Swansea UK, 1479-1492.

Mosalam, K. M., and Naito, C. J. (2002). "Seismic evaluation of gravity-load-designed column-grid system." *Journal of Structural Engineering*, V128, No.2, 160-168.

Mwafy, A. M., and Elnashai, A. S. (2001). "Static pushover versus dynamic collapse analysis of RC buildings." *Engineering Structures*, V23, No.5, 407-424.

Oesterle, R. G., Aristizabal-Ochoa, J. D., Fiorato, A. E., Russell, H. G., and Corley, W. G. (1979). "Earthquake resistant structural walls-tests of isolated walls-phase II." *Report No. NSF/RA-790275*, Construction Technology Laboratories, Portland Cement Association, Skokie, Ill.

Oesterle, R. G., Fiorato, A. E., Johal, L. S., Carpenter, J. E., Russell, H. G., and Corley, W. G. (1976). "Earthquake resistant structural walls-tests of isolated walls." *Report No. NSF/RA-760815*, Construction Technology Laboratories, Portland Cement Association, Skokie, Ill.

Otani, S. (1981). "Hysteresis models of reinforced concrete for earthquake response analysis." *Journal of Faculty of Engineering, University of Tokyo*, VXXXVI, No.2, 407-441.

Pan, T.-C. (1997). "Site-dependent building response in Singapore to long-distance Sumatra earthquakes." *Earthquake Spectra*, V13, No.3, 475-488.

Pan, T.-C., and Lee, C. L. (2002). "Site response in Singapore to long-distance Sumatra earthquakes." *Earthquake Spectra*, V18, No.2, 347-367.

Park, R. (1988)."Evaluation of ductility of structures and structural assemblages from laboratory testing." *Ninth World Conference on Earthquake Engineering*, Tokyo-kyoto, Japan.

Park, R., and Paulay, T. (1975). *Reinforced concrete structures*, John Wiley & Sons, New York.

Paulay, T., and Priestley, M. J. N. (1992). *Seismic design of reinforcecd concrete and masonry buildings*, John Wiley & Sons, Inc.

Paz, M., and Leigh, W. (2005). *Structural dynamics:theory and computation (fifth edition)*, Kluwer Academic Publishers.

Penelis, G. G., and Kappos, A. J. (1997). *Earthquake-resistant concrete structures*, 1st edition, E & FN Spon, Great Britain.

Perry, M. (2003). "Dynamic collapse analysis of RC structures," Bachelor thesis, National University of Singapore, Singapore.

Pilakoutas, K., and Elnashai, A. (1995). "Cyclic behavior of reinforced concrete cantilever walls, Part I: Experimental results." *ACI Structural Journal*, V92, No.3, 271-281.

Poulos, H. G. (1991). "Relationship between local soil conditions and structural damage in the 1989 Newcastle earthquake." *Transactions of the Institution of Engineers, Australia: Civil Engineering*, VCE33, No.3, 181-188.

Saiidi, M., and Sozen, M. A. (1979). "Simple and complex models for nonlinear seismic response of reinforced concrete structures." *Report No. UILU-ENG-79-2031*, Departmeng of Civil Engineering, University of Illinois, Urbana,Ill.

SAP2000. (1997). http://www.csiberkeley.com/products_SAP.html, Computers and structures Inc., Berkeley, California.

Seible, F., Priestley, M. J. N., Innamorato, D., Weeks, J., and Policellie. (1994). "Carbon fiber jacket retrofit test of circular shear bridge column." *Rep. No. ACTT-94/02*, University of California-San Diego.

Subedi, N. K., Marsono, A. K., and Aguda, G. (1999). "Analysis of reinforced concrete coupled shear wall structures." *Structural Design of Tall Buildings*, V8, No.2, 117-143.

Suyanthi, S. (2003). "Overstrength and ducitlity of reinforced concrete structures designed in accordance with BS8110 by dynamic collapse analysis," Master thesis, National University of Singapore, Singapore.

Tan, K. H. (2002). "Strength enhancement of rectangular reinforced concrete columns using fiber-reinforced polymer." *Journal of Composites for Construction, ASCE*, V6, No.3, 175-183.

Teng, J. G., Chen, J. F., Smith, S. T., and L., L. (2001). *FRP strengthened RC structure*.

Triantafillou, T. C., and Antonopoulos, C. P. (2000). "Design of concrete flexural members strengthened in shear with FRP." *Journal of Composites for Construction*, V4, No.4, 198-205.

Wyllie, L. (1996)."Strengthening strategies for improved seismic performance." *Proceedings of Eleventh World Conference on Earthquake Engineering*, 1424.

Zachriasen, J., Sieh, K., Taylor, F. W., Edwards, R. L., and Hantoro, W. S. (1999). "Submergence and uplift associated with the giant 1833 Sumatran subduction earthquake: Evidence from coral microatolls." *Journal of Geophysical research-solid earth*, V104, No.B1, 895-919.

APPENDIX A CALCULATION OF PARAMETERS FOR RUAUMOKO (2D VERSION)

A.1 Elastic section properties

Elastic (Young's) modulus of the concrete E can be obtained from the test. If the test value is not available, E can be calculated based on ACI code (ACI318 2002):

$$E = 4730\sqrt{f_c'} \tag{A.1}$$

Where,

$f_c' = 0.8 f_{cu}$, concrete compressive cylinder strength

f_{cu} =concrete compressive cube strength

Shear modulus G for a member is calculated from E:

$$G = \frac{E}{2(1+\upsilon)} \tag{A.2}$$

Where,

ν =0.2, Poisson ratio of concrete

The cross-sectional area A is the gross area of a section. The effective shear area A_s is a ratio (shear area ratio), of the cross-sectional area A. The shear area ratio is taken as approximately 9/10 for a solid circular section, and 5/6 for a solid rectangular section. For thin wall sections such as I beam and box beams etc. A_s is usually taken as the web area "A_w" in the direction of shear considered, or alternatively may be approximated as half the total area. For an "Euler-Bernoulli" beam analysis, shear deformation is often neglected and A_s is input as zero.

Weight/unit length (WGT) of member is used to calculate the member mass and does not contribute to the distributed load. This means that the input of distributed load is independent of WGT here. It is noted that, if the distributed weight input here, the corresponding contribution of these distributed weight in members should be deduced from the lumped node weight in Weight option. A simple way is to set WGT=0, but incorporate the contribution of the distributed weight of members in the lump weight input on nodes.

A.2 Parameters for the axial force-moment interaction yield surface

A.2.1 Parameters needed to be defined

For the concrete beam-column member, the interaction between axial force and moment is involved by defining the interaction yield surface (as shown in Figure A.1). The definition of this yield surface involves 6 points: (*PYC*,0), (*PB*,*MB*),(2/3*PB*, *M1B*),(1/3*PB*,*M2B*),(0,*M0*) and (*PYT*,0). Here, *PYC* denotes the axial compression yield force, *PB* denotes the axial compression force at point B, *MB* denotes the yield moment at B, *M1B* is the yield moment corresponding to the axial force of 2/3*PB*, *M2B* is the yield moment corresponding to the axial force of 1/3*PB*, *M0* is the yield moment when the axial force is zero, and *PYT* is the axial tension yield force. This yield surface can be divided into three parts: two straight lines (a line from point (*PYC*,0) to point (*PB*,*MB*) and another line from point (*PYT*,0) to point(0,*M0*)), and a cubic curve between these two lines.

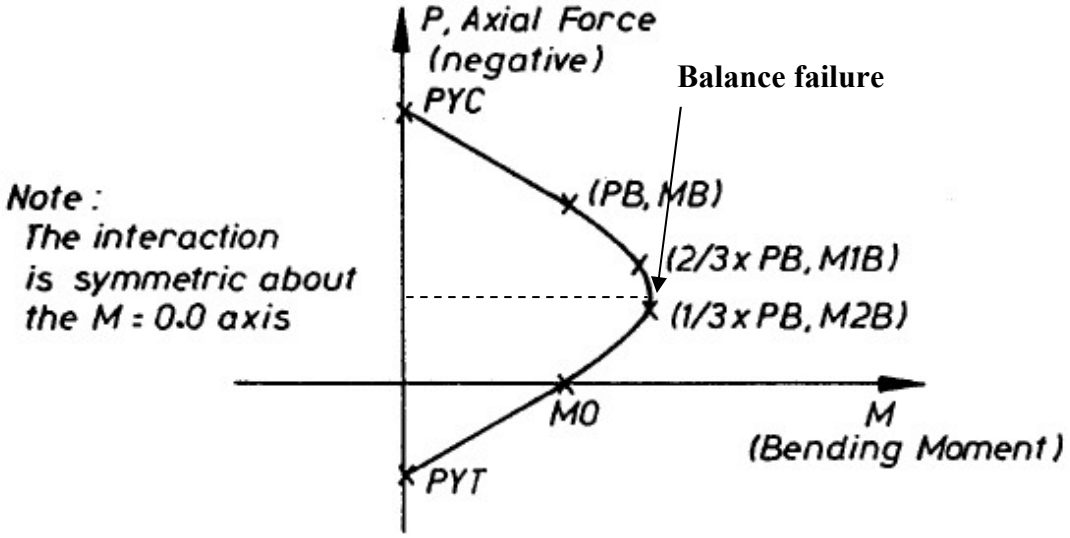

Figure A.1 Axial load-moment interaction yield surface (Carr 2002a)

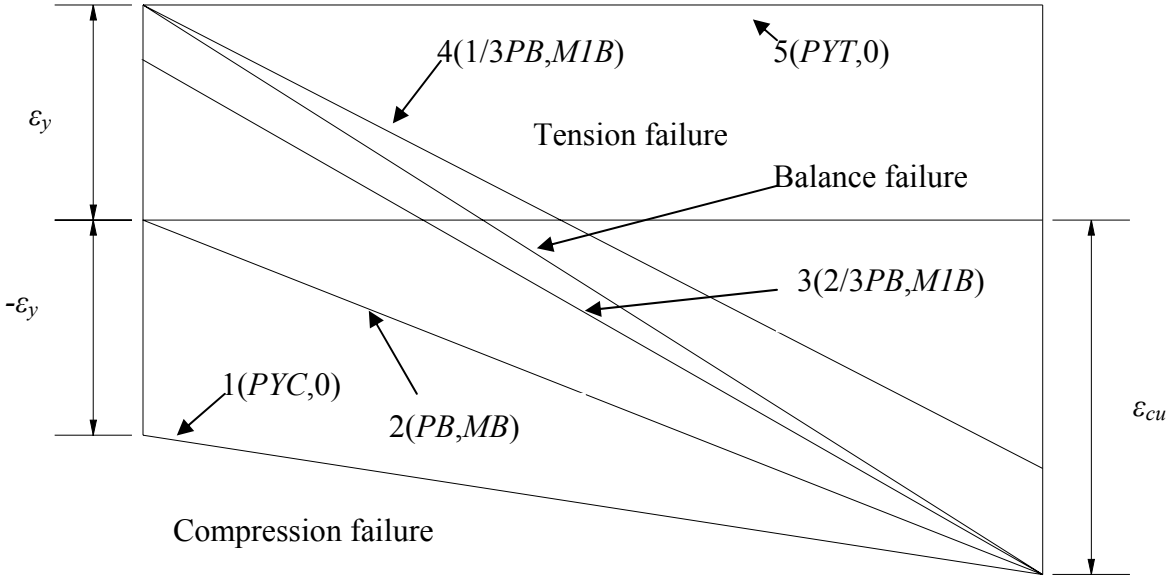

Figure A.2 Strain distribution in a section.

A.2.2 Determination of the parameters

In order to determinate the values of the parameters needed for calculation, it is necessary to have a look at the strain distribution in a section under different axial loads (as shown in Figure A.2, where ε_y is the yield strain of the reinforcing bars and ε_{cu} is the ultimate strain of the concrete, which is taken as 0.004 as suggested by

Paulay et al.(1992)). When $\varepsilon_s = \varepsilon_y$ and $\varepsilon_c = \varepsilon_{cu}$ (where ε_s is the strain of the outermost tension reinforcing bars and ε_c is the compression strain of concrete), the section is subjected to a balance failure. The failure when $\varepsilon_s < \varepsilon_y$ and $\varepsilon_c = \varepsilon_{cu}$ is referred to as compression failure, and the failure when $\varepsilon_s > \varepsilon_y$ and $\varepsilon_c = \varepsilon_{cu}$ is referred to as tension failure.

In the upper half part of the yield surface of Figure A.1, from point (*PYC*, 0) to the point of balance failure, which is a point in between points (2/3*PB*, *M1B*) and (1/3*PB*,*M2B*), the section will be subjected to compression failure. In the lower half part of the yield surface of Figure A.1, from the point of balance failure to point (*PYT*, 0), the section will be subjected to tension failure.

If a section is subjected to compression failure (high axial load), concrete will crush (when $\varepsilon_c = \varepsilon_{cu}$) before the yielding of reinforcement occurs, and thus the yield surface is controlled by the condition of $\varepsilon_c = \varepsilon_{cu}$. Therefore, the determination of the points of the upper half curve in Figure A.1 is based on $\varepsilon_c = \varepsilon_{cu}$. If a section is subjected to tension failure (low axial load), the yielding of reinforcement occurs before concrete crush, and thus the yield surface is controlled by the condition $\varepsilon_s = \varepsilon_y$. Therefore, the determination of the points of the lower half curve of Figure A.1 is based on $\varepsilon_s = \varepsilon_y$.

A.2.2.1 Determination of the points at the upper half curve

Points (*PYC*,0), (*PB*,*MB*) and (2/3*PB*,*M1B*) are at the upper half curve of Figure A.1, and the corresponding control condition is $\varepsilon_c = \varepsilon_{cu}$.

Since the portion from point (*PYC*,0) to point (*PB*,*MB*) is a line, the relationship between the axial load and moment is linear. The strain distribution at point ε_s=0 represents the onset of cracking of the least compressed side of the column. After this point, the section is partially cracked. Thus the section before this point (ε_s=0) is still in uncracked elastic status, and the relationship between axial force and moment is linear. Therefore, point B corresponds to the situation of ε_s=0 and $\varepsilon_c = \varepsilon_{cu}$. The height of neutral axis corresponding to this situation can be calculated, and *PB*, *MB* can be calculated, based on the equilibrium of the section.

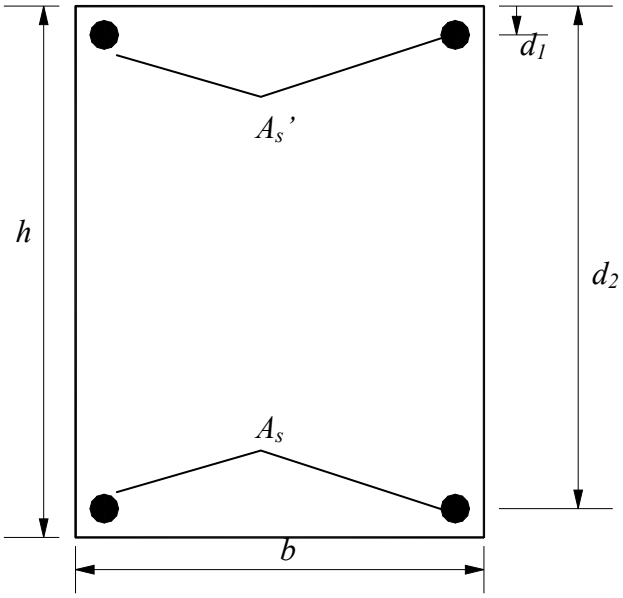

Figure A.3 Rectangular reinforced concrete column section

Here, we take a rectangular section as an example (as shown in Figure A.3) to show how to calculate the corresponding parameters. The height, width, effective height and reinforcement are denoted in Figure A.3. It is noted that the compressive strain, stress and force are negative, and the tensile components are positive.

The calculation of axial compression yield force *PYC* is determined by assuming the whole section is under compression, and that the stress of reinforcing bars and concrete reaches the strength stress. Thus,

$$PYC = (bh - A_s' - A_s)0.85f_c' + (A_s' + A_s)f_y \tag{A.3}$$

Where,

f_c'=compressive cylinder concrete strength

f_y=yield strength of reinforcing bars

A_s=area of the tensile reinforcing bars

A_s'=area of the compressive reinforcing bars

The calculation of axial tension yield force *PYT* is determined by assuming the whole section is under tension, and that the tension force contribution from concrete is zero. Thus,

$$PYT = (A_s' + A_s)f_y \tag{A.4}$$

In order to calculate moment in the section, the height of the plastic centroid should be calculated first. According to Park and Paulay (1975), the plastic centroid is determined by assuming the concrete reaches its compressive stress $0.85f_c'$ and the reinforcing bars reach their yield strength f_y. The height of the plastic centriod *PC* can be calculated based on the equilibrium of the section:

$$PC = \frac{0.85f_c'bh^2/2 + A_s'f_y d_1 + A_s f_y d_2}{0.85f_c'bh + A_s'f_y + A_s f_y} \tag{A.5}$$

Where,

d_1=effective depth of the compressive reinforcing bars

d_2=effective depth of the tensile reinforcing bars

As discussed above, point B corresponds to ε_s=0 and $\varepsilon_c = \varepsilon_{cu}$. Thus, the force in the tension reinforcing bars F_s is zero, and the height of the neutral axis is:

$$c = (\frac{\varepsilon_{cu}}{\varepsilon_{cu} + \varepsilon_s})d_2 = d_2 \tag{A.6}$$

The strain in the compression reinforcing bars is:

$$\varepsilon_s' = (\varepsilon_{cu} + \varepsilon_s)\frac{d_1}{d_2} - \varepsilon_{cu} = (\frac{d_1}{d_2} - 1)\varepsilon_{cu} \tag{A.7}$$

The strain hardening of steel is considered with the hardening ratio of 0.01. Thus, the stress in the compression reinforcing bars is:

$$f_s' = \begin{cases} -[f_y + 0.01E_s(|\varepsilon_s'| - \varepsilon_y)] & when\ |\varepsilon_s'| > \varepsilon_y \\ \varepsilon_s' E_s & otherwise \end{cases} \tag{A.8}$$

Where,

E_s = Modulus of Elasticity of the reinforcing bars

The compression force in reinforcing bars is

$$F_s' = \begin{cases} A_s'(f_s' + 0.85f_c') & when\ d_1 < 0.85c \\ A_s' f_s' & otherwise \end{cases} \tag{A.9}$$

The compression force developed in concrete is

$$F_c = -0.85c \times 0.85 f_c' b = -0.7225 f_c' bc \tag{A.10}$$

Therefore, the axial load and moment are:

$$P = F_c + F_s' + F_s \tag{A.11}$$

$$M = M_c + M_s' + M_s = F_c(PC - \frac{0.85c}{2}) + F_s'(PC - d_1) + F_s(d_2 - PC) \tag{A.12}$$

The procedure of determination of point (2/3*PB*, *M1B*) is as follows. First, we assume the height of neutral axis *c*, according to the assumption that the strain

distribution will keep as a plane after bending, the strain of the tension and compression reinforcing bars is:

$$\varepsilon_s = \varepsilon_{cu}(\frac{d_2 - c}{c}) \tag{A.13}$$

$$\varepsilon_s' = \varepsilon_{cu}(\frac{d_2 - c}{c}) \tag{A.14}$$

The force in the tension reinforcing bars is:

$$F_s = \begin{cases} A_s[f_y + 0.01E_s(\varepsilon_s - \varepsilon_y)] & when\ \varepsilon_s > f_y \\ A_s\varepsilon_s E_s & otherwise \end{cases} \tag{A.15}$$

The forces in the compression reinforcing bars and concrete are calculated using equations (A.9) and (A.10). If the total axial load, calculated using equation (A.11), is not equal 2/3*PB*, a new *c* should be assumed, and the above calculation procedure should be repeated until the calculated axial load is equal to 2/3*PB*. Then the obtained *c* is used in equation (A.12) to calculate the target moment *M1B*.

A.2.2.2 Determination of the points at the lower half curve

Points (*PYT*, 0), (1/3*PB*, *M2B*) and (0, *M0*) are at the lower half curve of Figure A.1, and the corresponding control condition is $\varepsilon_s = \varepsilon_y$.

The tensile yield force *PYT* is calculated by assuming all the reinforcing bars reach their yield strength. The equation is:

$$PYT = A_s f_y + A_s' f_y \tag{A.16}$$

The procedure of determination of point (1/3*PB*, *M2B*) is as follows. First, we assume the height of neutral axis *c*, since $\varepsilon_s = \varepsilon_y$, the strain of the concrete and compression reinforcing bars is:

$$\varepsilon_c = \varepsilon_y(\frac{c}{d_2 - c}) \tag{A.17}$$

$$\varepsilon_s' = \varepsilon_y(\frac{c - d_1}{d_2 - c}) \tag{A.18}$$

The force in tension reinforcing bars is:

$$F_s = A_s f_y \tag{A.19}$$

And the force in compression concrete is calculated based on equivalent rectangular stress distribution, according to equation (A.20).

$$F_c = \alpha f_c \beta b c \tag{A.20}$$

Where,

αf_c =the average concrete stress of the equivalent rectangular block

$$f_c = \begin{cases} f_c' & 0.002 < |\varepsilon_c| \le \varepsilon_{cu} \\ f_c'[2\frac{\varepsilon_c}{0.02} - (\frac{\varepsilon_c}{0.02})^2] & \frac{0.4 f_c'}{E_c} < |\varepsilon_c| \le 0.002 \\ E_c \varepsilon_c & |\varepsilon_c| \le \frac{0.4 f_c'}{E_c} \end{cases}$$

βc =the extent of the equivalent rectangular concrete stress block

The values of α and β depend on the stress distribution of concrete. ε_c is negative since concrete is under compression. If $|\varepsilon_c|$ calculated from equation (A.17) is less than $\frac{0.4 f_c'}{E_c}$, the distribution of concrete is considered as linear. If $\frac{0.4 f_c'}{E_c} < |\varepsilon_c| \le 0.002$, the distribution of concrete is parabolic distribution. Thus, the

values of α and β are: $\alpha = 0.5$ and $\beta = 1$ when $|\varepsilon_c| \le \frac{0.4 f_c'}{E_c}$; $\alpha = 0.67$ and $\beta = 1$ when $\frac{0.4 f_c'}{E_c} < |\varepsilon_c| \le 0.002$; $\alpha = 0.85$ and $\beta = 0.85$ when $0.002 < |\varepsilon_c| \le \varepsilon_{cu}$ (Macgregor 1997).

The moment resistance from concrete is:

$$M_c = F_c(PC - \gamma\beta c) \tag{A.21}$$

Where,

γ=1/3 when $|\varepsilon_c| \le \frac{0.4 f_c'}{E_c}$, γ=0.375 when $\frac{0.4 f_c'}{E_c} < |\varepsilon_c| \le 0.002$, and γ=0.5 when $0.002 < |\varepsilon_c| \le \varepsilon_{cu}$ (Macgregor 1997)

The forces in the compression reinforcing bars are calculated using equations (A.9). Then the total axial load can be calculated using equation (A.11). If this total load is not equal to 1/3*PB*, a new *c* should be assumed, and the above calculation procedure should be repeated until the calculated axial load is equal to 1/3*PB*. Finally the obtained *c* is used in equation (A.22) to calculate the target moment *M2B*.

$$M = M_c + M_s' + M_s = F_c(PC - \gamma\beta c) + F_s'(PC - d_1) + F_s(d_2 - PC) \tag{A.22}$$

Similarly to the determination of point (1/3*PB*, *M2B*), point (0, *M0*) is determined with the corresponding axial load equal to 0 instead of 1/3*PB*.

A.3 Calculation of moment of a beam section corresponding to yielding

Figure A.4 shows a beam section when the first yielding in tension reinforcing bars occurs. The corresponding concrete strain at the compression side can be found by

assuming the height of neutral axis *c* and performing trial and error procedure until the equilibrium of the section. This procedure is the same as that in determination of point (0, *M0*) in a column section as specified in Section A.2.

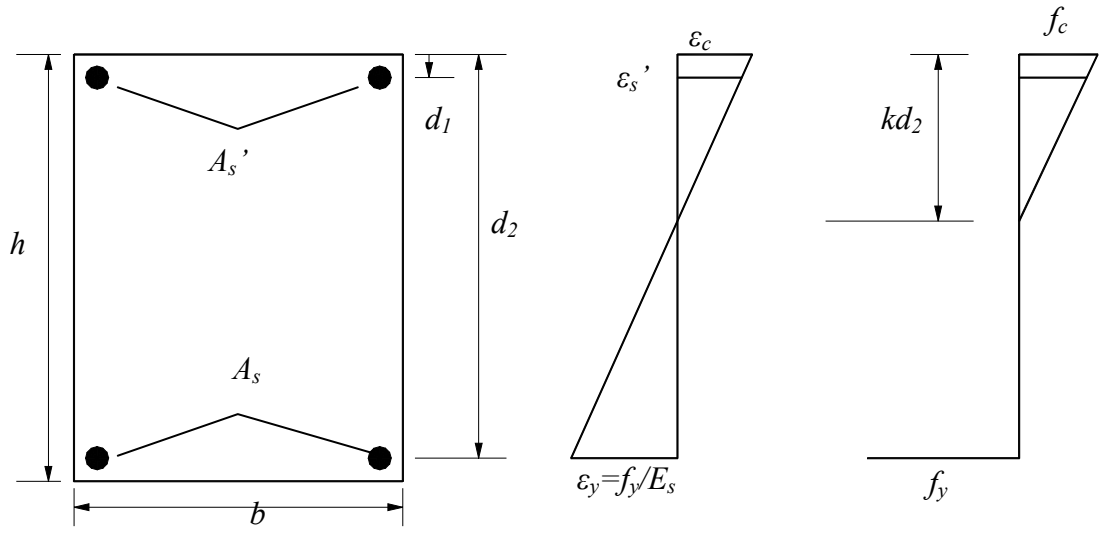

Figure A.4 Beam section when the tension reinforcing bars reach the yield strength

For symmetrically reinforced ($A_s = A_s'$) section, the compression concrete stress is generally small when the first yielding of reinforcement occurs, and thus the distribution of concrete stress can be assumed as linear. At this situation, the calculation procedure can be simplified as follows:

Based on the linear distribution of stress and strain as shown in Figure A.4, the factor *k*, the ratio of neutral axis depth over the effective depth of the section, can be calculated based on the equation (A.23)

$$k = [(\rho + \rho')^2 n^2 + 2(\rho + \frac{\rho' d_1}{d_2})n]^{0.5} - (\rho + \rho')n \qquad \text{(A.23)}$$

Where,

$$n = \frac{E_s}{E_c}$$

$$\rho = \frac{A_s}{bd_2}$$

$$\rho' = \frac{A_s'}{bd_2}$$

E_s = Modulus of Elasticity of steel

E_c = Modulus of Elasticity of concrete

According to the linear strain distribution, the concrete strain at the outmost compression side is:

$$\varepsilon_c = \varepsilon_y \frac{kd_2}{d_2 - kd_2} \tag{A.24}$$

Since the distribution of compressive concrete stress is linear, the force developed by concrete is

$$F_c = \frac{1}{2}\varepsilon_c E_c b k d_2 \tag{A.25}$$

The strain in the compression reinforcing bars is:

$$\varepsilon_s' = \varepsilon_c \frac{kd_2 - d_1}{kd_2} \tag{A.26}$$

And the compression force in the reinforcing bars is:

$$F_s' = A_s' \varepsilon_s' E_s \tag{A.27}$$

With the compression force from concrete and reinforcing bars, the distance from the compression edge, where the total compression force is acting, can be calculated as:

$$\bar{y} = \frac{d_1 F_s' + (kd_2/3)F_c}{F_s' + F_c} \tag{A.28}$$

Thus, the yield moment is calculated as:

$$M_y = A_s f_y (d_2 - \bar{y}) \quad \text{(A.29)}$$

A.4 Determination of flexural moment capacity

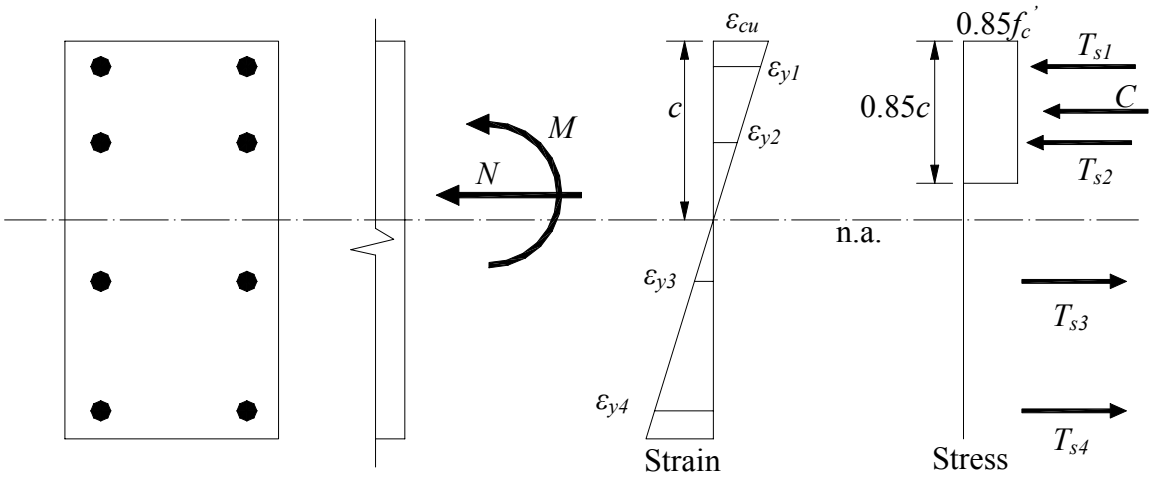

Figure A.5 Section analysis

Theoretical calculation of flexural moment capacity for sections is based on equilibrium section analysis. A section subjected to applied moment (M) and axial load (N) is shown in Figure A.5. The section after deformation is assumed to remain plane, so that the strain distribution over the section is linear. The maximum compression strain of concrete is assumed to be $\varepsilon_{cu} = 0.004$, as suggested by (Paulay et al.(1992). The parabolic stress distribution of concrete is simplified to rectangular distribution according to ACI code (ACI318 2002). And the bilinear stress-strain relationship of steel is assumed, with steel hardening ratio of 0.01. In calculation, compression force is negative and tensile force is positive.

The procedure of calculation is: firstly the height (c) of neutral axis (n.a) is assumed, then the total resistant force from concrete (F_c) and the total force from

reinforcing bars ($F_s=\sum F_{s\,i}$) are calculated, based on the stress-strain relationship of concrete and steel. If $N = F_c + F_s$, then M is obtained by summing the resistant moment from concrete and steel, otherwise, another c should be assumed and the above process should be repeated until the equilibrium is reached.

A.5 Calculation of bilinear factor *r* based on the sectional analysis

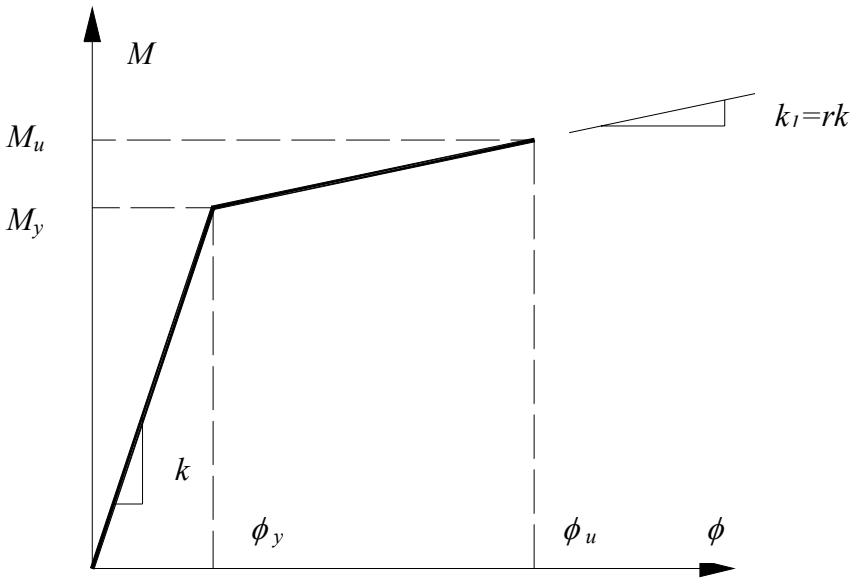

Figure A.6 Bilinear moment-curvature curve

Bilinear moment-curvature relationship is assumed in RUAUMOKO analysis (as shown in Figure A.6). The calculation of values corresponding to the concrete crush ($\varepsilon_{cu} = 0.004$): moment (M_u), the height of neutral axis (c_u) is specified in Section A.4. And the calculation of values corresponding to the first yielding: moment (M_y), the height of neutral axis (c_y) and concrete strain at the outermost compression surface ε_{cy}, is the same as the calculation of *M2B* as specified in A.2.2.2 Then the curvature corresponding to first yielding ϕ_y and that corresponding to concrete crushing ϕ_u is calculated according to equations (A.30) and (A.31).

$$\phi_y = \frac{\varepsilon_{cy}}{c_y} \tag{A.30}$$

$$\phi_u = \frac{\varepsilon_{cu}}{c_u} \tag{A.31}$$

Finally, *r* is calculated according to equation (A.32). It is often in a range of 0.01 to 0.2 for most cases.

$$r = \frac{k_1}{k} = \frac{\phi_y (M_u - M_y)}{M_y (\phi_u - \phi_y)} \tag{A.32}$$

A.6 Parameters for the FRP retrofitted section

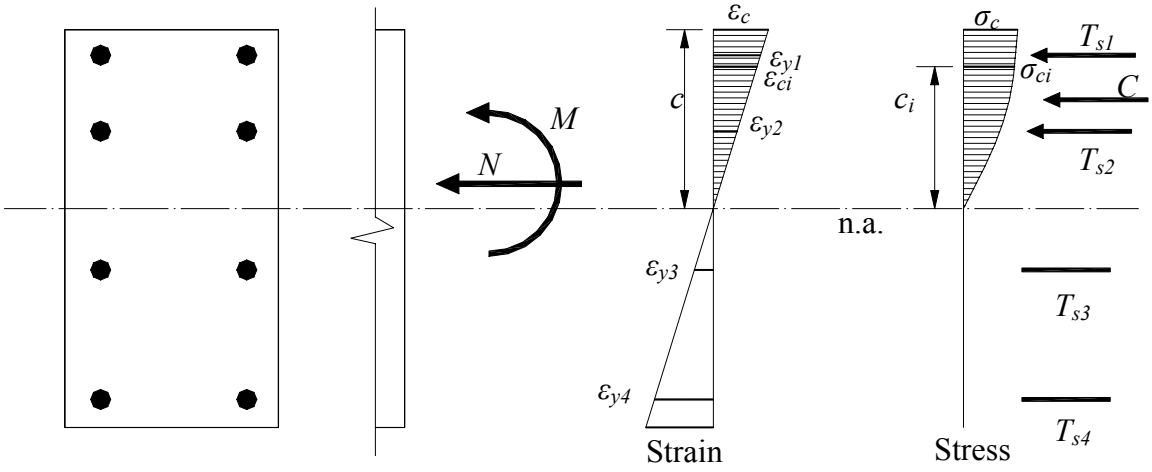

Figure A.7 Section analysis for FRP retrofitted structures

For FRP retrofitted structures, the stress-strain relationship of concrete (as shown in Figure 5.15 and equation (5.1)) proposed by Teng et. al. (2001) is used to consider the improvement of concrete due to FRP confinement. In this case, the distribution of concrete cannot be simplified as equivalent rectangular shape, and thus the calculation of concrete force will be different from the above mentioned methods.

As shown in Figure A.7, the stress distribution of concrete is separated into small parts. If the separated part is small enough, it can be simplified as a rectangular shape, and the forces from concrete can be obtained by the sum of the forces from all these small rectangular parts. The procedure for the sectional analysis is as follows.

1 Assume a neutral axis *c*. Separate the compression area into *n* (for example, *n*=100) parts. The width of each part is $\Delta c = c/n$, and the distance from the *i*th part to the neutral axis is $c_i = (i-0.5)\Delta c$. The concrete strain at the middle of *i*th part is $\varepsilon_{ci} = \frac{c_i}{c}\varepsilon_c = (i-0.5)\varepsilon_c / n$, and thus the corresponding concrete stress σ_{ci} is obtained according to equation (5.1).

2 The force from concrete is $F_c = \sum_i \sigma_{ci}\Delta c$ and the force from steel is $F_s = \sum F_{si}$

3 Repeat the step 1 and 2 until $N = F_c + F_s$

4 And then the moment of the section can be calculated as follows:

$$M = M_c + M_s = \sum_i F_{ci}(c - c_i - PC) + \sum F_{si} d_i$$

Where,

PC=the plastic centriod, which can be obtained from equation (A.5)

Through the above mentioned procedure, the yield surface, moment capacity, and bilinear factor *r* of a FRP retrofitted section can be calculated according to the sections A.2 to A.5. It is noted that when bilinear factor *r* is calculated, ε_{cu} is taken as 0.004.

APPENDIX B CALCULATION OF SHEAR FORCE CAPACITY

Based on ACI code, the theoretical shear capacity of reinforced concrete members was calculated using equation (B.1):

$$V = V_c + V_s = (1 + \frac{N_u}{14A_g})(\frac{\sqrt{f_c'}}{6})b_w d + \frac{A_v f_y d}{s} \quad \text{(B.1)}$$

Where,

N_u = axial compression force;

A_g = area of the cross section;

f_c' = compressive cylinder strength of concrete;

b_w = width of the web;

A_v =area of horizontal shear reinforcement within a vertical distance *s* and horizontal distance *d*

For simplified and conservative consideration, shear capacity can be obtained by assuming axial compression force N_u equal to 0.

APPENDIX C CALCULATION OF PARAMETERS FOR RUAUMOKO (3D VERSION)

C.1 Elastic section properties

The calculation of E, G, A, A_s and WGT is specified in Appendix A.1. The calculation of one new input option in 3D version, torsional second moment of area of a section in x-x direction J_{xx} , is highlighted here and is calculated as follows.

For solid circular sections, J_{xx} is approximately the same as the polar moment of area and this can estimated as:

$$J_{xx} = I_{yy} + I_{zz} \tag{C.1}$$

Where,

I_{yy} =moment of inertia (second moment of area) of a section in y-y direction;

I_{zz} =moment of inertia (second moment of area) of a section in z-z direction

For other sections, J_{xx} will be significantly less than the polar moment of area, i.e.:

For solid rectangular sections J_{xx} can be calculated as:

$$J_{xx} = bt^3 / \beta \qquad (t < b) \tag{C.2}$$

Where,

b=length of the longer side of the rectangular section;

t= length of the shorter side of the rectangular section;

β=a factor based on the value of b/t, which is listed in Table C.1

Table C.1 Values of β

b/t	1	1.5	1.75	2	2.5	3	4	6	8	10	>10.0
β	7.1	5.1	4.7	4.4	4	3.8	3.6	3.3	3.2	3.2	3

Note: for thin rectangular sections, β=3

For open thin wall sections J_{xx} can be calculated as:

$$J_{xx} = \sum (b_i t_i^3 / 3) \tag{C.3}$$

Where,

b_i =length of the longer side of the *i* rectangular section;

t_i = length of the shorter side of the *i* rectangular section;

C.2 Parameters for the axial force-moment interaction yield surface

Definition of 3D concrete beam-column frame-type yield surface needs five parameters: *PC* (axial compression yield force), *PB* (axial compression force at balance point), *MBz* (yield moment at *P=PB* about z-z axis), *MBy* (yield moment at *P=PB* about y-y axis) and *PT* (axial tension yield force). 3D axial force-moment interaction yield surface is shown in Figure C.1. Note that the compression force is negative and tension force is positive.

A simple section (as shown in Figure A.3) is also taken as an example to show how to calculate these parameters. The calculation procedure is quite similar to that of the 2D interaction yield surface parameters. *PC* can be calculated using equation (A.3) and *PT* can be calculated using equation (A.16).

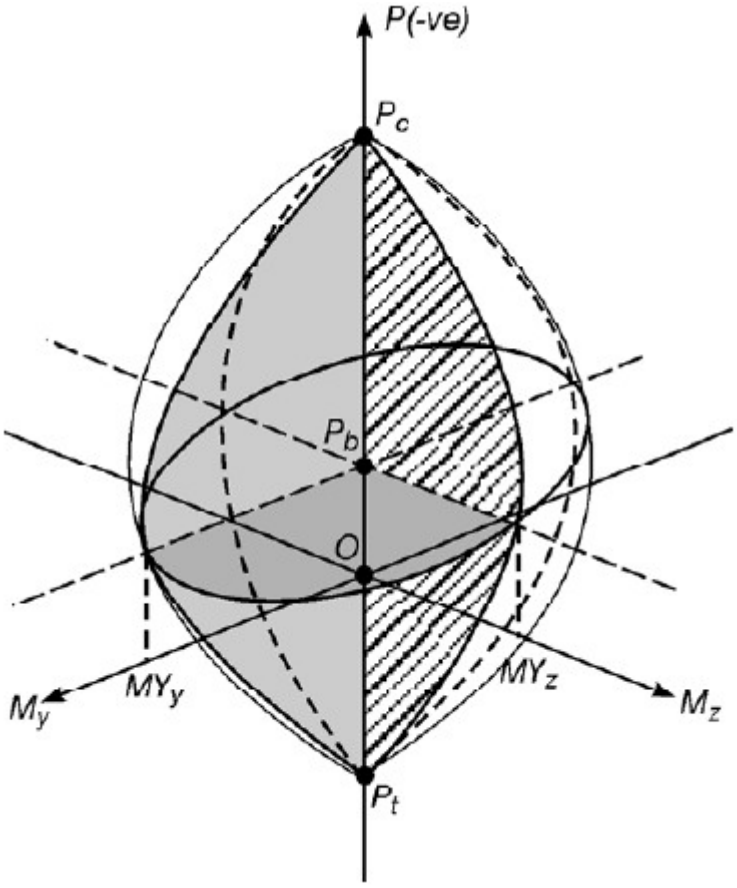

Figure C.1 Interaction diagram for reinforced concrete beam-columns (Carr 2002b)

Please note that the parameter *PB* here corresponds to the balance failure as shown in Figure A.2, where $\varepsilon_s = \varepsilon_y$ and $\varepsilon_c = \varepsilon_{cu}$. This is different from the point B in 2D version, where $\varepsilon_s = 0$ and $\varepsilon_c = \varepsilon_{cu}$. Therefore, when calculate *PB*, the tension force in the tensile reinforcing bars is:

$$F_s = A_s f_y \tag{C.4}$$

The strain in compression reinforcing bars is:

$$\varepsilon_s' = (\varepsilon_{cu} + \varepsilon_s)\frac{d_1}{d_2} - \varepsilon_{cu} = (\varepsilon_{cu} + \varepsilon_y)\frac{d_1}{d_2} - \varepsilon_{cu} \quad \text{(C.5)}$$

And the depth to neutral axis is:

$$c = (\frac{\varepsilon_{cu}}{\varepsilon_s + \varepsilon_{cu}})d_2 \quad \text{(C.6)}$$

Then the compression force F_s' in the reinforcing bars can be calculated using equations (A.8) and (A.9), compression force developed in concrete F_c can be calculated using equation (A.10). With F_s, F_s' and F_c, the axial load P and corresponding moment (*My* or *Mz* based on the target axis) is calculated using equations (A.11) and (A.12).

C.3 Parameters for beam flexural yield conditions

Four parameters are used to define the yield conditions: *MYz*+ (positive yield moment about z-z axis), *MYz*- (negative yield moment about z-z axis), *MYy*+ (positive yield moment about y-y axis) and *MYy*- (negative yield moment about y-y axis). The calculation of *MYz* and *MYy* can be calculated according to the procedure as described in Appendix A.3 based on the axis chosen. For FRP retrofitted structure, the procedure of moment calculation is given in Appendix A.6.

APPENDIX D PROCEDURE FOR CALCULATION OF RESPONSE SPECTRA

The response spectra is a plot of the maximum response (maximum displacement, velocity, acceleration, or any other quantity of interest) to a specified load function for single-degree-of freedom system. The abscissa of the plot is the natural frequency (or period) of the system, and the ordinate is the maximum response. Herein, the load function under study is the base earthquake excitation.

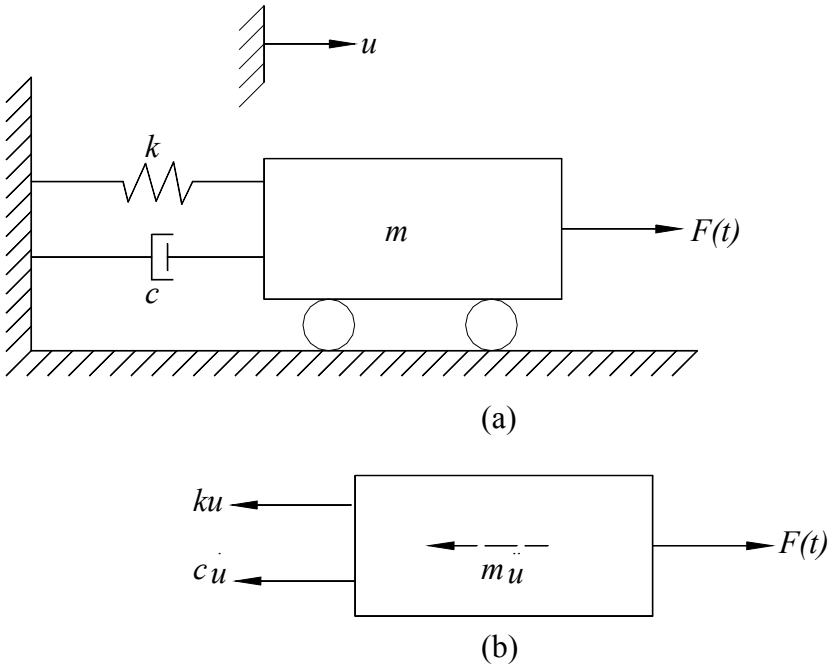

Figure D.1 (a) damped simple oscillator excited by the force *F(t)*; (b) free body diagram (Paz and Leigh 2005)

A single-degree-of freedom system subjected to a general type of force is shown in Figure D.1. The differential equation of motion, based on the dynamic equilibrium of the forces in the free body diagram is:

$$m\ddot{u} + c\dot{u} + ku = F(t) \tag{D.1}$$

Where,

F(t)= the force applied to the mass of the oscillator.

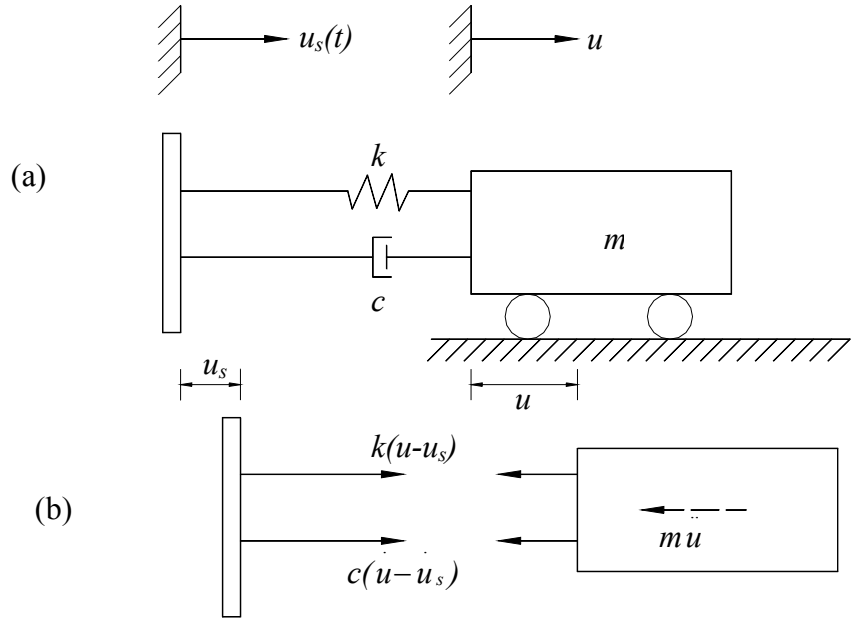

Figure D.2 (a) damped simple oscillator excited by the displacement $u_s(t)$; (b) free body diagram (Paz and Leigh 2005)

Figure D.2 shows a single-degree-of freedom system excited by a motion at its base. The equation of motion obtained using the free body diagram is:

$$m\ddot{u} + c(\dot{u} - \dot{u}_s) + k(u - u_s) = 0 \tag{D.2}$$

Where,

u = the absolute displacement;

u_s = the excited displacement at the base.

For convenience, relative displacement $u_r = u - u_s$ is introduced. Equation (D.2) can be represented as:

$$m\ddot{u}_r + c\dot{u}_r + ku_r = -m\ddot{u}_s(t) = F_{eff}(t) \tag{D.3}$$

The solution of the equation (D.3) gives the response for the structure excited at the base, in terms of the relative motion u_r. In order to solve equation (D.3), Direct Integration (Paz and Leigh 2005), a numerical integration procedure, is introduced.

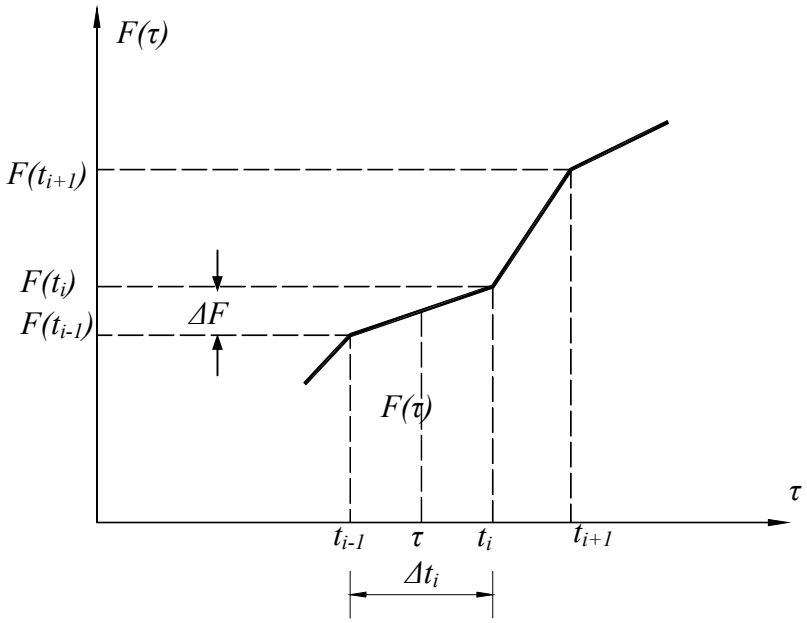

Figure D.3 Segmental linear loading function (Paz and Leigh 2005)

The time duration of the based excitation can be divided into *N* equal time intervals with the interval Δt. If Δt is small enough, the excitation function $F_{eff}(t)$ can be approximated by a piecewise linear function as shown in Figure D.3 and can be expressed as:

$$F_{eff}(t) = (1-\frac{t-t_i}{\Delta t})F_{eff,i} + (\frac{t-t_i}{\Delta t})F_{eff,i+1} = -m[(1-\frac{t-t_i}{\Delta t})\ddot{u}_{s,i} + (\frac{t-t_i}{\Delta t})\ddot{u}_{s,i+1}],\ t_i \le t \le t_{i+1} \tag{D.4}$$

Thus, equation (D.3) can be expressed as:

$$m\ddot{u}_r + c\dot{u}_r + ku_r = -(1-\frac{t-t_i}{\Delta t})m\ddot{u}_{s,i} - (\frac{t-t_i}{\Delta t})m\ddot{u}_{s,i+1}, \quad t_i \le t \le t_{i+1} \qquad \text{(D.5)}$$

According to Paz and Leigh (2005), the solution to equation (D.5) is

$$\begin{cases} u_{r,i+1} = e^{-\xi\omega\Delta t}[C_i \cos\omega_D\Delta t + D_i \sin\omega_D\Delta t] + B_i + A_i\Delta t \\ \dot{u}_{r,i+1} = e^{-\xi\omega\Delta t}[D_i(\omega_D \cos\omega_D\Delta t - \xi\omega\sin\omega_D\Delta t) - C_i(\xi\omega\cos\omega_D\Delta t + \omega_D \sin\omega_D\Delta t)] - A_i \\ \ddot{u}_{r,i+1} = \ddot{u}_{s,i+1} + 2\xi\omega\dot{u}_{r,i+1} + \omega^2 u_{r,i+1} \end{cases}$$

(D.6)

Where

$$A_i = \frac{F_{eff,i+1} - F_{eff,i}}{k\Delta t} = -\frac{\ddot{u}_{s,i+1} - \ddot{u}_{s,i}}{\omega^2\Delta t}$$

$$B_i = \frac{F_{eff,i} - cA_i}{k} = -\frac{\ddot{u}_{s,i+1} + 2\xi\omega A_i}{\omega^2}$$

$$C_i = u_{r,i} - B_i$$

$$D_i = \frac{\dot{u}_{r,i} \quad A_i \quad \xi\omega C_i}{\omega_D}$$

$$\omega_D = \omega\sqrt{1 \quad \xi^2}$$

From equation (D.6), with an assumed critical damping ratio ξ and the input base excitation $\ddot{u}_s$, for each circular period ω or period T, a serials of relative displacement u_r, relative velocity $\dot{u}_r$, and relative acceleration $\ddot{u}_r$ can be solved. The maximum value of the relative displacement is referred to as the spectrum displacement $S_d = \max(u_r)$. And the spectrum acceleration $S_a = \omega^2 S_d$, spectrum velocity $S_v = \omega S_d$. Actually $S_a \approx \max(\ddot{u}_r)$ and $S_v \approx \max(\dot{u}_r)$. For a series of ω (or T), a series of S_d, S_v and S_a can be solved and the corresponding response spectral can be obtained.

Based on equation (D.6), a program using Fortran 90 was written to calculate the response spectra. The program is as shown below.

Fortran program

```
      PROGRAM elastic_response_spectra
      DIMENSION TC(100000),R(100000),FP(100000)
      REAL NE,FI,DF,FF,XSI,H,G
!NUMBER OF POINTS DEFINING THE EXCITATION        NE
!INITIAL PERIOD (S)                              FI
!PERIOD INCREMENT (S)                            DF
!FINAL PERIOD (S)                                FF
!DAMPING RATIO                                   XSI
!TIME STEP INTEGRATION                           H
!ACCELERATION GRAVITY ratio                      G
!-------------------------------------------------------------------------------------
      CHARACTER*12 NAME1,NAME2
      WRITE(*,1)
    1 FORMAT(1X,23HINPUT DATA FILE NAME=> )
      READ(*,3) NAME1
      WRITE(*,2)
    2 FORMAT(1X,19HOUTPUT FILE NAME=> )
      READ(*,3) NAME2
    3 FORMAT(A12)
      OPEN(1,FILE=NAME1,STATUS='OLD')
      OPEN(2,FILE=NAME2,STATUS='NEW')
      READ(1,*) NE,FI,DF,FF,XSI,H,G
     Loop1: DO I = 1, NE
     READ(1,*) TC(I),R(I) !    TC(I) is time, R(I) is input base acceleration
      END DO LOOP1
     WRITE(2,*) 'PERIOD.     SD      SV      VMAX      SA        AMAX'
!---------------------------------- calculate response
      Loop2: DO I = 1, NE
        R(I)=R(I)*G           ! If the input base acceleration is the ratio of g, then
times g, otherwise, if the unit is m/s^2, g=1
      END DO Loop2

      TMAX=TC(NE)
      NT=TMAX/H
      N1=NT+1

      Loop3: DO I = 1, N1
        FP(I)=0
```

```
        END DO Loop3

        FP(1)=R(1)
        ANN=0
        II=1

        LOOP4: DO I=2,N1
           AI=I-1
           T=AI*H
           IF (T.GT.TC(NE)) THEN
              GOTO 30
           END IF
           IF (T.GT.TC(II+1)) THEN
              ANN=-TC(II+1)+T-H
              II=II+1
          ELSE
            ANN=ANN+H
           END IF
           FP(I)=R(II)+(R(II+1)-R(II))*ANN/(TC(II+1)-TC(II))
        END DO LOOP4

    30 PI=3.14159265 !LOOP OVER FREQUENCY VALUES
        Z=FI-DF
        K=0

        LOOP5: DO WHILE (Z.LE.FF)
           K=K+1
           Z=Z+DF                    ! Z is natural period
   40      W=2*PI/Z
           W2=W*W
           WD=W*SQRT(1-XSI*XSI)
!------------------------------------------ SUBROUTINE ANALYSIS
        PI=3.14159265
        DMAX=-100
        VMAX=-100
        ABMAX=-100
        Y1=0
        Y2=0
         DT=H
         XW=XSI*W
         E=EXP(-XW*DT)
         C=COS(WD*DT)
         S=SIN(WD*DT)
         IF (TC(2)-TC(1).EQ.DT) THEN
```

```
            RO=-R(1)
! Feff(I)=-m*a(I), m=1, a(I)=FP(I)=R(I),a(I) is input base acceleration
          ELSE
            RO=-FP(1)
          END IF
!------- LOOP OVER TIME AND CALCULATE MAXIMUM VALUES
            LOOP6: DO I=2, N1
            IF (TC(2)-TC(1).EQ.DT) THEN
                R1=-R(I)
              ELSE
              R1=-FP(I)
             END IF
          DFG=R1-RO
          FI=RO
          AI=DFG/DT/W2
          BI=(FI-2*XW*AI)/W2
          CI=Y1-BI
          DI=(Y2-AI+XW*CI)/WD
          Y11=E*(CI*C+DI*S)+BI+AI*DT
          Y22=E*(DI*(WD*C-XW*S)-CI*(XW*C+WD*S))+AI
          Y1=Y11
          Y2=Y22
          DDX=-2*XW*Y2-W2*Y1
          RO=R1
          !----------------------------------------
            IF(ABS(Y1) .GT. DMAX) THEN
               DMAX = ABS(Y1)
           END IF
            IF(ABS(Y2).GT. VMAX) THEN
               VMAX = ABS(Y2)
           END IF
            IF(ABS(DDX) .GT. ABMAX) THEN
               ABMAX = ABS(DDX)
           END IF
           END DO LOOP6
           SD=DMAX
           SV=DMAX*W
           SA=DMAX*W2
!-------------------------------------      PRINT RESULTS
           WRITE (2,900) Z,SD,SV,VMAX,SA,ABMAX
900        FORMAT (F5.2, 5F16.9)
           END DO LOOP5
          END
```

APPENDIX E BEDROCK ACCELEROGRAMS FOR THE DESIGN EARTHQUAKE

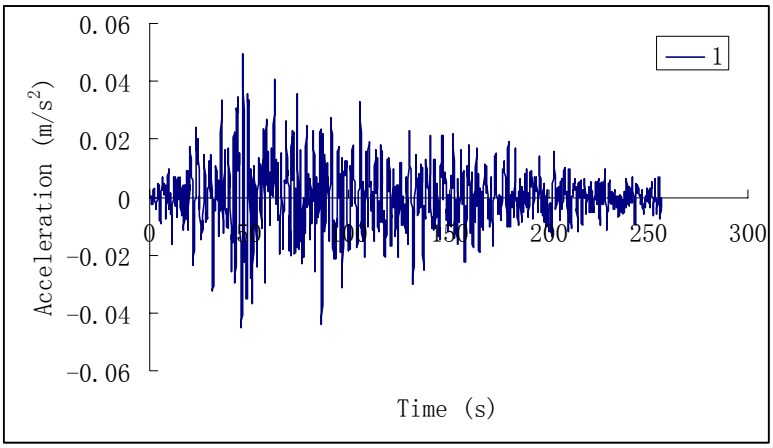

Figure E.1 Bedrock accelerogram for the design earthquake (signal 1)

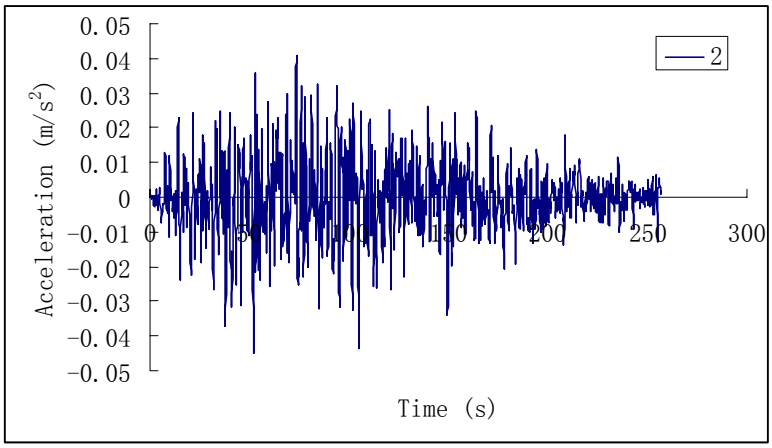

Figure E.2 Bedrock accelerogram for the design earthquake (signal 2)

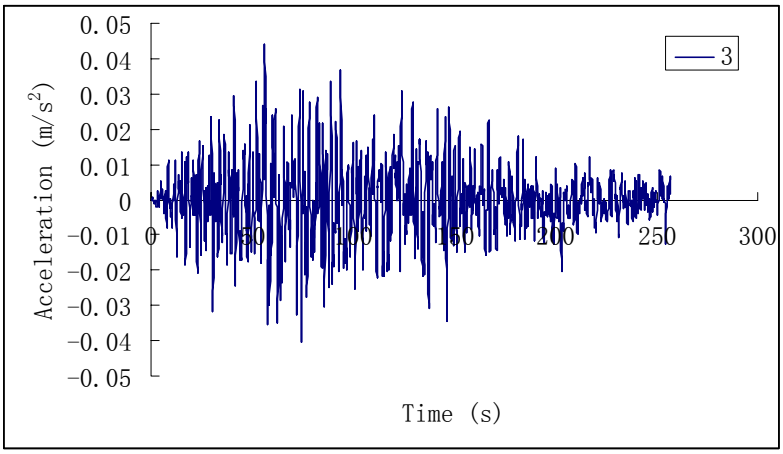

Figure E.3 Bedrock accelerogram for the design earthquake (signal 3)

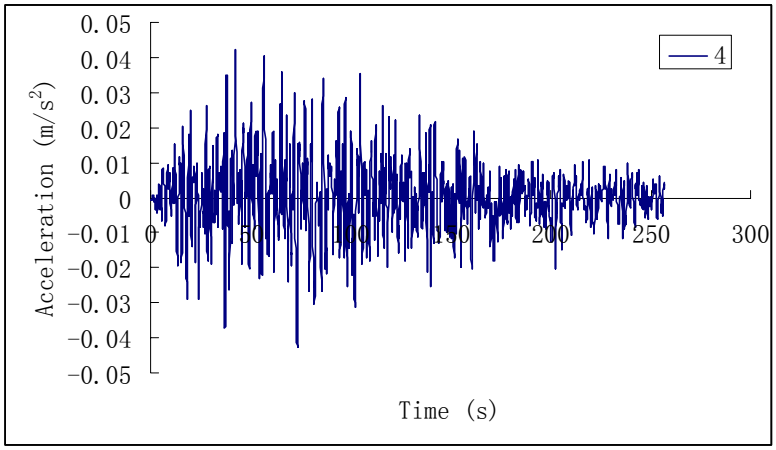

Figure E.4 Bedrock accelerogram for the design earthquake (signal 4)

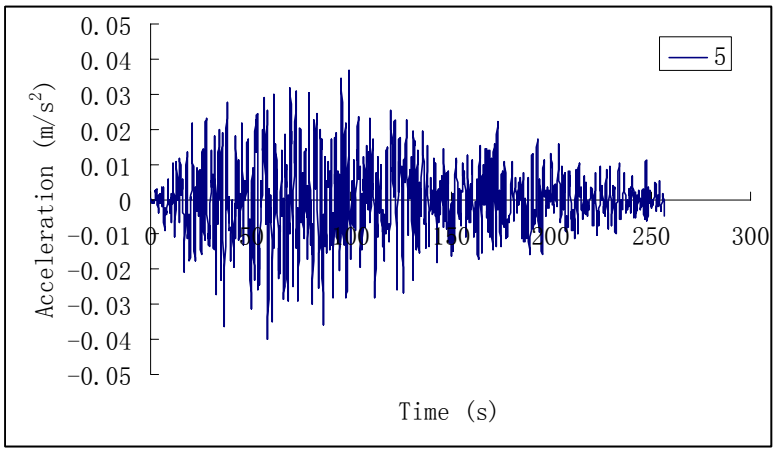

Figure E.5 Bedrock accelerogram for the design earthquake (signal 5)

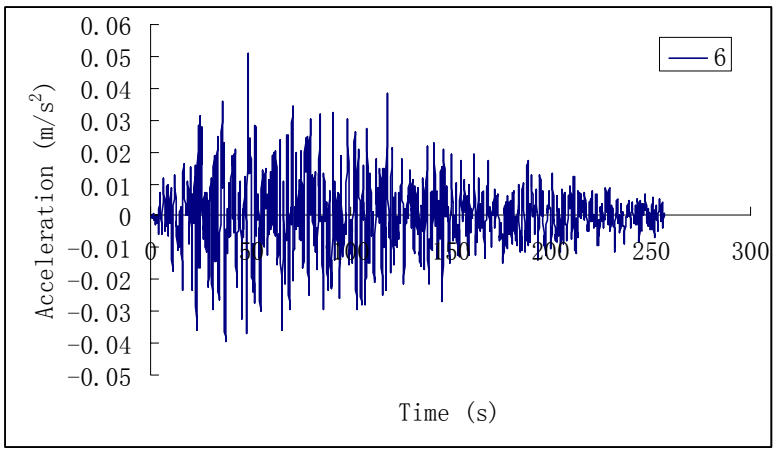

Figure E.6 Bedrock accelerogram for the design earthquake (signal 6)

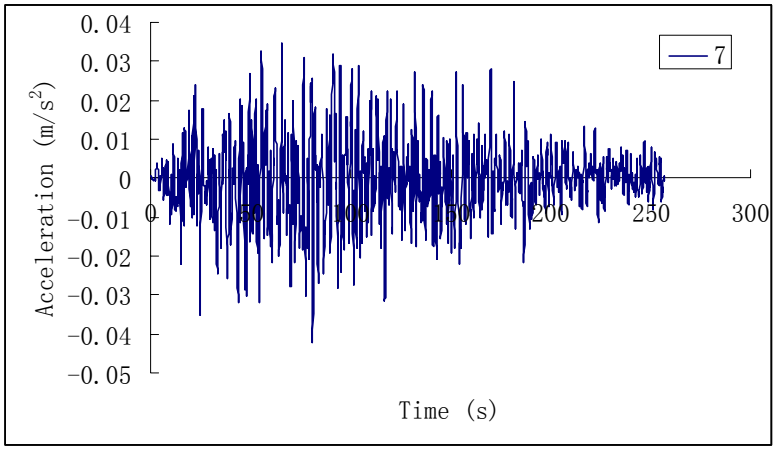

Figure E.7 Bedrock accelerogram for the design earthquake (signal 7)

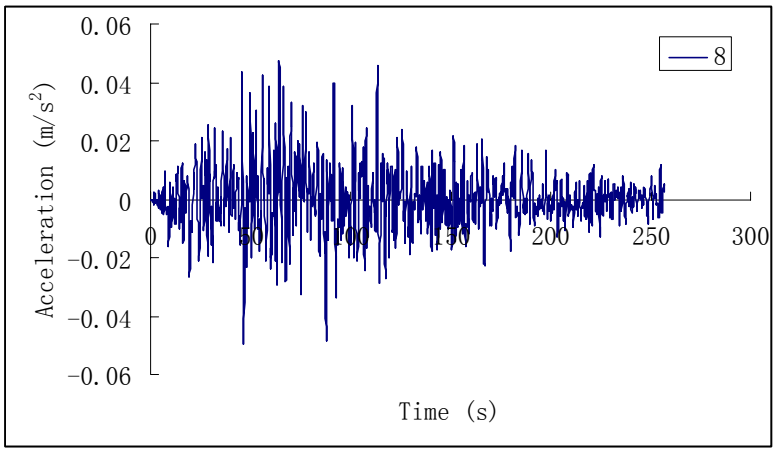

Figure E.8 Bedrock accelerogram for the design earthquake (signal 8)

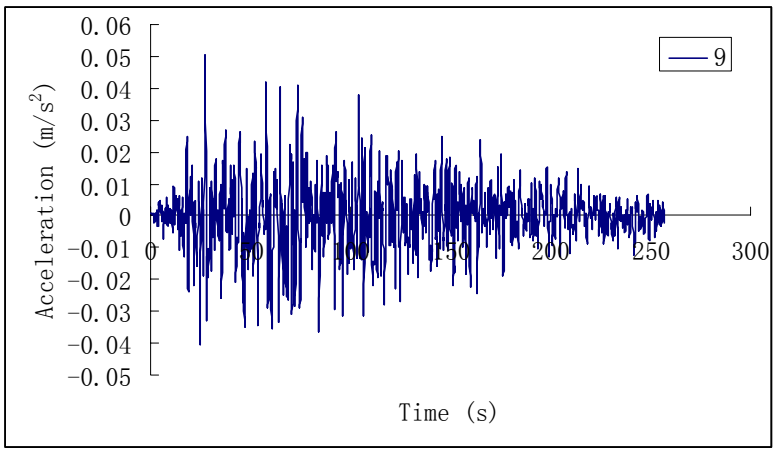

Figure E.9 Bedrock accelerogram for the design earthquake (signal 9)

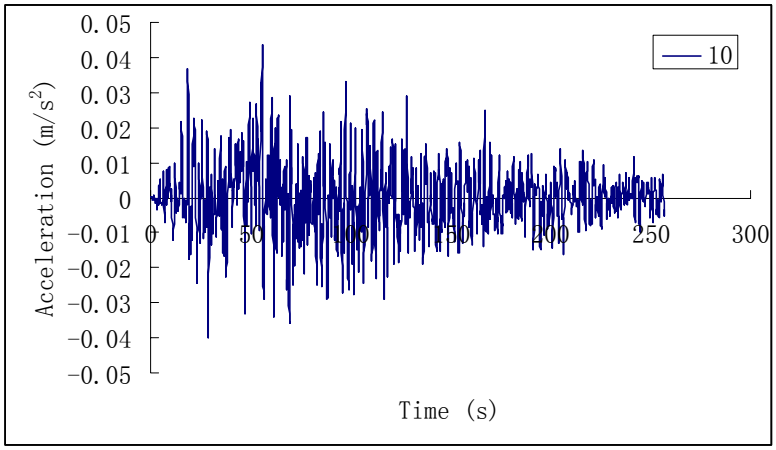

Figure E.10 Bedrock accelerogram for the design earthquake (signal 10)

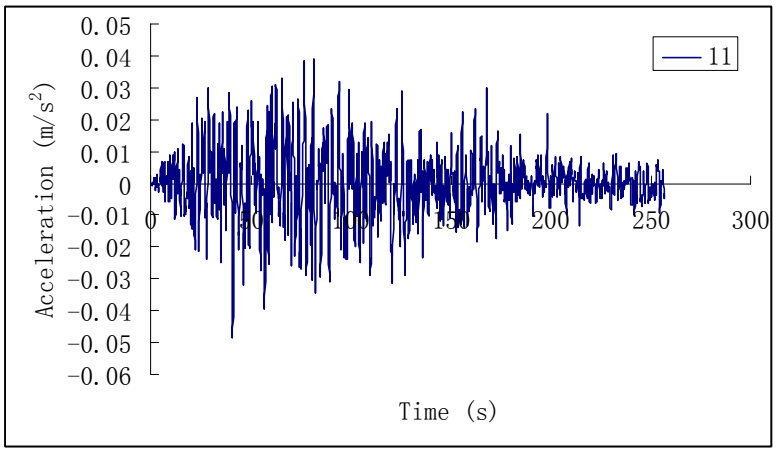

Figure E.11 Bedrock accelerogram for the design earthquake (signal 11)

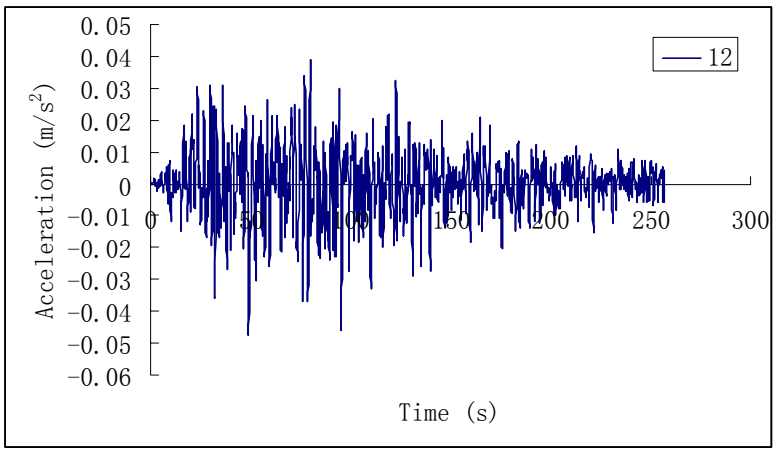

Figure E.12 Bedrock accelerogram for the design earthquake (signal 12)

APPENDIX F INPUT FILES OF SHAKE91

F.1 Input file for the KAP site

```
Option 1 - dynamic soil properties
      1
      3
      8       #1 modulus for clay
0.001     0.01      0.05      0.10      0.20      0.40      0.60      1.0
0.995     0.952     0.800     0.667     0.500     0.333     0.250
0.167
      8       Damping for clay
0.001     0.01      0.05      0.10      0.20      0.40      0.60      1.0
2.55      3.02      4.70      6.17      8.00      9.83      10.75
11.67
      8       #2 modulus reduction for sand
0.001     0.01      0.05      0.10      0.20      0.40      0.60      1.0
0.962     0.714     0.333     0.200     0.111     0.059     0.040
0.024
      8       Damping for sand
0.001     0.01      0.05      0.10      0.20      0.40      0.60      1.0
1.62      5.57      11.67     13.80     15.22     16.06     16.36
16.61
      8       #3 modulus for rock half space
0.0001    0.0003    0.001     0.003     0.01      0.03      0.1       1.0
1.000     1.000     0.9875    0.9525    0.900     0.810     0.725
0.550
      5       Damping in Rock
0.0001    0.001     0.01      0.1       1.0
0.4       0.8       1.5       3.0       4.6
      3     1     2     3
Option 2 -- Soil Profile
      2
      1     9       Kap Site
      1     1          21.32      1493      .050      .111
      2     1          42.64       292      .050      .100
      3     1           6.56      1844      .050      .120
      4     1          29.52       292      .050      .104
      5     1          13.12       468      .050      .104
      6     1          16.40      1673      .050      .120
      7     2          19.35      5508      .050      .136
      8     2          6.232      6698      .050      .141
      9     3                                .010      .141     11475
```

Option 3 -- input motion:

```
      3
 1285 2048     .2        01.prn                                  (8f10.6)
 1                              25.              0       8
```

Option 4 -- sublayer for input motion {within (1) or outcropping (0):

```
      4
      9        1
```

Option 5 -- number of iterations & ratio of avg strain to max strain

```
      5
      0       8       0.85
```

Option 6 -- sublayers for which accn time histories are computed & saved:

```
      6
      1       2       3       4       5       6       7       8       9       9
      0       1       1       1       1       1       1       1       1       0
      1       0       0       0       0       0       0       0       1       0
```

Option 9 -- compute & save response spectra:

```
      9
      9       0
      1       0         9.81
    0.05
```

Option 9 -- compute & save response spectra:

```
      9
      1       0
      1       0         9.81
    0.05
```

Option 10 -- compute & save amplification spectra:

```
     10
     9        0       1       0         0.05          - surface/rock outcrop
```

execution will stop when program encounters 0

```
     0
```

F.2 Input file for the KAT site

```
Option 1 - dynamic soil properties
      1
      3
      8       #1 modulus for clay
0.001       0.01        0.05        0.10        0.20        0.40        0.60        1.0
0.995       0.952       0.800       0.667       0.500       0.333       0.250
0.167
      8       Damping for clay
0.001       0.01        0.05        0.10        0.20        0.40        0.60        1.0
2.55        3.02        4.70        6.17        8.00        9.83        10.75
11.67
      8       #2 modulus reduction for sand
0.001       0.01        0.05        0.10        0.20        0.40        0.60        1.0
0.962       0.714       0.333       0.200       0.111       0.059       0.040
0.024
      8       Damping for sand
0.001       0.01        0.05        0.10        0.20        0.40        0.60        1.0
1.62        5.57        11.67       13.80       15.22       16.06       16.36
16.61
      8       #3 modulus for rock half space
0.0001      0.0003      0.001       0.003       0.01        0.03        0.1         1.0
1.000       1.000       0.9875      0.9525      0.900       0.810       0.725
0.550
      5       Damping in Rock
0.0001      0.001       0.01        0.1         1.0
0.4         0.8         1.5         3.0         4.6
      3     1     2     3
Option 2 -- Soil Profile
      2
      1    5          Kat Site
      1     2            25.91        873        .050       .109
      2     1            91.51        292        .050       .103
      3     1            43.30       1399        .050       .129
      4     1            13.78       4180        .050       .129
      5     3                                    .010       .134       11475
Option 3 -- input motion:
      3
 1285 1800     .2        12.prn                                (8f10.6)
 1                          25.           0      8
Option 4 -- sublayer for input motion {within (1) or outcropping (0):
      4
      5       1
```

Option 5 -- number of iterations & ratio of avg strain to max strain
5
0 8 0.85
Option 6 -- sublayers for which acc. time histories are computed & saved:
6
1 2 3 4 5 5
0 1 1 1 1 0
1 0 0 0 1 0
Option 9 -- compute & save response spectra:
9
5 0
1 0 9.81
0.05
Option 9 -- compute & save response spectra:
9
1 0
1 0 9.81
0.05
Option 10 -- compute & save amplification spectra:
10
5 0 1 0 0.05 - surface/rock outcrop
execution will stop when program encounters 0
0

F.3 Input file for the MP site

```
Option 1 - dynamic soil properties
      1
      3
      8       #1 modulus for clay
0.001       0.01        0.05        0.10        0.20        0.40        0.60        1.0
0.995       0.952       0.800       0.667       0.500       0.333       0.250
0.167
      8       Damping for clay
0.001       0.01        0.05        0.10        0.20        0.40        0.60        1.0
2.55        3.02        4.70        6.17        8.00        9.83        10.75
11.67
      8       #2 modulus reduction for sand
0.001       0.01        0.05        0.10        0.20        0.40        0.60        1.0
0.962       0.714       0.333       0.200       0.111       0.059       0.040
0.024
      8       Damping for sand
0.001       0.01        0.05        0.10        0.20        0.40        0.60        1.0
1.62        5.57        11.67       13.80       15.22       16.06       16.36
16.61
      8       #3 modulus for rock half space
0.0001      0.0003      0.001       0.003       0.01        0.03        0.1         1.0
1.000       1.000       0.9875      0.9525      0.900       0.810       0.725
0.550
      5       Damping in Rock
0.0001      0.001       0.01        0.1         1.0
0.4         0.8         1.5         3.0         4.6
      3     1     2     3
Option 2 -- Soil Profile
      2
      1    10        MP Site
      1     2            19.68         545        .050       .127
      2     1             9.84         292        .050       .105
      3     2             9.84        1202        .050       .116
      4     2             9.84        2165        .050       .123
      5     2             9.84         751        .050       .116
      6     2             9.84        1584        .050       .114
      7     1            29.52        2318        .050       .130
      8     1             9.84        3950        .050       .130
      9     1            21.16        5706        .050       .141
     10     3                                     .010       .141       11475
Option 3 -- input motion:
      3
```

```
 1285 2048      .2         12.prn                                  (8f10.6)
 1                              25.              0       8
Option 4 -- sublayer for input motion {within (1) or outcropping (0):
      4
     10       1
Option 5 -- number of iterations & ratio of avg strain to max strain
      5
      0       8       0.85
Option 6 -- sublayers for which accn time histories are computed & saved:
      6
      1       2       3       4       5       6       7       8       9       10      10
      0       1       1       1       1       1       1       1       1       1       0
      1       0       0       0       0       0       0       0       0       1       0
option 9 -- compute & save response spectra:
      9
     10       0
      1       0         9.81
    0.05
option 9 -- compute & save response spectra:
      9
      1       0
      1       0         9.81
    0.05
option 10 -- compute & save amplification spectra:
     10
     10       0       1       0         0.05           - surface/rock outcrop
execution will stop when program encounters 0
      0
```

APPENDIX G IDENTIFICATION OF GLOBAL FLEXURAL FAILURE

Two types of plastic collapse mechanisms are used to identify the global flexural failure as shown in Figure G.1. A beam sway type collapse mechanisms form if column moment capacities are larger than beam capacities framing into the same joint, and thus plastic hinges form at beam ends and a desired weak beam-strong column performance develops. A column-sway mechanism develops when plastic hinges form at the top and bottom of all columns at one level of a frame.

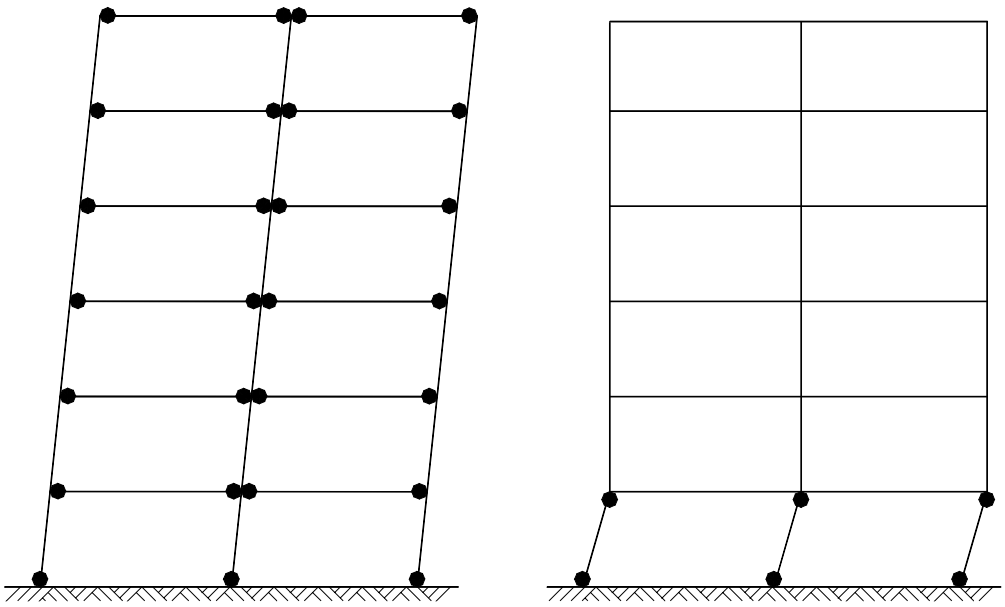

(a) (b)

Figure G.1 Plastic collapse mechanisms: (a) beam sway; (b) column sway (soft story)

APPENDIX H SECTIONAL PROPERTIES OF FEA MODELS IN CASE STUDIES

H.1 Case study 1 : a 25-story reinforced concrete point block

Table H.1 Relationship between members and section numbers

Section No.	Member	No.	Member	No.	Member	No.	Member
1	B1-1	26	B10a	51	C8(20-21)	76	I1(18-25)
2	B1-2	27	C2&3(0-2)	52	C8(22-23)	77	I2(1-2)
3	B2-1	28	C2&3(3)	53	C8(24-25)	78	I2(3-6)
4	B2-2	29	C2&3(4-5)	54	C5(1-2)	79	I2(7)
5	B2-3	30	C2&3(6-7)	55	C5(3)	80	I2(8)
6	B3	31	C2&3(8-9)	56	C5(4-5)	81	I2(9)
7	B4	32	C2&3(10-11)	57	C5(6-10)	82	I2(10-11)
8	B5-1	33	C2&3(12-13)	58	C5(11-13)	83	I2(12)
9	B5-2	34	C2&3(14-15)	59	C5(14-15)	84	I2(13)
10	B5-3	35	C2&3(16-18)	60	C5(16-25)	85	I2(14-25)
11	B6-1	36	C2&3(19-20)	61	C6(1)	86	I3(1-2)
12	B6-2	37	C2&3(21-25)	62	C6(2)	87	I3(3-6)
13	B9-1	38	C4(1-2)	63	C6(3-5)	88	I3(7)
14	B9-2	39	C4(3-10)	64	C6(6)	89	I3(8)
15	B11	40	C4(11-25)	65	C6(7)	90	I3(9)
16	B12	41	C7(1-2)	66	C6(8)	91	I3(10-11)
17	B12a	42	C7(3-6)	67	C6(9)	92	I3(12)
18	B15	43	C7(7-8)	68	C6(10)	93	I3(13)
19	B16	44	C7(9-25)	69	C6(11)	94	I3(14-25)
20	B13	45	C8(1-4)	70	C6(12)	95	L1(1)
21	B14	46	C8(5-7)	71	C6(13-15)	96	L1(2-10)
22	B17-1	47	C8(8-10)	72	C6(16-25)	97	L1(11-25)
23	B17-2	48	C8(11-12)	73	I1(1-3)	98	L2(1)
24	B18-1	49	C8(13-15)	74	I1(4-9)	99	L2(2-10)
25	B18-2	50	C8(16-19)	75	I1(10-17)	100	L2(11-25)

Note: numbers in the parenthesis denote the story levels.

Table H.2 Input parameters of elastic section properties and distributed load (ultimate loading case) in the members.

Section	A(m^2)	J_{xx}(m^4)	I_{zz}(m^4)	I_{yy}(m^4)	Load(kN/m)
1-2	1.62E-01	2.00E-03	1.03E-03	4.55E-04	-11.00
3-5	2.69E-01	3.65E-02	1.34E-03	4.55E-04	-14.60
6	1.31E-01	5.89E-04	8.59E-04	4.55E-04	-7.68
7	2.77E-01	5.07E-02	9.68E-04	4.05E-04	-15.70
8-9	2.88E-01	5.07E-02	1.38E-03	4.55E-04	-16.90
11	1.19E-01	4.63E-04	7.71E-04	4.55E-04	-24.50
12	1.02E-01	4.63E-04	4.49E-04	3.79E-04	-24.50
13-14	1.14E-01	5.89E-04	5.01E-04	3.79E-04	-8.64
15	1.33E-01	6.34E-04	8.75E-04	4.55E-04	-6.95
16	1.68E-01	2.54E-03	1.06E-03	4.55E-04	-4.77
17	8.41E-02	4.43E-04	2.73E-04	3.29E-04	-2.17
18	1.41E-01	5.71E-03	2.83E-04	1.43E-04	-10.80
19	1.41E-01	5.71E-03	2.83E-04	1.43E-04	-11.00
20	1.92E-01	9.70E-03	6.96E-04	3.79E-04	-15.30
21	1.32E-01	1.15E-03	5.63E-04	3.79E-04	-12.60
22-23	1.68E-01	6.86E-03	4.40E-04	3.29E-04	-13.20
24-25	1.68E-01	6.86E-03	4.40E-04	3.29E-04	-9.52
26	7.82E-02	4.43E-04	2.15E-04	3.03E-04	-2.01
27-28	4.18E-01	6.11E-03	3.60E-02	1.78E-03	-12.00
29	3.95E-01	5.72E-03	3.04E-02	1.68E-03	-11.40
30	3.72E-01	6.11E-03	2.53E-02	1.58E-03	-10.70
31	3.48E-01	4.94E-03	2.09E-02	1.48E-03	-10.00
32	3.25E-01	4.54E-03	1.70E-02	1.38E-03	-9.36
33	3.02E-01	4.15E-03	1.36E-02	1.29E-03	-8.70
34	2.79E-01	3.75E-03	1.07E-02	1.19E-03	-8.03
35	2.55E-01	6.11E-03	8.23E-03	1.09E-03	-7.36
36-37	2.32E-01	6.11E-03	6.18E-03	9.89E-04	-6.69
38-40	4.18E-01	6.11E-03	3.60E-02	1.78E-03	-12.00
41-44	2.21E-01	1.80E-03	9.42E-03	5.28E-04	-6.35
45	2.09E-01	1.69E-03	8.01E-03	5.01E-04	-6.02
46	1.92E-01	1.52E-03	6.17E-03	4.59E-04	-5.52
47-48	1.74E-01	1.35E-03	4.64E-03	4.17E-04	-5.02
49-50	1.57E-01	1.19E-03	3.38E-03	3.75E-04	-4.52
51	1.22E-01	8.52E-04	1.59E-03	2.92E-04	-3.51
52-53	1.05E-01	6.87E-04	1.00E-03	2.50E-04	-3.01
54-60	3.72E-01	5.33E-03	2.53E-02	1.58E-03	-10.70
61-64	4.66E-01	1.56E-02	1.50E-02	6.61E-03	-13.40
65	4.45E-01	1.40E-02	1.43E-02	5.75E-03	-12.80
66	4.03E-01	1.09E-02	1.30E-02	4.26E-03	-11.60
67	3.95E-01	1.04E-02	1.27E-02	4.01E-03	-11.40

Section	A(m^2)	J_{xx}(m^4)	I_{zz}(m^4)	I_{yy}(m^4)	Load(kN/m)
68-69	3.43E-01	7.26E-03	1.10E-02	2.62E-03	-9.87
70-71	2.44E-01	2.96E-03	7.86E-03	9.47E-04	-7.03
72	2.55E-01	3.35E-03	8.23E-03	1.09E-03	-7.36
73-76	1.11E+00	1.50E-02	1.77E+00	3.88E-03	-40.70
77-78	3.07E-01	6.16E-03	2.08E-02	1.90E-03	-8.85
79-85	2.30E-01	2.75E-03	1.56E-02	8.03E-04	-6.64
86	7.15E-01	1.62E-02	2.62E-01	4.43E-03	-24.90
87	7.15E-01	1.62E-02	2.62E-01	4.43E-03	-14.00
88-94	5.36E-01	7.01E-03	1.96E-01	1.87E-03	-19.70
95-97	3.72E-01	7.76E-03	3.68E-02	2.30E-03	-10.70
98-100	4.88E-01	1.06E-02	8.33E-02	3.02E-03	-14.00

Table H.3 Parameters for the yield surfaces and bilinear factors of members (the case of f_{cu}=20 MPa and ultimate loading).

Section	*PC* (kN)	*PB* (kN)	MB_z (kN.m)	MB_y (kN.m)	*PT* (kN)	r_z	r_y
1	NA	NA	244.4	58.5	NA	0.007	0.004
2	NA	NA	243.0	58.5	NA	0.002	0.004
3	NA	NA	279.9	82.7	NA	0.015	0.005
4	NA	NA	274.3	61.9	NA	0.004	0.004
5	NA	NA	264.2	61.9	NA	0.011	0.004
6	NA	NA	99.3	61.9	NA	0.012	0.004
7	NA	NA	258.2	64.8	NA	0.001	0.007
8	NA	NA	259.6	78.4	NA	0.013	0.005
9	NA	NA	253.2	78.5	NA	0.001	0.006
10	NA	NA	254.8	98.7	NA	0.004	0.004
11	NA	NA	98.7	45.2	NA	0.011	0.005
12	NA	NA	79.7	44.9	NA	0.012	0.005
13	NA	NA	56.6	26.2	NA	0.011	0.007
14	NA	NA	56.5	26.2	NA	0.010	0.007
15	NA	NA	69.8	31.9	NA	0.010	0.006
16	NA	NA	68.1	31.9	NA	0.010	0.006
17	NA	NA	87.6	44.6	NA	0.012	0.004
18	NA	NA	42.9	18.8	NA	0.011	0.005
19	NA	NA	42.9	18.8	NA	0.011	0.005
20	NA	NA	21.1	21.9	NA	0.013	0.008
21	NA	NA	56.6	31.7	NA	0.011	0.005
22	NA	NA	89.6	38.0	NA	0.012	0.004
23	NA	NA	89.1	32.7	NA	0.008	0.005
24	NA	NA	89.1	32.7	NA	0.008	0.005
25	NA	NA	89.6	38.0	NA	0.012	0.004
26	NA	NA	43.3	25.9	NA	0.012	0.005
27	-11344.3	-3357.4	2835.9	519.5	4392.1	0.003	0.001
28	-10873.5	-3327.8	2812.5	519.5	3904.1	0.003	0.001
29	-10007.8	-3109.7	2372.7	505.2	3416.1	0.003	0.001
30	-9171.6	-2895.4	2061.7	450.2	2958.6	0.003	0.001
31	-8416.3	-2687.6	1831.8	402.4	2585.0	0.005	0.001
32	-7690.5	-2499.8	1473.5	418.6	2241.8	0.009	0.001
33	-6721.8	-2298.5	1122.6	333.3	1647.1	0.011	0.015
34	-6062.2	-2110.7	866.1	319.0	1372.5	0.015	0.016
35	-5240.7	-1908.0	712.1	240.5	930.3	0.013	0.010
36	-4684.0	-1721.6	544.2	211.1	762.5	0.015	0.009
37	-4551.6	-1718.3	526.6	198.8	625.3	0.015	0.009
38	-9130.0	-3248.0	2146.9	445.0	2096.9	0.001	0.001
39	-8622.5	-3230.0	1916.2	397.8	1570.8	0.006	0.007

Section	*PC*	*PB*	MB_z	MB_y	*PT*	r_z	r_y
40	-7989.8	-3202.3	1658.9	339.0	915.0	0.008	0.011
41	-7921.9	-1779.9	1325.6	315.2	4323.5	0.008	0.001
42	-7296.7	-1752.9	1252.9	209.6	3675.4	0.011	0.001
43	-6575.7	-1732.6	1110.6	245.4	2928.1	0.011	0.001
44	-4751.4	-1671.6	743.9	144.7	1037.0	0.015	0.010
45	-6628.4	-1633.8	1118.4	253.2	3187.4	0.020	0.001
46	-6082.2	-1483.9	872.2	232.4	2928.1	0.027	0.001
47	-5315.3	-1319.7	724.4	200.2	2440.1	0.033	0.001
48	-4844.5	-1307.9	724.4	175.8	1952.1	0.011	0.001
49	-4107.0	-1157.7	513.1	145.1	1494.6	0.025	0.001
50	-4136.4	-1154.8	561.1	168.0	1525.1	0.021	0.001
51	-3058.6	-858.0	293.9	105.8	1021.8	0.037	0.001
52	-2490.3	-708.1	192.7	83.9	739.7	0.039	0.001
53	-2424.1	-710.4	192.7	80.4	671.0	0.028	0.005
54	-9142.2	-2893.7	447.2	2112.9	2928.1	0.001	0.001
55	-9142.2	-2893.7	447.2	2112.9	2928.1	0.001	0.001
56	-8340.4	-2874.8	416.4	1759.7	2096.9	0.001	0.001
57	-7568.0	-2843.4	344.7	1562.1	1296.3	0.006	0.005
58	-7214.9	-2843.4	311.9	1357.6	930.3	0.008	0.006
59	-7053.0	-2834.2	296.8	1298.5	762.5	0.007	0.008
60	-6920.6	-2826.6	284.5	1250.2	625.3	0.007	0.012
61	-15968.5	-1657.9	2346.7	2346.7	8338.2	0.001	0.001
62	-15372.6	-1777.2	2292.3	2292.3	7720.6	0.001	0.001
63	-14478.8	-2373.7	2148.3	2148.3	6794.1	0.001	0.001
64	-13585.1	-2457.4	2044.4	2044.4	5867.6	0.001	0.001
65	-13228.5	-1971.4	2056.6	2007.6	5867.6	0.001	0.001
66	-11908.8	-2185.1	1809.2	1571.4	5250.0	0.001	0.001
67	-12074.5	-1818.5	1909.4	1594.4	5558.8	0.001	0.001
68	-10590.8	-1477.2	1763.8	1310.6	4941.2	0.001	0.001
69	-10292.9	-1786.0	1650.0	1275.8	4632.3	0.001	0.001
70	-8317.7	-1252.5	1429.1	772.3	4323.5	0.001	0.001
71	-7721.9	-1252.5	1201.4	734.6	3705.9	0.001	0.001
72	-7322.7	-1955.4	1020.5	434.7	3088.2	0.032	0.006
73	-22836.3	-9170.9	15490.3	702.4	4026.1	0.003	0.001
74	-21137.0	-9011.5	13742.6	613.9	2264.7	0.002	0.001
75	-20607.4	-8959.7	13106.8	586.3	1715.7	0.002	0.001
76	-20276.3	-8808.7	12778.2	569.1	1372.5	0.002	0.024
77	-8187.6	-2604.1	1259.4	465.1	3073.0	0.024	0.023
78	-7746.2	-2355.4	1174.9	424.0	2615.5	0.021	0.024
79	-6881.8	-2035.7	1097.6	234.8	3073.0	0.024	0.001
80	-5690.1	-1862.2	921.8	195.7	1837.7	0.016	0.001
81	-5359.1	-1737.8	858.1	178.5	1494.6	0.012	0.001
82	-5263.5	-1837.0	814.4	173.5	1395.4	0.017	0.001

Section	*PC*	*PB*	MB_z	MB_y	*PT*	r_z	r_y
83	-5182.6	-1920.8	777.5	186.5	1311.5	0.021	0.001
84	-4652.9	-1721.9	675.5	141.7	762.5	0.010	0.001
85	-4586.7	-1790.5	645.3	138.2	693.9	0.018	0.012
86	-17277.1	-6202.4	6077.6	917.1	5314.8	0.001	0.001
87	-16835.7	-5814.4	5736.7	876.0	4857.3	0.001	0.001
88	-14239.6	-4829.3	5195.5	484.5	5314.8	0.001	0.001
89	-12327.0	-4568.3	4358.6	407.9	3332.2	0.001	0.001
90	-11996.0	-4295.0	4122.6	390.6	2989.1	0.002	0.001
91	-11848.9	-4758.5	4171.5	365.7	2836.6	0.008	0.001
92	-11113.3	-4646.1	3777.1	344.7	2074.1	0.007	0.001
93	-10583.6	-4208.9	3399.5	317.1	1525.1	0.006	0.000
94	-10252.6	-4340.6	3270.0	299.9	1181.9	0.008	0.026
95	-7420.8	-2841.1	1252.7	331.3	1143.8	0.001	0.001
96	-7222.2	-2845.7	1239.3	312.8	937.9	0.012	0.009
97	-7156.0	-2787.0	1213.9	306.6	869.3	0.013	0.010
98	-9395.0	-3793.6	2075.1	402.7	1143.8	0.003	0.001
99	-9196.4	-3791.7	2054.8	384.2	937.9	0.008	0.007
100	-9130.2	-3726.9	2014.5	402.7	869.3	0.009	0.010

H.2 Case study 2 : a sub-frame of a 4-story frame building

Table H.4 Parameters of elastic section properties, self-weight of columns, and bilinear factors

Section	A(m^2)	A_s(m^2)	I(m^4)	Self-weight(kN)	r
1	0.12	0.10	0.0020	-18.43	0.075
2	0.12	0.10	0.0020	-16.99	0.056
3	0.18	0.15	0.0067	-13.82	0.115
4	0.18	0.15	0.0067	-11.66	0.084
5	0.22	0.18	0.0122	-16.90	0.116
6	0.12	0.10	0.0020	-7.78	0.100
7	0.12	0.10	0.0020	-7.78	0.065
8	0.20	0.17	0.0092	-15.36	0.131
9	0.20	0.17	0.0092	-12.96	0.104
10	0.18	0.15	0.0007	0.00	0.026
11	0.18	0.15	0.0007	0.00	0.026

Table H.5 Input values to define the yield surface of members

Section	*PYC* (kN)	*PB* (kN)	*MB* (kN.m)	*M1B* (kN.m)	*M2B* (kN.m)	*M0* (kN.m)	*PYT* (kN)
1	-2170.25	-1589.41	128.66	194.25	197.23	110.63	554.65
2	-1987.33	-1478.60	113.47	169.88	164.76	74.64	366.16
3	-2390.54	258.98	405.15	412.44	209.02	739.53	739.53
4	-2921.77	-2249.92	229.16	361.48	347.28	142.42	488.21
5	-3889.09	-3005.09	367.80	590.12	584.68	279.05	924.42
6	-2170.25	-1600.94	129.38	194.17	195.24	102.76	554.65
7	-1987.33	-1492.94	113.28	170.20	161.24	69.72	366.16
8	-3617.09	-2737.98	323.71	507.47	523.81	276.03	924.42
9	-3312.22	-2557.85	284.33	451.22	439.84	188.83	610.26
10	NA	NA	NA	NA	NA	119.25	NA
11	NA	NA	NA	NA	NA	119.25	NA